

NAVAL POSTGRADUATE SCHOOL

Monterey, California



DISSERTATION

**THE CALIFORNIA COASTAL JET: SYNOPTIC
CONTROLS AND TOPOGRAPHICALLY INDUCED
MESOSCALE STRUCTURE**

by

Patrick S. Cross

March, 2003

Dissertation Supervisor:

Wendell Nuss

Approved for public release; distribution is unlimited.

THIS PAGE INTENTIONALLY LEFT BLANK

REPORT DOCUMENTATION PAGE			Form Approved OMB No. 0704-0188	
1. AGENCY USE ONLY (Leave blank)		2. REPORT DATE March 2003	3. REPORT TYPE AND DATES COVERED Doctoral Dissertation	
4. TITLE AND SUBTITLE: The California Coastal Jet: Synoptic Controls and Topographically Induced Mesoscale			5. FUNDING NUMBERS	
6. AUTHOR(S) Patrick S. Cross				
7. PERFORMING ORGANIZATION NAME(S) AND ADDRESS(ES) Naval Postgraduate School Monterey, CA 93943-5000			8. PERFORMING ORGANIZATION REPORT NUMBER	
9. SPONSORING / MONITORING AGENCY NAME(S) AND ADDRESS(ES) N/A			10. SPONSORING / MONITORING AGENCY REPORT NUMBER	
11. SUPPLEMENTARY NOTES The views expressed in this thesis are those of the author and do not reflect the official policy or position of the Department of Defense or the U.S. Government.				
12a. DISTRIBUTION / AVAILABILITY STATEMENT Approved for public release; distribution is unlimited.			12b. DISTRIBUTION CODE	
13. ABSTRACT (maximum 200 words) <p>The low-level jet along the coast of southern Oregon and California is examined in detail through an extensive data set and the application of COAMPS, a mesoscale model, for the purpose of improving forecasts in challenging littoral environments. The jet forms within the broad equatorward flow established by the pressure gradient between cool ocean and warm land. The inception of the jet along the coast is about 250 km south of the axis of a northeastward extension of the eastern North Pacific high, and the jet may extend equatorward and offshore for hundreds of kilometers. Wind magnitudes increase in association with a reorientation of the coastal surface pressure gradient such that an increased down-coast component exists. Within 200 kilometers of the coast, considerable diurnal and spatial variability are observed and predicted by the model. The frequently observed low-level high wind areas at specific locations along the coast are caused by the combined effects of supercritical expansion within the boundary layer and mountain wave-type flow above the marine layer over six coastal mountain areas in close proximity to the coast. While the expansion fan effects are localized near a coastal bend, it is the offshore extension of the mountain wave that accounts for the large spatial extent of the maximum wind areas offshore.</p>				
14. SUBJECT TERMS coastal jet, low-level winds, marine boundary layer, mountain wave, supercritical flow, COAMPS, mesoscale modeling, lee-side wind maxima, topographic effects, orographic effects, expansion fans, littoral meteorology, coastal meteorology			15. NUMBER OF PAGES 195	
			16. PRICE CODE	
17. SECURITY CLASSIFICATION OF REPORT Unclassified	18. SECURITY CLASSIFICATION OF THIS PAGE Unclassified	19. SECURITY CLASSIFICATION OF ABSTRACT Unclassified	20. LIMITATION OF ABSTRACT UL	

NSN 7540-01-280-5500

Standard Form 298 (Rev. 2-89)
Prescribed by ANSI Std. Z39-18

THIS PAGE INTENTIONALLY LEFT BLANK

Approved for public release; distribution is unlimited.

**THE CALIFORNIA COASTAL JET: SYNOPTIC CONTROLS AND TOPOGRAPHICALLY
INDUCED MESOSCALE STRUCTURE**

Patrick S. Cross
Lieutenant Commander, United States Navy
B.S., New Mexico Institute of Mining and Technology, 1982
M.S., Naval Postgraduate School, 1993

Submitted in partial fulfillment of the
requirements for the degree of

DOCTOR OF PHILOSOPHY IN METEOROLOGY

from the

**NAVAL POSTGRADUATE SCHOOL
March 2003**

Author: _____
Patrick S. Cross

Approved by:

_____ Wendell Nuss Associate Professor of Meteorology Dissertation Supervisor	_____ Carlyle H. Wash Professor of Meteorology Dissertation Committee Chair
_____ Leslie K. Rosenfeld Research Associate Professor of Oceanography	_____ Qing Wang Associate Professor of Meteorology
_____ Russell L. Elsberry Distinguished Professor of Meteorology	

Approved by: _____
Carlyle H. Wash, Chair, Department of Meteorology

Approved by: _____
Carson K. Eoyang, Associate Provost for Academic Affairs

THIS PAGE INTENTIONALLY LEFT BLANK

ABSTRACT

The low-level jet along the coast of southern Oregon and California is examined in detail through an extensive data set and the application of COAMPS, a mesoscale model, for the purpose of improving forecasts in challenging littoral environments. The jet forms within the broad equatorward flow established by the pressure gradient between cool ocean and warm land. The inception of the jet along the coast is about 250 km south of the axis of a northeastward extension of the eastern North Pacific high, and the jet may extend equatorward and offshore for hundreds of kilometers. Wind magnitudes increase in association with a reorientation of the coastal surface pressure gradient such that an increased down-coast component exists. Within 200 kilometers of the coast, considerable diurnal and spatial variability are observed and predicted by the model. The frequently observed low-level high wind areas at specific locations along the coast are caused by the combined effects of supercritical expansion within the boundary layer and mountain wave-type flow above the marine layer over six coastal mountain areas in close proximity to the coast. While the expansion fan effects are localized near a coastal bend, it is the offshore extension of the mountain wave that accounts for the large spatial extent of the maximum wind areas offshore.

THIS PAGE INTENTIONALLY LEFT BLANK

TABLE OF CONTENTS

I.	INTRODUCTION	1
A.	DEFINITION.....	1
B.	MOTIVATION	1
II.	BACKGROUND	5
A.	EARLY COASTAL JET STUDIES	5
B.	CALIFORNIA MARINE BOUNDARY LAYER STRUCTURE	6
C.	CALIFORNIA COASTAL JET STRUCTURE AND DYNAMICS.	8
D.	SUMMARY AND DIRECTION.....	16
III.	METHOD.....	25
A.	OVERVIEW	25
B.	DATA.....	25
C.	PERIOD OF STUDY.....	27
D.	THREE-DIMENSIONAL MULTIQUADRIC INTERPOLATION	28
E.	ATMOSPHERIC MODEL	29
IV.	OBSERVATIONAL ANALYSES	35
A.	SYNOPTIC DESCRIPTIONS.....	35
1.	9 and 10 June Event	35
2.	14 and 15 June Event	36
3.	17 and 18 June Event	37
B.	BUOY WINDS	39
C.	REMOTELY SENSED DATA.....	41
D.	PRESSURE GRADIENT ORIENTATION VERSUS OBSERVED WINDS.....	44
V.	COAMPS TM VALIDATION	67
A.	NOGAPS ANALYSES	67
B.	BUOY WINDS	69
C.	CODE DATA.....	72
D.	AIRCRAFT DATA FROM JUNE 1997	74
E.	COASTAL WAVES 1996.....	75
F.	SUMMARY	80
VI.	THE LARGE-SCALE CALIFORNIA COASTAL JET	91
A.	SYNOPTIC CONTROLS ON THE LARGE-SCALE JET.....	91
B.	SPATIAL DISTRIBUTION OF WINDS WITHIN THE COASTAL JET....	96
C.	CROSS-COAST VERTICAL STRUCTURE OF THE JET	99
D.	ALONG-COAST STRUCTURE.....	101

E.	DIURNAL VARIABILITY	105
VII.	DISCUSSION	133
A.	SUMMARY OF FINDINGS	133
B.	IMPACT OF FLOW ABOVE THE MARINE LAYER	135
C.	COMPARISON WITH MOUNTAIN WAVE THEORY	143
VIII.	CONCLUSIONS AND RECOMMENDATIONS	159
A.	PROJECT SUMMARY	159
B.	CONCLUSIONS.....	159
C.	RECOMMENDATIONS FOR FURTHER STUDY	163
	LIST OF REFERENCES	167
	INITIAL DISTRIBUTION LIST	171

THIS PAGE INTENTIONALLY LEFT BLANK

LIST OF FIGURES

- Figure 1.** Conceptual model of the average lower atmosphere in Summer in the eastern North Pacific during periods of persistent north-northwesterly winds (from Beardsley et al. 1987)..... 20
- Figure 2.** Tethered balloon and kite sounding data from Gualala, CA (south of Point Arena) during CODE II from Beardsley et al. (1987). The local times (abscissa) are on 29 July 1982. Wind barbs are in m s^{-1} with each barb representing 2 m s^{-1} . The dashed line indicates the main inversion base. 20
- Figure 3.** Representative example of vertical profiles of wind, potential temperature, and mixing ratio near Point Arena from CODE II (Zemba and Friehe 1987).... 21
- Figure 4.** Schematic from Burk and Thompson (1996) of thermal wind with warm land to the east (right) and cool ocean to the west (left), showing stronger wind with decreasing altitude from a relatively level upper pressure surface. Friction below creates characteristic jet wind profile. 21
- Figure 5.** Along-shore wind component during CODE I and II from Beardsley et al. (1987). Sea Ranch is located nearest to the coast, while C5 is a buoy farthest from shore. Note the predominance of down-coast winds, interrupted by a periodic wind relaxation events. The focus of the present study is on this down-coast wind regime. 22
- Figure 6.** Winant et al. (1988) model of marine layer structure in the vicinity of Point Arena from the CODE data. Note the deeper marine layer upstream, followed by a shallowing at the turn and increase in wind speed, followed by a hydraulic jump to slower winds and deeper marine layer downstream. This model does not consider changes above the marine layer. 22
- Figure 7.** Fields from the Navy Operational Regional Atmospheric Prediction System (NORAPS) from 21 July 1992 (Burk and Thompson, 1996): (a) cross-sections along 38°N of winds (top) and potential temperature (bottom), and (b) a horizontal view of winds at 425 m. 23
- Figure 8.** Map showing key locations discussed in this study, including NOAA moored buoys, wind profilers, key land stations, significant coastal mountains, and offshore coast-parallel cross-section locations. 31
- Figure 9.** A typical NOAA moored buoy. Note the anemometer on top of the buoy at a height of 5 m. 32
- Figure 10.** Buoy wind (m s^{-1}) time series from NOAA buoy 46028 (Buoy 28). Time scale is Pacific Daylight Time. Note distinct high wind events of 9-10 and

17-18 June 1996, with weaker winds between. Vertical lines bracket the time periods for the three COAMPS runs in this study.	32
Figure 11. COAMPS horizontal grid domains (a) and a depiction of the lower 37 of 45 vertical levels (b) for the three model runs in this study. Above 4500 m are 8 more levels at 5500, 7000, 9000, 11000, 13000, 15000, 17000, and 19000 m.	33
Figure 12. NOGAPS 500 mb height analyses from (a) 0000 UTC 9 June, (b) 1200 UTC 9 June, (c) 0000 UTC 10 June, and (d) 1200 UTC 10 June 1996.....	48
Figure 13. NOGAPS 850 mb height analyses from (a) 0000 UTC 9 June, (b) 1200 UTC 9 June, (c) 0000 UTC 10 June, and (d) 1200 UTC 10 June 1996.....	49
Figure 14. NOGAPS sea-level pressure analyses from (a) 0000 UTC 9 June, (b) 1200 UTC 9 June, (c) 0000 UTC 10 June, and (d) 1200 UTC 10 June 1996...	50
Figure 15. NOGAPS 500 mb height analyses from (a) 0000 UTC 14 June, (b) 1200 UTC 14 June, (c) 0000 UTC 15 June, and (d) 1200 UTC 15 June 1996.....	51
Figure 16. NOGAPS 850 mb height analyses from (a) 0000 UTC 14 June, (b) 1200 UTC 14 June, (c) 0000 UTC 15 June, and (d) 1200 UTC 15 June 1996.....	52
Figure 17. NOGAPS sea-level pressure analyses from (a) 0000 UTC 14 June, (b) 1200 UTC 14 June, (c) 0000 UTC 15 June, and (d) 1200 UTC 15 June 1996.....	53
Figure 18. NOGAPS 500 mb height analyses from (a) 0000 UTC 17 June, (b) 1200 UTC 17 June, (c) 0000 UTC 18 June, and (d) 1200 UTC 18 June 1996.....	54
Figure 19. NOGAPS 850 mb height analyses from (a) 0000 UTC 17 June, (b) 1200 UTC 17 June, (c) 0000 UTC 18 June, and (d) 1200 UTC 18 June 1996.....	55
Figure 20. NOGAPS sea-level pressure analyses from (a) 0000 UTC 17 June, (b) 1200 UTC 17 June, (c) 0000 UTC 18 June, and (d) 1200 UTC 18 June 1996.....	56
Figure 21. Buoy wind time series during June 1996 as in Fig. 10. Plots are presented from north to south, beginning with (a) Buoy 27 near the Oregon border and progressing to (i) Buoy 23 west of Point Conception. Winds are in m s^{-1} and time is PDT, with the tick mark for each day representing 0000 PDT on that day. Vertical lines again indicate the three model study periods.	57,58

Figure 22a.	Visible satellite imagery from GOES-9 at 0830 (top) and 1700 (bottom) PDT 9 June 1996.....	59
Figure 22b.	Visible satellite imagery from GOES-9 at 0830 (top) and 1700 (bottom) PDT 14 June 1996.....	60
Figure 22c.	Visible satellite imagery from GOES-9 at 1030 (top) and 1700 (bottom) PDT 17 June 1996.....	61
Figure 23a.	Vertical wind profiler data from Bodega Bay from 8-10 (top), 13-15 (middle), and 16-18 (bottom) June 1996. Location is shown in Fig. 8...	62
Figure 23b.	As in Fig. 23a, except for the Fort Ord profiler.	63
Figure 23c.	As in Fig. 23a, except for the Piedras Blancas profiler.	64
Figure 24.	Wind speeds at Buoy 28 (blue) as in Fig. 10, and pressure difference (mb) between Buoy 28 and Buoy 42 (green). Positive values indicate down-coast pressure gradient.	65
Figure 25.	As in Fig. 24, except pressure difference is between Buoy 28 and Naval Air Station Lemoore, CA. Positive values indicate cross-coast gradient directed toward land.....	65
Figure 26.	Surface pressures (mb) at Buoy 28 (top) and Lemoore (middle), and pressure difference between the two (bottom). Absolute pressure difference is obtained by subtracting 980 from the plotted values.	66
Figure 27.	36-h predictions from the 81 km outer domain of COAMPS, including (a) 850 mb heights valid at 1200 UTC 10 June, (b) sea-level pressure valid at 1200 UTC 10 June, (c) 850 mb heights valid at 1200 UTC 15 June, (d) sea-level pressure valid at 1200 UTC 15 June, (e) 850 mb heights valid at 1200 UTC 18 June, and (f) sea-level pressure valid at 1200 UTC 18 June 1996. Contour interval and domain match Figs. 12-20 for direct comparison.	82,83
Figure 28.	Isotachs of winds at 990 mb from the inner COAMPS nest valid at 1900 PDT on (a) 9, (b) 14, and (c) 17 June 1996. Color shading begins at 12 m s^{-1} to indicate approximate outer boundary of coastal jet winds.....	83, 84
Figure 29.	Comparison of observed (o) surface winds at Buoy 28 with the COAMPS predictions (x) during the 12-36-h period for the events of (a) 9-10 June, (b) 14-15 June, and (c) 17-18 June 1996.	85
Figure 30.	Comparison of (a) CODE 33-m measured wind speed (m s^{-1}) between 1400 and 1600 PDT 26 July 1982 in the vicinity of Point Arena (from Beardsley et al., 1987), (b) COAMPS prediction of 10-m winds in the same area	

	valid at 1500 PDT 9 June 1996, and (c) 33-m measured winds from 17 May 1982 (from Winant et al. 1988).	86
Figure 31.	East-west cross-sections along 37.5°N, with the eastern end near the Santa Cruz Mountains, of (a) aircraft measured winds (m s^{-1}) from 13 June 1997 (from Parrish 2000) and (b) COAMPS winds valid at approximately the same time of day on 14 June 1996.	87
Figure 32.	An example from Rogers et al. (1998) of 30-m winds measured near Cape Mendocino during Coastal Waves 96. The distinct wind minimum to the north and maximum in the lee are quite similar to the COAMPS predictions from the current study at this location.	88
Figure 33.	Direct comparison of winds near Point Sur on 17 June 1996 (a) as measured from aircraft during Coastal Waves 96 from 1200-1800 PDT (from Dorman et al. 1999), and (b) from the COAMPS inner nest valid at 1600 PDT. Measured winds are adjusted to 10 m and model winds are at 10 m.	88
Figure 34.	Along-coast cross-sections (see dotted lines paralleling the coast in Fig. 33a) of winds (m s^{-1}) and potential temperature (K) near Point Sur during the afternoon of 17 June 1996. Cross-sections (a) and (c) are along the innermost line from Dorman et al. (1999) measurements and from COAMPS (valid 1700 PDT), respectively, while (b) and (d) are along the offshore line. Light lines are winds and dark lines are θ	89
Figure 35.	Cross-sections of winds (m s^{-1}) and potential temperatures (K) along 39.9°N near Cape Mendocino from (a) Strom et al. (1999) aircraft measurements on 12 June 1996 and (b) the COAMPS simulation valid at 1100 PDT 14 June 1996. Winds are shown as gray shades in (a) and color shades in (b).	90
Figure 36.	COAMPS 850 mb heights (m, 15-m interval) from the 27-km nest, with isotachs at 980 mb (shaded above 12 m s^{-1}) from the 9-km nest, valid at 1900 PDT on (a) 9, (b) 14, and (c) 17 June 1996.	112, 113
Figure 37.	1000 mb isotachs (m s^{-1}) from COAMPS valid at 1700 PDT 14 June 1996, with color shading above 18 m s^{-1} to highlight areas of highest winds along the coast. Also shown with color shading are the terrain heights above 400 m with a 200-m contour interval.	114
Figure 38.	East-west cross-sections from COAMPS valid at 1900 PDT 9 June 1996 of winds (solid lines, 1 m s^{-1} contour interval, color shading above 12 m s^{-1}) and potential temperatures (dashed lines, 1 K contour interval) along (a) 42°N, (b) 41°N, (c) 40°N, (d) 39°N, (e) 38°N, (f) 37°N, (g) 36°N, (h) 35°N, and (i) 34°N.	115-119
Figure 39.	As in Fig. 38, except for 1900 PDT 14 June 1996.	120-124

Figure 40. Near-shore along-coast cross-section (shown in Fig. 8) from COAMPS valid at 1900 PDT on (a) 9 June and (b) 14 June 1996. The plot convention is the same as the cross-coast sections in Figs. 38-39.	125
Figure 41. As in Fig. 40, except along an offshore section (parallel, but 50 km farther from shore) that is shown in Fig. 8.	126
Figure 42. 1000 mb isotachs (m s^{-1} , color shading above 18 m s^{-1}) from COAMPS valid at (a) 0500, (b) 1100, and (c) 2000 PDT 9 June 1996.	127
Figure 43. Cross-sections of COAMPS winds (solid, m s^{-1}) and potential temperature (dashed, K) along 35°N (as in Fig. 38h), valid at (a) 0500, (b) 1100, and (c) 2000 PDT 9 June 1996. Winds above 18 m s^{-1} are color shaded. ...	128
Figure 44. As in Fig. 43, except cross-section is along 39°N	129
Figure 45. As in Fig. 43, except cross-sections are valid at (a) 0500, (b) 1100, and (c) 2000 PDT 14 June 1996.	130
Figure 46. As in Fig. 45, except cross-sections are along 39°N	131
Figure 47. Along-coast cross-sections of winds (solid, m s^{-1} , shaded above 12 m s^{-1}) and potential temperatures (dashed, K) valid at 0500 PDT on (a) 9 June, and (b) 14 June 1996. Cross-sections are in the same position as those in Fig. 40.	132
Figure 48. Along-coast cross-sections of scalar tangent winds (solid, m s^{-1} , 2 m s^{-1} contour interval) and potential temperatures (dashed, K, 2K contour interval) from COAMPS beginning over land in southern Oregon, crossing over water off northern California, and crossing Cape Mendocino near Taylor Peak. Sections are valid at 1900 PDT on (a) 9 and (b) 14 June 1996.	148
Figure 49. As in Fig. 48, except cross-section begins over land near Point Arena, crosses near Cold Spring Mountain, and ends over water to the south of the point.	149
Figure 50. As in Fig. 48, except cross-section crosses over the Santa Cruz Mountains, Monterey Bay, and Mount Carmel in the northern Santa Lucia Mountains.	150
Figure 51. As in Fig. 48, except cross-section begins over Monterey Bay, crosses the northern Santa Lucia Range, and crosses the coast at an oblique angle along the Big Sur coast.	151
Figure 52. As in Fig. 48, except cross-section begins over the mountains northeast of Point Conception and emerges over water east of the point.	152

Figure 53. 850 mb wind (arrows, length proportional to speed) and 1000 mb isotachs (2 m s^{-1} contour interval) from COAMPS for the northern portion of the coast from southern Oregon to northern California, valid at 1900 PDT on (a) 9, (b) 14, and (c) 17 June 1996.	153,154
Figure 54. As in Fig. 53, except for the central portion of the coast.	155
Figure 55. As in Fig. 53, except for the southern portion of the coast.....	156,157
Figure 56. Theoretical mountain wave solutions for the case of (a) a sinusoidal series of infinite mountain ridges with $aL \ll 1$, (b) a sinusoidal series of mountains with $aL \gg 1$, and (c) a bell-shaped ridge (from Durran 1986).	158

THIS PAGE INTENTIONALLY LEFT BLANK

ACKNOWLEDGMENTS

This project was long in the making. Much time was spent in developing the analysis technique, a process that took far longer than anticipated due to complex coding challenges. I left NPS to continue my Navy career at sea, hoping to be able to wrap up the work in my spare time. A busy sea tour, as it turns out, offers little in the way of spare time, and only very slow additional progress was made during that time. Finally, with final setup problems worked out in March 2002, I was able to spend considerable time focused on bringing the effort to some scientific conclusions.

Perhaps the delays in completing the work have made me even more thankful than I would otherwise have been to those who have helped me get here. First, I simply would not have been able to reach completion without the countless hours spent in conference with Wendell Nuss, my principal advisor and dissertation supervisor. In addition to being the primary developer of the analysis technique, his help as a scientific sounding board was indispensable. Toward the end, he juggled heavy teaching and research loads and still managed to provide timely critiques of my work and address some challenging figure generation issues. I also received invaluable assistance from Doug Miller, who worked out the mechanics of running COAMPS for my cases. Doug was helpful as someone off whom to bounce scientific ideas, and he provided many helpful insights in the preparation of the dissertation. Professor Chuck Wash, Meteorology Chairman, also helped out by providing me with office space, technical and administrative assistance, procedural advice, and moral support during my periodic visits to Monterey during the last year.

I thank the other members of my committee, Qing Wang, Leslie Rosenfeld, and Russell Elsberry for their timely and thorough reviews of my work, and also for their encouragement along the way. Professors Terry Williams and Ken Davidson also helped out by providing frequent injections of encouragement at times when it started to feel hopeless. And I pay tribute here to Mr. Forrest Williams, former meteorology instructor at NPS, whose love of the science of meteorology was a true inspiration. Not to be overlooked, Chuck Wash and Leslie Rosenfeld provided a couple of excellent meals along the way when I was a geographic bachelor in Monterey.

I received immense support from the staff of the Meteorology Department. First and foremost was Bob Creasey, who was constantly offering ideas on how to keep the work moving from remote locations. When it came to preparation of the dissertation, Bob assisted by creating several key figures, helping me learn the tools I needed for analysis and visualization, and teaching me the fine points of UNIX, FTP, GARP, GEMPAK, and various other acronyms I had washed my hands of. Mary Jordan answered my MATLAB questions every time. The folks in the Meteorology front office were always cheerful and eager to help. In particular, Michael Vinluan did large quantities of scanning and copying for me, always with short deadlines looming. In the final stages of document preparation, when my stress was reaching panic levels, I discovered Tamar Neta, who calmly figured out my lingering document formatting problems. Her help in getting my document through final processing was indispensable.

I would be remiss if I failed to acknowledge the support provided by my current command, COMSUBPAC, in the last few months. Recognizing the value of completing this degree (to me personally, but more importantly to the Navy), RADM Padgett and CAPT Thieman have graciously allowed me (or is that ordered me?) to spend considerable time away from my desk to finish it up. Since so much of the work had to be done in Monterey, I absolutely could not have done it without that time allowance.

I wish to thank my family. My parents, who are responsible for, among other things, my intellectual curiosity, have agonized along with me throughout the last several years. They have felt the impact of the delayed completion on my career, my life, and my emotional state, and they always kept me going. My brother Charley was also a strong supporter, and provided valuable assistance in the final stages by scanning some documents and providing some much needed computer advice. My sisters Carol and Anita always knew I could finish, even when I lost sight of that. My children, Ian, Colin, and Kari, have grown into adults during this process and I offer them my apologies for not being as available as I could have during certain phases of the project or the following sea tour.

Lastly, I thank my wife Marie for her continual love and support during the last several years. The stress involved with the delays while at NPS, having to leave without the degree, completing an arduous sea tour with it hanging over me, and the time away

from home during the last few months have all been extremely difficult to bear. Marie was always there for me, and kept picking me back up. She supported me regardless of what I accomplished, and never doubted I could finish if given the opportunity. I love her, and I thank her from the bottom of my heart.

THIS PAGE INTENTIONALLY LEFT BLANK

I. INTRODUCTION

A. DEFINITION

A coastal jet is a low-tropospheric wind feature driven by the pressure gradient produced by a sharp contrast between high temperatures over land and lower temperatures over the sea. As will be seen in the next chapter, coastal jets occur in all areas of the world where such contrasts exist. This study will examine the behavior of the jet off the coast of California, where it is quite well defined from early May through September each year, but can occur at other times of the year as well. While coastal jets have been observed and described in a variety of studies published in the literature, their behavior has not adequately been tied to synoptic-scale meteorology. That is, the link between the synoptic-scale weather patterns and mesoscale features of the jet has not been fully established, which inhibits any real low-level wind forecast skill from being achieved. In the case of the California coastal jet, several studies have examined jet behavior near specific capes and points. However, no comprehensive effort has been made to describe its large-scale spatial or temporal variability. Thus, the intent of this study is both to provide that description of the variability of the California coastal jet during a study period representative of the summer season and to relate that variability to changes in the synoptic pattern. In the process, a clearer understanding of the nature of the coastal winds as they interact with significant topographic features along the coast will be obtained.

B. MOTIVATION

Improved understanding of the California coastal jet is an essential piece of the broader need to better describe and predict coastal processes in both the ocean and atmosphere. Winds in the core of the jet (above the surface) have been measured in excess of 32 m s^{-1} (Zemba and Friehe 1987) and modeled in this and other studies in peak areas as high as 38 m s^{-1} . Associated surface winds routinely exceed 15 m s^{-1} . The jet is a broad feature that extends well offshore and along the coast from Oregon to Southern California. It is a persistent feature of the spring to fall wind pattern. It is thus impossible to understand and accurately forecast warm season weather near the coast

without a better understanding of coastal jet variability. These forecasts are of great importance to fishermen, recreational boaters, and the merchant fleet in this heavily utilized marine environment. Given that modern Naval operations are so often conducted in littoral waters, improvements in our understanding of coastal wind patterns will lead directly to improvements in forecasts that are critical to tactical planning. Meteorological parameters relevant to Naval operations include winds, visibility, ceiling heights (all essential to carrier and other aviation forecasts), moisture and aerosol distribution, electromagnetic and electro-optical propagation characteristics, sea state, and surf conditions. When the high winds of the jet reach down to the surface, the potential exists for winds that could be dangerous to a variety of marine operations (Reynolds 1998). Improvements in the general forecast of jet location and magnitude will undoubtedly lead to higher confidence in surface wind forecasts and increased safety for the users of such forecasts.

A close tie also exists between the spatial distribution of coastal winds and the nature of stratus cloud cover. While other processes (e.g., large-scale subsidence and turbulent processes in the boundary layer) are important in determining the distribution of summertime stratus, an accurate representation of the low-level wind field is essential. Specifically, clearing patterns associated with decreases in marine layer depth on the large scale and on smaller scales near major coastal topography are both potentially related to the low-level wind patterns. Thus, coastal stratus and jet behavior are closely linked and it is expected that this study will yield greater insights into the forecast of the stratus distribution in coastal areas. While it is not a specific goal of this study to carefully analyze coastal cloud patterns, improved understanding of coastal winds promises to contribute to understanding of coastal stratus as well.

Finally, the persistent along-shore winds of the coastal jet are translated to the ocean surface in the form of high wind stresses that in conjunction with earth rotation cause surface waters to be displaced offshore. That surface water is replaced by cold, nutrient-rich water upwelled from below. The importance of this upwelled water to the fishing industry and to the habitat of an enormous diversity of marine life, as well as a feedback effect on coastal meteorology, has led to many studies of controls and behavior along the California coast and in other areas of the world where upwelling is a feature of

the ocean circulation. Such studies are limited by the quality of the wind forcing used in ocean models. Thus, any modeling study of ocean processes, particularly in coastal upwelling areas, would benefit from surface forcing that more accurately represents the location of specific wind features, particularly those that are tied to the coastal topography and are thus quite persistent. This forcing will allow more accurate representations of upwelling characteristics, surface and subsurface currents, ocean mixed layer dynamics, and other processes.

THIS PAGE INTENTIONALLY LEFT BLANK

II. BACKGROUND

To properly define the relevance of the present study, a review of existing papers on the broad subjects of California marine boundary layer (MBL) characteristics and coastal jets is presented here. The current state of knowledge of these wind features will be described, together with a clear description of the voids in that knowledge that this study will fill.

A. EARLY COASTAL JET STUDIES

Jet-shaped wind profiles in areas of coastal upwelling have been observed in the course of several studies. A particularly strong jet was observed by Bunker (1965) off the coast of Somalia. Surface winds of 12 m s^{-1} increasing to 25 m s^{-1} at 1000 m were measured by aircraft in his study. Strong baroclinity between the hot air on land and the air overlying the cold, upwelled waters were thought to be the cause of this jet. Johnson and O'Brien (1973) and Elliott and O'Brien (1977) studied a much weaker, but structurally similar jet off the coast of Oregon. A. Miller (in Lester 1985) examined winds off the San Francisco Bay using tracked balloons and found a wind maximum near the base of a strong marine inversion. This was again explained as being due to strong baroclinity as a result of heating over the adjacent land. Using land station data from the Peruvian coast, Enfield (1981) found a 5 m s^{-1} jet at 200 m at the coastline and proposed a positive feedback mechanism, in which increased winds led to an increase in the magnitude of the upwelling, which led to colder surface waters and stronger baroclinity, and thereby enhanced the jet. More recent work by Burk and Thompson (1996), the current study, and others appear to refute such a positive feedback with the sea surface as being a significant contributor to MBL structure or jet behavior.

Low-level jets have also been found over oceanic waters farther offshore. Grossman and Friehe (1986) described a jet in the Arabian Sea that occurred under monsoonal conditions, with the structure of the wind maximum in the vertical caused by friction below and thermal wind effects above. Similarly, Gerber et al. (1989) studied the winds at San Nicholas Island off southern California in the wake of a Santa Ana offshore wind event as conditions returned to more normal westerly flow. They found a jet that

was also associated with baroclinic effects in a sloping inversion. In this case, the downward sloping inversion to the north was associated with a broader regional sea-surface temperature gradient with warmer waters to the southeast. Thus, the jet they describe, while located in a coastal regime, is not truly a coastal jet in that it does not require a land-sea temperature contrast and could occur in other ocean areas where there are significant surface thermal gradients that lead to sloping inversion heights. Such jets are also far less likely to produce the high winds associated with a true coastal jet near a hot interior where the associated thermal contrasts occur over a much shorter distance.

B. CALIFORNIA MARINE BOUNDARY LAYER STRUCTURE

The subtropical anticyclone that predominates in the eastern Pacific for much of the summer establishes the basic structure of the marine boundary layer during that season. The high is typically centered about 1000 km west of northern California at an average latitude of 40°N (Beardsley et al. 1987), and a thermal low exists over the southwestern United States that extends on most days northwestward up the Central Valley of California. Thus, the California coast is between these two strong forcing regimes, which produces northerly to northwesterly coast-parallel geostrophic winds in the lower atmosphere along the coastline. Subsiding dry air on the eastern flank of the eastern North Pacific high warms adiabatically and comes in contact with cool, moist marine air near the surface, which forms an inversion that persists throughout almost the entire warm season, with the exception of infrequent short-wave passages.

The inversion tends to slope upward offshore due to the combination of increasing sea-surface temperatures (SSTs) and weakening synoptic-scale subsidence to the west (Beardsley et al. 1987). Lowest SSTs are generally located close to shore due to the previously discussed upwelling. Farther to the west, a dramatic increase in SST occurs beyond about 20-80 km, followed by a more gradual increase westward to the vicinity of the Hawaiian Islands. The higher SSTs increase the heat flux from the ocean to the atmospheric boundary layer, which, combined with decreasing subsidence aloft, promotes greater vertical mixing of heat energy with increased distance from the coast. The combination of greater heating from below and reduced subsidence from above results in a downward sloping inversion base toward the coast. Beardsley et al. (1987)

point out that daytime return flow of warm air from land to sea above the inversion subsides and acts to further depress the inversion near the shore than might be expected from the combination of upper-level subsidence and low SST. The downward slope of the inversion from the west toward the coast thus becomes steeper close to shore as the previously described forcing interacts with local sea breeze circulations. Beardsley et al. (1987) present a schematic (Fig. 1) of the key elements of this structure as seen in the Coastal Ocean Dynamics Experiment (CODE), which was an intensive investigation of the coastal upwelling regime between Point Arena and Point Reyes in northern California conducted in the spring and summer of 1981 and 1982. Whereas the height of the inversion base averages around 400 m along that part of the coast, it reaches above 1500 m farther west. The inversion height near the shore was such that the top of the marine boundary layer was generally well below the tops of the mountains that border that portion of the coast.

Near the coast, the inversion height has been shown by Beardsley et al. (1987), Zemba and Friehe (1987), and Burk and Thompson (1996) to exhibit considerable diurnal changes. These studies show that the coastal inversion is most shallow in the afternoon, when daytime heating of the land causes onshore winds with low-level divergence in the boundary layer over the ocean, and the compensating subsidence, in accordance with the continuity equation, lowers the inversion height. This effect, which is closely tied to subsiding return flow from the sea breeze circulation, creates inversions as low as 30 m in some daytime cases (Winant et al. 1988). As insolation ceases in the evening, the boundary layer deepens over the ocean (close to shore) and quickly reaches nighttime levels of up to several hundred meters higher than during the day. Tethered balloon data from a land station in CODE (Fig. 2) revealed minimum inversion heights near 60 m in the late afternoon coincident with the time of maximum northwesterly winds. By 1800 PST, the inversion lifted to 190 m and the winds near the surface dropped to near zero (Beardsley et al. 1987). These inversion heights are low compared with typical values of 200-800 m as measured in recent years at the Fort Ord profiler site (near Monterey) well south of the CODE region, which suggests significant along-coast variability in marine layer structure. Examination of recent radio acoustic sounder system (RASS) data from other profilers along the coast shows further evidence of this variability.

Much of the published California coastal jet knowledge base is derived from the data collected during the two phases of CODE. No thorough treatment of the coastal jet and marine boundary layer variability along the entire coast has yet been published in the literature.

The cloud patterns typical of the eastern Pacific warm season are directly tied to this boundary layer structure. An area of low stratus often extends well offshore and frequently comes ashore in the evening hours as the marine layer deepens near the coast. During the day, land areas usually clear of fog as the coastal inversion is depressed and surface heating mixes the moisture vertically and reduces the relative humidity of the entire column below the saturation point. This clearing may extend offshore later in the diurnal cycle when the inversion height depression, to a level below that of the lifting condensation level, extends farther offshore, or when drier air is advected offshore and mixed with the moist MBL air.

The nature of the coastal clearing appears to be strongly dependent on the characteristics of the low-level flow. Burk and Thompson (1996) hypothesize that flow acceleration and deceleration in the coastal jet acts to produce divergence/convergence that may in part control the stratus distribution. In addition, along-shore SST patterns may also have an impact, as well as the increased divergence created offshore of coastal valleys as they are heated during the day. Whether on a relatively large scale, such as the San Francisco Bay area or the Monterey Bay and Salinas Valley, or on a smaller scale, such as the many narrow canyons in the Coast Range or the very narrow coastal plain that exists in some places, these sources of additional surface heating can apparently produce sufficient divergence in the MBL to significantly lower the inversion height adjacent to these locations (Burk and Thompson 1996) and alter the local cloud and wind patterns. However, these along-coast variations have not been well documented in the literature.

C. CALIFORNIA COASTAL JET STRUCTURE AND DYNAMICS

Until recently, the most complete observational study of winds in a coastal upwelling regime had been the CODE study mentioned previously. Data were obtained from aircraft, land stations along the coast, tethered balloon flights at one station on the coast, and meteorological sensors on buoys offshore. The range of meteorological conditions observed during CODE are best described in Beardsley et al. (1987), with the

cases in which the synoptic situation was basically as described in Chapter I (subtropical high to the west, thermal low to the east and southeast) emphasized here. The basic structure of the coastal jet as measured during two representative flights in the CODE area is described by Zemba and Friehe (1987). For the typical northerly flow regimes, they observed that winds at 1000 m were weak to moderate ($5\text{--}10\text{ m s}^{-1}$), and increased downward to a maximum of $15\text{--}32\text{ m s}^{-1}$ at the level of the temperature inversion. Also detected at this level was a sharp increase (moving downward) in mixing ratio, which resulted in a distinct density gradient. This inversion can be clearly seen in Fig. 3 (from Zemba and Friehe (1987)) at about 200 m, which is the same level as the particularly strong wind maximum of nearly 32 m s^{-1} on that day. The winds back with height below the inversion, and veer above.

Considerable variability in inversion structure was measured on other CODE flights. Zemba and Friehe examined in detail two flights in which vertical profiles were measured with the aircraft. In the first, the structure was very similar to Fig. 3, while in the second (not shown), the boundary layer was not as well mixed, the inversion was diffuse and stretched to about 1000 m, and a wind maximum of 22 m s^{-1} was evident at about 150 m when the aircraft conducted an along-shore profile. The lack of repeatability in their results is evident in the cross-shelf profiles from that second flight, in which the jet has about the same magnitude (24 m s^{-1}), but is much less vertically focused than in Fig. 3, and extends from about 200 to 900 m. Despite these differences, there are some important similarities between the two flights. Both flights sampled a jet that was strongly equatorward and parallel to the coast, and reached a maximum in the vertical within the inversion. Of note, Parish (2000) observed the jet off central California in the course of several flights and found a similar relationship between the temperature inversion/mixing ratio change and the vertical maximum in along-shore winds. However, they sampled a jet that extended much farther offshore than previously expected. These disparate and isolated observations of the California coastal jet point to the need for a comprehensive look at the jet along the entire coast and extending well offshore.

A simple schematic to explain the coastal baroclinity and resultant jet is presented in Fig. 4 (Burk and Thompson 1996). While the upper pressure surface is relatively flat,

the lower surface is sloped downward toward the land due to the higher temperatures and thicker column of air found there, especially during the day. The result is a stronger geostrophic wind at the lower level than at the upper level. This alone would produce downwardly increasing winds with a maximum at the surface. However, frictional effects in the MBL reduce the surface wind speed and a core of maximum winds above the surface results. This schematic highlights an important issue about the variability of the jet. The slope of the lower pressure surface is related to the sloping inversion and coastal baroclinity. The slope of the upper surface is due to synoptic-scale effects above the MBL.

How these coastal influences and synoptic-scale effects are related and act to modify each other over time or at different locations along the coast is not known. Variations in synoptic-scale forcing, SST variations, radiational differences associated with stratus (or no stratus), and sea/land breeze effects all act on the basic structure of Fig. 4 over varying time scales, and will be seen to dictate the spatial and temporal variability in the coastal jet winds.

Using temperature values at the endpoints of the cross-shelf flights, Zemba and Friehe (1987) computed a crude thermal wind that was qualitatively similar to the observed coastal jet. However, large local horizontal pressure gradients of 1.2 mb/10 km were measured in CODE, which suggests that the primarily one-dimensional analysis of Zemba and Friehe is insufficient to explain the complete dynamics of the jet or account for its variability.

All CODE I (1981) flights were conducted during the day, so no diurnal jet variability was examined (Zemba and Friehe 1987). In CODE II (1982), some night flights revealed that the jet profile was largely unchanged except very near the coast, where the jet was weaker and actually reversed direction on one flight. Zemba and Friehe point out the existence of strong baroclinity well *above* the inversion. Offshore and onshore potential temperature profiles from the two flights they analyzed exhibited much warmer air over land up to 1200 m. This temperature difference creates a thermal wind with a magnitude that increases downward to the inversion and which does not disappear entirely at night, due to the vertical extent of the thermal contrast. The forcing of the larger-scale jet thus appears to continue throughout the normal diurnal cycle, which

is a result that can be inferred from the CODE data and will be corroborated in the current study. Further, Zemba and Friehe (1987) point out the existence of a smaller magnitude poleward thermal wind in the lowest levels of the marine layer, owing to the SST gradient (warmer water offshore, cooler inshore). This thermal wind could explain the nighttime reversal measured on one of their flights, as the thermal contrast above the inversion was reduced at night, while the surface temperature gradient remained relatively constant.

A compilation of the along-shore component of the surface wind in CODE I and II is presented in Fig. 5 from Beardsley et al. (1987). Positive along-shore values correspond to southerly winds. Relaxation/reversal events are clearly evident, as is the overwhelming predominance of along-shore winds and the much greater diurnal variability at Sea Ranch (at the coast) than at buoy C5 (farthest offshore). These surface measurements do not necessarily reflect the variations in the jet core, although, as mentioned by Zemba and Friehe, turbulent mixing within the boundary layer typically causes a reduced magnitude extension to the surface of the winds in the jet core aloft. Beardsley et al. also point out that the diurnal variability of the winds is greater during periods of stronger equatorward winds. As will be discussed in Chapter IV, the opposite appears to be true in an examination of buoy winds near Point Sur in the present study, which again suggests significant variability in jet behavior. In the case of Sea Ranch during CODE, average winds were weak and southeasterly at 0200 PST, strengthened rapidly and shifted to northwesterly between 0600 and 1400, and decayed abruptly to near zero at 1930 PST.

An insightful summary of the apparent diurnal evolution of the coastal winds in the CODE region is presented in Beardsley et al. (1987). Morning heating destabilizes the marine layer at the coast and lowers the pressure over land, which allows onshore penetration of air with high along-shore momentum (below the inversion). A return flow above the inversion depresses the near-shore inversion in concert with the low-level divergence described by Burk and Thompson (1996), which leads to an acceleration of the along-shore winds at and below inversion level. In the evening, the weak return flow ends, low-level divergence in the near-shore marine layer decreases or ends completely as the winds at the shore reduce to near calm, the inversion moves higher, and the coastal

marine layer stabilizes. The high momentum air offshore is thus isolated from the coast. Thus, rather than a classical sea breeze, what is described here is an acceleration of along-shore coastal winds due to inclusion of high momentum offshore winds (which remain relatively strong) at the coast due to reduced afternoon stability. Thus, the offshore coastal jet moves closer to shore, strengthens, and moves lower as the inversion level decreases in the afternoon at the shore.

Although this conceptual model of the diurnal evolution is supported by the model simulations of Burk and Thompson, it has not been generally substantiated in other studies. The modeling portion of this study will corroborate this hypothesized evolution quite well. The observations of diurnal jet variability described above are limited in spatial extent, which points to the need for a larger scale examination of the jet variations through the diurnal cycle.

A distinct along-shore maximum in the jet magnitude, with a corresponding decrease in MBL thickness, was observed by Beardsley et al. (1987) at Sea Ranch, which is downstream of Point Arena. It has been hypothesized by Dorman (1985) and others that such accelerations downstream of an obstruction, coupled with decreases in the thickness of the marine layer, are an example of two-layer supercritical hydraulic flow. Winant et al. (1988) present a model of such supercritical channel flow to explain the along-shore variability in coastal winds in the CODE area. Their model is based on a particular synoptic regime that produces a low inversion and strong northwesterly flow, which results in winds that are complex and have rapid variations over short distances along the coast. As mentioned earlier, this regime is representative of the large majority of summertime days. More recently, Dorman et al. (1999) and Rogers et al. (1998) suggest that similar features to those found near Point Arena in CODE are observed near Point Sur and Cape Mendocino under some synoptic conditions, and both studies again suggest a supercritical flow response. In all cases, the boundaries of the channel are formed by the strong capping inversion above and the coastal topography to the left of the flow. The relationship between the synoptic scale and the nature of these mesoscale responses is not firmly established.

The basic model of Winant et al. (1988) occurs under supercritical flow, which is defined as flow with a Froude number greater than 1. The Froude number Fr is defined as:

$$Fr = \frac{V}{(g'h)^{1/2}},$$

where V is the velocity of the layer, h is the layer height, and $g' = g \mathbf{Dr}/\mathbf{r}$ is the reduced gravity. Thus, Fr is the ratio of the speed of the flow in the layer to the phase speed of gravity waves propagating on top of the layer (Samelson 1992). In subcritical flow, circulation changes are felt both upstream and downstream of the geometry change via gravity waves propagating radially away from the flow obstruction. When the flow becomes supercritical, so that the gravity wave can not propagate upstream, the obstruction affects only the downstream flow and adjusts it to the new boundary by depressing the inversion height, with a hydraulic jump farther downstream. This hydraulic theory dictates that the height of the flow decreases when the velocity increases and assumes that the coastal MBL behaves as a channel. As will be shown in this study, along-shore variations in V and h not due to this hypothesized supercritical adjustment do occur and may contribute to substantial variability beyond this simple model.

The impact of supercritical adjustment on the marine layer as it flows along a convex bend in the coastline is a spreading of the flow, in what is called an expansion fan, to follow the contours of the coastline. The result is a thinning of the marine layer and a corresponding increase in boundary layer wind speed. Subsequently, a compression, as the coastal boundary extends into the flow, dictates convergence of the flow characteristic lines and necessitates a sudden jump in the inversion height with a sharp decrease in wind speeds. These changes are shown schematically in Fig. 6 for the Point Arena area. The resolution of the aircraft data in CODE was not sufficient to resolve the spatial details of either the expansion or the compression, but the basic features of the theory are reasonably well substantiated in that data.

Samelson (1992) points out that the Winant et al. model, while attractive in its simplicity, fails to predict the near-shore velocity maximum in the data, overpredicts the acceleration downstream of the point, and does not account for an observed deceleration upstream from the hydraulic jump. Samelson developed a numerical model that includes

the effects of friction, rotation, and upper-level pressure variation not included by Winant et al. (1988). The addition of friction has a significant effect on the structure of the expansion fan. Offshore and upstream of the simulated Point Arena, friction acts to slow the boundary layer flow by 3 m s^{-1} , and results in a corresponding thickening of the layer by 60 m. In the expansion fan, the inshore, thinner portion of the fan is decelerated more by friction than is the outer portion, in contrast to observations. In the Samelson model, the highest speeds encountered in the fan are near the center, rather than downstream close to the hydraulic jump. The effect of upper pressure forcing is less clear, and depends upon the direction of the pressure gradient relative to the coast. The Coriolis effect acts to turn the along-shore winds offshore, which intensifies the expansion fan through additional low-level divergence. The net impact of including these additional terms in the Samelson model is to produce good quantitative agreement between the observed 33-m wind speeds (the level of most CODE flights) and the model-derived 33-m winds. In this model, friction plays an important role in more correctly predicting the along-shore extent of intensified winds downstream of a point, and pressure forcing has some effect on the details of the marine layer structure. This indicates the importance of careful treatment of friction and rotation in any modeling effort and the need to accurately represent the evolving pressure forcing above the MBL due to synoptic-scale variations, which is a focus of this study.

Burk and Thompson (1996) address the larger scale controls on the coastal low-level jet during summer along the California coast utilizing the Navy Operational Regional Atmospheric Prediction System (NORAPS). The model has a terrain-following σ coordinate with 30 vertical levels and a horizontal resolution of 20 km. Mellor and Yamada (1972) turbulence closure and a radiation parameterization that uses the liquid water pathlength of clouds to explicitly calculate transmissivity are used. Surface fluxes are computed using the Louis (1979) approach over land and the Liu et al. (1979) method over the ocean. Data were assimilated via an optimal interpolation analysis combined with the 12-hour forecast. As the model developed mesoscale detail, it was retained for subsequent forecasts. The 20-km resolution of NORAPS is incapable of resolving many of the details in the CODE observations, or features modeled by Winant et al. or

Samelson on smaller scales. However, the larger scale MBL variations and their impact on jet structure are nicely highlighted in the Burk and Thompson study.

The basic features of the jet that emerge from the NORAPS model are visible in Fig. 7 from Burk and Thompson (1996). The cross-section along 38°N (Fig. 7a) indicates a jet flowing out of the page. The jet core of 22 m s^{-1} at about 400 m is off the coast at 123.4°W. A secondary maximum above the coastal mountains is simulated in this afternoon model run. The X in Fig. 7a is the position of the jet core 12 hours earlier during the 1200 UTC model run. The core moves lower and closer to the coast during the day, which is attributed to low-level divergence and corresponding thinning of the MBL in response to daytime sea-breeze/mountain-valley (SBMV) circulations along the coast. Along with this thinning, the maximum horizontal temperature gradient is displaced shoreward, which causes the jet core to move toward land as well as down. A potential temperature cross-section is shown in the lower portion of Fig. 7a. A downward sloping inversion that intersects the coastal topography is clearly evident. The simulated spatial variability of the jet can be seen in the plan view (Fig. 7b) with distinct maxima south of Cape Mendocino, Point Reyes, and Point Sur.

Sensitivity experiments by Burk and Thompson (1996) reveal that the east-west SST gradient does not explain the deepening of the boundary layer to the west. Near-shore divergence and subsidence are used to explain the eastward shallowing of the MBL. Also, the idea that cold water patches cause a lower inversion, and thus a stronger jet, is not supported by their simulations, since similar wind maxima are evident even without any SST variability. Other sensitivity studies indicate that the topography is not required to produce the large-scale coastal jet. Without topography, warm air generated over central California takes longer to rise, move coastward, and affect baroclinity at the coast than it does when the Sierras and Coast Ranges are present. This is due to the role that the heating of that elevated terrain plays in establishing baroclinity aloft more quickly. The slowed, and reduced, baroclinity aloft (between 1 and 4 km) produces a weaker, but characteristic coastal jet. The existence of any jet in this simulation seems to refute, at least in part, the results from the model simulations of Chao (1985), who claims topography is required for the existence of a coastal jet. In the case of California, coastal

baroclinity is a dominant effect and its variations play an important role in jet intensity and core position.

As mentioned above, low-level divergence is important in determining the MBL structure and thus the structure of the coastal jet. Divergence associated with the SBMV circulations is complicated by a pattern of convergence upwind of coastal prominences and divergence downwind. Flow blocking and mountain wave type responses are also evident in the Burk and Thompson simulation of flow over Cape Mendocino. Although the authors do simulate features representative of supercritical channel flow, as in Winant et al. (1988) and Samelson (1992), their model shows that flow alteration associated with a cape or point, such as Cape Mendocino, exists well above the top of the inversion, and thus outside of the channel. Subsidence and adiabatic warming downwind of the cape act to compress the boundary layer and accelerate the flow. For these reasons, Burk and Thompson (1996) conclude that the acceleration downstream of a coastal prominence, and associated boundary layer thinning, are due at least in part to mountain wave effects, and not purely to hydraulically supercritical channel flow. More recently, Strom et al. (1999) also suggest that aircraft data collected during Coastal Waves 1996 near Cape Mendocino indicate that mountain wave effects play at least a partial role in creating the observed low-level high winds in the lee of the cape. These additional mechanisms involved in the creation of high winds downstream of a cape or point and their relationship to synoptic-scale variations are explored in detail in the present study.

D. SUMMARY AND DIRECTION

Certain aspects of the summer wind patterns off the coast of California are now well documented and accepted. The quasi-stationary eastern North Pacific high, in juxtaposition to a very persistent thermal low that extends from the desert Southwest up the Central Valley of California to the Oregon border, produces a consistent pattern of equatorward geostrophic winds in the lower atmosphere. Large-scale subsidence on the eastern flank of the high, combined with turbulent mixing in the marine boundary layer, produce a varying strong thermal inversion that effectively confines the cool, moist air to a shallow layer. Due to the high thermal contrast between land and sea in the lower troposphere, a vertical wind profile persists in which roughly coast-parallel winds increase downward until the effects of friction and turbulent mixing in the boundary layer

cause a decrease in wind toward the surface. The result is a core of consistently high-magnitude winds that reaches its peak in the vertical near the top of the MBL.

Much of the initial knowledge base for the California coastal jet is derived from data collected during the CODE experiments of the early 1980's in northern California. More recent work has substantiated the essential elements of the boundary layer structure and the jet characteristics at isolated locations along the coast. What has not yet been achieved is a comprehensive description of coastal jet variability along the entire coast from the Oregon border to Point Conception (the region in which the jet is best established). Also, previously published studies of the jet behavior have been based on data collected at or very near the coast. Thus, the first objective of this study is to provide a description of the jet, based on a comprehensive data set and mesoscale atmospheric modeling (both described in the next chapter), in that entire region and extending hundreds of kilometers offshore.

It is clear that boundary layer structure (including inversion height and strength and boundary layer depth) and associated jet behavior are related to synoptic-scale changes in the atmosphere above the MBL. These synoptic effects include large-scale subsidence and pressure patterns, and wind direction and thermal/moisture advection above the marine layer. These large-scale effects are only minimally considered in some of the previous studies. What is lacking is a treatment of how changes in these governing synoptic-scale patterns alter the structure of the marine boundary layer or the nature and behavior of the coastal jet. While not all of these large-scale effects are treated in detail, the second objective of this study involves defining those elements of the synoptic weather pattern that are most critical in determining the nature of the marine boundary layer, examining the impacts of changes in those elements on MBL structure, and relating those changes to coastal jet variability. The goal is to provide a link between the relatively high forecast skill of the synoptic pattern and the mesoscale behavior of low-level winds in the coastal regime.

Certain aspects of the diurnal variability of the MBL and coastal jet have been presented in previous studies. The boundary layer near the coast undergoes significant change as the land areas are heated during the day. As mentioned previously, daytime heating over land, with associated sea-breeze circulations, results in low-level divergence

and depression of the inversion height, with an associated increase in winds within the MBL. This diurnal variability is seen in the CODE data and modeled by Burk and Thompson (1996). From Beardsley et al. (1987), there may also be important changes in the stability of the near-shore MBL that result in diurnal isolation/inclusion of high-momentum offshore air. These observations of the diurnal cycle have been few and widely scattered along the coast, and have focused on areas very near the coastline, generally within about 40 km. This lack of larger-scale observations precludes any generalization about the diurnal cycle of low-level winds along varying topography. Therefore, an additional objective of this study is to broaden current understanding of the jet diurnal cycle, and treat near-shore and offshore variability as well as impacts of varying coastal topography.

There is a general acceptance in the literature that some sort of hydraulically supercritical channel flow response occurs in the lee of coastal prominences. Many aspects of the supercritical channel model fit the data fairly well, but the degree to which this supercritical effect describes the flow in these areas appears to vary, which may be due to combinations with other effects. As mentioned, Burk and Thompson (1996) suggest that the flow near Cape Mendocino may be more of a mountain wave response. Also, flow blocking upstream from the capes and the downwind response to that blocking appear to be significant factors. For these reasons, the final objective of this study is to examine in detail the interplay between the effects of supercritical channel flow, mountain wave effects, and flow blocking in altering the coastal jet behavior in the near-shore region, specifically near capes and points, and to examine these effects at all locations along the coast where they routinely occur. This objective turns out to be closely related to the large-scale description of the jet, as these effects alter marine layer structure and wind speeds much farther offshore than discussed in published studies.

In summary, the overarching purpose of this research is to provide a general description of the California coastal jet and associated marine boundary layer structure along the coast from central Oregon to the California Bight as it occurs during the predominant summer synoptic pattern. Given the existence of such a jet, the day to day variability is then tied to changes that occur within that pattern. Additional variability exists in the winds on smaller scales, both temporally (primarily diurnal heating effects)

and spatially (effects near coastal prominences). To complete the description of the coastal jet and more thoroughly understand its structure and governing dynamics, this variability is also addressed, with particular emphasis on the persistent low-level high wind areas that have been observed at specific locations along the coast on most days. The result is a more comprehensive treatment of the California coastal jet, which can be related to similar low-level jets around the world and improve the state of knowledge of winds in the important coastal region.

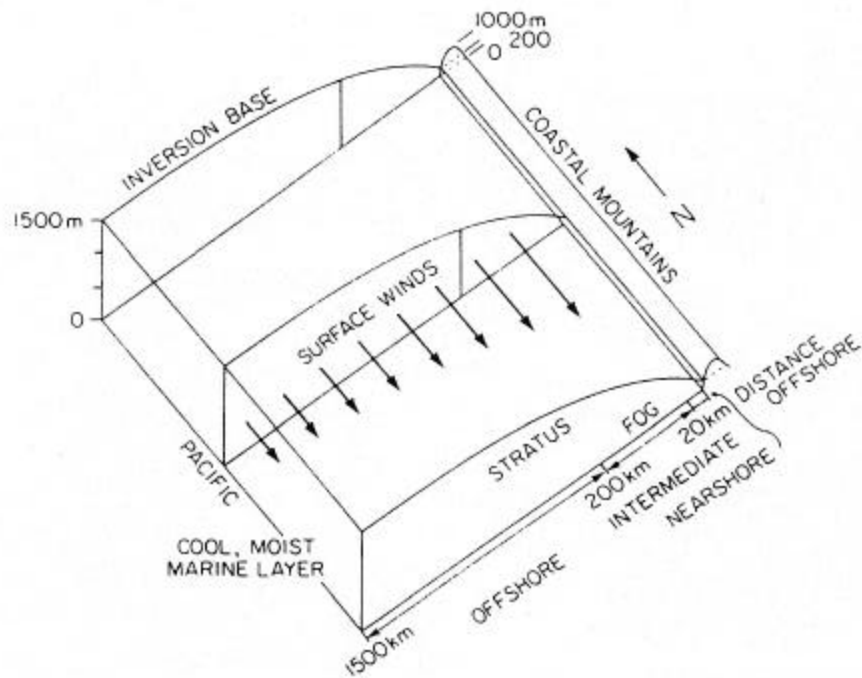


Figure 1. Conceptual model of the average lower atmosphere in summer in the eastern North Pacific during periods of persistent north-northwesterly winds (from Beardsley et al. 1987).

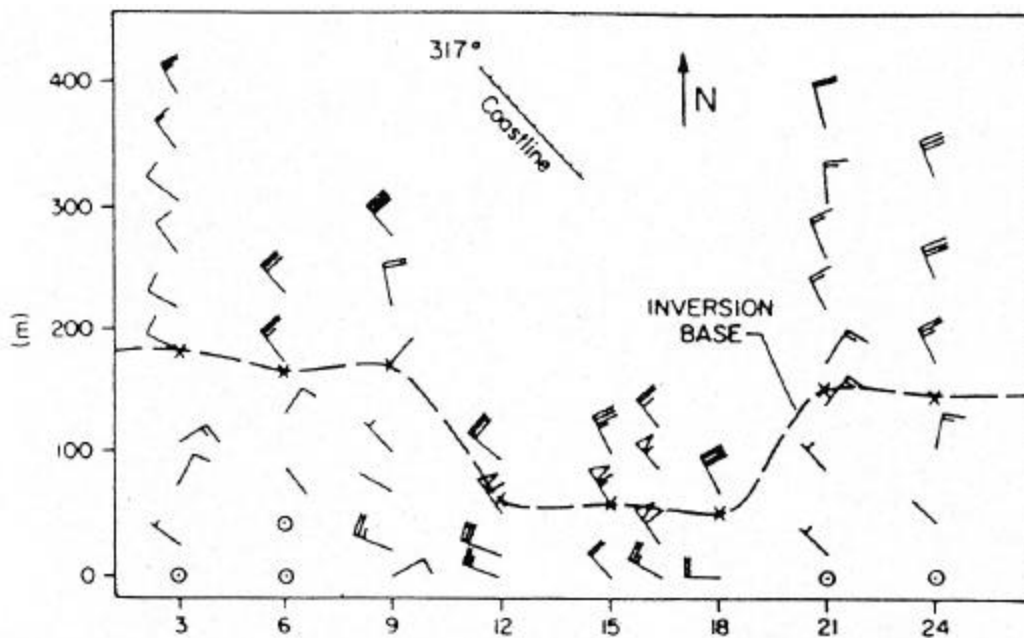


Figure 2. Tethered balloon and kite sounding data from Gualala, CA (south of Point Arena) during CODE II from Beardsley et al. (1987). The local times (abscissa) are on 29 July 1982. Wind barbs are in m s^{-1} with each barb representing 2 m s^{-1} . The dashed line indicates the main inversion base.

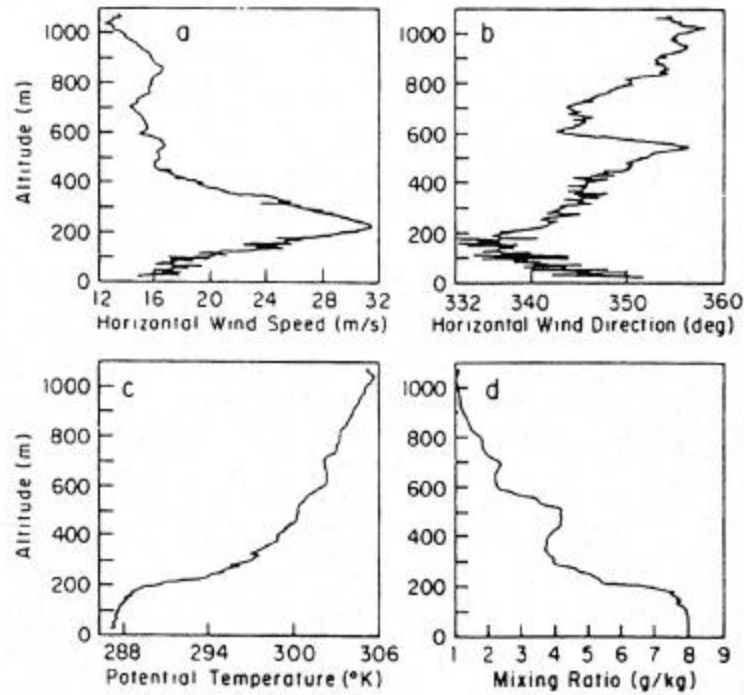


Figure 3. Representative examples of vertical profiles of wind, potential temperature, and mixing ratio near Point Arena from CODE II (Zemba and Friehe 1987).

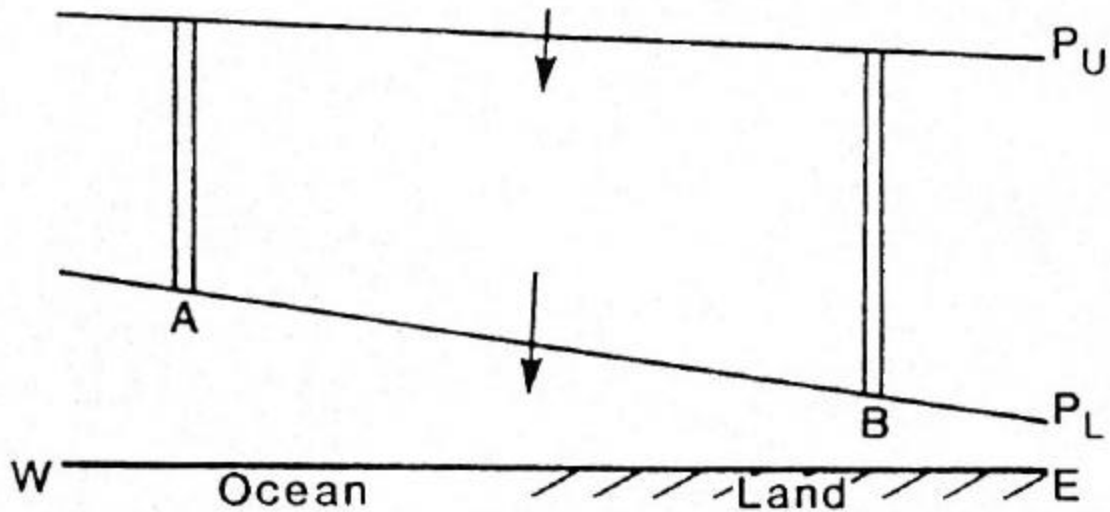


Figure 4. Schematic from Burk and Thompson (1996) of thermal wind with warm land to the east (right) and cool ocean to the west (left), showing stronger wind with decreasing altitude from a relatively level upper pressure surface. Friction below creates characteristic jet wind profile.

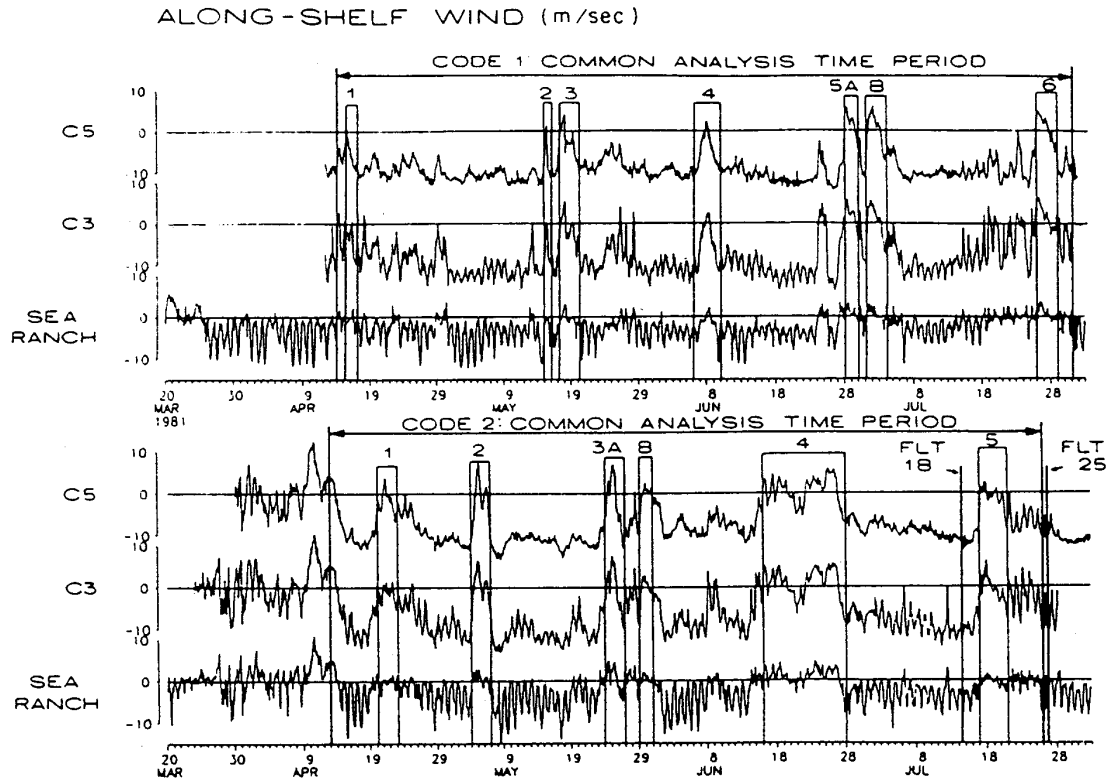


Figure 5. Along-shore wind component (m s^{-1}) during CODE I and II from Beardsley et al. (1987). Sea Ranch is at the coast and C3 and C5 are buoys, with C5 farthest from shore. Note the predominance of down-coast winds (negative values), interrupted by periodic wind relaxation events.

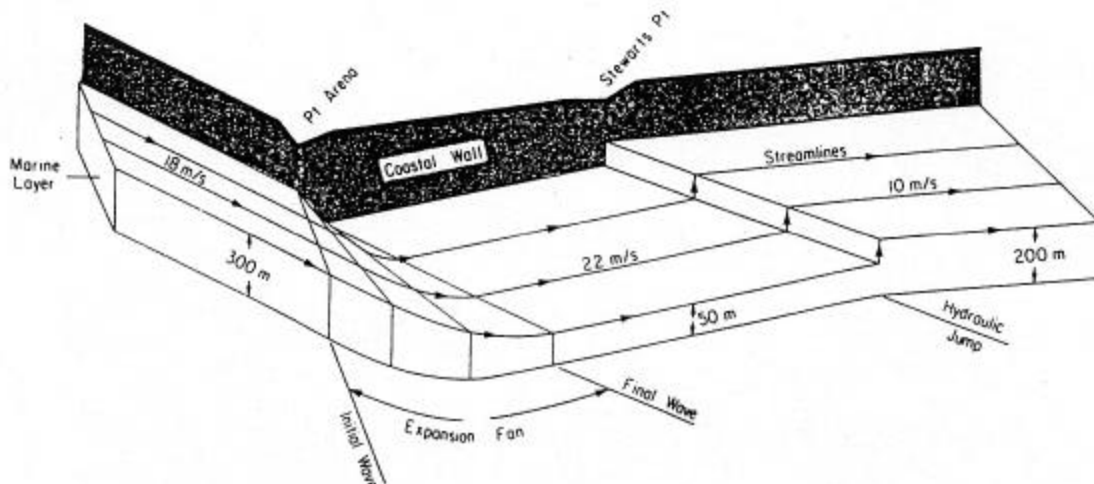


Figure 6. Winant et al. (1988) model of marine layer structure in the vicinity of Point Arena from the CODE data. Note the deeper marine layer upstream, followed by a shallowing at the turn and increase in wind speed, followed by a hydraulic jump to weaker winds and deeper marine layer downstream. This model does not consider changes above the marine layer.

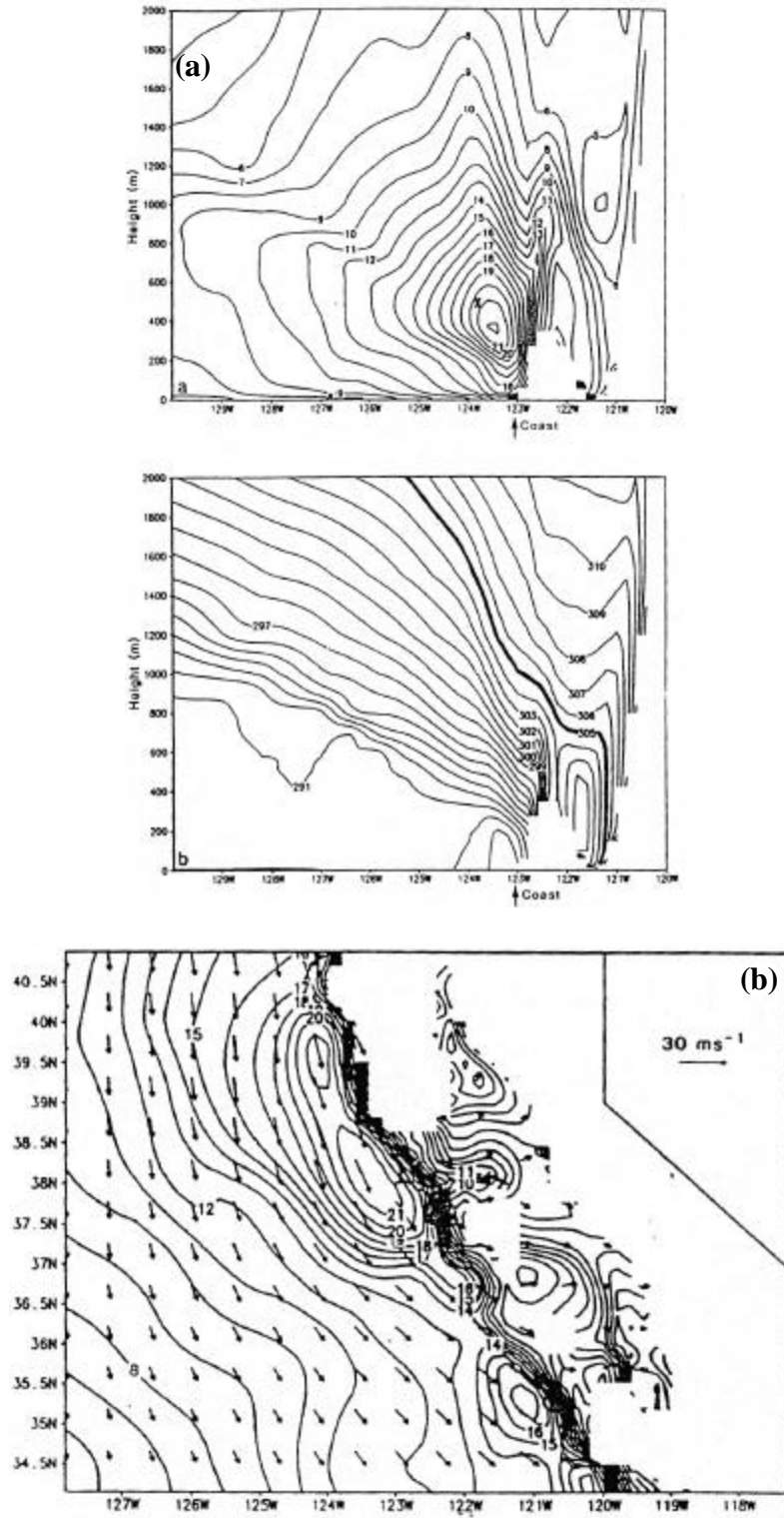


Figure 7. Fields from the Navy Operational Regional Atmospheric Prediction System (NORAPS) from 21 July 1992 (Burk and Thompson, 1996): (a) cross-sections along 38°N of winds (top, m s^{-1}) and potential temperature (bottom, K), and (b) a horizontal view of winds (m s^{-1}) at 425 m.

III. METHOD

A. OVERVIEW

To achieve the goals mentioned in the last chapter, a wide array of data, much of which came from the Coastal Waves 1996 (CW96) experiment, was analyzed. These data included surface data from land stations and moored buoys, and upper data from vertical wind profilers and aircraft. These will be detailed in the next section. Variability in the surface data, particularly that from the offshore buoys, drove the focus of the modeling portion of this study to three distinct periods in June 1996. These events were chosen to study a range of surface wind conditions off the coast, as discussed in Section C of this chapter. Since a data set does not exist that can adequately represent the four-dimensional variations in the coastal jet, a mesoscale numerical model was used to examine the behavior of the coastal low-level winds on each of these three days. The Coupled Ocean Atmosphere Mesoscale Prediction System (COAMPSTM) was selected for this purpose. The specifics of the application of this model to the present study will be described in Section E of this chapter. The model was initialized using a three-dimensional multiquadric (3DMQ) interpolation scheme developed specifically for application to meteorology. This technique and its benefits relative to other types of analyses will be discussed in Section D.

B. DATA

Data utilized in this study were obtained from a wide variety of sources. Land station observations were quite comprehensive. The standard meteorological synoptic reporting stations were supplemented with data from both the California Irrigation Management Information System (CIMIS) and California Department of Forestry (CDF). Both CIMIS and CDF data included station pressure, temperature, and winds. These stations provide data at 1-hour intervals, although some are shut down during night hours. This data set provided a fairly high density of land surface observations and included stations at elevation.

The most critical set of data in terms of observing offshore winds came from moored buoys along the entire coast. These buoys, the locations of which are shown in

Fig. 8, are operated and maintained by the NOAA National Data Buoy Center. The buoys have a five-digit designator, which will be shortened to two digits in this paper for simplicity. For example, buoy 46012 off Half Moon Bay will be referred to as Buoy 12, and so on. A typical buoy is shown in Fig. 9. Of note, the height of the anemometer on these buoys is 5 m above the buoy's waterline. This is important when considering these winds as representative of the winds in the coastal jet. A first-order assumption is made that temporal variations in these near-surface winds are representative of changes in the MBL as a whole. As will be described later, the core of the jet is generally well above the surface (above the direct effects of friction), typically on the order of 100-600 m above sea level. Thus, the assumption is that when the winds in the core of the jet increase, there will also be a near-surface expression of that increase reflected in the buoy data. Given the turbulent nature of the MBL, this seems a reasonable, and necessary, assumption, since no dynamic boundary exists between the winds of the jet core and the winds as recorded by the buoys.

Qualitative observations of MBL variations at coastal locations will be derived from several vertical wind profilers, some of which were placed at strategic locations strictly for the period of CW96 (Fig. 8). These profilers measure hourly winds up to a height that varies according to the profiler frequency and the degree of reflective turbulence in the air, but generally do an excellent job of providing winds through the MBL. These profilers are also equipped with a radio acoustic sounding system (RASS) that measures virtual temperature to a similar height. Thus, the general characteristics of the MBL are reasonably well captured by these instruments. The primary limitation of the profilers is that they are necessarily only on land (all but one are at or very near the coastline), and as such can only capture boundary layer characteristics at the very edge of the wind regime of interest.

Finally, a comprehensive set of visible satellite imagery was obtained to qualitatively relate cloud distribution to coastal wind variability. The imagery has a resolution of 1 km and is the best tool available for observing the distribution of the low stratus associated with the coastal MBL. It was not a focus of this study to examine cloud patterns in any detail, or draw conclusions as to the relationships between coastal

jet variability and stratus distribution. The images are presented only to give the reader an idea of the relative cloud characteristics on the three days of interest.

C. PERIOD OF STUDY

As mentioned previously, the study period was June 1996 due to the combination of data availability and the predominance of typical summertime conditions conducive to the existence of a coastal jet. Such conditions normally exist to some degree almost continuously from May to October, but the most intensive data collection effort took place during June. In the observational portion of the study, particular attention was paid to the period from 5 to 28 June. Offshore wind variability was analyzed during this period in relation to cross-shore and along-shore pressure variations, as will be described in the next chapter. To examine jet variability in detail using the COAMPSTM model, three days within this period were chosen for 36-h model simulations. These days (9, 14, and 17 June) are all representative of typical summertime conditions that produce a coastal jet, but significant differences in synoptic patterns exist on each day that produce distinct wind variability at different locations along the coast.

While the moored buoys depicted in Fig. 8 are placed at similar distances offshore, they exist in a variety of locations relative to coastal features. For example, Buoys 26 and 42 are adjacent to the openings of San Francisco Bay and Monterey Bay, respectively, while Buoy 30 is near the point at Cape Mendocino and Buoy 14 is close to the steep topography north of Point Arena. Buoy 28 (Cape San Martin, south of Point Sur) is particularly well located to represent the extension at the surface of coastal jet winds aloft. While it is potentially in the lee of Point Sur (modeled position of that jet maximum varies relative to buoy location), the coastal characteristics in that area are reasonably representative of the average coastline, and its location is somewhat farther offshore than the other buoys, which places it farther from the direct effects of coastal friction and land/sea breeze circulations. It thus exhibits a less complex wind speed signal during the period of interest. The primary driver for the selection of days on which to run COAMPSTM was the wind speed time series from Buoy 28 (Fig. 10). Distinct high wind events are evident on 9-10 June and 17-18 June, while 14-15 June is characterized by relatively weaker winds. These days proved to be illustrative of important wind and pressure variability at all locations along the coast. The general characteristics of the

synoptic situation on each of these days, along with the associated differences in wind patterns at the buoy locations, will be presented in the next chapter.

D. THREE-DIMENSIONAL MULTIQUADRIC INTERPOLATION

The California coast is characterized by steep and varied topography. Since the focus of this study was the wind behavior near the coast, which is known to be driven in large part by the characteristics of the coast, it was deemed extremely important to accurately place available observations in three dimensions in the initial analysis for the COAMPSTM integrations. Multivariate optimal interpolation (OI) and other two-dimensional analysis techniques were deemed to fall short in this regard, in that the interpolations are done on a series of horizontal layers, and thus limit the impact of a given observation to one level. Three-dimensional multiquadric interpolation (3DMQ) appeared to best address the need to extend these impacts vertically and thus represent the coastal atmosphere in three dimensions.

Multiquadric interpolation was originally developed as a tool for improved topographic mapping. A full mathematical development of the technique is contained in Hardy (1971). Developed as a means of contouring irregularly spaced data points to most accurately depict the important aspects of topography, the method uses the computation of first, second, and third derivatives to mathematically locate significant features. Hyperboloid radial basis functions are then computed in a distance weighting scheme to interpolate the data to the model grid. As opposed to the single length scale used in an OI scheme, this allows for better representation of mesoscale structure. In this way, relative highs and lows, as well as the inflection points and peak gradients between them, are identified in the data set. This technique ensures that the most significant aspects of the observations are captured for ingest into the numerical model.

The application of multiquadric interpolation to meteorological fields is discussed in Nuss and Titley (1994). An excellent case is made for the validity of the method in providing analyses suitable for use in numerical weather prediction models. However, the interpolation done in that study was two-dimensional (2DMQ), which means that mathematically significant features of the data set were only calculated in a series of horizontal layers that were independent of one another. The 3DMQ method applied in the present study computes derivatives and basis functions in both the horizontal and

vertical, which allows a more accurate and coherent representation of significant atmospheric structure in three dimensions. That is, a given observation impacts the analysis at multiple levels. Such analyses were run at 0000 UTC 9 June, 0000 UTC 14 June, and 0000 UTC 17 June 1996 to provide initial conditions for the model. Using the Navy Operational Global Atmospheric Prediction System (NOGAPS) analysis as a first guess, 3DMQ then blended available observations in the manner described to produce an analysis that could be input into COAMPSTM. A similar 3DMQ analysis was done every 12 hours after the initial time to provide analyzed boundary conditions for the model simulations.

E. ATMOSPHERIC MODEL

As previously stated, the model used in this study is COAMPSTM, as trademarked by the Naval Research Laboratory and described by Hodur (1997). While COAMPSTM is under development to become a true coupled ocean/atmosphere model, only the atmospheric portion of the model was used in this case. The ocean surface was specified as a non-evolving sea-surface temperature, which reflected climatological norms, including a pattern of low inshore temperatures due to the upwelling mentioned previously. As discussed by Burk and Thompson (1996), and reaffirmed in this study, the coastal winds are quite insensitive to changes in SST. For this reason, this simplification of the treatment of the sea surface is deemed to have an insignificant effect on the coastal jet as simulated by the model.

COAMPSTM is a non-hydrostatic, fully compressible model based on Klemp and Wilhelmson (1978). It includes predictive equations for momentum, non-dimensional pressure perturbation, potential temperature, and mixing ratios of water vapor, clouds, rain, ice and snow. Surface fluxes of momentum, heat, and moisture are parameterized based on Monin-Obukov similarity theory (Louis 1979) and the sea-surface temperature fields.

The model was run with a triple nest as shown in Fig. 11a. The outermost nest has a spatial resolution of 81 km, the middle nest 27 km, and the innermost nest 9 km. The outer nest, whose boundary conditions were obtained from the 3DMQ analyzed fields using observations and analyses from NOGAPS, was made sufficiently large to prevent any error in boundary conditions from reaching the inner nest, which is the area

of greatest interest, within the 36-h integration. The inner nest boundary conditions are interpolated from the next outer grid. COAMPSTM was initialized with the output of the 3DMQ analysis on 45 vertical levels (Fig. 11b). Due to the interest in the mesoscale behavior of the lower atmosphere, the distribution of those levels was set to be dense near the surface and less dense in the upper atmosphere. Specifically, the lowest σ level is at 10 m above the surface, followed by the next at 40 m, then 80 m, and so on with 40 m spacing up to 880 m. Above that is a layer at 925 m, then 50 m spacing to 1175 m, then steadily increasing layer thickness to 7000 m. Finally, the vertical spacing is set at 2000 m from 7000 m up to the model top at 19,000 m. The model was run with the standard set of parameterizations used by the Navy operationally, as described in Hodur (1997).

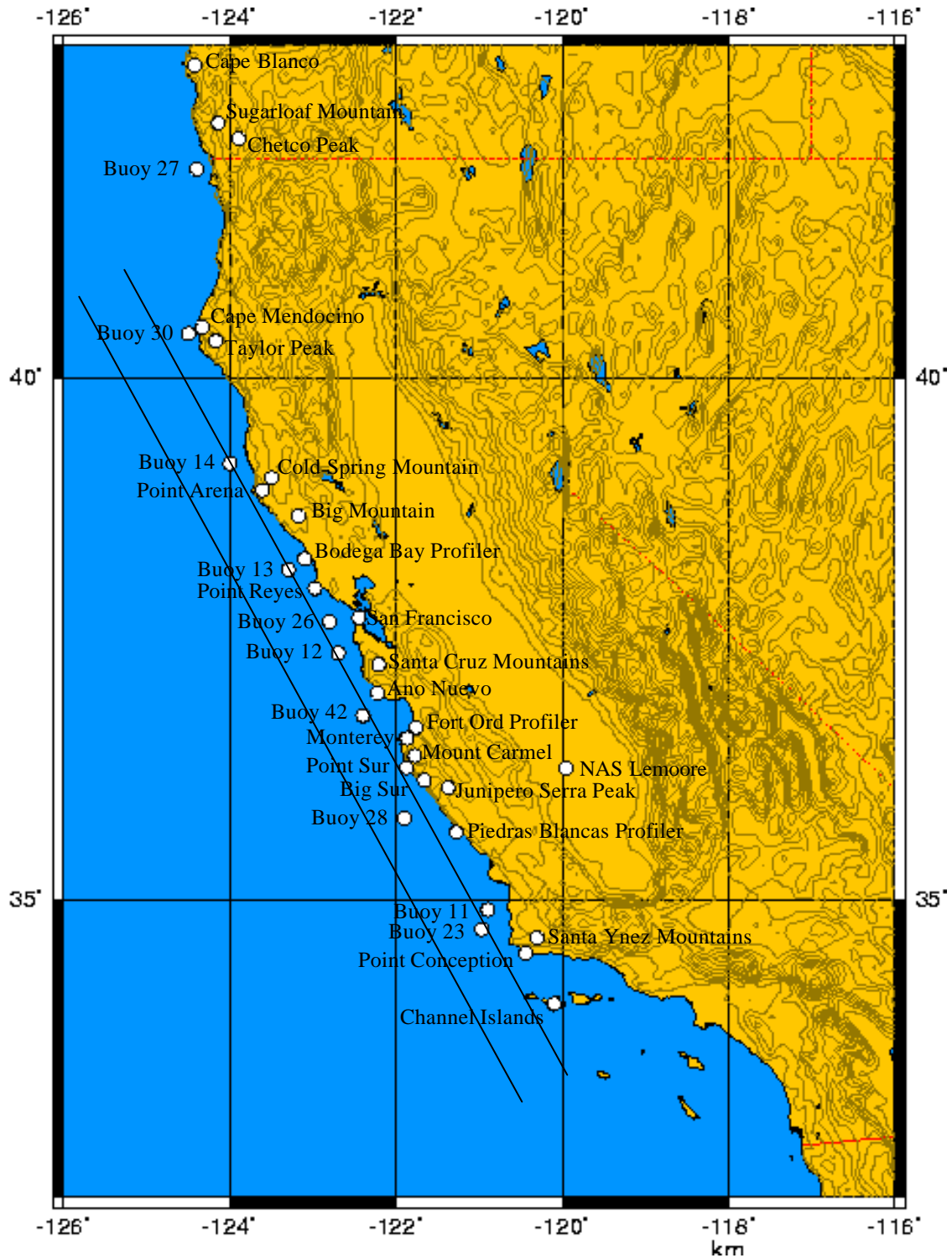


Figure 8. Map showing key locations discussed in this study, including NOAA moored buoys, wind profilers, key land stations, significant coastal mountains, and offshore coast-parallel cross-section locations.

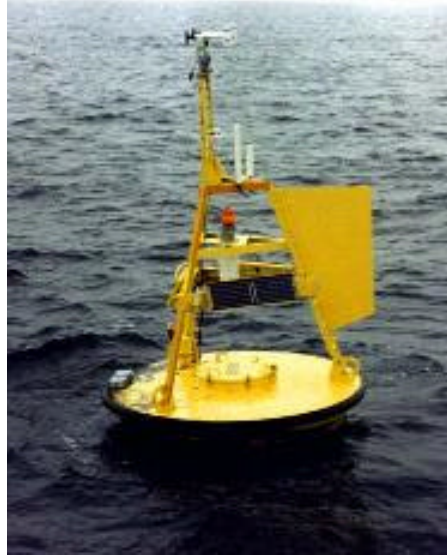


Figure 9. A typical NOAA moored buoy. Note the anemometer on top of the buoy at a height of 5 m.

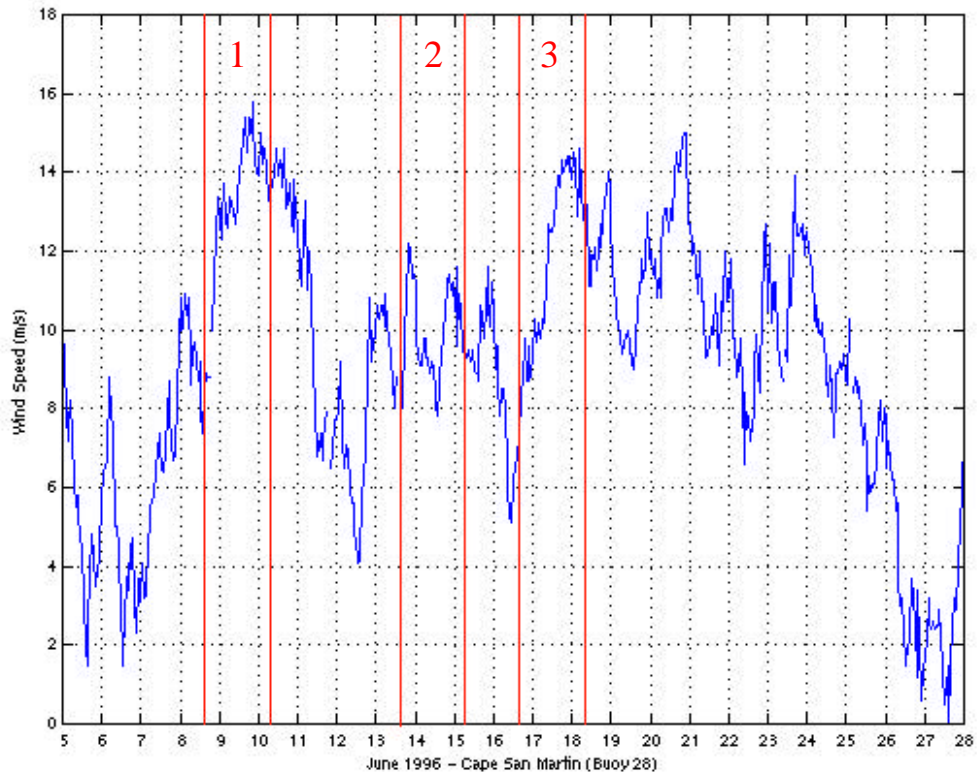


Figure 10. Buoy wind (m s^{-1}) time series from NOAA buoy 46028 (Buoy 28). Time scale is Pacific Daylight Time. Note distinct high wind events of 9-10 and 17-18 June 1996, with weaker winds between. Vertical lines bracket the time periods for the three COAMPS runs in this study.

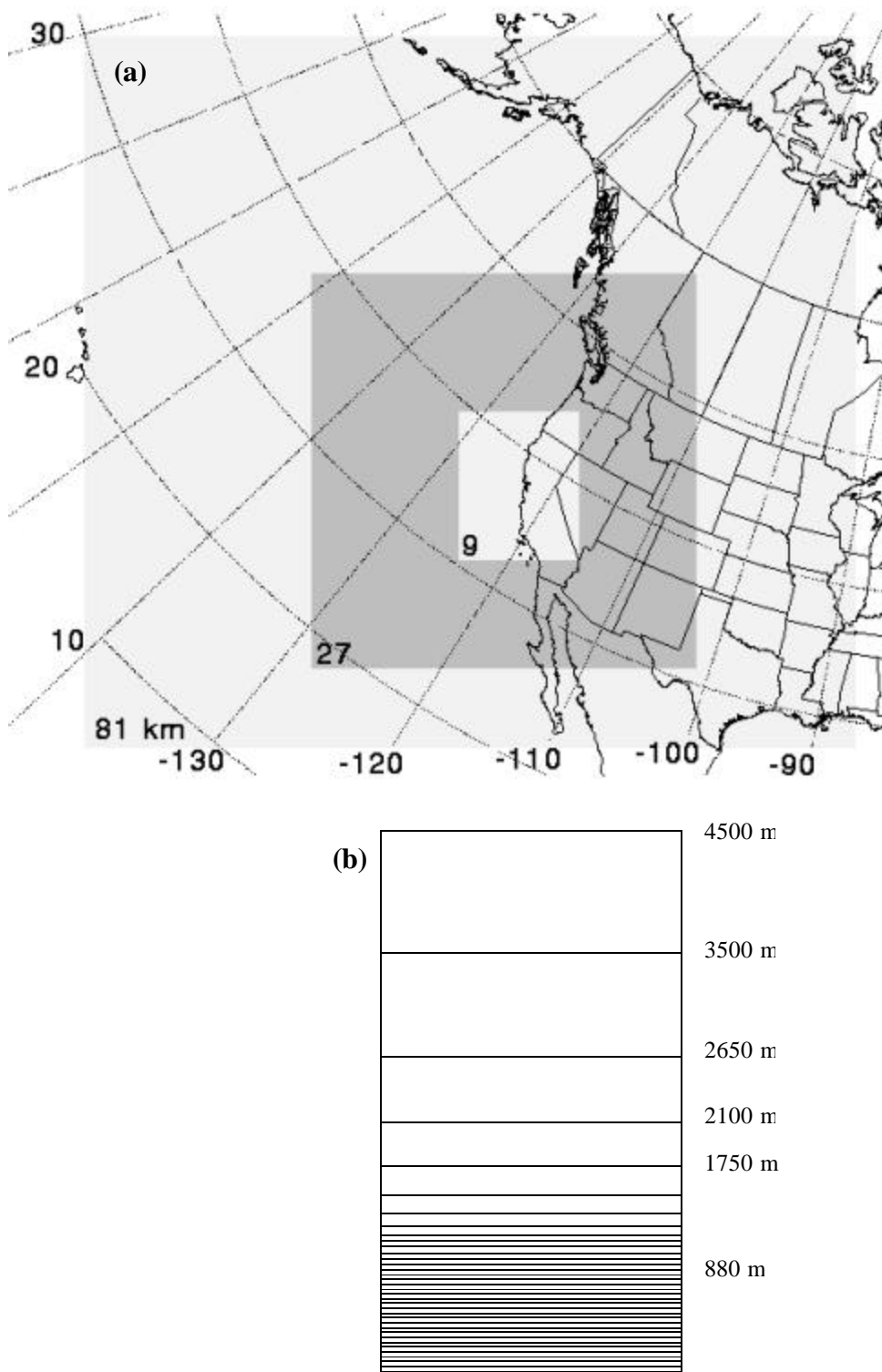


Figure 11. (a) COAMPS horizontal grid domains and (b) a depiction of the lower 37 of 45 vertical levels for the three model runs in this study. Above 4500 m are 8 more levels at 5500, 7000, 9000, 11000, 13000, 15000, 17000, and 19000 m.

THIS PAGE INTENTIONALLY LEFT BLANK

IV. OBSERVATIONAL ANALYSES

A. SYNOPTIC DESCRIPTIONS

The following synoptic discussions derived from the 12-h NOGAPS analyses (Figs. 12-20) are presented to provide a framework for the later discussions of both the large-scale jet variability during the three days of interest and the mesoscale response to differing synoptic conditions, particularly near capes and points. The relevant characteristics of the synoptic height patterns at 500 mb and 850 mb, as well as the surface pressure pattern, are discussed. The 36-h sequences of 500 mb NOGAPS analyses for each of the three events, with the initial time in the upper left, are shown in Figs. 12 (9-10 June), 15 (14-15 June), and 18 (17-18 June), the 850 mb sequences in Figs. 13, 16, and 19, and the surface sequences in Figs. 14, 17, and 20.

The NOGAPS analyses presented here were generated at the U.S. Navy Fleet Numerical Meteorology and Oceanography Center in Monterey, California. As described in Hogan (1991), NOGAPS is a global, hydrostatic, spectral model. The version used here was run with 15 vertical levels, although only the lowest 12 were used for creation of the COAMPSTM first-guess fields. These levels are 1000, 925, 850, 700, 500, 400, 300, 250, 200, 150, 100, and 50 mb. The model output horizontal resolution is 2.5 degrees.

1. 9 and 10 June Event

The 500 mb and 850 mb heights, along with sea level pressure, for the first of the three model periods are shown in Figs. 12-14, respectively. The model was initiated at 0000 UTC 9 June (Fig. 12a), when the California coast was along the downstream side of a broad 500 mb trough, which resulted in relatively strong southwesterly flow over northern California between the trough and a 5920 m high over southern Arizona. By 0000 UTC 10 June (Fig. 12c), the axis of the trough had flattened, which reduced the gradient over northern California and produced a more zonal flow. By 1200 UTC 10 June (Fig. 12d), near-zonal flow extends over the entire coastline, although still strongest near the Oregon border.

The eastern North Pacific high (as discussed previously as a surface feature) becomes apparent at 850 mb, with varying degrees and positions of ridges over the area of interest on the three days of the study. At 0000 UTC 9 June (Fig. 13a), the ridge axis is aligned from southwest to northeast, with the axis crossing the coast at approximately Cape Mendocino in northern California before turning to a more northward orientation toward the Pacific Northwest. This ridge remains in approximately that position throughout the forecast period, although the inland extension becomes more aligned toward the east, with a closed high near Yellowstone by 1200 UTC 10 June (Fig. 13d). However, the orientation of the height contours along the central and southern California coast varies diurnally. For example, the 1200 UTC 9 June (Fig. 13b) and 10 June (Fig. 13d) analyses depict a low pressure area over the southern California deserts, which extends northeastward into Nevada and Utah. This low is apparently due to the delayed effect of daytime heating over the deserts reaching vertically to above the 850 mb level. It causes a reorientation of the pressure gradient (∇p) along the California coast such that the isoheights cross the coast at a greater angle, while they are more parallel to the coast at 0000 UTC (Figs. 13a,c).

The surface expression of the 850 mb ridge, which is a northeastward extension of the broad eastern North Pacific high, has an axis that is farther to the north and west than at 850 mb, and crosses the coast near the Oregon/Washington border during the entire 36-h period (Fig. 14). This results in isobars that intersect the coastline at a shallow angle in far northern California and an increased angle along the central California coast. The isobars in the southern California Bight area are roughly coast-parallel. While there is again diurnal oscillation in the thermal pattern and inland pressure pattern, roughly the same isobar orientation along the coast persists during the 36-h period.

2. 14 and 15 June Event

The NOGAPS analyses for this event are presented in Figs. 15-17. The 500 mb geostrophic flow (Fig. 15) over California is significantly weaker than on 9-10 June (Fig. 12). As on 9-10 June, a low in the Gulf of Alaska is the dominant feature on the charts, which creates only a broad trough in the region of California. Again, the pressure gradient weakens from northern California southward. The flow direction varies

gradually between southwesterly and westerly, depending on the exact location of the trough axis.

At 850 mb (Fig. 16), the same basic circulation features exist as during the 9-10 June period (Fig. 13). That is, a ridge extends northeastward from the eastern North Pacific high and crosses over the coast in the north, and a low exists over the southwest and Great Basin that varies diurnally in intensity. The primary difference between this period and the 9-10 June period is that both the ridge and interior low are farther north, with the low over eastern Nevada and Utah (as opposed to southern California) and the ridge axis crossing the coast near the Oregon/Washington border. The ridge axis crosses the coast, again in a northeastward direction, over southern Oregon at 0000 UTC 14 June (Fig. 16a), and shifts northward to the Washington coast by 1200 UTC 15 June (Fig. 16d). In this case, the diurnal modulation results in a roughly coast-parallel geostrophic flow at 850 mb on the 0000 UTC analyses 14 June and 15 June (although with a significant offshore component in far northern California (Figs. 16a,c)), and more of an offshore flow from Cape Mendocino southward at 1200 UTC 14 June (Fig. 16b). The interior low at 1200 UTC 15 June (Fig. 16d) has less of an offshore expression and thus fails to significantly alter the along-coast orientation of isoheights, as was evident on the 0000 UTC analyses.

The surface analyses (Fig. 17) vary little during this period. The surface ridge is again displaced to the west relative to the 850 mb ridge, and a heat low persists in the interior, with the axis oriented northwestward from southern Arizona. The resultant isobars in the region of the coast have a significant offshore component in far northern California, but are generally coast-parallel from about Point Arena southward past Point Conception. As during the 9-10 June event, little variation in this approximate orientation of the coastal pressure gradient occurs during the period.

3. 17 and 18 June Event

The third model run was initialized at 0000 UTC 17 June. The initial and subsequent 36-h period NOGAPS analyses are shown in Figs. 18-20. This event was somewhat different from the first two in that a transitory upper-level low pressure system was moving across the northern portion of the primary area of interest. This somewhat unusual summertime pattern is evident at 500 mb at 0000 UTC 17 June (Fig. 18a) as the

trough is then still west of the coast, which results in a fairly strong southwesterly geostrophic flow along the entire California coast, with the strongest gradient again occurring at the far northern coast. By 1200 UTC 17 June (Fig. 18b), the gradient in the north has increased and the trough axis has pushed east, so that the flow becomes closer to zonal, although still with a southerly component. A local trough axis is less evident by 0000 UTC 18 June (Fig. 18c) and the pressure gradient has increased further as the low center has moved over the Pacific Northwest. The flow direction has become westerly. By the end of the period at 1200 UTC 18 June (Fig. 18d), the low has moved to the Pacific Northwest, with a ridge beginning to build in behind the trough, which causes the geostrophic flow to be from the northwest over northern California and more zonal farther south.

At 850 mb (Fig. 19), a low is initially well west of Vancouver Island, with a ridge similar to those during the previous two events, such that the axis crosses the coast near the Oregon/Washington border. A large interior low is over Nevada, which causes a geostrophic flow orientation that is roughly coast-parallel, wrapping around the low, over the California coast. However, a significant offshore component exists in the region between Cape Mendocino and Point Arena. The ridge begins to weaken by 1200 UTC 17 June (Fig. 19b), as the low moves eastward closer to the coast, and the ridge axis is near Cape Mendocino. The daytime heating effect mentioned previously has merged with the interior low to create a broad area of lower pressures from Montana to well off southern California. An offshore orientation of isoheights now exists from about Cape Mendocino to Point Sur. The offshore extension of the low is eliminated by 0000 UTC 18 June (Fig. 19c), which results in an offshore geostrophic flow orientation from Point Arena southward. At 1200 UTC 18 June (Fig. 19d), a somewhat unusual east-west oriented 850 mb ridge extends from offshore over northern California to western Nevada. This limits the cross-coast geostrophic flow to south of San Francisco and causes the direction to be nearly easterly, which is in contrast to the more normal coast-parallel or north-south isoheights orientation.

Despite the migratory low and strong gradient at 500 mb, the surface pattern (Fig. 20) during this period is very similar to the climatological norm discussed in Chapter I. The eastern North Pacific high is well established and a thermal trough extends from the

southwestern deserts northward to eastern Oregon and Washington. This places the California coast in a region of near coast-parallel isobars at 0000 UTC 17 June (Fig. 20a), with only a slight offshore component from Point Sur southward. By 1200 UTC 17 June (Fig. 20b), the low in the interior has weakened (as expected diurnally), but is displaced into the southern California desert region, which results in isobars that cross the coast at a significant angle from Point Arena southward. That orientation continues at 0000 UTC 18 June (Fig. 20c), although the pressure gradient has increased slightly and the offshore orientation has extended north to Cape Mendocino. By 1200 UTC 18 June (Fig. 20d), there is a ridge nosing in from offshore, which is similar to 850 mb. The surface ridge is farther north than at 850 mb, and extends to the east over central Oregon. The result is a northeasterly to easterly orientation of the geostrophic winds over the California coast from the Oregon border to Point Conception. As will be demonstrated in the discussion of the character of the coastal jet, the low-level winds in the coastal zone tend to be highly ageostrophic, and maintain a coast-parallel direction regardless of the local ∇p orientation.

B. BUOY WINDS

The only continuous source of low-level wind data available offshore was the NOAA moored buoys (Fig. 8). The time series of winds observed at the buoys for the period 5-28 June are shown in Fig. 21, beginning with Buoy 27 in the north near the Oregon border (Fig. 21a) and progressing south to Buoy 11 off Santa Maria (Fig. 21i). A seven-hour shift from universal time is applied such that the times are in Pacific Daylight Time (PDT), which allows easier reference to the local diurnal cycle. Where bad data or no data were obtained, gaps exist in the plots. These gaps were few and short lived at most locations, with the exception of Buoy 23 off Point Arguello in the south (not shown), which was not functioning until 12 June and experienced frequent gaps thereafter. The portion of the time series that was obtained is very similar to Buoy 11 nearby, which is included in Fig. 21.

As mentioned in the last chapter, and seen most clearly at Buoy 28 (Fig. 10, 21h), the southern buoys (23, 11, 28) exhibit relatively high winds during the first and third focus periods, with weaker winds during the interval between that includes the middle

time period on 14-15 June. This pattern is also evident at Buoy 42 (Monterey Bay), Buoy 12 (Half Moon Bay), Buoy 26 (San Francisco), and even Buoy 13 (Bodega Bay), although to a decreasing extent with increasing latitude. Continuing northward to Buoy 14 (Point Arena), that pattern no longer exists. In fact, the 9-10 June period is actually a weaker wind day than the other two days at that latitude. Finally, the opposite pattern, with weaker winds for the first and third events and stronger winds in the middle period, is clearly evident at Buoy 30 (Blunt's Reef - Cape Mendocino).

These buoys are in a variety of positions relative to important features of the coastal topography, which is manifest in the very different character of the wind signal. One apparent difference among the buoys is the magnitude of high frequency variability measured. For example, a relatively smoother signal in the wind speed trace occurs at Buoys 30 and 28, while higher frequency variability is evident at Buoy 26, which is apparently due to the strong land/sea breeze signal near the mouth of San Francisco Bay. On the other hand, Buoy 30 is close to the high terrain of Cape Mendocino and experiences a greatly reduced sea breeze. As mentioned, Buoy 28 is farther offshore than the others, which reduces its land-induced variability. In general, the buoys that are closer to the coastline exhibit greater variability due to complex interactions with the topography at scales from turbulence to the mesoscale effects mentioned. At all locations, the winds are subject to the competing effects of synoptic variability, land/sea breeze circulations, effects near capes, boundary layer turbulence, and other sources of coastal jet variability, which will be discussed in detail later.

Another aspect of the winds that varies with location is the magnitude of the diurnal variability. Buoy 27 (St. Georges, at the Oregon border) has a very different wind signal from all other locations. Based on a comparison of the buoy wind speeds with wind directions, this is because this buoy is at the northern extreme of conditions conducive to a coastal jet (as discussed in Chapter VI) and is subject to a substantial sea breeze signature. The result is winds that can reach 17 m s^{-1} in the late afternoon/early evening and fall to near calm by late that night. Such large variations are generally not seen at locations farther south, due to the greater persistence of coastal jet conditions. In particular, the frequent near calms at Buoy 27 are not found farther south. As mentioned, Buoy 26 exhibits a fairly large diurnal signal, due to both diurnal jet changes and sea

breeze effects. Buoy 14 also has a fairly strong diurnal signal due mostly to diurnally modulated lee effects, which will also be discussed in Chapter VI.

Wind directions are not shown here as they provide little further insight into the jet dynamics. That is, the low-level wind directions at all locations from Cape Mendocino southward (not including Buoy 27) exhibit an extremely persistent north to northwesterly coast-parallel direction. All undergo a slight afternoon turning toward land that relaxes by evening. This turning is somewhat stronger at San Francisco and occasionally at Monterey Bay, although that buoy is far enough offshore that it does not always feel the effect of the sea breeze generated by the heating of the Salinas and Central Valleys. At locations that are not near a break in the coastal mountains, this diurnal direction shift is reduced, but is still present as daytime heating of the coastal mountainsides and small valleys that cut into the terrain causes increased, very localized, low-level divergence.

C. REMOTELY SENSED DATA

Visible satellite imagery was obtained for the purpose of qualitative comparison of relative cloud cover during the three periods. Representative 1 km resolution images for 9, 14, and 17 June are shown in Fig. 22. A morning and an afternoon image are presented to illustrate the degree of clearing that occurs in association with daytime heating over land. Clear skies prevail along the entire coast on 9 June (Fig. 22a), with the exceptions of a few thin bands of stratus in the morning to the west of Cape Mendocino (just at the northern edge of this view), a narrow band of coastal stratus north of Point Conception, and fairly extensive stratus cover in the California Bight. By 1900 UTC (1200 PDT) (not shown), the entire coast is clear except in the Bight, and by 10/0000 UTC (Fig. 22a, bottom) the Bight is largely clear as well.

The morning of 14 June (Fig. 22b, top) is marked by substantial stratus cloud cover from Point Reyes (north of San Francisco) southward, with deep inland penetrations around Monterey Bay, down the Salinas Valley, and in a broad band north and east of Point Conception. Roughly coast-parallel bands of clearing are evident from Point Reyes northward. By 0000 UTC 14 June (Fig. 22b, bottom), the area of clear skies in the north extends to San Francisco and the inland penetrations are limited to southern Monterey Bay and narrow bands along the coast south of San Francisco and north of

Point Conception. Of note, a narrow band of clearing is present along the coast south of Point Sur, which is a common feature on days with extensive stratus coverage. This afternoon cloud pattern persists until sunset that day with only minor changes.

As on 9 June, 17 June is a largely clear day along most of the coast. In the morning (Fig. 22c, top), some very thin stratus is offshore of Cape Mendocino and stratocumulus is well offshore of the central California coast. Very small stratus patches are present in the south near Point Conception. By afternoon (Fig. 22c, bottom), the coast is completely clear and the only cloud cover in the region is some stratocumulus cover a few hundred kilometers offshore.

Vertical wind profilers with associated temperature profilers were available at various locations along the coast. Since their wind signal is not truly representative of coastal jet winds due to their onshore location, a close examination of these winds was not made. The profiler winds generally indicate the expected coast-parallel direction in the boundary layer, with more variability in direction above. More useful in terms of qualitative assessment of the MBL conditions during the three events were the temperature soundings from the RASS, which provides an excellent measure of marine layer thickness. Profiler data from Bodega Bay, Fort Ord, and Point Piedras Blancas are shown in Fig. 23. (Notice that the temperature scales vary from plot to plot.) These locations are indicated on the map in Fig. 8. Data gaps exist in some cases, but the available data provides a good idea of marine layer characteristics on the days of interest. At Bodega Bay at 0000 UTC 9 June (Fig. 23a, top), the inversion base is very shallow (below the lowest range gate at 130 m), with temperatures increasing from about 15°C to over 29°C at 500 m. The entire column cools during that night and then warms to 18°C at 150 m to 24°C from 400 to 600 m by 0200 UTC 10 June. The inversion base never exceeds about 150 m during this 36-h period.

Similar heights and trends are found at Bodega Bay during the 14-15 June event (Fig. 23a, middle), except that temperatures in the boundary layer are lower and the inversion is more diffuse vertically. The diurnal heating cycle is particularly evident above the marine layer between 0000 UTC and 0600 UTC 15 June, which is coincident with a shift in winds from light and onshore to stronger and more northerly. This represents an increased offshore component above the marine layer and is also consistent

with compression of the depth of the inversion during that interval. The 17-18 June event (Fig. 23a, bottom) at Bodega Bay is characterized by stronger winds and a cooler marine layer. The marine layer and inversion appear to be somewhat deeper, with significantly lower temperatures aloft due to the passage of the upper-level trough on that day. An unusual late afternoon low temperature in the MBL can be seen from 0000-0100 UTC 18 June.

The profiler at Ford Ord (Fig. 23b) records more frequently and at better vertical resolution than the other profilers. Notice an inversion base at about 350 m is present at 0000 UTC 9 June, and then the inversion gradually descends closer to the surface and broadens vertically until 1300 UTC 9 June (Fig. 23b, top). During the daily heating cycle the MBL warms to about 15°C and the air above the inversion to over 25°C, and the inversion base has shallowed by this time to approximately 200 m. The warm wedge of air above the inversion is gone by 0200 UTC 10 June as the inversion base again rises above 300 m. By contrast, the marine layer is clearly much deeper during the 14-15 June event (Fig. 23b, middle), with a base at about 500 m at 0000 UTC 14 June, shallowing to 400 m, then rising again to over 500 m by the morning of 15 June. The MBL is also somewhat cooler on this day, which was marked with extensive stratus at the Fort Ord site. The marine layer reaches a depth of approximately 600 m by the end of this 36-h cycle, with only slight warming above the MBL during daytime heating. An even deeper marine layer exists at 0000 UTC 17 June (Fig. 23b, bottom) with an inversion base near 700 m. This depth is constant until about 0700 UTC, and then begins a gradual shallowing to about 500 m until 1600 UTC. The marine layer then warms and shallows sharply as daytime heating begins, and as the upper-level trough axis passes. The result is a much shallower inversion base (below 50 m) by the end of this period at 1200 UTC 18 June, and this shallow base continues after daytime heating has ceased. This day is also characterized by lower temperatures above the inversion than during the other two events.

At Piedras Blancas (Fig. 23c), a similar pattern of marine layer variability as that at Fort Ord exists. Similar to Bodega Bay, the lowest range gate being 180 m prohibits accurate determination of the inversion base in many cases. The 9-10 June event (Fig. 23c, top) is characterized by a fairly shallow marine layer, which shallows initially after

0000 UTC 9 June and reaches its most shallow value at 0100 UTC 10 June, when very warm air exists above (30°C at 500 m). The inversion remains quite shallow through the rest of that 36-h period, despite moderate cooling aloft during nighttime hours. As at Fort Ord, the 14-15 June event (Fig. 23c, middle) is characterized by a deeper MBL, although not as deep as occurred at Fort Ord. This is consistent with the lack of clearing on that day at Fort Ord, while the coast near Piedras Blancas did clear by afternoon. The marine layer reaches its maximum depth of 500 m in this cycle at 1700 UTC 14 June, and then shallows to about 300 m by early evening, even though it remains quite cool at 10°C . A very deep MBL (over 600 m) exists at the start of the third event at 0000 UTC 17 June (Fig. 23c, bottom). This deeper MBL holds steady until 0900 UTC before shallowing sharply in association with the passage of the upper-level trough. By 0700 UTC 18 June, the MBL is no longer apparent at depths above 150 m. It is likely that a shallow boundary layer did exist after 0700 UTC, but it is not detected by the profiler due to the range gate limitation. As at Fort Ord, the air aloft is cooler during this third event than during the previous two events.

In summary, the 9-10 June and 17-18 June events are characterized by skies that are mostly clear in the areas of interest, while the 14-15 June event is marked by substantial stratus. The most shallow MBL existed during the 9-10 June event, particularly in the south. Both the 14-15 June and 17-18 June events began with relatively deep marine layers at the two southern locations, although the MBL shallowed dramatically from 17 June into 18 June due to the passage of an upper-level trough. This sharp change was not apparent in the cloud pattern, as the day began predominantly clear.

D. PRESSURE GRADIENT ORIENTATION VERSUS OBSERVED WINDS

Station pressure at each buoy was compared with other buoys and land stations to examine the relationship between the buoy wind variations and the local ∇p . The winds at Buoy 28 are replotted in Fig. 24 with the along-shore pressure difference between Buoy 28 and Buoy 42 ($P_{42}-P_{28}$), which is approximately 100 km to the north of Buoy 28 off Monterey Bay. A clear correlation exists between along-shore ∇p and wind speed at Buoy 28. When the wind speeds are a maximum, the north-south pressure gradient is also a maximum, and exceeds 2 mb. This is particularly evident during the 9-10 June and

17-18 June events. During the intervening time, which includes the 14-15 June event, the along-shore ∇p is near zero, or even slightly south to north, and the winds at Buoy 28 slow from about 15 m s^{-1} late on 9 June to an average of about 10 m s^{-1} , while retaining their coast-parallel northwesterly direction. Of note, coincident with these weaker winds is an increase in the diurnal change of wind speed relative to the diurnal variability during the 9-10 June event. A $3\text{-}4 \text{ m s}^{-1}$ diurnal cycle is clearly evident from 13-16 June.

To determine if a relationship also exists between the cross-coast pressure gradient and observed winds, a central California inland station near sea level was needed. Station pressures at Naval Air Station Lemoore (south of Fresno) were compared with pressures at Buoy 28 (Fig. 25). Separation between these stations is 175 km. Somewhat unexpectedly, the cross-coast pressure gradient has the opposite relationship to the winds at Buoy 28. That is, the higher winds during the 9-10 June and 17-18 June events correspond to minima in the pressure difference (values near 9-10 mb), while relatively weaker winds occur between during a period of increased cross-coast pressure difference (values near 14 mb). While this pattern is particularly clear at Buoy 28, a similar pattern is evident at other buoy locations.

Thus, the highest winds at Buoy 28 occurred when the along-shore pressure gradient was a maximum in a north to south sense and when the cross-coast pressure gradient was a minimum. Referring to the sea-level pressures in Figs. 14, 17, and 20, the weaker winds are associated with a period when the pressure gradient is directed perpendicular to the coast, as is particularly clear at 0000 UTC 15 June (Fig. 17c). When the surface isobars are reoriented such that they cross the coast at a significant angle, as on 9-10 and 17-18 June, the winds at the buoy are stronger. Since the buoy winds are at 5 m, it is reasonable to expect that they would have a large ageostrophic component down the pressure gradient due to frictional effects. When the pressure gradient is directed onshore, this ageostrophic component is blocked by the steep topography of the Big Sur coastline and is redirected along-shore, which is along the isobars in a direction consistent with geostrophy. When there is a significant coast-parallel component to the gradient, as during the first and third events, less flow blocking occurs and the winds reach higher down-coast magnitudes. From Fig. 24, this down-coast component is approximately 2 mb per 100 km between Buoys 42 and 28 on 9 June, falls to

approximately zero on 14 June, and increases to an average of about 1.5 mb per 100 km on 17 June. Meanwhile the cross-coast component from Fig. 25 is actually a maximum at 7.4 mb per 100 km on 14 June, with values near 5.5 mb per 100 km on 9 June and 17 June. It could reasonably be concluded that offshore winds would be maximized in the extreme case of a high down-coast component with zero cross-coast component. However, it is important to note that the existence of a coastal jet depends on the presence of a substantial cross-coast gradient. The magnitude modulations at a given location are then governed by these reorientations of the local gradient. Thus, in the presence of the normal summertime pattern (i.e., when a jet is present), when the down-coast gradient is at or below zero, down-coast winds will continue, but will be near their minimum magnitudes. When that gradient climbs to 2 mb per 100 km or greater, down-coast winds will accelerate to their maximum values.

Additionally, the flow may be less affected by diurnal changes associated with coastal heating during the periods of higher down-coast pressure gradient, due to reduced impingement of the winds on the coastal topography. This reduced flow interaction with the land could explain the reduced diurnal variability in wind speed during the higher wind periods. (The modeling portion of this study was not designed to examine this hypothesis, since variations in the diurnal response at a particular location are not adequately represented in a series of 36-hour model runs.)

The satellite imagery and profiler data between the higher wind events (12-16 June) indicate stratus coverage was more extensive and the marine boundary layer was deeper along the central California coast than it had been on 9-10 June. It could be argued that this deeper marine layer contributes to a higher surface pressure at Buoy 28, and thus a greater pressure difference between the buoy and Lemoore, and this results in the observed wind speed reduction as described above. However, the raw pressures at Buoy 28 and Lemoore (Fig. 26) reveal that pressure changes at Lemoore are the primary driver of the gradient between the two sites. Thus, assuming an existing favorable pressure pattern for down-coast winds, periods of increased pressure in the interior of central California produce a reduced cross-coast pressure gradient, and an alignment of the surface pressure pattern that allows higher coastal jet winds at the surface. Similarly, lower interior pressures create a higher cross-coast pressure gradient and a reduction in

offshore jet winds. More generally, the magnitude of the coastal jet, as represented in the 5 m winds at Buoy 28 off central California, is modulated by changes in the orientation of the surface pressure gradient relative to the coastline. When that orientation is such that the down-coast component of the local pressure gradient is maximized, the offshore winds are also at a maximum. When viewed on the larger scale, this reorientation of the surface pressure pattern is driven largely by changes in the interior California pressure pattern, and particularly the position and intensity of the thermal low.

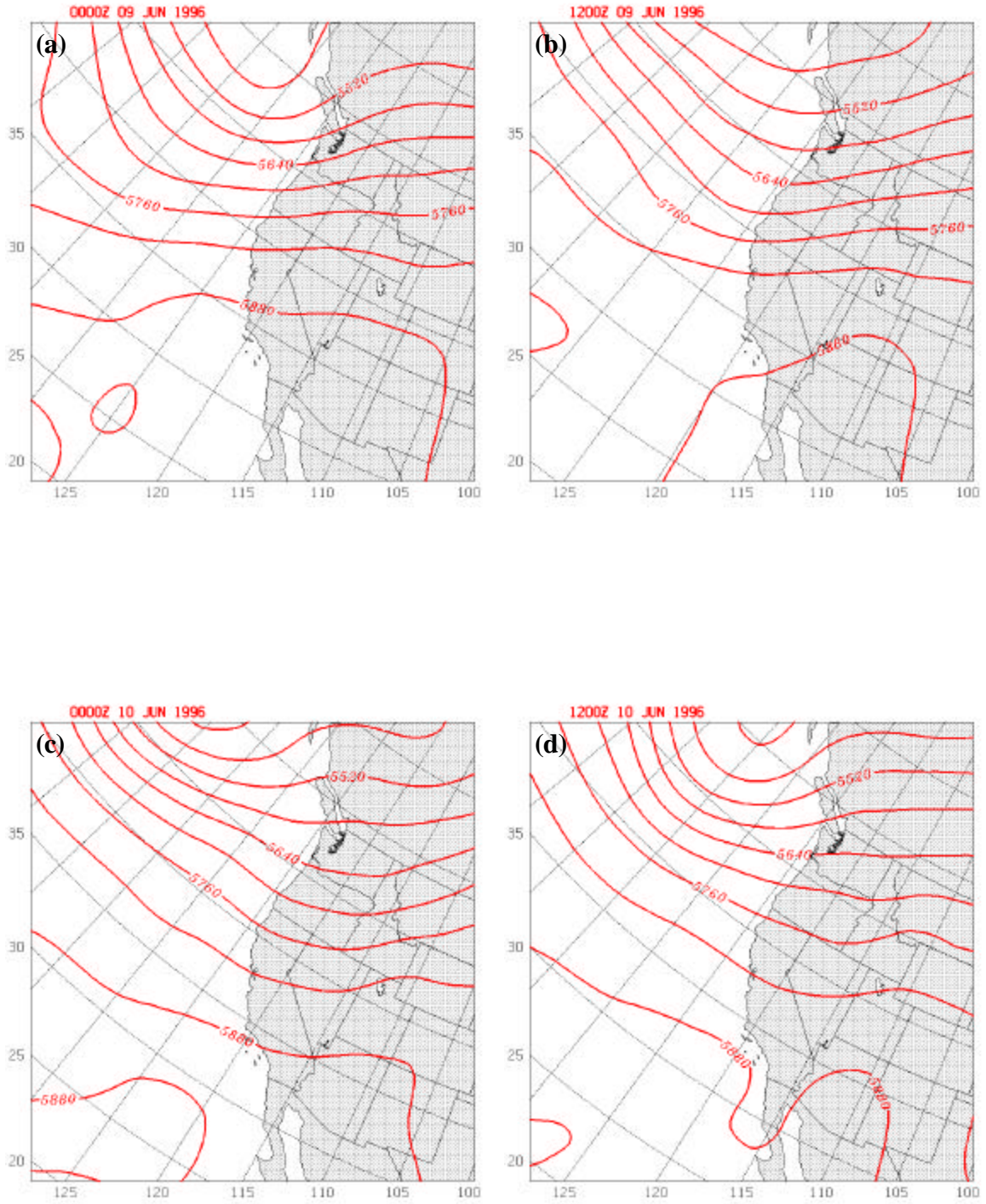


Figure 12. NOGAPS 500 mb height analyses from (a) 0000 UTC 9 June, (b) 1200 UTC 9 June, (c) 0000 UTC 10 June, and (d) 1200 UTC 10 June 1996.

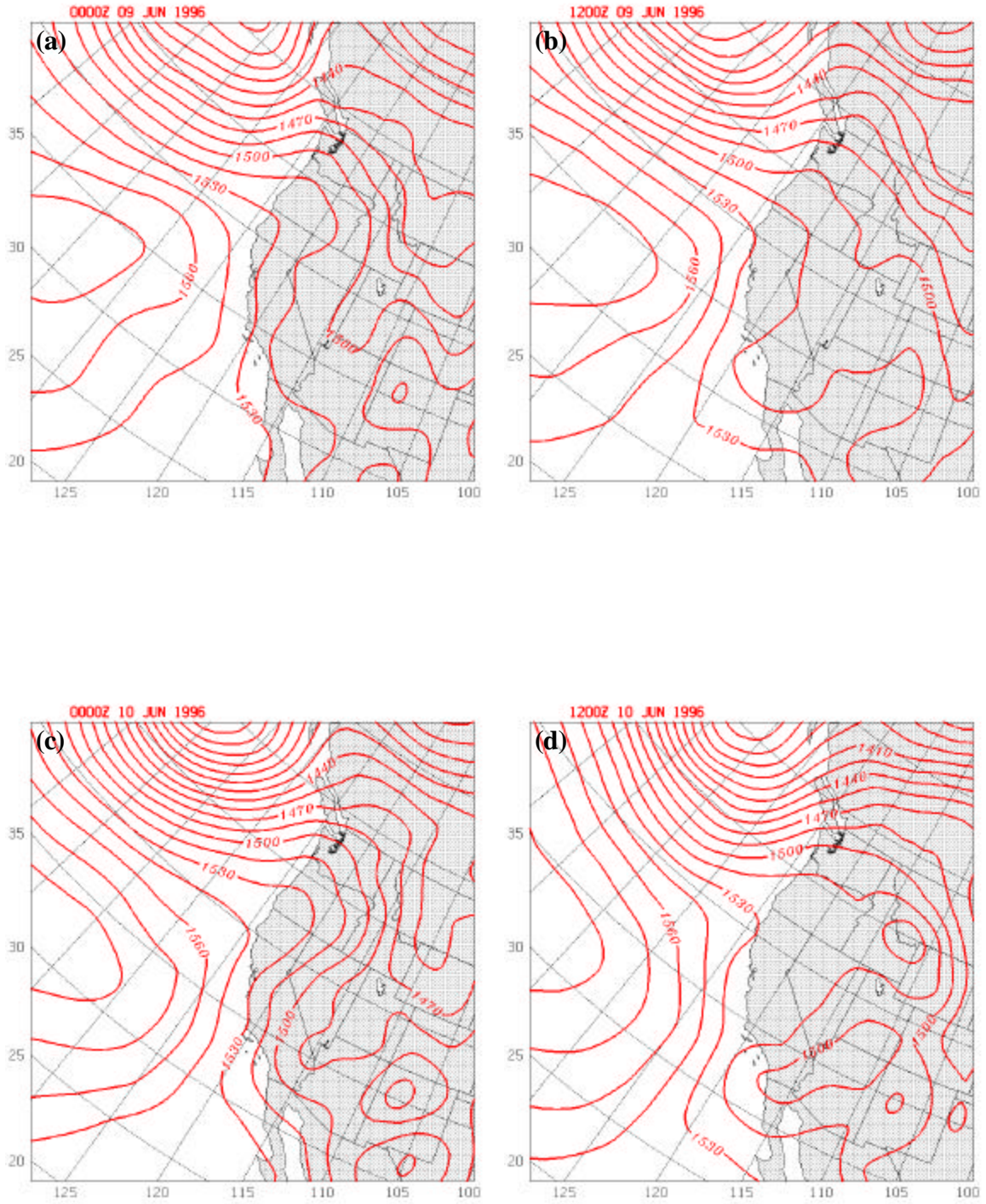


Figure 13. NOGAPS 850 mb height analyses from (a) 0000 UTC 9 June, (b) 1200 UTC 9 June, (c) 0000 UTC 10 June, and (d) 1200 UTC 10 June 1996.

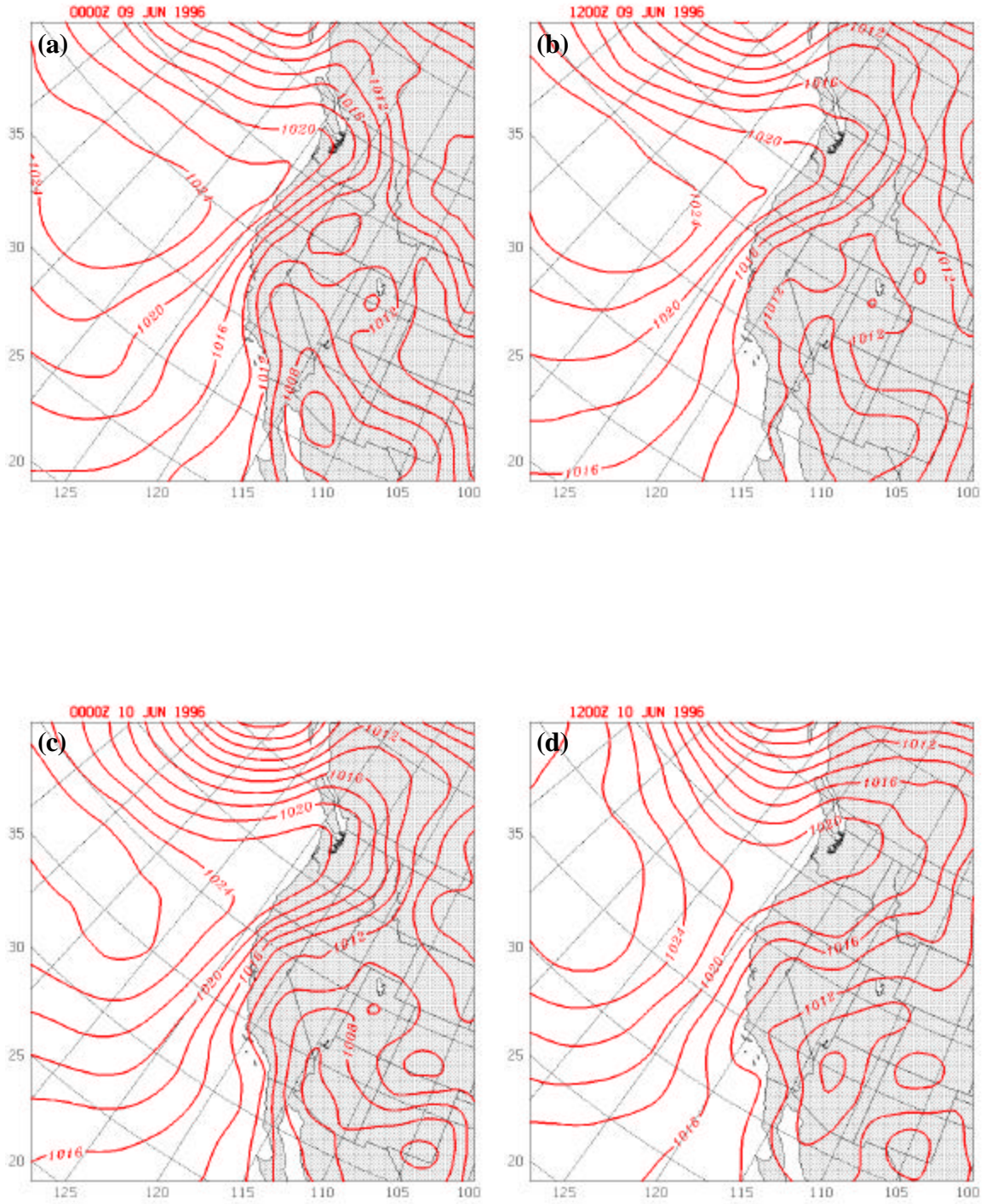


Figure 14. NOGAPS sea-level pressure analyses from (a) 0000 UTC 9 June, (b) 1200 UTC 9 June, (c) 0000 UTC 10 June, and (d) 1200 UTC 10 June 1996.

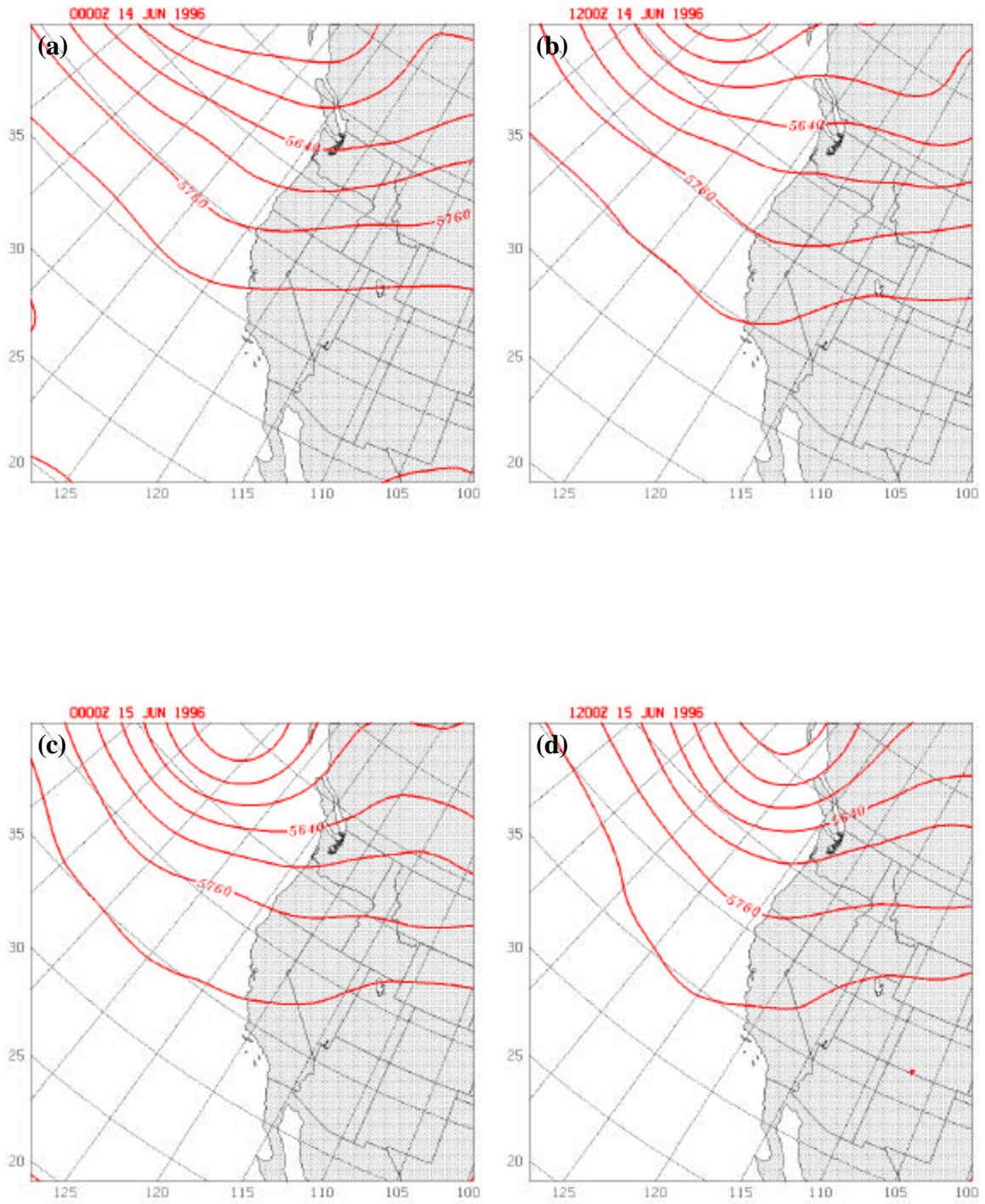


Figure 15. NOGAPS 500 mb height analyses from (a) 0000 UTC 14 June, (b) 1200 UTC 14 June, (c) 0000 UTC 15 June, and (d) 1200 UTC 15 June 1996.

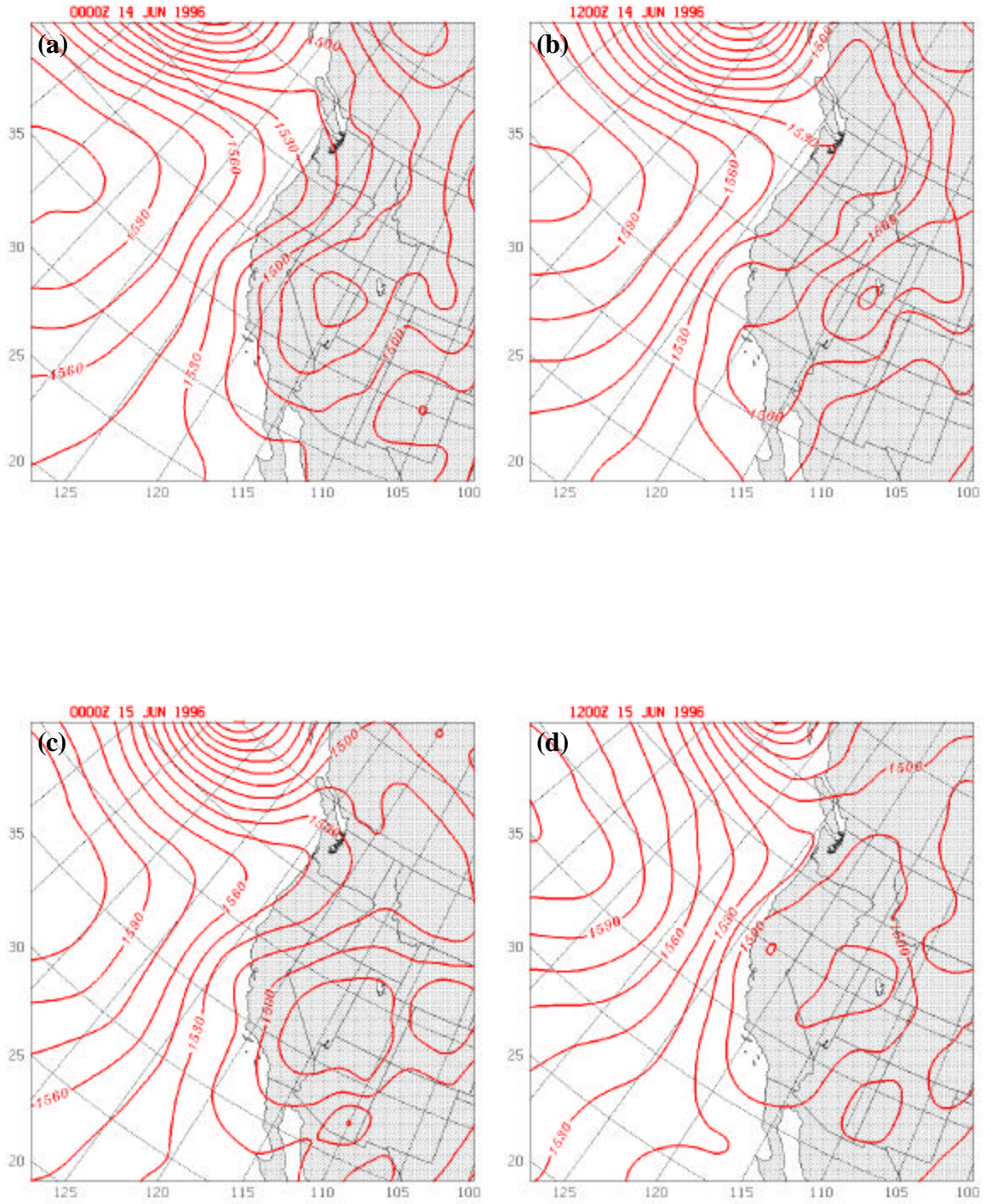


Figure 16. NOGAPS 850 mb height analyses from (a) 0000 UTC 14 June, (b) 1200 UTC 14 June, (c) 0000 UTC 15 June, and (d) 1200 UTC 15 June 1996.

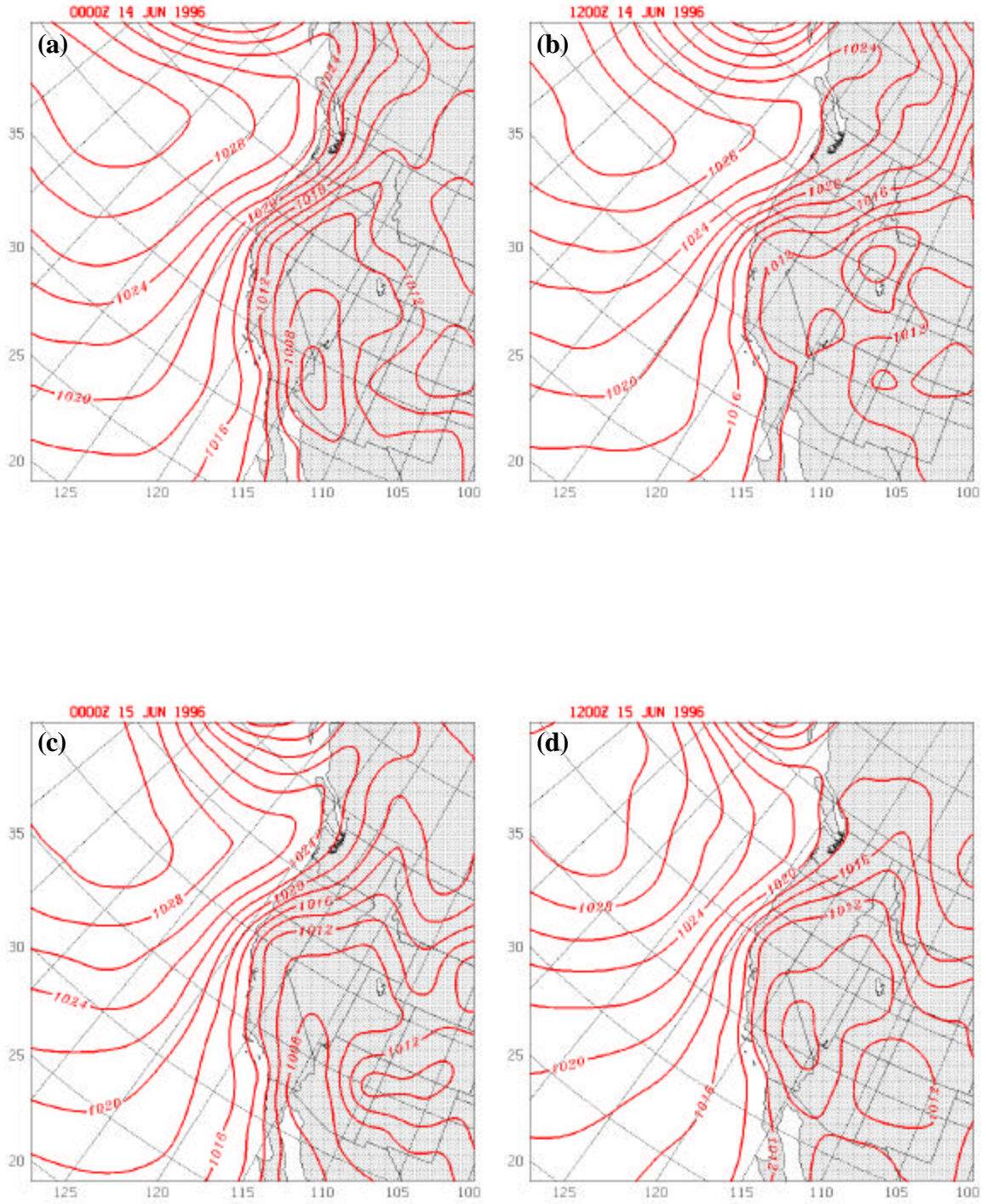


Figure 17. NOGAPS sea-level pressure analyses from (a) 0000 UTC 14 June, (b) 1200 UTC 14 June, (c) 0000 UTC 15 June, and (d) 1200 UTC 15 June 1996.

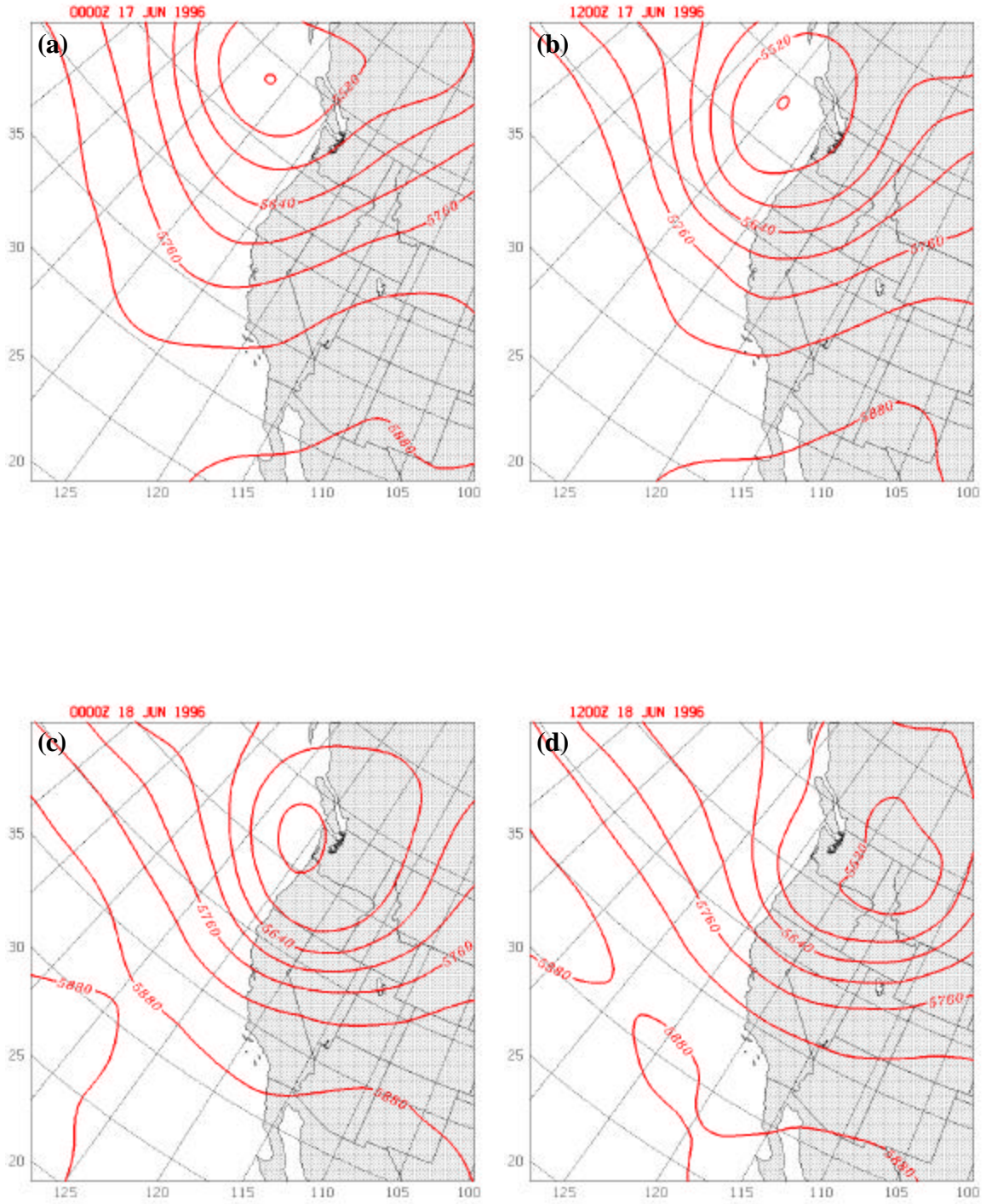


Figure 18. NOGAPS 500 mb height analyses from (a) 0000 UTC 17 June, (b) 1200 UTC 17 June, (c) 0000 UTC 18 June, and (d) 1200 UTC 18 June 1996.

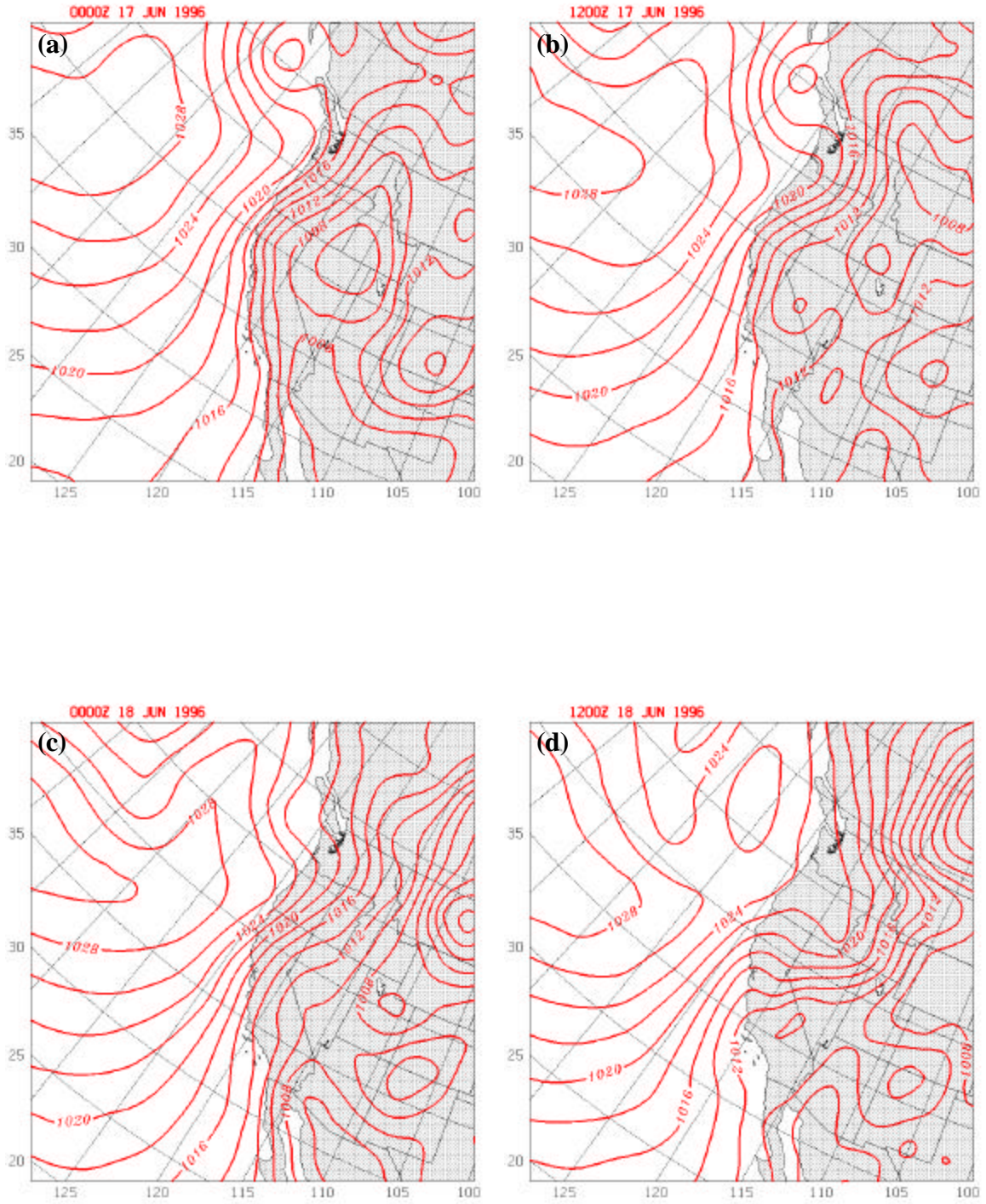


Figure 20. NOGAPS sea-level pressure analyses from (a) 0000 UTC 17 June, (b) 1200 UTC 17 June, (c) 0000 UTC 18 June, and (d) 1200 UTC 18 June 1996.

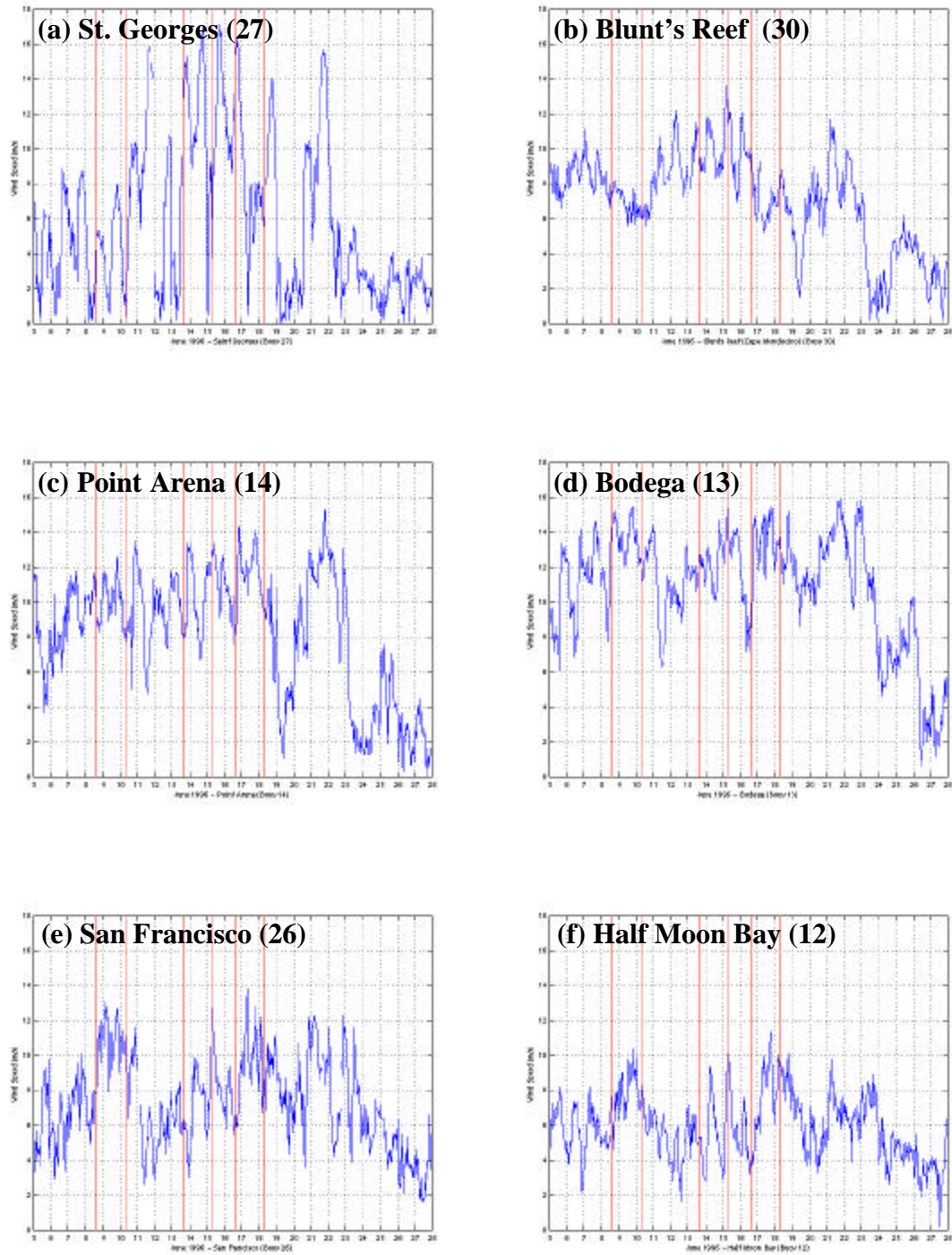


Figure 21. Buoy wind time series during June 1996 as in Fig. 10. Plots are presented from north to south, beginning with (a) Buoy 27 near the Oregon border and progressing to (i) Buoy 23 west of Point Conception. Winds are in m s^{-1} and time is PDT, with the tick mark for each day representing 0000 PDT on that day. Vertical lines again indicate the three model study periods.

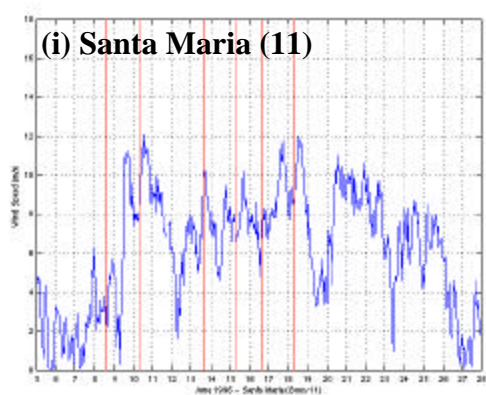
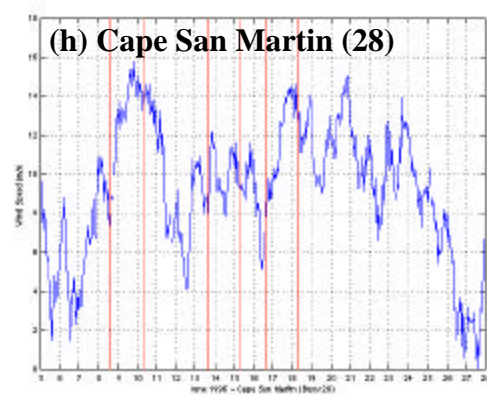
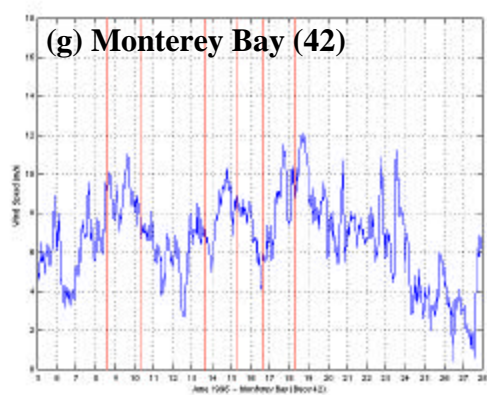


Figure 21. Continued.

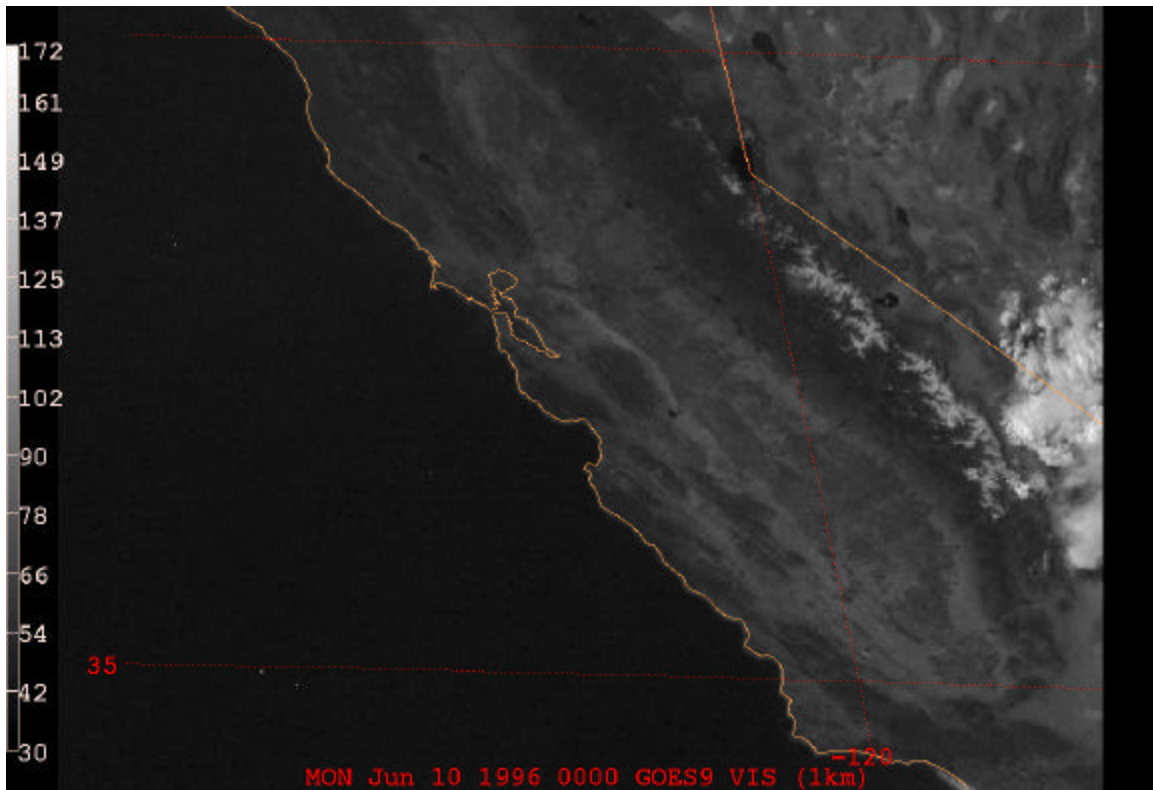
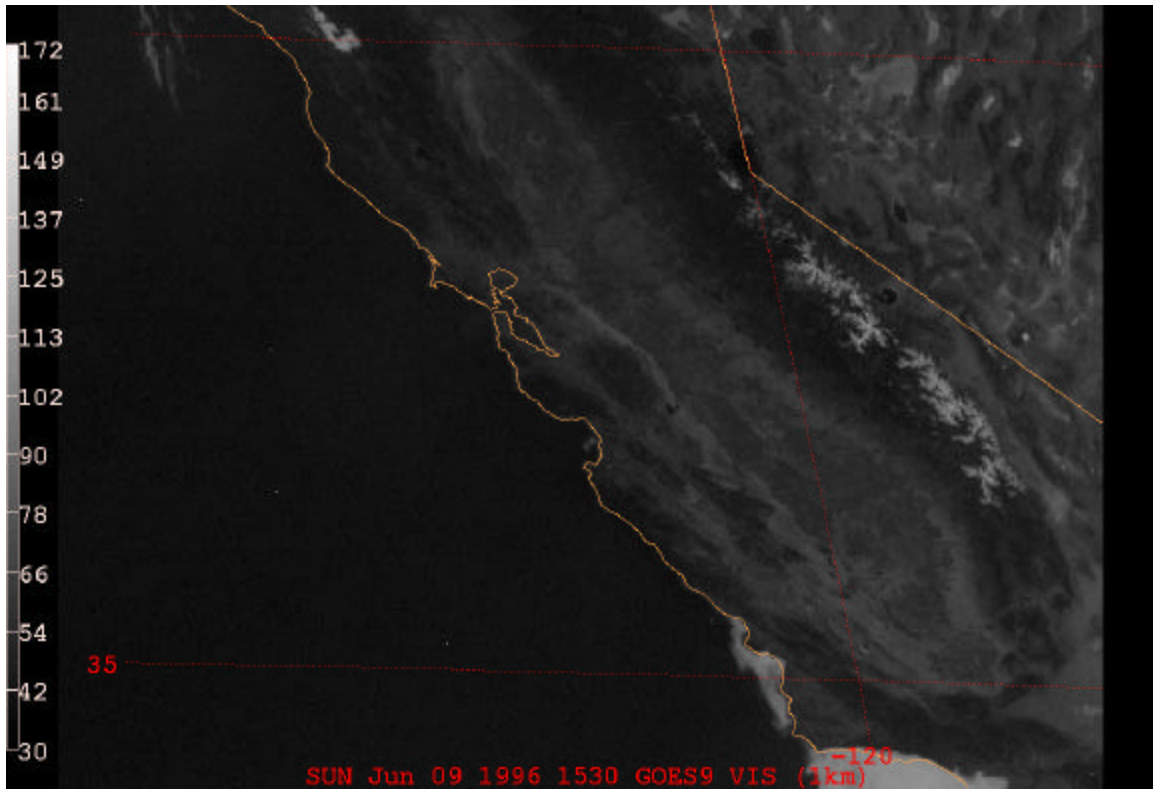


Figure 22a. Visible satellite imagery from GOES-9 at 0830 (top) and 1700 (bottom) PDT 9 June 1996.

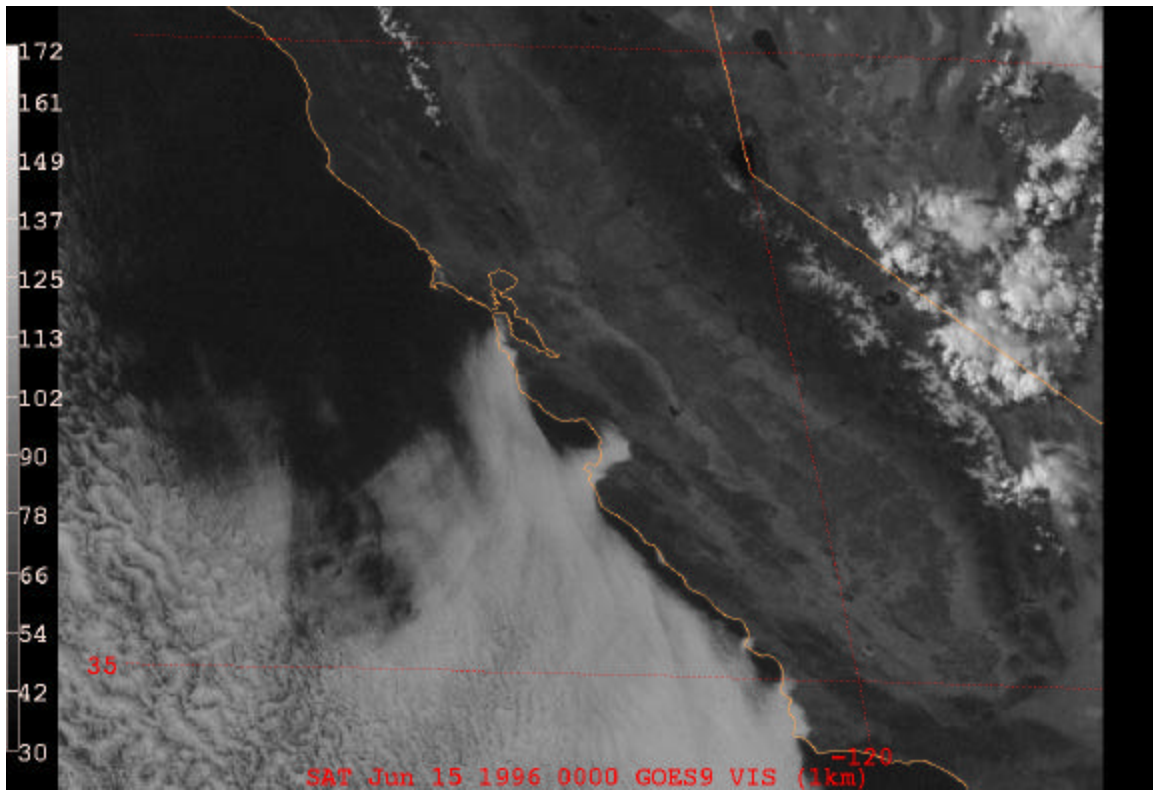
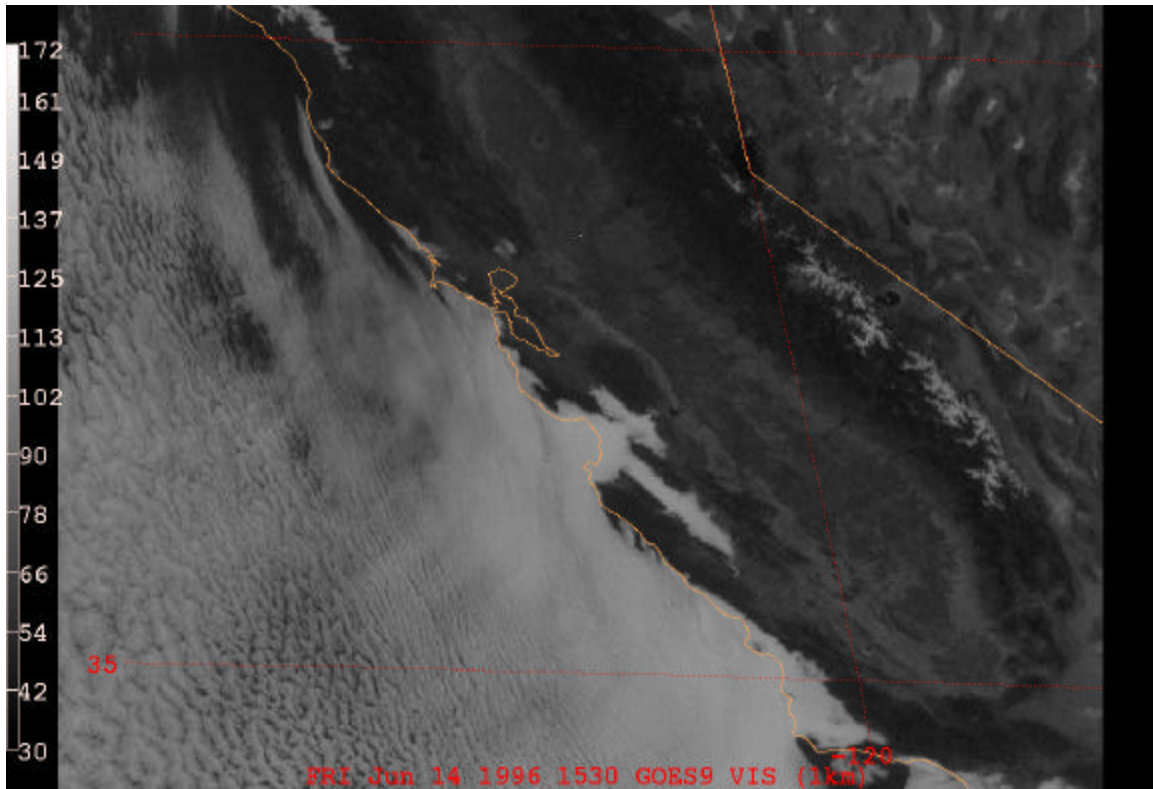


Figure 22b. Visible satellite imagery from GOES-9 at 0830 (top) and 1700 (bottom) PDT 14 June 1996.

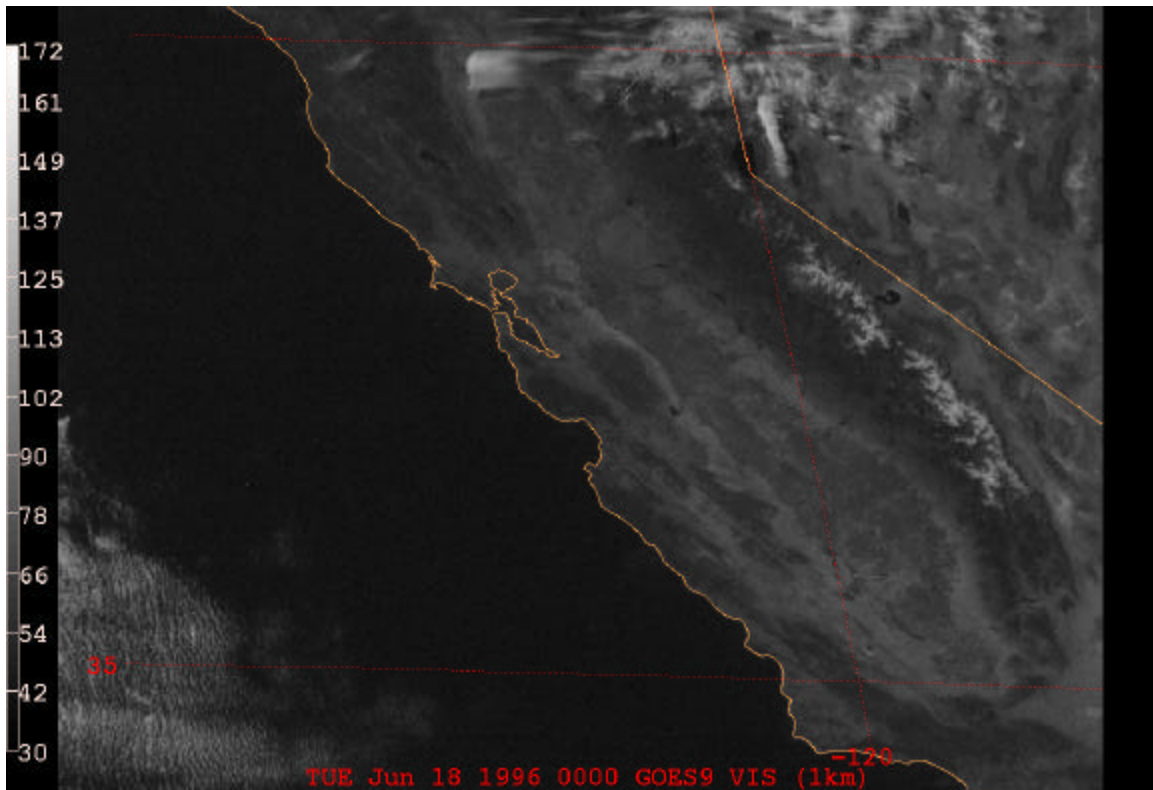
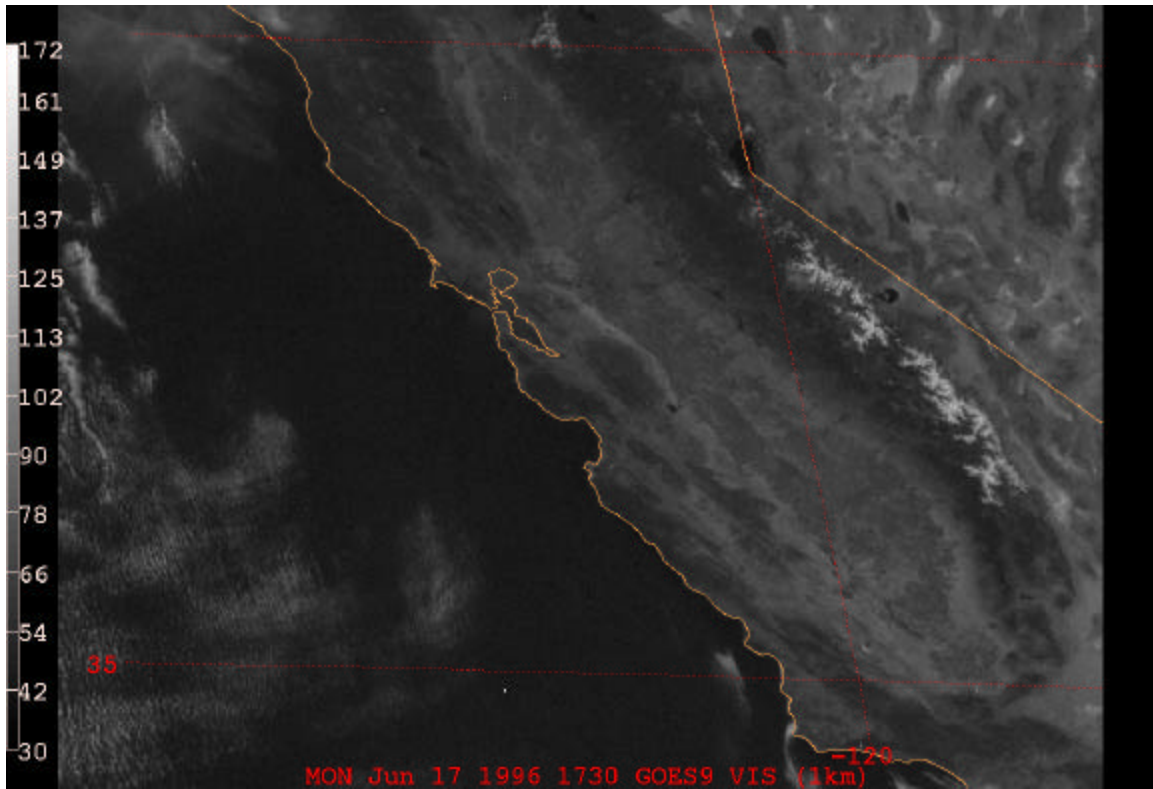


Figure 22c. Visible satellite imagery from GOES-9 at 1030 (top) and 1700 (bottom) PDT 9 June 1996.

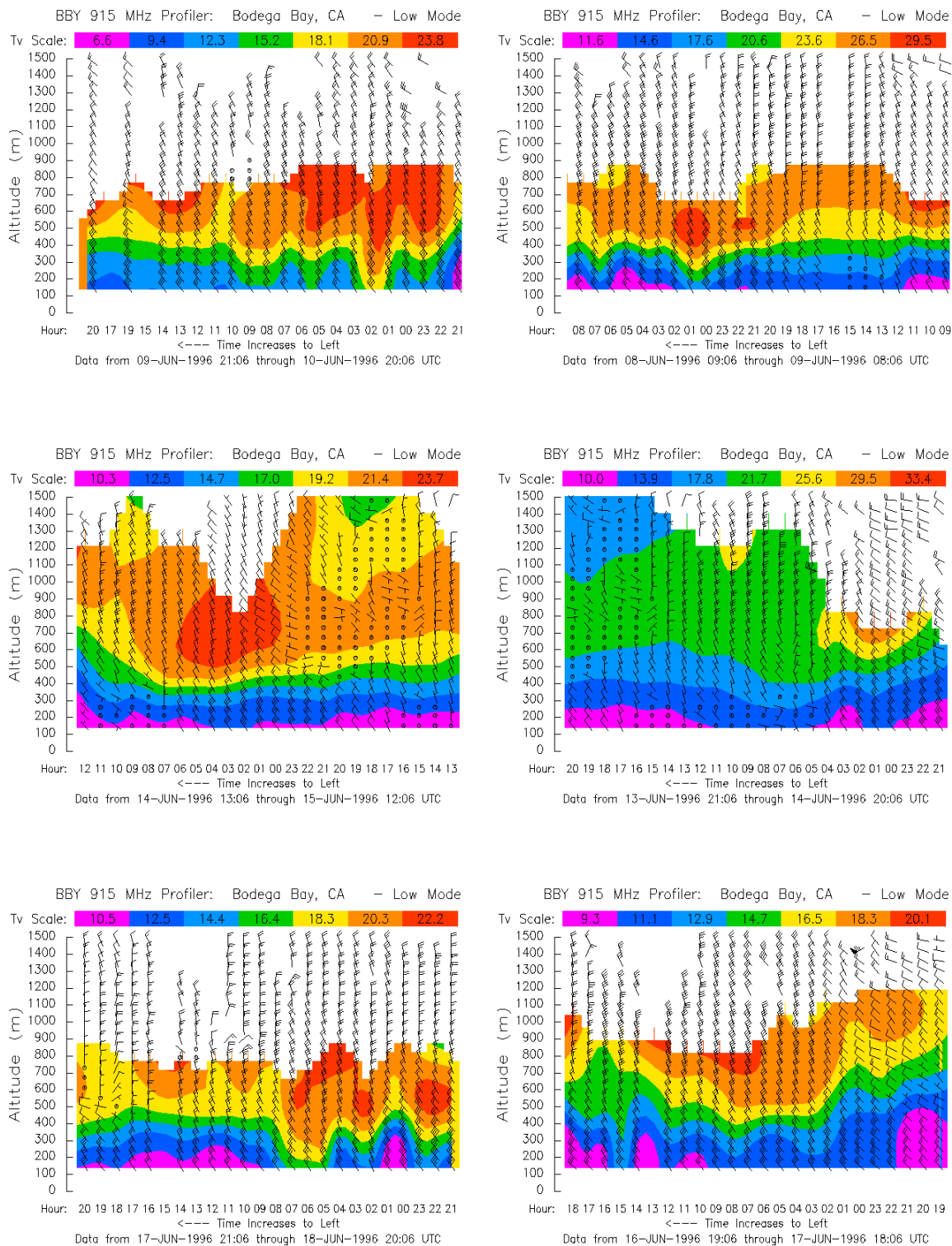


Figure 23a. Vertical wind profiler data from Bodega Bay from 8-10 (top), 13-15 (middle), and 16-18 (bottom) June 1996. Note that color scale varies from plot to plot and time (UTC) increases from right to left. Location is shown in Fig. 8.

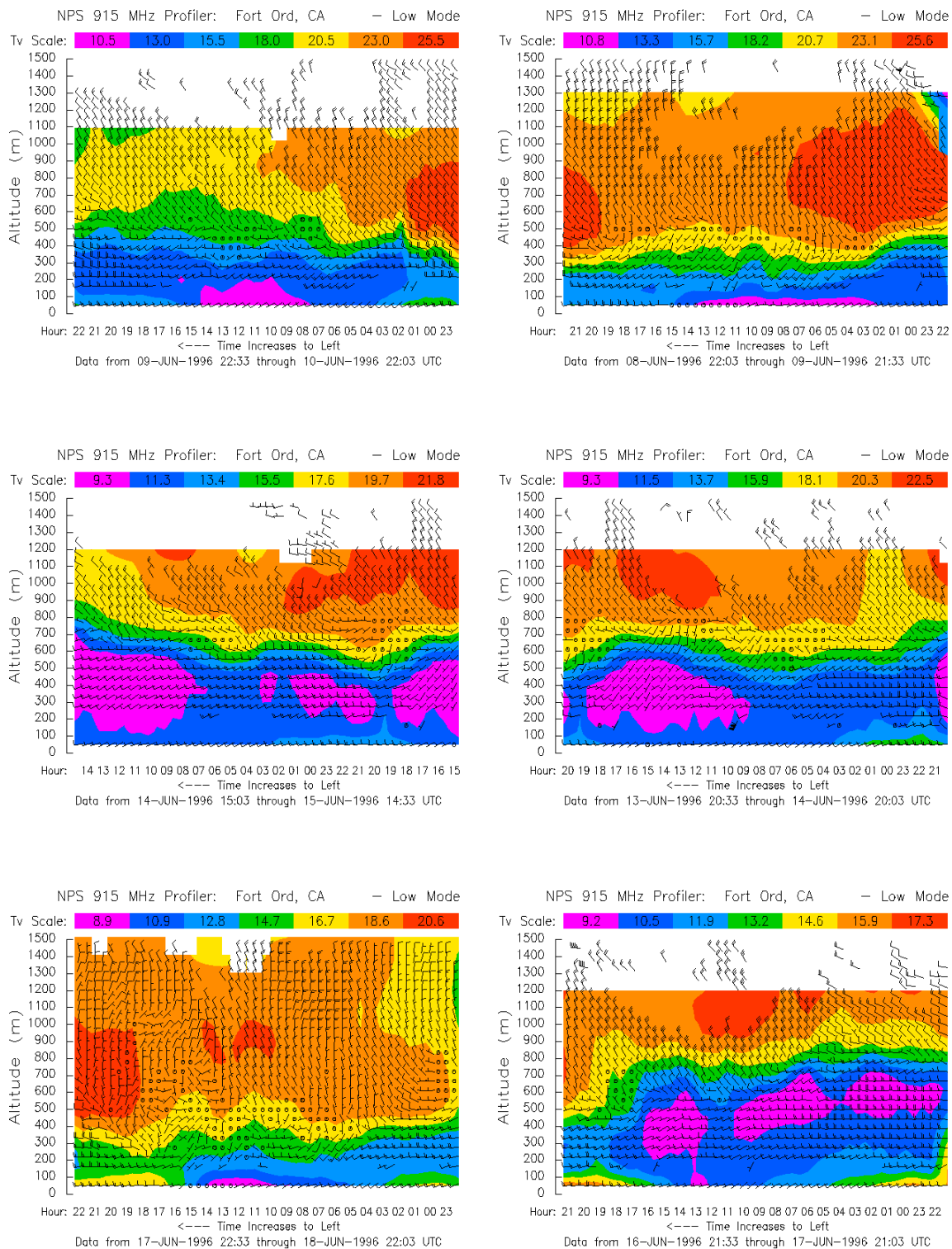


Figure 23b. As in Fig. 23a, except for the Fort Ord profiler.

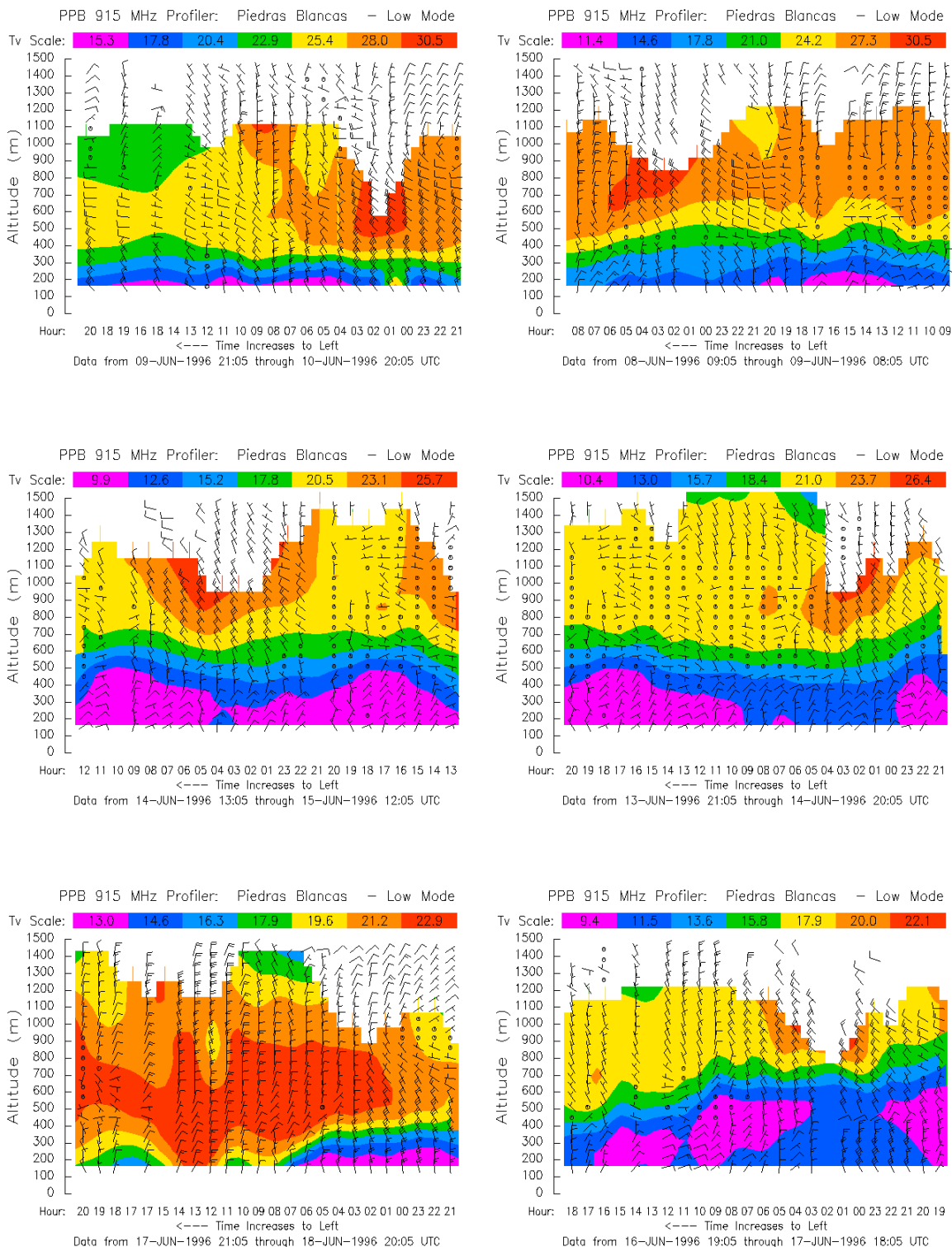


Figure 23c. As in Fig. 23a, except for the Piedras Blancas profiler.

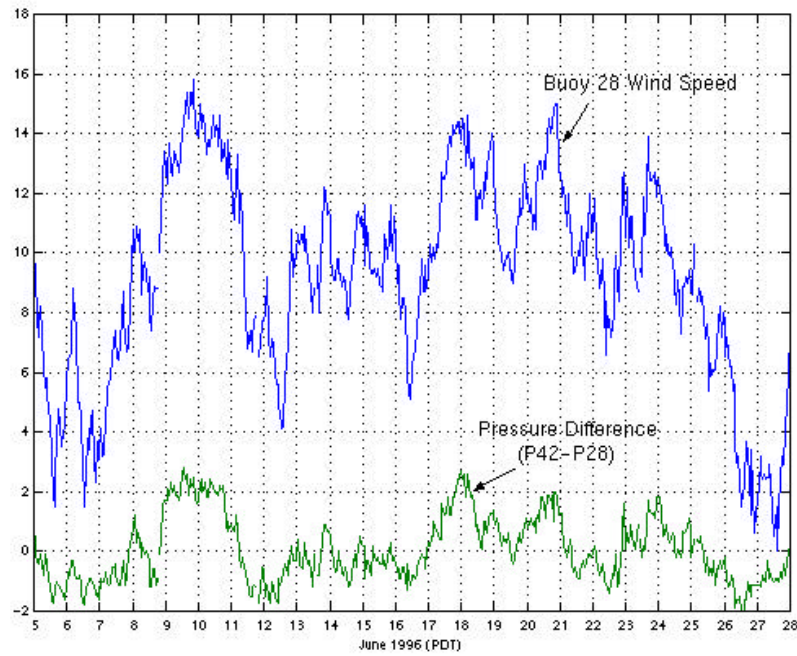


Figure 24. Wind speeds at Buoy 28 (blue) as in Fig. 10, and pressure difference (mb) between Buoy 28 and Buoy 42 (green). Positive values indicate down-coast pressure gradient.

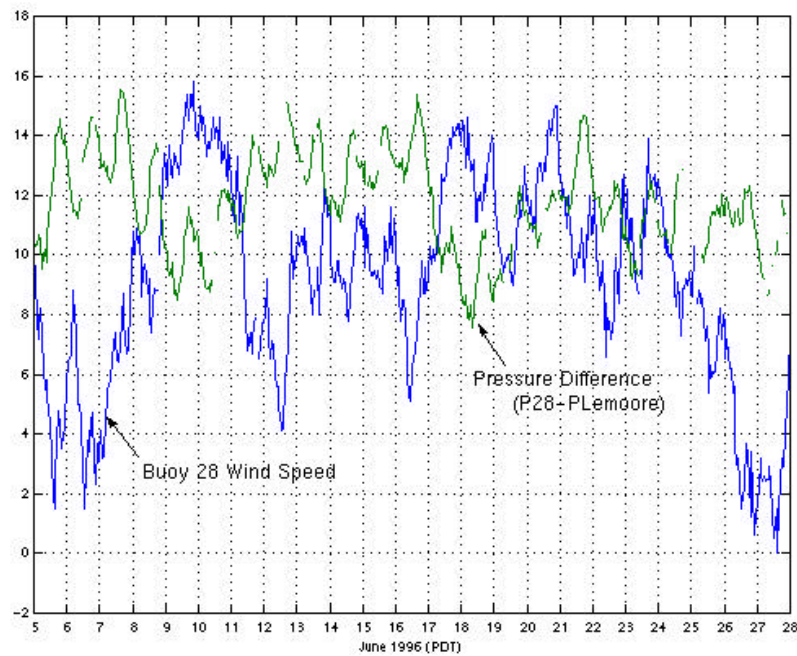


Figure 25. As in Fig. 24, except pressure difference is between Buoy 28 and Naval Air Station Lemoore, CA. Positive values indicate cross-coast gradient directed toward land.

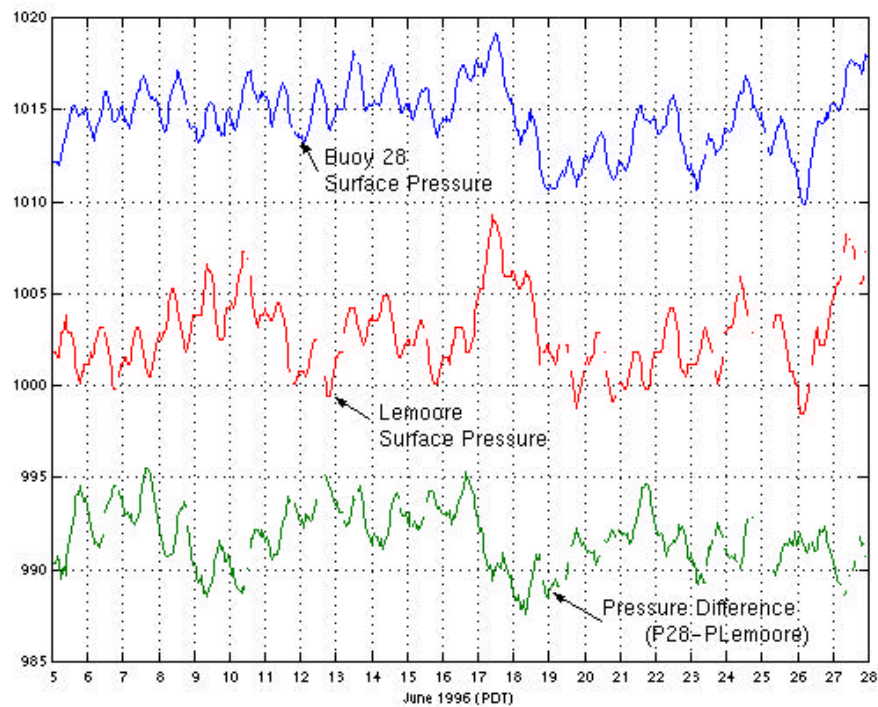


Figure 26. Surface pressures (mb) at Buoy 28 (top) and Lemoore (middle), and pressure difference between the two (bottom). Absolute pressure difference is obtained by subtracting 980 from the plotted values.

V. COAMPSTM VALIDATION

To establish the credibility of the predictions from the COAMPSTM model, several comparisons between the model output and observations from this study and from other published papers are presented here. Analyses from NOGAPS and measured winds from the NOAA buoys are directly compared with the COAMPSTM model output. Direct comparison is also possible in the case of the observations in Dorman et al. (1999), since that study focused on the winds near Point Sur on 17 June, which is during one of the three events in this study. Additionally, model output is compared with observations in the CODE papers, aircraft data from Parish (2000), and Coastal Waves 96 data in Rogers et al. (1998) and Strom et al. (1999). Since the COAMPSTM model runs were not spatially or temporally coincident with observations from these studies, direct comparisons are not possible. However, the data in these studies adds further evidence of the range of observed MBL structure and coastal jet winds during the same time of year under similar synoptic conditions. It is shown in this chapter that the model produces synoptic and mesoscale structures that are consistent with both the data presented in this study and the range of observations from other studies.

Note: the comparisons of NOGAPS analyses with COAMPSTM predictions in the following section are based on the outer 81 km COAMPSTM domain. All COAMPSTM discussion thereafter is based on the inner 9 km domain, unless specifically noted.

A. NOGAPS ANALYSES

The NOGAPS analyses (see Chapter IV) were used as a quality check on the large-scale behavior of the mesoscale model over the simulation period. Due to the small number of offshore observations available for the 3DMQ analysis that uses the NOGAPS analysis as a first guess, the initial COAMPSTM analyses are nearly identical to those from NOGAPS over the ocean. More illustrative of the validity of COAMPSTM predictions relative to NOGAPS analyses are the sea-level pressure and 850 mb heights from the 81 km COAMPSTM domain at 1200 UTC 10 June, 1200 UTC 15 June, and 1200 UTC 18 June (the end of each 36-h run) as shown in Fig. 27. The COAMPSTM predictions over land are not smoothed in the way that NOGAPS is, and subterranean

height values at 850 mb are not interpolated to the plot. Consequently, obvious differences over the interior of the continent exist when comparing these predictions to the NOGAPS analyses at corresponding times (Figs. 12-20). However, the similarities in the basic pattern over water and near the coast are important to note.

On 10 June, the predicted surface high (Fig. 27a) is of similar magnitude and orientation, a ridge extends to the northeast over Oregon and Washington, and the isobars cross the coast at a significant angle from the Oregon border southward. At 850 mb (Fig. 27b), the COAMPSTM eastern North Pacific high and Gulf of Alaska low are situated very close to where they are in the NOGAPS analysis, with the ridge between crossing the coast in both cases near the Oregon border. The thermal low is deeper at this level in the model than in the analysis, which creates stronger 850 mb geostrophic flow at the coast, but the orientation of the isoheights is similar. On 14 June, the broader surface ridge in the Pacific Northwest is well represented in COAMPSTM (Fig. 27c), as is the orientation of the isobars, which cross the coast at a significant angle only in far northern California and become more coast parallel from about Point Arena southward. The offshore high and low are again accurately predicted in COAMPSTM at 850 mb (Fig. 27d), although the ridge axis is slightly farther south in COAMPSTM (over northern Oregon versus southern Washington). The resulting 850 mb isoheight orientation along the California coast is quite similar to the analysis, with less of a tendency to overdevelop the interior low and corresponding near-shore height gradient. Finally, while the 18 June closed offshore surface high in NOGAPS is less distinct in COAMPSTM (Fig. 27e), a very similar coastal pressure pattern is clearly predicted. Specifically, the significant cross-coast component of the isobars (or downcoast component of the pressure gradient) is predicted from southern Oregon to well south of Point Sur. At 850 mb on this day (Fig. 27f), a ridge in the NOGAPS analysis extends to the east over northern California (not well pronounced at the coast) and another to the north into the Gulf of Alaska. These features are captured nicely in COAMPSTM, although the eastern ridge is less obvious and located farther north. The resulting cross-coast geostrophic flow in the COAMPSTM prediction extends from Cape Mendocino southward, while it begins over the northern San Francisco Bay area in the NOGAPS analysis.

The primary conclusion from these comparisons is that the basic synoptic structure evident in the NOGAPS analyses is predicted in the larger-scale domain of the COAMPSTM integrations at 36-h. The positions of key features, such as the eastern North Pacific high, Gulf of Alaska low, and the ridging that extends to the north and east of the high, are well represented in COAMPSTM. Most importantly to the goals of this study, the orientation of surface isobars relative to the coast, which (as discussed in the last chapter) are important in assessing the relative magnitude and distribution of along-shore winds, is predicted by COAMPSTM much as it appeared in the NOGAPS analyses. Since the model predicts synoptic-scale structure that is quite similar to the NOGAPS analyses, it is reasonable to suggest that the mesoscale structure predicted in the inner nest near the coast is likely to be a valid response to local topographic forcing, rather than being an artifact of erroneous circulations on the outer nest propagating inward.

B. BUOY WINDS

As another check on the large-scale performance of the model, the winds at the buoys during the three events were compared with the magnitude of the coastal jet produced on those days in the model. Representative isotach plots from the model (from early evening when the jet tends to be particularly well developed) are shown in Fig. 28 for each of the three events. The COAMPSTM winds are on the 990 mb level, which typically ranges from near 300 m well offshore in the northwestern part of the inner nest to near 200 m in the vicinity of the coastline. These elevations are high enough to sample the jet away from direct surface effects, but low enough to qualitatively compare with buoy winds. Winds in excess of 12 m s^{-1} are highlighted with color shading to provide an approximation of coastal jet extent. While there are significant diurnal changes in the model in both the position and intensity of local jet maxima, as well as in the shape and size of the larger-scale coastal jet, a general statement of the relative jet behavior during the three events can be made.

For both the 9-10 June and 17-18 June events (Figs. 28a,c), the jet is concentrated farther south than during the 14-15 June event (Fig. 28b). For the first and third events, the area of accelerated winds begins near Cape Mendocino and Point Arena, respectively, while for the second event a substantial jet exists as far north as the lee of Cape Blanco in southern Oregon and a much weaker jet exists from Point Sur southward. A comparison

of the predicted jet winds in the lee of Cape Mendocino and Point Sur with the buoy wind traces from Cape Mendocino (Buoy 30) and Cape San Martin (Buoy 28) reveals that the pattern of low/high/low winds in the north and high/low/high winds in the south is captured quite well in the model.

The short 36-h integration of the model in each event precludes a meaningful time series comparison with the NOAA moored buoy data. This is particularly true since the first several hours of each model integration do not reliably contain realistic mesoscale structures near the coast as some time is required for the smooth initial flow to adjust to the coastal topography. Consequently, most of the predictions described here are from the final 24-h of each 36-h integration.

Despite the inability to produce a long model time series to compare with the wind data from the entire study period, the 24-hour diurnal cycle of winds from Buoy 28 beginning at 0500 PDT on each day, corresponding to the 12-h to 36-h model 10-m winds, is shown in Fig. 29. At 0500 PDT 9 June (Fig. 29a), the COAMPSTM winds are near 13.7 m s^{-1} , reach a broad peak of between 15.0 and 15.4 m s^{-1} from 0900 PDT to 2100 PDT, and then drop sharply to 13.3 m s^{-1} by early morning. The Buoy 28 winds begin near 12.6 m s^{-1} , rise to over 15 m s^{-1} between 1000 PDT and 1500 PDT, reach an absolute maximum on that day of 15.8 m s^{-1} at 2100 PDT, and drop to about 14 m s^{-1} by 0500 PDT 10 June. While the high frequency fluctuations due to MBL turbulence are not evident in the model, both the timing of the diurnal maxima and minima and the absolute magnitudes are in reasonable agreement with the data.

On 14 June (Fig. 29b), the model winds are noticeably weaker than on 9 June, rise very gradually from 13.5 m s^{-1} at 0500 PDT to a shallow peak of about 14.3 m s^{-1} between 2000 PDT and 2300 PDT, and then fall only very slightly. While the timing of the daily maximum and gradual increasing trend are captured well in the model, these winds are notably higher than those at the buoy, where winds ranged from 8.1 m s^{-1} to 11.7 m s^{-1} . Also, the minimum of 8.1 m s^{-1} at 1300 PDT and the magnitude of the diurnal signal are not captured in the model. The higher winds in the model in this case could be related to the fact that they are 10 m winds, vice 5 m at the buoy. However, this vertical difference exists on all three days. It is possible that the surface winds on 14 June were more effectively decoupled from the winds above due to differences in the turbulence

characteristics in the boundary layer on that day, which was characterized by a deeper, cloudier marine layer. Another error source in the model is the position of the local maximum in the lee of Point Sur relative to the buoy location. A shift of the center of this maximum by a few kilometers can produce significantly different wind magnitudes at a given point. It is possible the model more accurately represented the position of the wind maximum on 9 and 17 June, at least partially accounting for the better match in wind magnitudes on those days. The characteristics of these lee accelerations will be discussed in the next chapter. Further, the fact that the model diurnal signal is too small and the winds are too strong may suggest that the winds in the model are not interacting with the coastal topography to the degree that they do in the real atmosphere. This wind offset is noteworthy, but not considered a significant detractor from the two primary foci of this study – the large-scale description of the coastal jet and the response in the lee of capes and points.

At 0500 PDT 17 June (Fig. 29c), model winds begin at 13.7 m s^{-1} , again rise gradually to a peak of 15.7 m s^{-1} at 2100 PDT, and then fall more sharply to 14.2 m s^{-1} by early morning. Over the same period, the Buoy 28 winds rise from less than 10 m s^{-1} to a broad peak of 14.3 m s^{-1} from 1600 PDT to 0100 PDT 18 June, and then fall to 13.0 m s^{-1} by 0500 PDT. This evolution is again indicative of good agreement between data and model. As during the second event, the winds in the model are somewhat high, particularly at the beginning, although the differences are less than on 14 June. Of note, winds at 990 mb (Fig. 28) are significantly higher than the near-surface winds on all three days due to the reduced effect of friction relative to 5 or 10 meters. A general weakness of the data set in this study is that there are no continuous measurements of winds at a level higher than the 5-m measurements at the buoys. Some aircraft measurements were made during CW96, and these will be discussed later in this chapter.

A similar comparison at Buoy 30 off Cape Mendocino (not shown) also reveals imperfect, but encouraging results. On 9 June, the 10-m model winds vary between 8 and 10 m s^{-1} with no distinct diurnal signal (significant diurnal change occurred in the lee of the cape, but very little at the cape). The Buoy 30 winds varied from 6 to 8 m s^{-1} , also with no discernable diurnal signal. On 14 June, the predicted winds are consistently near 13.5 m s^{-1} from 0500 PDT until late in that day, fall slightly to a minimum of about 12.5

m s^{-1} between 2200 PDT and 0100 PDT, and then rise again to 13.2 m s^{-1} by 0500 PDT 15 June. The Buoy 30 winds ranged between 8.2 and 12 m s^{-1} during the same period, which is again lower than the model winds. Also, the amplitude of the diurnal signal in the measured winds is again not well captured in the model, although the measured and modeled winds do reach a minimum late in the day on 14 June. Model winds on 17 June are 9.5 m s^{-1} at 0500 PDT, fall to 7 m s^{-1} by 1800 PDT, and then rise to near 10 m s^{-1} by the end of the model run at 0500 PDT 18 June. The Buoy 30 winds start at 5.5 m s^{-1} , rise to just under 8 m s^{-1} at 2000 PDT, fall back below 7 m s^{-1} by 0200 PDT, and then rise sharply to 8.6 m s^{-1} at 0500 PDT. While there are similarities in that pattern with the model, there are also notable differences. During all three events, the winds at Cape Mendocino were generally higher in the model than observed, but do exhibit the same pattern from day to day as observed (low winds on 9 June, relatively higher winds on 14 June, lower again on 17 June). Again, the higher frequency changes in buoy wind speeds, due to turbulent processes and complex topographic interactions on various time and space scales, are not contained in the model wind time series.

Such examinations of model winds relative to buoy winds at other locations reveal a similar result. In summary, the model does a reasonable job of capturing relative wind magnitudes from place to place on a given day and from day to day at a given location. The pattern of wind variations on a given day at a given location is captured well in some cases, but is largely missed in others. Much of this appears to be due to the fact that while the model appears to accurately parameterize turbulent boundary layer processes, it can not fully represent such processes with a 9 km horizontal resolution. Such sub-mesoscale variability was not the focus of this study. What the model does well is represent the larger-scale changes in wind magnitude and distribution.

C. CODE DATA

As mentioned in Chapter II, much of what is currently known about the California MBL and coastal jet originated in the studies done near Point Arena during CODE I and II in the early 1980's. While no direct comparisons can be made with model results from the current study, some general observations made during CODE can be compared with the COAMPSTM predictions. Compare the 33-m winds on 26 July 1982 (Fig. 30a) in the lee of Point Arena from Beardsley et al. (1987) with the COAMPSTM-predicted 10-m

winds (Fig. 30b) at 2200 UTC 9 June (1500 PDT, to correspond diurnally with the CODE plot). The CODE analysis was made from aircraft data on a day that was similar to all three events in this study in that consistent northwesterly winds were established along the coast. A wind maximum in the lee of Point Arena is evident in both the data from CODE (Fig. 30a) and the model (during all three events). The maximum in the CODE analysis exceeds 14.6 m s^{-1} , while the COAMPSTM maximum reaches 15.7 m s^{-1} . The primary difference between the two is that the model produces a maximum that is larger in scale and centered farther south near Bodega Bay. This displacement is consistent with the other days modeled, and the predicted horizontal scale of the lee maximum is larger than in the CODE analysis at other locations and times as well.

While an acceleration of the winds in the lee of the cape is present in both the data and the model, the differences are likely due to a combination of factors. First, the 9 km resolution of the COAMPSTM model precludes identification of features as small as those in the CODE plot. Second, as will be discussed in the next chapter, many variables influence the character of the wind distribution on any given day. The synoptic conditions, cloud distribution, and flow above the marine layer all exhibit variability that could at least partially account for the differences seen between these two plots. As characterized by Winant et al. (1988), 25 July 1982 was a day with a fairly weak, complex northerly wind pattern with large changes in the winds over short spatial scales. Indeed, other measurements made during CODE, such as the along-coast flight from 14 July 1982 (Beardsley et al. (1987) – not shown), point to the large degree of variability during that extended study period. A second CODE wind analysis (Fig. 30c) was made on a day (17 May 1982) that had synoptic conditions more similar to the 9 June event in this study in that the surface isobars crossed the coast at a significant angle near Point Arena. A much better agreement in the size and position of the lee maximum is evident relative to those during the three events in this study, although the maximum on 17 May 1982 was still slightly farther north than those during any of the three 1996 events.

Good qualitative agreement is also found between the vertical structure of offshore winds during CODE and that predicted in the model. As was shown in Fig. 3 (from Zemba and Friehe (1987) and Beardsley et al. (1987)), a pronounced vertical maximum in the winds, which is coincident with a sharp increase in potential temperature

and decrease in mixing ratio, is present on days that exhibit the typical northwesterly low-level flow. This jet profile is consistent with those at similar locations in the model, with vertical wind maxima ranging from 17 to 24 m s^{-1} at similar heights. The model vertical maxima tend to resemble those in the cross-shelf profile from CODE (Zemba and Friehe's Fig. 5a, not shown here) in that they are more diffuse/less vertically focused than those in Fig. 3. Vertical plots of potential temperature also reveal a tendency in the model to create an inversion that is less vertically confined than it is on many of the days in CODE and other studies. However, a vertical maximum in winds within a temperature inversion at the top of a well-mixed MBL exists in both the CODE data and the COAMPSTM predictions from this study, and the heights of those features are consistent.

D. AIRCRAFT DATA FROM JUNE 1997

Data collected during June 1997 from an instrumented King Air research aircraft operated by the University of Wyoming are illustrated here for further comparison with the COAMPSTM output from the current study. Whereas no direct comparison is possible, the data were obtained at the same time of year in synoptic conditions that were similar to this period in 1996, and particularly to the 14 June case. An interior surface low was over eastern Nevada, with cross-coast surface isobar orientation in northern California and coast-parallel orientation in the south. A composite cross-section from the sawtooth leg of the 13 June 1997 flight along 37.5°N (near Half Moon Bay) is shown in Fig. 31a, with a corresponding cross-section from the COAMPSTM prediction at 2300 UTC 14 June 1996 (Fig. 31b), which is the approximate time of the 1997 flight. The two cross-sections have jet profiles of similar magnitude (absolute maximum of 26 m s^{-1} in the model versus 28 m s^{-1} in the 1997 data), with a relatively flat underside (beyond about 35 km offshore), upward sloping top toward the west (especially within about 60 km of the coast), a wind maximum near 370 m near 123.7°W, and a jet maximum whose offshore extent is at least west of 124°W. The primary difference is that the downward slope of the jet axis toward the coast in the data is not evident in the model on this scale. Of note, a broader view from the model prediction at this latitude reveals two points relative to the Parish (2000) paper. First, as observed by Parish, the jet extends much farther offshore than the flight reached. While the model indicates that the flight

measurements may have come close to detecting the absolute maximum horizontally, the jet structure continues to exist west of 127°W, which is some 400 km offshore. Second, when viewing a cross-section through the broader scale jet in the model, a downward slope of the core toward the coast is evident. However, the slope is sufficiently small that when the view is zoomed to the scale of the Parish plot, it becomes difficult to discern.

As in the observations, potential temperature cross-sections from the model reveal a well-mixed MBL with a strong inversion above, the mean height of which matches well with observations from Parish (2000). However, the 1997 observations indicate significantly more slope in the isentropes than in the model, which is consistent with the lack of coastward slope in the wind pattern. Variations in this slope with respect to coastal features will be discussed in Chapter VI and may partially explain this difference between 1996 model results and 1997 data. Finally, the jet core is in the lower portion of the temperature inversion in both the observations and in the model.

E. COASTAL WAVES 1996

As discussed in Chapter I, Coastal Waves 1996 (hereafter CW96) was an extensive field experiment that has produced several studies relating to the behavior of the low-level coastal wind field. The observations from those studies provide further validation of the performance of COAMPSTM in the present study, and in a few cases allow direct comparison of aircraft observations with these model results. An overview of the experiment, with some preliminary results, is presented in Rogers et al. (1998). Their example of wind distribution around Cape Mendocino at 30 m (Fig. 32) has a pattern very similar to that in the current modeling study: (i) an area of weak winds on the upwind side of the cape; (ii) an acceleration to an intermediate value at the cape; and (iii) a further acceleration to a pronounced wind maximum in the lee. As in the model, the wind maximum extends from the lee shore of the cape to well downstream, with a weak wind area in a narrow band close to the coast beginning just south of the cape.

The cross-coast cross-sections of potential temperature and winds in Rogers et al. (1998) for the 7 and 12 June flights near Cape Mendocino (not shown) can not be directly compared with model output from this study. However, they again represent a pattern very similar to typical structures in the COAMPSTM predictions. Specifically, the 7 June

data set has a steeply sloping wind maximum that is associated with a steep slope in inversion height near the coast, while on 12 June a deeper MBL was present with less slope near the coast. Very similar structures are found in the model predictions from 9 June and 14 June. Since the 7 June data set and the 9 June model prediction were characterized by very similar synoptic conditions, as were the 12 June data set and 14 June model prediction, the relationship between marine layer slope and inversion height is evidently well captured by the model.

The flights in CW96 used lidar to measure marine layer depth variations that may be associated with gravity waves and other small-scale changes. Although the model horizontal resolution precludes detection of such waves, the pattern of marine layer shallowing from offshore toward the coast (most pronounced within about 50 km of the coast), and of shallowing in the lee of capes and points is consistently captured in the COAMPSTM predictions. The base of the inversion was about 600 m offshore during the 12 June Cape Mendocino flight and shallowed to less than 100 m close to shore. These values compare favorably with those simulated on 14 June in this study, where offshore values a similar distance from shore are typically 500-700 m, and shallow to less than 200 m near shore. In the model, the degree of shallowing close to the coast depends on the position relative to major coastal features. The distinct height increases associated with hydraulic jumps detected in the aircraft data can not be represented in the model. However, the along-shore changes in marine layer depth in the model are quite consistent with measured depths of 300-500 m upstream and 100-200 m downstream.

A case study for the 17 June flight near Point Sur from CW96 is presented in Dorman et al. (1999). Since one of the events in the current study includes 17 June, some direct model comparisons with the measurements on that day are possible. Measured winds at 10 m (corrected from a flight level of 30 m using the Large and Pond (1981) technique described in Dorman and Winant (1995)) are shown in Fig. 33 along with the COAMPSTM 10-m winds at 2300 UTC 17 June (during the flight) from this study. Whereas the 9 km resolution of the model inner nest can not predict the fine scale structure in the Dorman et al. plot, it does indicate weak winds upstream of Point Sur and near the coast well downstream and a wind maximum in excess of 16 m s^{-1} offshore, downstream of the point. Measured winds downstream of the point reached 18 m s^{-1} very

close to the point with a broader 16 m s^{-1} maximum that extended farther south. Further, the axis of the wind maximum to the south of Point Sur is very closely aligned with the axis of highest winds in the model. The most significant difference between the analysis and the model is the area of high winds adjacent to the coast immediately south of Point Sur in the analysis but not in the model. This appears to be due to a combination of model resolution and lack of aircraft data shoreward of the innermost flight leg. In other words, the 18 m s^{-1} contour from Dorman et al. (1999) could also be drawn as a very small closed contour offshore along the inner flight leg, which is a feature that is too small to be resolved in this application of COAMPSTM. An examination of the broader wind maximum following the 16 m s^{-1} contour reveals reasonable agreement with the pattern predicted by the model, with an almost identical magnitude. Also, when viewing model output from closer to the inversion height (990 mb), an extension of the offshore wind maximum onto the coast near the point, very similar to that shown in Dorman et al., is present, although not continuously through the diurnal cycle (only appears on this day late at night into early morning).

The model output is consistent with cross-coast and along-coast lidar data presented in Dorman et al. (1999). Specifically, the inversion slopes down from offshore toward the coast and exhibits a sharp drop associated with high winds in the lee of the point. Further, the pressure and wind traces along the low-level flight tracks are reasonably well replicated in the model. Measured winds rose from about 12 m s^{-1} offshore to a peak of over 18 m s^{-1} about 18 km from the coast, whereas model winds over the same distance rose from 12 m s^{-1} to about 16 m s^{-1} . The cross-coast maximum in the model 10-m winds, along the same track as the flight, occurs somewhat farther offshore at about 25 km. The along-coast track also matches well, in that it exhibits low winds upstream of the point, along with higher pressures, and high winds in the lee associated with lower pressures and a shallower marine layer. The sharp drop in wind speeds upstream of Point Sur, termed a hydraulic jump by Dorman et al. (1999), is not predicted in the model at this location, again due largely to smoothing at 9 km resolution.

Along-shore cross-sections of wind and potential temperature from Dorman et al. (1999) are shown in Fig. 34, along with similar COAMPSTM cross-sections in corresponding locations from this study. Fig. 34a is a section close to the coast (about 10

km), while Fig. 34b is approximately 42 km offshore. A 22 m s^{-1} upstream wind maximum in the inversion is evident at the north end of both inshore cross-sections in Fig. 34, although it is somewhat higher in the model (Fig. 34c). The downstream maximum in the aircraft data is not predicted by the model, nor is the subsequent rise in isentropes or secondary downstream maximum. This difference results from the model wind maximum being farther offshore and downstream than the observed maximum, such that the model cross-section largely misses it. A comparison of the cross-sections farther offshore (Figs. 34b,d) reveals a better match of wind magnitudes and vertical distribution, but the shape of the wind maximum and the downward slope of potential temperatures are greatly smoothed relative to the observations. The fact that the wind maximum extends beyond this cross-section farther south is mentioned by Dorman et al. (1999) and is evident here in COAMPSTM. It is important to note that by slightly altering the position of such an along-shore cross-section, it is possible to produce a significantly better match with the observed data from 17 June in Fig. 34a. This sensitivity to position will be seen in the presentation of major findings contained in the following chapters.

The same short spatial scale variability is found in cross-sections drawn perpendicular to the coast. As previously stated, the basic characteristics are reasonably well matched, but exact placement and configuration of key features, such as wind maxima and areas of steepest isentropic slope, depend heavily on the position of the cross-section relative to significant features in the spatial distribution of winds and potential temperatures. Thus, relatively minor flaws in the model's ability to resolve such features spatially, due to resolution inadequacy or other factors, can result in dramatic differences in cross-sections at a specific location. Dorman et al. (1999) observed such variability in their three cross-coast flight legs, and they noted that the cross-coast minimum in inversion base height occurred very near the coast on their northern and middle legs, but some 40 km offshore on the southern leg. This tendency for a wind maximum to be oriented such that it is closer to the coast near the northern end and farther offshore to the south is seen to varying degrees at all locations in the model where local wind maxima occur regularly (described in the next chapter). They also point out that inversion slope varies with latitude near Point Sur, with significantly less slope at and upstream from the point than in the lee. This is also predicted in the model,

where the local inversion slopes toward the coast are highly dependent on position relative to coastal topography.

The CW96 flight data also reflected an upward trend in wind speeds during the course of the event. This acceleration is also evident in the model prediction on that day, as maximum winds in the lee of Point Sur increased from less than 15 m s^{-1} to about 17 m s^{-1} . Such an increase is also evident in the data from Buoy 28. Similarly, the height of the inversion base lowered over the same period, which is a trend that also exists in the model prediction.

Another study that used these data from CW96 was Strom et al. (1999). The focus here was on the wind and boundary layer behavior near Cape Mendocino from three flights on 7, 12, and 26 June 1996. 26 June was a day with anomalously weak synoptic forcing and was not representative of conditions examined in the present study. However, 7 June and 12 June were days with fairly strong northerly-northwesterly flow, which allows more meaningful comparison. Observed vertical profiles of potential temperature and wind speed are actually more similar to those modeled by COAMPSTM in this study than were those obtained during CODE (Fig. 3), in that they show a less vertically distinct inversion and less focused vertical wind maximum. Heights and magnitudes are again consistent with model results on similar days. An east-west cross-section of winds (gray shades) and potential temperatures from an aircraft flight in the lee of Cape Mendocino on 12 June is shown in Fig. 35a, with a COAMPSTM cross-section from the same location from 1800 UTC 14 June (Fig. 35b). The synoptic conditions were similar on these days and the two cross-sections have obvious similarities. The wind maximum occurs within the inversion, wind magnitudes are similar, a steep coastward slope exists in the isentropes very near the coast, and the jet core is offshore from that steeply sloping region. The model jet core is somewhat higher with respect to the inversion than the core observed on 12 June, and there is an upward isentropic slope farther offshore in the observations that is not evident in the model prediction on 14 June. The other cross-sections presented in Strom et al. (1999) give further amplification that considerable temporal and spatial variability exists in such sections. This example from two similar days at the same location provides a strong indication that the COAMPSTM

model can predict structures in the vicinity of significant coastal topography that is quite consistent with observed atmospheric responses in such areas.

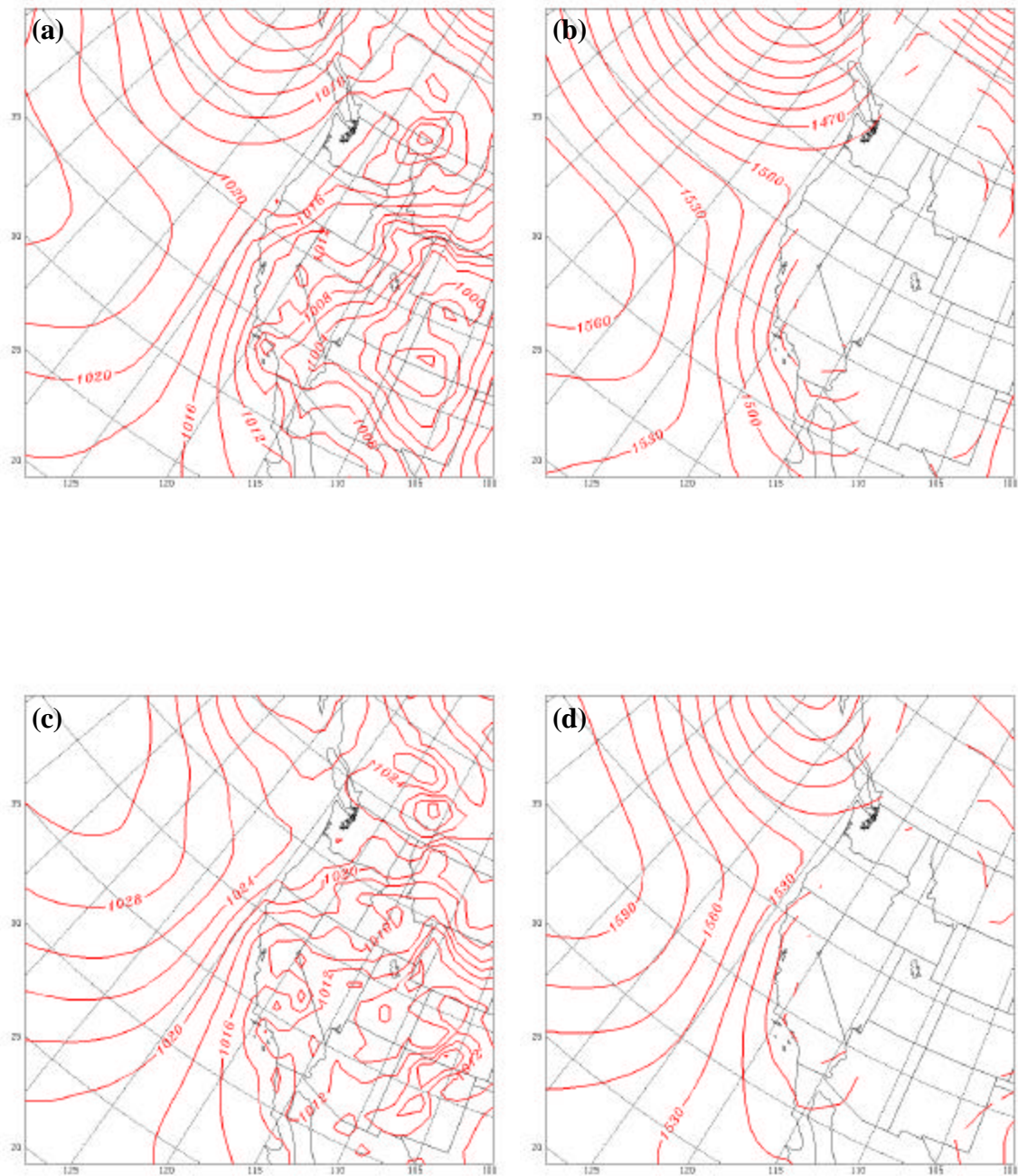
The spatial distribution and day-to-day variability of winds measured near the cape is also captured reasonably well in the model. Specifically, wind maxima were observed on both days in the lee of the cape, with much weaker surface winds to the north. This characteristic at Cape Mendocino is predicted by the model, as it is at Point Sur and other locations to be discussed later. Further, the measured wind maximum on 7 June is fairly localized in the close-in lee of the cape, while on 12 June it extends well to the south. This spatial distribution is very similar to that predicted by the model on 9 June and 14 June, respectively.

F. SUMMARY

As applied to this study, the COAMPSTM model has been shown to predict features that are consistent with observations by several investigators. This is true on the larger scale in that a good match is found between the 36-h COAMPSTM forecasts and the archived NOGAPS analyses at corresponding times. The regional distribution of higher wind areas and the longer time-scale changes in relative wind magnitudes at a given location are also consistent with observations and lend further support to the skill in the COAMPSTM large-scale wind forecasts.

Model predictions consistent with real atmospheric responses are also evident at smaller scales, as documented in the similarities with CODE observations, the observations made by Parish et al. (1997), and the aircraft data collected on various days in CW96. Specifically, the model consistently produces a well-mixed marine boundary layer capped by a strong thermal inversion. This inversion slopes downward from offshore toward the coast, with maximum slope close to the coast, and this slope is increased in the lee of significant coastal topography. Looking along the flow, which is nearly parallel to the coast, the model predicts sharp drops in isentropic surfaces in such lee areas, especially near the coast, but to a lesser degree well offshore. The spatial distribution of model-predicted winds consistently has areas of maximum winds in the lee of coastal prominences, with weaker wind areas upstream and very close to the coast well downstream. These areas are sometimes fairly localized, but can extend well downstream and offshore. These wind maxima are evident at the surface, but reach their

vertical peak aloft, within the strong potential temperature gradient. Model winds undergo a diurnal cycle that is associated with varying scales of heating over land areas, and that tends to produce maximum offshore winds and most shallow MBL depths in the late afternoon and early evening. All of these consistent model tendencies are in reasonable agreement with the limited body of data available on the California summertime MBL and coastal jet. Thus, it is reasonable to utilize the more complete model fields to explore other aspects of the California coastal jet.



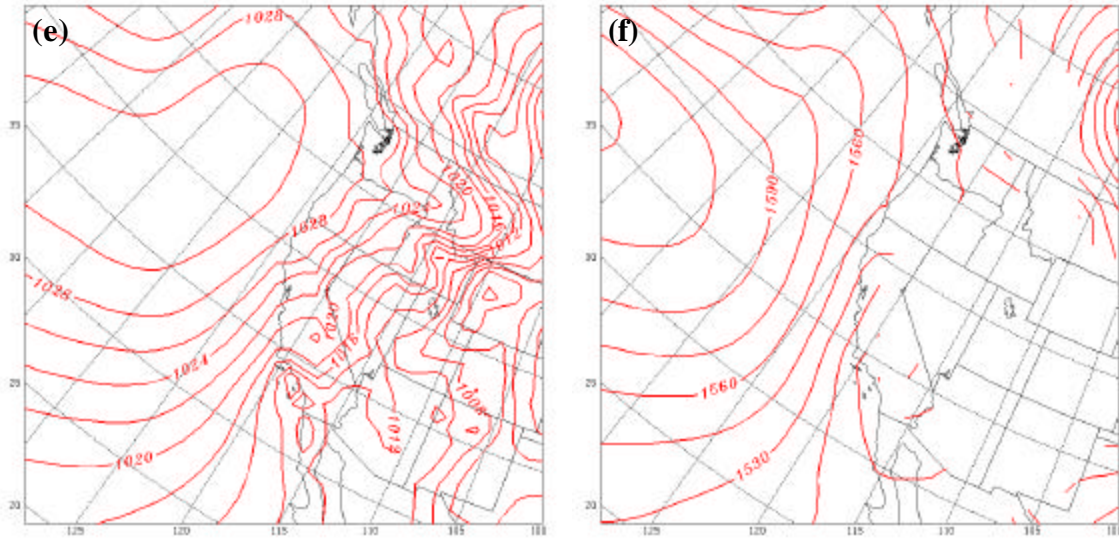


Figure 27. Continued.

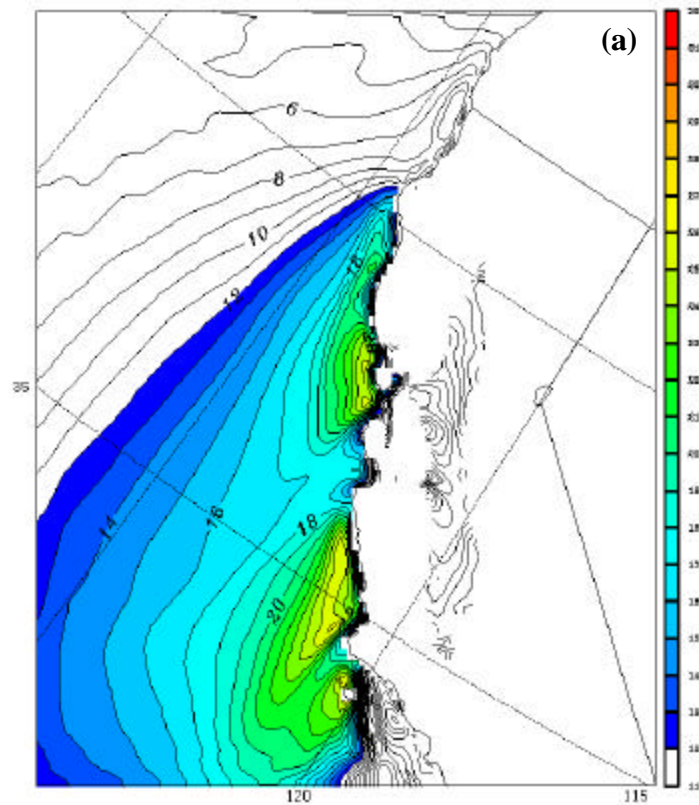


Figure 28. Isotachs of winds at 990 mb from the inner COAMPS nest valid at 1900 PDT on (a) 9, (b) 14, and (c) 17 June 1996. Color shading begins at 12 m s⁻¹ to indicate approximate outer boundary of coastal jet winds.

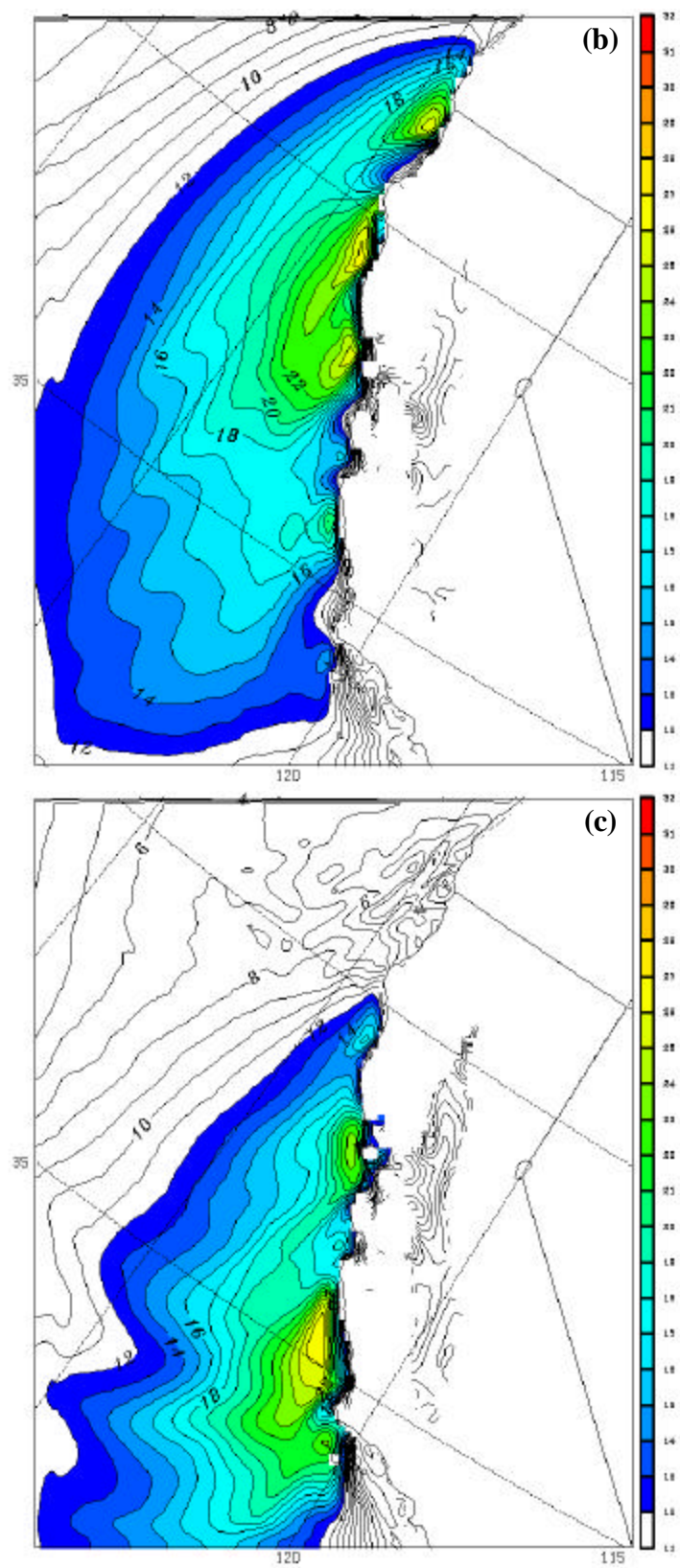


Figure 28. Continued.

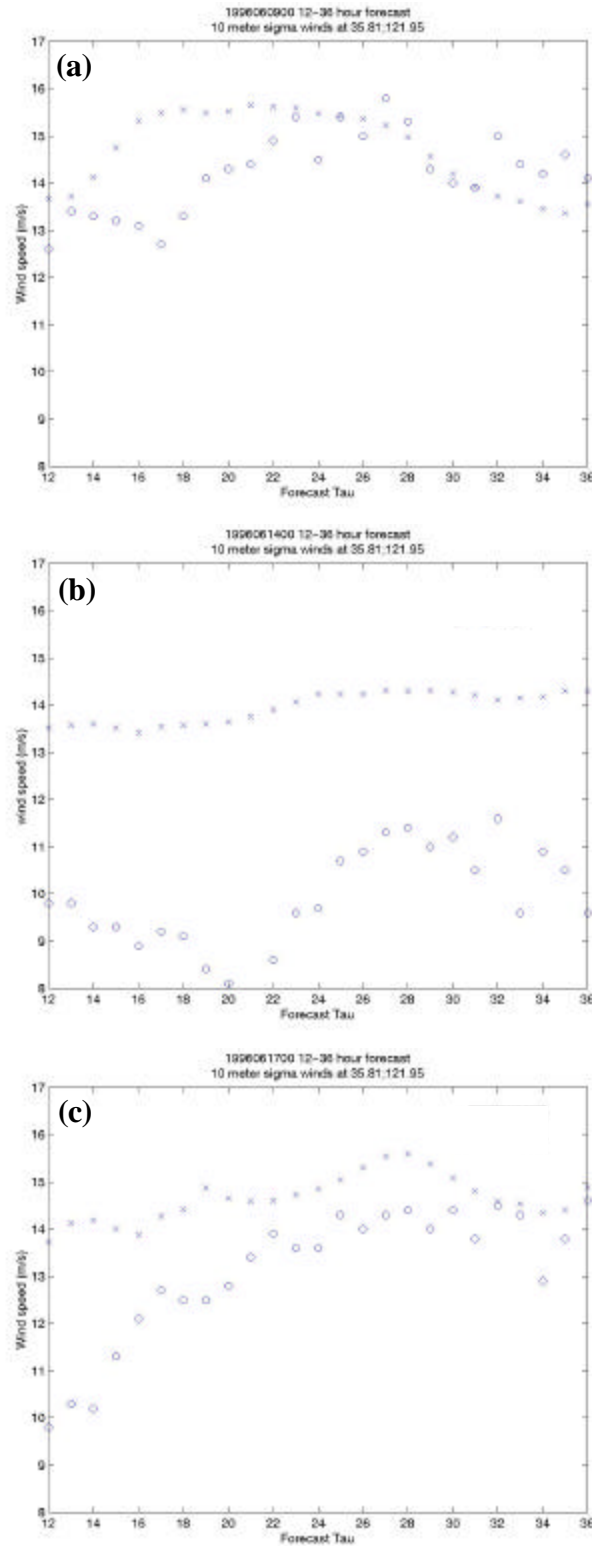
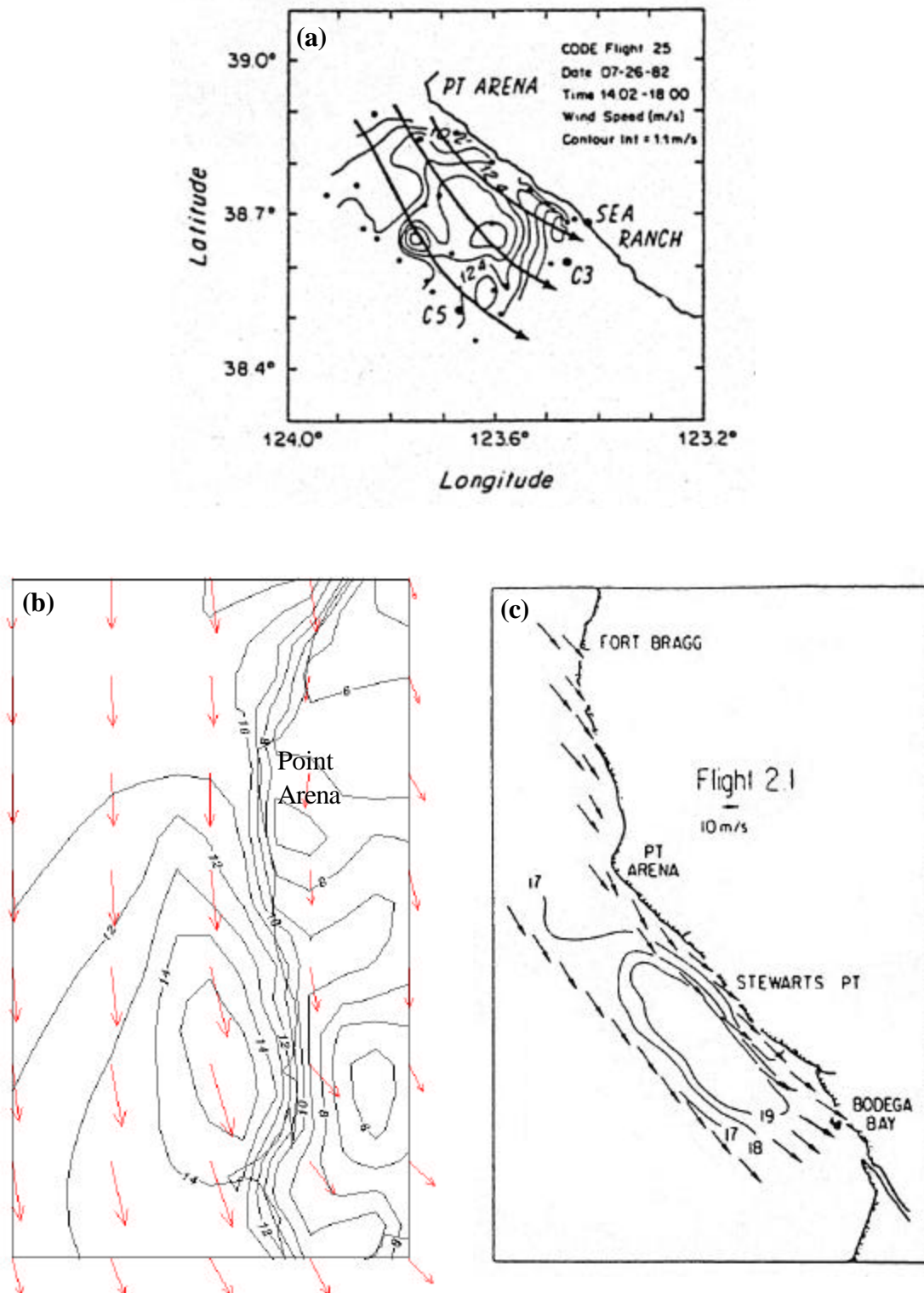


Figure 29. Comparison of observed (o) surface winds at Buoy 28 with the COAMPS predictions (x) during the 12-36-h period for the events of (a) 9-10 June, (b) 14-15 June, and (c) 17-18 June 1996.



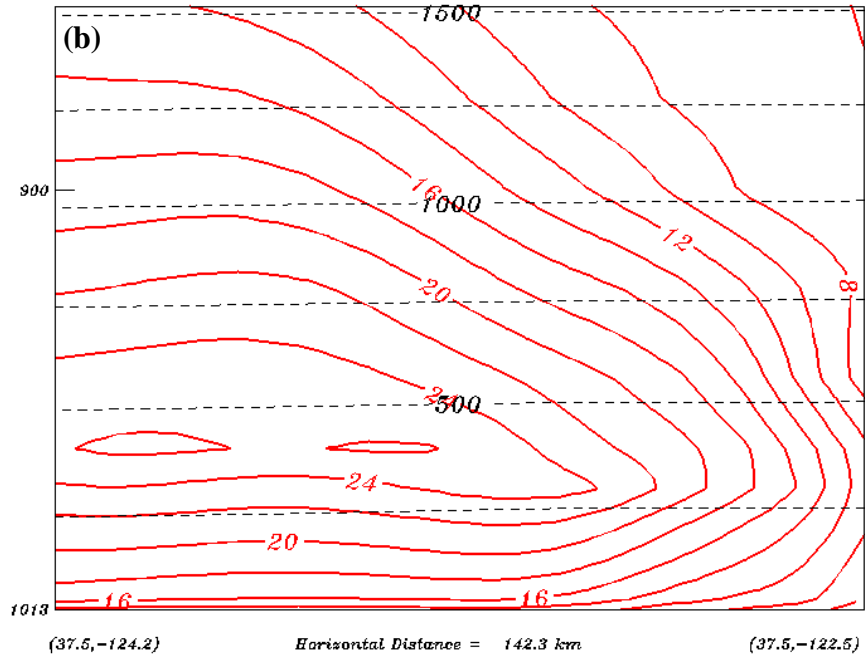
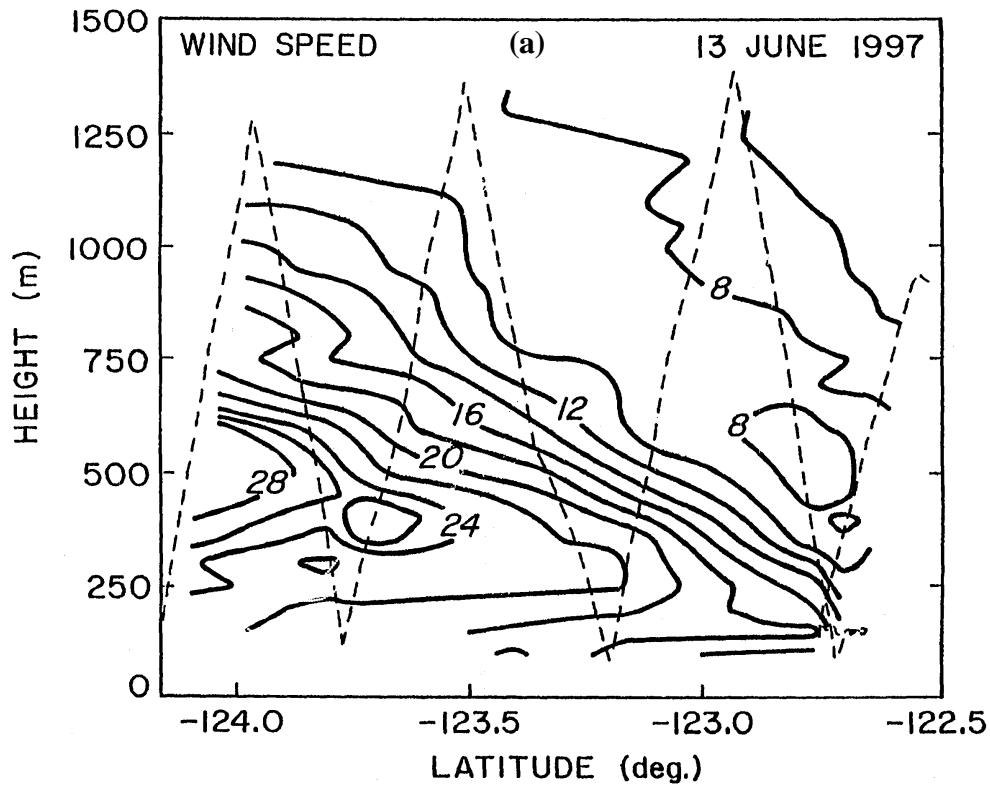


Figure 31. East-west cross-sections along 37.5°N , with the eastern end near the Santa Cruz Mountains, of (a) aircraft measured winds (m s^{-1}) from 13 June 1997 (from Parish 2000) and (b) COAMPS winds valid at approximately the same time of day on 14 June 1996. Height (m) is shown with dashed lines in Fig. 31b.

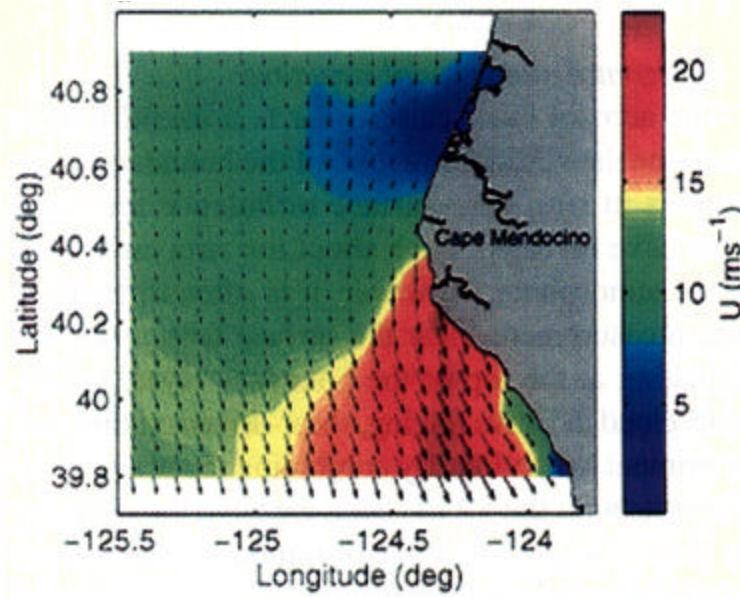


Figure 32. An example from Rogers et al. (1998) of 30-m winds measured near Cape Mendocino during Coastal Waves 96. The distinct wind minimum to the north and maximum in the lee are quite similar to the COAMPS predictions from the current study at this location.

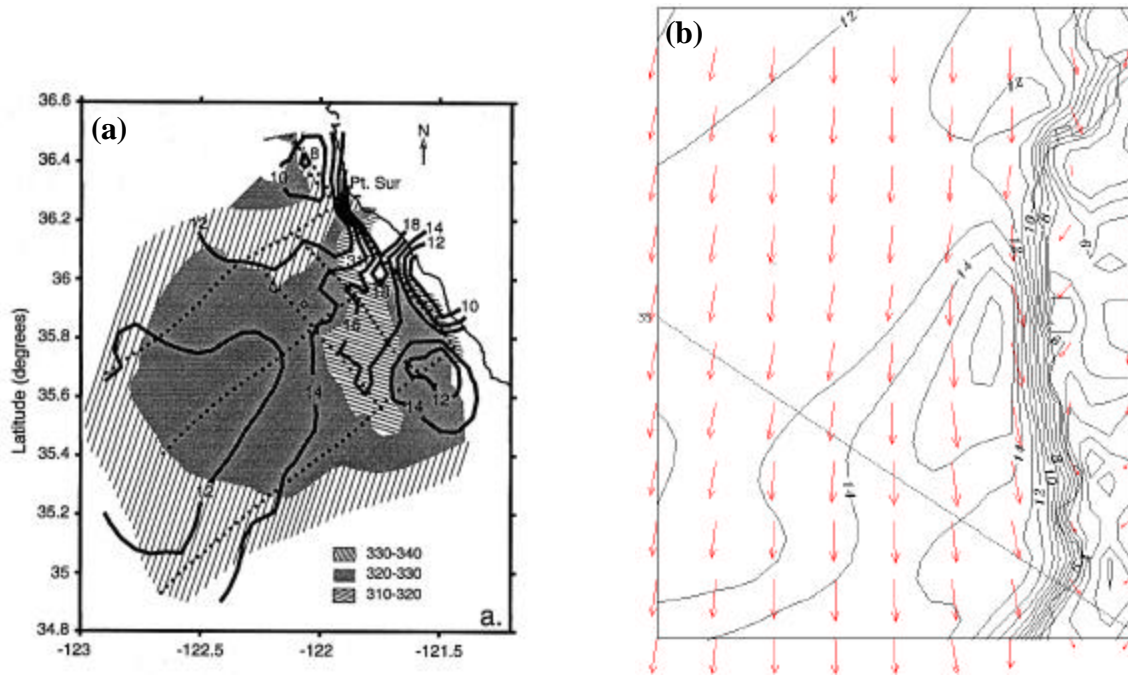


Figure 33. Direct comparison of winds near Point Sur on 17 June 1996 (a) as measured from aircraft during Coastal Waves 96 from 1200-1800 PDT (from Dorman et al. 1999), and (b) from the COAMPS inner nest valid at 1600 PDT. Measured winds are adjusted to 10 m and model winds are at 10 m. Wind direction is shown with gray shades in (a).

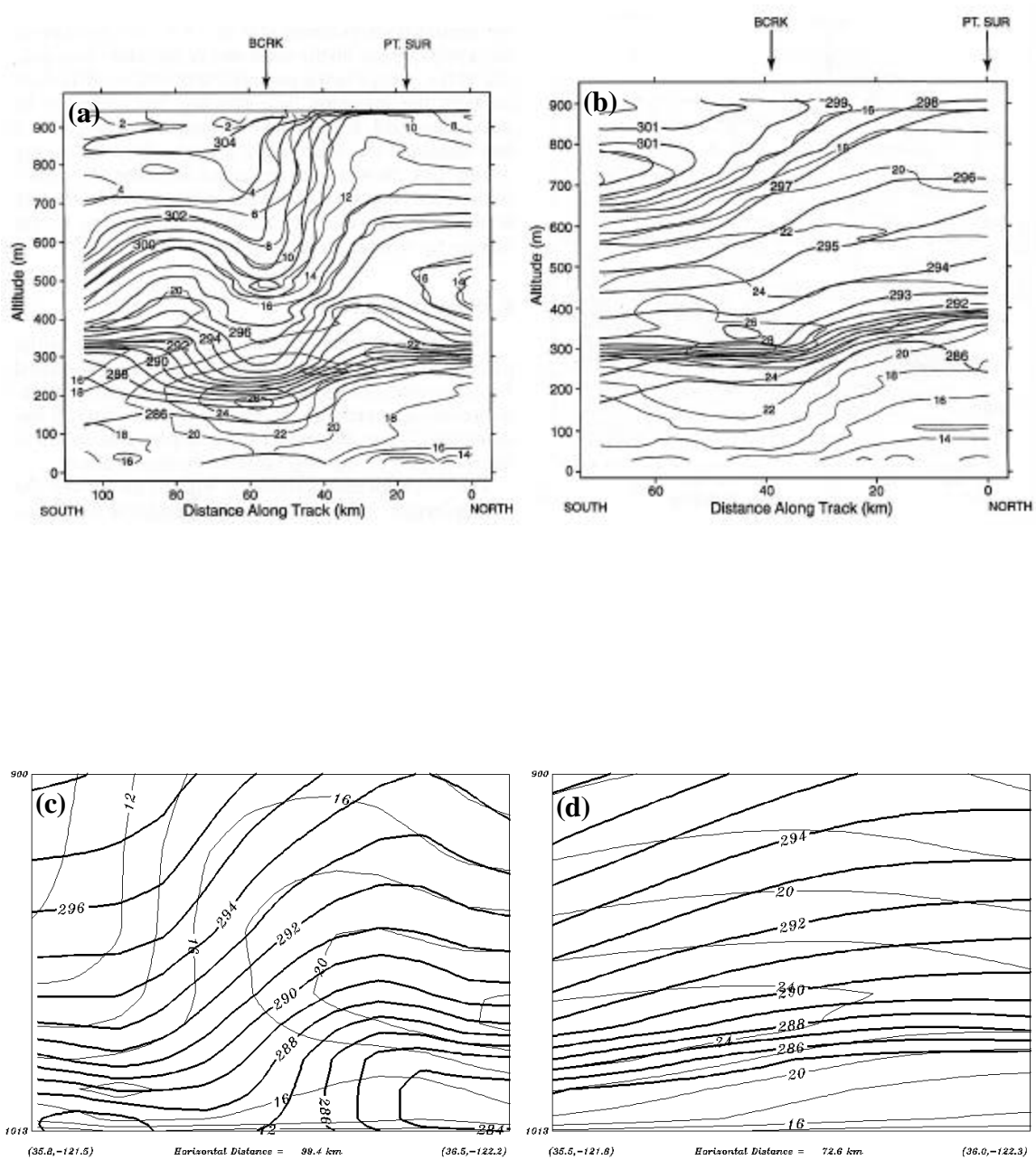


Figure 34. Along-coast cross-sections (see dotted lines paralleling the coast in Fig. 33a) of winds (m s^{-1}) and potential temperature (K) near Point Sur during the afternoon of 17 June 1996. Cross-sections (a) and (c) are along the innermost line from Dorman et al. (1999) measurements and from COAMPS (valid 1700 PDT), respectively, while (b) and (d) are along the offshore line. Light lines are winds and dark lines are θ . Note that (a) and (b) are slightly more vertically stretched than (c) and (d).

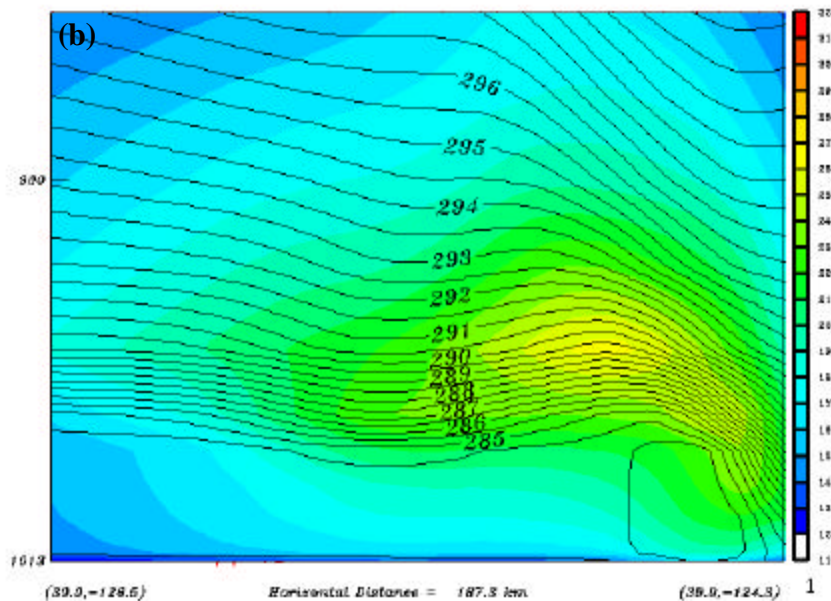
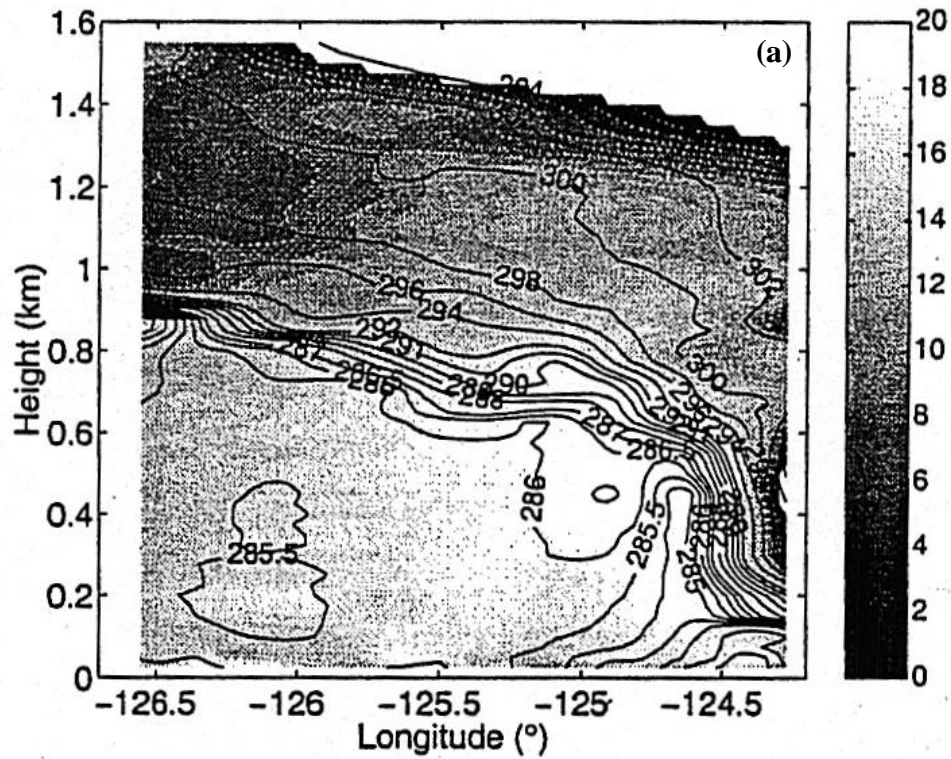


Figure 35. Cross-sections of winds (m s^{-1}) and potential temperatures (K) along 39.9°N near Cape Mendocino from (a) Strom et al. (1999) aircraft measurements on 12 June 1996 and (b) the COAMPS simulation valid at 1100 PDT 14 June 1996. Winds are shown as gray shades in (a) and color shades in (b).

VI. THE LARGE-SCALE CALIFORNIA COASTAL JET

As stated in Chapter I, a major emphasis of this study was to provide a more comprehensive description of the California coastal jet than has previously been published in the literature. Much of the focus of past studies has been on the mesoscale wind response near specific coastal features. What will follow is a description of the jet as it is simulated along the entire coast from southern Oregon to the California Bight during three events in June 1996 that are deemed to be representative of conditions that exist along the coast on the vast majority of summer days. Specifically, all three events very consistently exhibited the northerly to northwesterly coast-parallel, low-level winds that result from the juxtaposition of the eastern North Pacific high and the thermal low in the interior. The differences among the three events are illustrative of the variability that exists within this coast-parallel flow pattern. In particular, the 14-15 June event exhibited a deeper marine layer over much of the coast than the 9-10 or 17-18 June events, with a shift to the north of the higher winds. Periods with anomalously weak or strong synoptic forcing and days during which coastal flow was not from the northwest (such as 5 June when a coastally trapped southerly surge occurred) were deliberately avoided.

As illustrated in Chapter V, the coastal jet and the marine boundary layer as modeled by COAMPSTM are consistent with the range of available observations. It is thus expected that the four-dimensional low-level structure produced in these model integrations represents a realistic large-scale and mesoscale simulation of the atmosphere at the scales of interest. What follows is a detailed discussion of that model structure, which will be corroborated with data when available. Whereas the inclusion of such data in the discussions will always be specifically mentioned, the reader should assume that any other description refers to the model atmosphere.

A. SYNOPTIC CONTROLS ON THE LARGE-SCALE JET

The relationship between the low-level winds as measured at the buoys and the orientation of the surface pressure gradient was discussed in Chapter IV. The tendency toward higher along-shore winds to be associated with periods during which a significant down-coast component to the pressure gradient exists has been established. This

relationship allows an excellent first approximation of the location of enhanced winds. Changes in the magnitude and orientation of the offshore ridge or especially of the interior low cause reorientation of that coastal gradient to modulate the magnitude of the offshore winds, although the direction remains strongly tied to the coastal orientation (northerly to northwesterly). The goal of this section is to broaden that understanding of the relationship between patterns on typical synoptic-scale weather charts and the behavior of the winds in the lower atmosphere – the coastal jet.

It is not possible to establish direct relationships between the synoptic 500 mb heights and vorticity and the nature of the low-level wind field in the coastal environment, particularly along the west coast of the United States during summer. Much of the variability in MBL structure and coastal jet behavior discussed in this study can occur under very similar 500 mb conditions, and consistent coast-parallel flow can exist under a variety of typical summertime 500 mb patterns, as seen in Figs. 12-20. Of course, the lower atmosphere can not be viewed entirely separately from the upper, but the relevance of 500 mb and higher-level synoptic conditions to the low-level winds is limited to their role in determining the nature of the 850 mb pattern. A much more direct link exists between the 850 mb heights, the sea-level pressure pattern, and the low-level wind distribution.

A very strong correlation exists between the 850 mb height pattern near the coast and the location of the large-scale region of winds representative of the coastal jet. To demonstrate this, the 850 mb heights, derived from the middle of the three COAMPSTM nests, for each of the three events are plotted in Fig. 36 superposed with the 980 mb isotach pattern from the inner nest. While it is not possible to choose one vertical level that will capture the vertical core of the jet in all cases, 980 mb is chosen for the purpose of representing the spatial extent of the jet, since that level is generally near the core both inshore and offshore. (Typically, the core of the jet is lower near the coast and higher well offshore.) The predictions are valid at 0200 UTC (1900 PDT) on each day, which is a time representative of near-peak wind conditions along the coast. As an approximation of the lateral extent of the coastal jet, wind speeds in excess of 12 m s^{-1} are highlighted with color shading. A clear relationship is found between the position of the 850 mb ridge and the location of coastal jet winds. When the ridge axis is over the far northern

California coast, as during the 9-10 June and 17-18 June events, the area with 980 mb winds in excess of 12 m s^{-1} begins around Cape Mendocino and extends to the south, with the maximum values occurring in the region to the south of Monterey Bay and extending beyond Point Conception. When the ridge axis is farther to the north over northern Oregon, as during the 14-15 June event, these higher winds begin in southern Oregon, have maxima near Cape Mendocino and Point Arena, and are less well defined south of Monterey, and greatly reduced near Point Conception. As pointed out in Chapter IV, this pattern is quite consistent with the distribution of higher winds in the NOAA buoy data.

The relationship between the 850 mb ridge position and location of winds meeting coastal jet criteria provides a starting point for identifying locations along the coast where complex interactions with coastal topography are likely to occur. Regions of highest winds within the broad jet in Fig. 36 are not closely tied to the magnitude of the geostrophic flow at 850 mb, which is above the marine layer. For example, the strongest jet in Fig. 36a occurs north of Point Conception and near the coast, while the largest 850 mb height gradient occurs farther south and west. From a thermal wind argument, assuming a similar MBL thermal structure, it would be expected that where the 850 mb pressure gradient is maximized, the winds below that would also be maximized, albeit with a reduction due to friction within the boundary layer. While the large-scale jet does tend to exist beneath a region of relatively strong 850 mb height gradient, the low-level mesoscale near-coast wind variability does not have a significant correlation with that gradient. Instead, this variability is directly linked to the coastal topography, as detailed in the next section.

The northern extent of the coastal jet winds is at a fairly consistent distance (about 250 km) south of the point at which the 850 mb ridge axis crosses the coast. Whereas this distance is dependent on the shape of the ridge, it is defined here as the point along the coast south of the ridge axis where the 850 mb isoheights first cross the coast in an offshore direction. The inception of coastal jet winds is thus approximated by that point downstream of the ridge where the 850 mb geostrophic flow becomes roughly oriented with the coastline.

From a surface pressure gradient perspective, the positioning of the 850 mb ridge across the coast sets up the necessary north to south gradient below to accelerate the wind down the coast. That is, since the magnitude and along-coast orientation of the strong baroclinity that exists at the surface also generally exists at 850 mb, with only slight spatial offset, similar geostrophic orientations are present at both levels near the coast, although greater down-gradient flow occurs at the surface due to frictional effects. Reorientations of the low-level gradient may occur in response to both large-scale changes in the pressure distribution (primarily the diurnal evolution of the thermal low) and smaller-scale changes due to topographic interaction.

Given that the 850 mb ridge extension to the northeast from the offshore eastern North Pacific high is a very persistent feature of the summertime pattern, conditions favorable for coastal jet occurrence are similarly persistent. Thus, the existence of coastal jet winds is determined primarily by the existence of such a ridge, given the existence of offshore high pressure and onshore low pressure. That is, if an 850 mb ridge extends from offshore across the coast, an enhancement of low-level winds off the coast, relative to regional mean values, will exist. Further, the along-shore positioning of this enhanced wind area is based on the position at which the ridge crosses the coast. Finally, winds within the broad coastal jet are altered on smaller scales based on their interaction with coastal topography, which will be explained more completely later.

A relationship is also sought between the synoptic pattern and the southern and offshore extent of enhanced winds. For the purposes of this discussion, the coastal jet is defined as that area adjacent to the west coast of the United States that experiences winds above 12 m s^{-1} that are roughly parallel to the coast. Particularly when defining the southern and offshore extent of the jet, the wind direction is important, since winds of 12 m s^{-1} or greater are sometimes found to the south and west of what will be here considered the coastal jet. However, these winds tend to be more northerly in the southeastern quadrant of the eastern North Pacific high, and are thus deemed to no longer meet the roughly coast-parallel criterion. The numbers for offshore jet extent noted in the following paragraphs refer to an approximation of the region where 12 m s^{-1} winds retain their coast-parallel orientation at jet level. It should also be noted that winds close to the coast may exhibit a coastal jet-like structure, but not meet the 12 m s^{-1} guideline, such as

near the Oregon/California border on 9 June, where winds reach only about 9 m s^{-1} , even though there is a clear jet profile in cross-section (shown in Section C of this chapter).

Applying this coastal jet definition, the jet that begins near Cape Mendocino on 9 June (Fig. 36a) has an outer edge to the south-southwest near 34°N , 126°W , which is some 500 km off the central California coast. These high winds extend to the south beyond the boundary of the inner nest, but an examination of the middle nest reveals a southward extent at approximately 30°N , 300 km off the northern Baja coast. On 14 June (Fig. 36b), the jet begins near Cape Blanco in Oregon and extends more sharply offshore initially, and then the outer edge curves to conform to the general coastal orientation south of 38°N . Beyond that point, it maintains an offshore width of 450-500 km. In this case, the southern edge is defined within the inner domain to the west of the outer Channel Islands. On 17 June (Fig. 36c), the jet begins south of Cape Mendocino and again extends south-southwestward to near 34.5°N , 127.7°W , which is approximately 400 km off the central California coast. The outer edge then extends roughly parallel to the coast, before tapering off the northern Baja coast, but not quite as far south as on 9 June.

In summary, a consistent picture of the low-level coastal jet emerges from the COAMPSTM simulations of these three events. The jet begins in the north in an area that depends on the location of the 850 mb ridge and associated surface pressure gradient. It is initially a feature with limited offshore extent, but the jet quickly broadens well offshore toward the south and reaches offshore widths of 500 km or more. This is a significantly broader feature than is typically described in the literature as a coastal jet. However, it is clear that these are low-level, generally coast-parallel winds that are enhanced well beyond the magnitudes they would reach in the absence of the heating from the adjacent land. It therefore seems appropriate to characterize them as part of the coastal jet. The southern limit of coastal jet winds appears to be related to the northern inception point. Specifically, when the surface pressure conditions are such that jet strength winds begin far to the north, as on 14 June, the southern extent of the jet is limited to the area off southern California. This appears to be due to a pronounced weakening and gradual turning to the south of the 850 mb flow at that latitude, and the associated loss of sufficient down-coast surface pressure gradient to maintain 12 m s^{-1}

winds. Based on a qualitative examination of satellite imagery and profiler data, combined with a plan view of COAMPSTM potential temperatures (not shown), this decrease in wind speeds is roughly correlated with the northern edge of the deeper marine layer on that day. When the jet begins farther to the south along the California coast, the synoptic pressure gradient that results in jet winds is also shifted to the south, and the southern limit of the coastal jet is off of Mexico.

B. SPATIAL DISTRIBUTION OF WINDS WITHIN THE COASTAL JET

Within this broad feature referred to as the coastal jet, considerable spatial variability exists that is not necessarily consistent with the 850 mb height pattern. First, the winds at 980 mb increase rather uniformly along the entire north-south extent of the jet from the arbitrary 12 m s^{-1} at the outer edge to near 20 m s^{-1} about a third to halfway between the offshore extent and the coast. Associated with these gradually increasing winds is a gentle downward slope in inversion height toward the coast. Closer to shore, lateral variability increases dramatically. Jet wind magnitudes occasionally reach above 30 m s^{-1} and frequently exceed 25 m s^{-1} close to the coast. However, such high wind areas do not occur uniformly along the coast. While sea breeze circulations and coastal mountain-valley breezes alter the winds diurnally, a more dominant spatial pattern emerges regardless of time in the diurnal cycle. That is, distinct local wind maxima occur at favored locations along the coast (Fig. 36). It is at this point that a simple thermal wind explanation of the jet, as in Burk and Thompson (1996) (Fig. 4), falls short of explaining such variability, because the thermal and pressure pattern above the marine layer at 850 mb can not explain these smaller-scale wind features. Rather, the structure within the boundary layer and inversion appear to locally alter the larger-scale thermal wind balance and change the slope of the lower surface in Fig. 4, which produces favored regions of higher winds. As discussed in Chapter II, these accelerated wind areas have been closely examined near Cape Mendocino, Point Arena (in CODE), and Point Sur, and have been hypothesized to be primarily related to hydraulically supercritical flow response to bends in the coast away from the direction of flow. COAMPSTM very consistently predicts wind maxima in such areas whenever there is sufficient along-shore wind.

While this relationship between coastal bends and regions of anomalously high winds has been fairly well established in those locations, a distinction is made here to clarify the relationship. Highest winds at 1000 mb (a good level for examining the low-level winds close to the coast) at 1700 PDT 14 June (Fig. 37) are clearly related to the presence of high terrain close to the coast. A similar relationship is found on the other two days (not shown). While this high terrain is generally in close proximity to a bend in the coastline, the winds appear more closely tied to the presence of the high terrain than to the location of the bend. This terrain dependency is particularly evident in the cases of the fairly subtle bends such as at Point Arena and Point Sur. Specifically, if an axis is drawn from a nearby upwind relative high point in the coastal topography to the center of the wind maximum in the lee, a consistent pattern emerges. Each such line is oriented from north-northeast to south-southwest, which is a direction that very closely parallels the direction of flow above the marine layer along the coast. An exception in Fig. 37 is the maximum south of Point Sur, where the highest low-level winds are more to the southwest of the highest terrain. Since the flow was weaker at this southern latitude on 14 June, it appears that a different lee response has resulted. A less consistent spatial relationship exists between nearby coastal bends and their associated wind maxima.

It is therefore hypothesized here, and explored further in this and the next chapter, that the favored downstream regions of high winds are governed not solely by a bend in the coastline, but to a greater degree by the presence of high terrain (well above the height of the coastal MBL) close to the coast. In the case of weaker flow above the marine layer, the resulting downstream maximum may be more closely related to expansion fan effects due to the coastal turn.

Relative minima in the winds are evident in Fig. 37 upstream of each of these maxima, e.g., north of Cape Mendocino, near Point Arena, off the San Francisco Peninsula, in southern Monterey Bay, and to a slight degree north of Point Conception. These areas are also a direct result of the flow encountering these high points in the near-coastal topography, as the winds above the marine layer are forced upward and the marine layer deepens. (These topographic interactions will become more clear in the discussions of vertical structure contained in the next sections.) Again, the degree to which these conditions exist varies diurnally, with the relative low-level wind minima

Coastal Reference Pt.	Associated High Coastal Terrain	Max. Elevation (ft.)
Cape Blanco	Sugarloaf Mtn./Chetco Pk.	3562/4648
Cape Mendocino	Taylor Pk.	3390
Point Arena	Cold spring Mtn./Big Mtn.	2736/2675
Point Ano Nuevo	Santa Cruz Mtns.	3200
Point Sur	Mount Carmel/Junipero Serra Pk.	4430/5844
Point Conception	Santa Ynez Mtns.	2000-3400

Table 1. Areas with high terrain in close proximity to the coast.

and maxima occurring at the same time of day, but the existence of such minima is as prevalent a feature of the coastal wind distribution as the more thoroughly analyzed downwind maxima.

The local wind responses near Cape Mendocino, Point Arena, and Point Sur have been discussed in the literature. However, these are not the only locations where accelerations are consistently seen downwind and weak wind areas upstream from coastal features. Referring to Fig. 8 for geographic locations, Table 1 provides a listing of areas where such maximum winds are seen whenever the low-level (about 850 mb and below) flow is roughly coast-parallel. While there is, in some cases, higher terrain farther inland, each of the mountain peaks or ranges in Table 1 is within 20 km of the coastline. The low-level flow is at least partially blocked by this terrain, since a component of that flow onto the terrain exists in each case (with some diurnal variability exhibited). This flow impingement causes a sharp decrease in wind speeds at a given vertical level well upstream from the mountain, and this accounts for the weak wind areas in Figs. 36 and 37. Downstream from the flow obstruction, the along-shore pressure gradient is locally enhanced by low pressures in the lee (for reasons to be amplified later) and produces the familiar high wind areas to the south of each area where high terrain is in close proximity to the coast.

Both the low wind areas to the north and the higher wind areas to the south of each obstruction extend offshore and downstream with diminishing magnitude at an

angle that varies slightly with the impact angle of the upstream flow on the topography. For example, the most prominent case where the topography juts out into the flow is at Cape Mendocino, where upstream wind direction is nearly perpendicular to high coastal terrain. In this case, the angle between the orientation of the axis of weak winds upstream and the local coastline orientation is approximately 40° , as it is in southern Monterey Bay, where the flow also tends to impact directly into the high terrain near Mount Carmel. At other locations where the incident angles are reduced, such as near Point Arena and Ano Nuevo, the horizontal axis of weaker winds also has a shallower angle with the general coastal orientation.

C. CROSS-COAST VERTICAL STRUCTURE OF THE JET

To complete the description of general coastal jet characteristics over its large spatial extent, it is useful to examine a series of vertical cross-sections. In order to emphasize the tendency for the jet to broaden as it extends farther south, and to examine the downstream extent of the various features spawned by topographic interactions, a series of east-west cross-sections of winds and potential temperature along integer latitude lines is presented in Fig. 38 for 9 June and Fig. 39 for 14 June. Such cross-sections for 17 June are not presented, as the description of latitudinal variability from the plots for 9 and 14 June is not significantly augmented by additional plots for 17-18 June event, which is spatially quite similar to 9 June. Each plot covers seven degrees of longitude so that the relative offshore scale of the jet can easily be compared at varying latitudes. These cross-sections are at 0200 UTC (1900 PDT), which is near the typical diurnal wind maximum. Diurnal changes to the patterns that emerge will be discussed in the last section of this chapter.

The series of cross-sections from 9 June (Fig. 38) show a southward vertical structure evolution consistent with the broadening jet seen in the horizontal plots (Fig. 36). From a large-scale perspective, the primary result is that as the jet broadens, the isentropes slope less steeply over a longer distance. This is particularly evident when comparing the cross-section at 40°N (Fig. 38c) to that at 36°N (Fig. 38g). The narrow jet at 40°N is accompanied by steeply sloped isentropes near the coast that begin to flatten out offshore. In contrast, the broad jet at 36°N is associated with a wide band of gently

sloping isentropes well offshore in addition to the steep slope at the coast. This wide band is accompanied by an increased MBL inversion strength that produces a strong horizontal thermal gradient even with the reduced slope. Also, offshore jet winds extend to heights well above the inversion (1500 m or more) in association with isentropes that have a coastward slope to similar heights.

Some important variability is present on smaller scales as well, particularly with respect to the position of the cross-section relative to the six locations in Table 1. On the upwind side of such a feature, the isotachs rise along the face of the terrain, with weaker winds below, as the flow in and above the marine layer impinges on the terrain. This is particularly evident at 41°N (Fig. 38b) upstream from Cape Mendocino. When a cross-section is drawn such that it crosses the coast at or near one of the six mountain locations, such as the section along 39°N (Fig. 38d), the area of increased winds above the terrain is quite evident as a secondary maximum at a height of about 2000 m. On these sections at and on the upstream side of a coastal mountain, an upward isentropic slope is typically present inshore of the steeper downward sloping isentropes. This upward slope appears to be due to a localized deepening of the marine layer as the winds impinge on that terrain.

Also evident in the sections in Fig. 38, particularly with decreasing latitude, is the downstream extension of the wind maxima away from their point of origin. For example, the section through 37°N (Fig. 38f), which intersects the coast on the north side of Monterey Bay, crosses the wind maximum in the lee of Point Arena. The jet core is displaced farther offshore and higher than it was farther north, where the jet maximum is initiated. The downward isentropic slope toward the coast in association with that response is evident, with an upward slope inshore from that associated with flow impingement on the Santa Cruz Mountains, and a second downward slope associated with the inception of that lee response. A cross-section in the close lee of one of the six mountains in Table 1, such as the sections along 36°N (Fig. 38g) or 40°N (Fig. 38c), exhibits a steep downward slope associated with the compressed marine layer in the lee, with no significant inshore upward slope until the next flow impingement occurs. The lateral extent of these wind maxima is particularly evident on 9 June in the 35°N (Fig. 38h) and 34°N (Fig. 38i) sections, both of which continue to sample the Santa

Lucia/Point Sur maximum with increasing distance from shore, although the 34°N section also samples the lee response south of Point Conception.

Very similar structure with respect to coastal features is evident upon examination of the cross-sections from 14 June in Fig. 39. The more northern origin of the jet winds discussed previously is immediately apparent, with the most dramatic difference at 42°N (Fig. 39a). As expected in the presence of the higher winds in the north, the downward isentropic slope is also steeper than on 9 June (Fig. 38a), and the strength of the inversion is greater. Of note at 41°N on 14 June (Fig. 39b), the upward slope of isentropes close to shore associated with marine layer deepening as the flow approaches Taylor Peak at Cape Mendocino is more pronounced than it was on 9 June. It thus appears that the tendency for inshore isentropes to slope upward near major coastal terrain, and for an extension of higher winds aloft over the coastline to occur, is directly proportional to the magnitude of the incident winds.

An important difference between 9 and 14 June is evident along 38°N, where the 14 June section (Fig. 39e) samples the much more southerly extension of the Cape Mendocino maximum, due to the higher winds farther north on that day. This section again displays a steepening of the offshore isentropes in the location of that offshore maximum, followed by an elevation of isentropes traced back to flow impingement on the Point Arena topography, followed by a much steeper slope associated with the lee response to that topography. The sections farther south show the smaller scale of the wind maxima relative to 9 June, which is related to reduced larger-scale wind speeds and reduced inversion slope. In summary, the same features relative to coastal topography are evident in the wind and potential temperature patterns, but their magnitude is proportional to that of the incident flow.

D. ALONG-COAST STRUCTURE

To complete the three-dimensional view of the marine boundary layer and coastal jet winds, and highlight the along-coast variations, a series of cross-sections roughly aligned with the direction of flow are examined. It is not possible to draw a single cross-section through all wind maxima, due primarily to the major coastal bend at Cape Mendocino. However, cross-sections that very closely parallel the coast from near Cape

Mendocino to Point Conception for 9 and 14 June are shown in Fig. 40, with the same vertical scale and time of day as in Figs. 38 and 39. The plane of the cross-section is shown on Fig. 8, which shows it to be very close to the coast along most of its length. From Point Arena southward, this section is close to ideal for sampling the near-shore structure. At the northern end, it diverges from the coast somewhat and is thus less than ideal for sampling the wind maximum in the lee of Cape Mendocino, although it captures its outer edge and southern extreme. It lies outside of the lee effect south of Cape Blanco.

The 20 m s^{-1} maximum near the north end of the 9 June section in Fig. 40a is the southern extremity of the lee response downwind from Cape Mendocino. This is followed by elevated isentropes and a relative minimum in low-level winds, and then quickly by another descent in isentropes that leads into the broad maximum downwind from the topography near Point Arena. Continuing southward, two more low-level wind minima are coincident with elevated isentropes. These are the successive flow responses to impingement on the Santa Cruz Mountains and Mount Carmel, near Point Sur. Of note, two elevated relative wind maxima are found above and slightly downstream of the low-level wind minima. These maxima are coincident with the descent in isentropes on the lee side of each feature. While the southern elevated maximum corresponds to accelerated flow over the Point Sur topography and leads down into the pronounced, elongated low-level wind maximum that was evident in the cross-coast sections at 36°N , 35°N , and 34°N (Figs. 38g, h, and i), the northern elevated maximum corresponds to flow over the Santa Cruz Mountains, which is prevented from spawning a low-level maximum by the immediate presence of Mount Carmel and the northern Santa Lucia Mountains. The next feature southward is a distinct area of elevated isentropes associated with the Point Conception topography (again with a relative low-level wind minimum), followed in turn by another sharp descent in isentropes upstream of the southernmost low-level maximum in the cross-section, which is in the lee of Point Conception and is where the strongest winds along the entire section occur.

The same section on 14 June (Fig. 40b) reveals the more northerly location of the higher winds than on 9 June (Fig. 40a). Although the highest winds occur in the lee of Cape Mendocino, that maximum is not well represented due to the cross-section

orientation in this area. This broad, high maximum is associated with a steep downward slope in the isentropes. Despite the fact that the northern end of this section is well offshore, the upstream elevated isentropes, associated with flow impingement at Taylor Peak, is evident at the far northern end. The region downstream from this maximum is the much better sampled, and has much more pronounced elevated isentropes associated with the terrain near Point Arena, which is followed by a low-level wind maximum in its lee. The two low-level wind minima are again seen in response to the flow encountering the Santa Cruz and Santa Lucia Mountains, successively. The low-level relative maximum between them is more evident on this day, and represents the brief and weak lee response to the Santa Cruz terrain. Finally, the Point Sur lee response is clearly evident (although much weaker than on 9 June) and is followed again by elevated isentropes (gentler than on 9 June) and a relatively weak maximum in the lee of Point Conception. Note that the deeper marine layer beginning at about the Santa Cruz Mountains and extending southward coincides with the decrease in magnitude of southern jet features, relative to those farther north.

A prominent feature of the along-shore cross-sections from both days is the vertical extent of higher winds associated with areas where the isentropes exhibit a pronounced descent along the direction of flow. Wind direction is not shown on these plots, but it is consistently close to the plane of the cross-section at low levels. There is slightly more directional variability above the marine layer, but the winds at 850 mb are also approximately aligned with the direction of the cross-section. The vertical extent of these relative wind maxima generally increases southward on 9 June (Fig. 40a) and decreases southward on 14 June (Fig. 40b). They also show a tilt back to the north, as does the axis of the elevated isentropes (and subsequent sharp descent) associated with each coastal mountain peak. It is clear from these cross-sections that the flow response to the near-coast topographic features discussed previously is not limited to the MBL, or even to the inversion above it. This will be discussed further in the next chapter.

To get a sense of the offshore extent of these changes in isentropic elevation, and their associated wind speed changes, cross-sections parallel to those in Fig. 40 but farther offshore by 50 km are shown in Fig. 41. The three major descents in isentropic surfaces in the lee of the terrain near Point Arena, Point Sur, and Point Conception remain quite

prominent offshore on 9 June (Fig. 41a). The Cape Mendocino response on the north end is more subtle, but again, this cross-section lies farther offshore at the northern end than over the rest of its length. The distinct areas of elevated isentropes inshore are less prominent offshore, and appear more as level areas between each steeper drop. The most prominent descent in isentropes along the section is downwind of Point Sur and the Santa Lucia Mountains, which leads down into the highest winds (30 m s^{-1}) near the southern end of the section. Two prominent wind maxima are found in the lower levels (although they are at higher elevation than their counterparts closer to shore). One maximum is the offshore extension of the lee response to the mountains near Point Arena and the other is a response to the Santa Lucia Mountains. The intervening relative wind minimum between the two, with a flattening (or slight elevation) of the isentropes aloft, is the offshore extension of the flow impingement on both the Santa Cruz and Mount Carmel area terrain, the effects of which become combined offshore into one broad feature. A similar (but subtle) feature is at the far southern end in response to the Santa Ynez Mountains. Over the whole cross-section, a gradual decrease in marine layer depth toward the south is evident, with the lowest inversion base coinciding with the highest winds.

The offshore section from 14 June (Fig. 41b) reflects the presence of higher winds to the north as discussed relative to Fig. 40b. Three prominent descents in the isentropes are in response to, successively, the high terrain near Cape Mendocino, Point Arena, and, less prominently, Point Sur. The two northern isentropic descents lead into one elongated downstream wind maximum, which contains the highest winds in the section (29 m s^{-1}). This maximum represents the merging offshore of the two lee responses. The third descent is associated with a subtle maximum south of Point Sur. Of note, the elevated isentropes near the center of the inshore cross-section (Fig. 40b), which are related to flow impingement on the Santa Cruz Mountains, remain quite prominent offshore, especially above the temperature inversion. This offshore extension appears to be due to the large magnitude of the winds impinging on that terrain, as a much more subtle isentrope flattening was predicted at this location on 9 June (Fig. 41a), when the incident flow speeds were smaller. Coincident with this location is a deepening of the marine layer relative to farther north, and a sharp decrease in wind speeds, with only the slight

enhancement downwind from Point Sur. While it was earlier assumed that the weakening of winds to the south on this day was simply related to a gradual decrease in synoptic-scale pressure forcing, it is possible that the winds weaken in more of a discrete jump at this location as the strong flow impinges on the Santa Cruz terrain, which causes a jump in marine layer depth that extends well offshore. The synoptic-scale subsidence is then insufficient to drive the marine layer down to near its upstream level, which results in a continued deep marine layer, with associated higher pressures and weakened winds. Continuing south, the marine layer remains relatively deep and the winds relatively weak, and then gradually tapers off to the south as the height of the vertical wind maximum rises to about 950 mb. A common feature in the two sections in Fig. 41 is the same upstream tilt of areas of increased isentropic slope, and associated relative wind maxima at elevation, as was the case in the inshore cross-sections (Fig. 40).

These offshore cross-sections illustrate that changes in marine layer depth and wind speed induced as the flow interacts with coastal topography extend well beyond the near-shore region implied in past studies. Similar cross-sections as far as 200 km farther offshore from those in Fig. 40 have the same periodic steepening of isentropic surfaces (and shallowing of the marine layer) as they slope downward to the south (albeit much more subtly). Each of these features is the offshore extension of a lee response to the high points in the coastal terrain. An examination of such along-shore cross-sections at increasing distances from the coast reveals that the changes in isentropic slope occur at decreasing latitude. That is, the effects of the flow interactions with the topography close to the coast have both an offshore and a downstream extent. The degree of this effect away from the coastal feature depends directly on the magnitude of the incident flow and can extend as many as 400 km offshore from an initial point of interaction, such as the case of the maximum in the lee of Point Sur on 9 June (Fig. 36a), the effect of which appears evident at the southern extreme of the inner model domain off the northern Baja coast. The combined Cape Mendocino/Point Arena response on 14 June (Figs. 36b, 37) has a similarly large southward extension.

E. DIURNAL VARIABILITY

As documented in the measurements from the buoys (Fig. 21), a substantial diurnal signal is often present in the wind offshore. This is expected given that the

coastal jet is forced by the thermal contrast between the cool marine boundary layer, which undergoes little diurnal temperature change, and the heating over land, which undergoes dramatic change in summer. What may be a less-expected result is that coastal jet winds (as defined in this study) continue so persistently during the diurnal cycle. That is, strong northerly to northwesterly, coast-parallel winds are evident offshore nearly continuously. Thus, while the preceding discussions of the spatial and vertical distribution of coastal jet winds were focused on a time in the diurnal cycle when jet features are particularly well developed, especially close to shore, they are representative of other times of day as well. What varies diurnally is the magnitude, not the existence, of the features discussed. Specifically, the downward cross-coast isentropic slopes in the lee of significant topography and the inshore upward slopes at and upstream from that topography undergo diurnal strengthening as the heating cycle progresses. The along-shore response is also altered diurnally as the incident flow magnitudes change. As these features become more or less pronounced, their associated relative wind maxima and minima are similarly modulated. With increasing distance from the coast, these diurnal changes have smaller magnitudes, such that beyond about 200 km from shore, variability in the winds is driven largely by synoptic-scale changes.

It is not intended here to illustrate the full range of diurnal variability at different locations and under differing synoptic conditions. Rather, only the major, recurring aspects of this diurnal cycle are discussed. The 1000 mb wind distribution at representative times on 9 June are shown in Fig. 42 with winds in excess of 18 m s^{-1} shaded to emphasize the location of significant wind maxima. At the beginning of the daytime heating cycle at 1200 UTC (0500 PDT) (Fig. 42a), both the magnitudes and lateral extents of these accelerated wind regions are near their minimum values. The most prominent wind feature at this level along the coast is the maximum downwind from the Point Arena topography near San Francisco. By 1100 PDT (Fig. 42b), in association with the heating cycle on land, the areal extent of the southern maxima (from Point Arena southward) has extended to the south. The wind speeds have increased slightly near Cape Mendocino (reaching above the 18 m s^{-1} shading threshold) and more so downwind from Point Sur (from near 18 m s^{-1} to over 22 m s^{-1} in the center of the jet maximum). The San Francisco area isotach maximum has its greatest southern extension

around this time and retreats thereafter. On the other hand, the maximum south of Point Sur continues to grow offshore and to the south, reaches its greatest extent around 2000 PDT (Fig. 42c), and becomes a more prominent feature of the wind distribution than the area farther north. The areal extent of the southern maxima then shrinks sharply during the night, while the northern maxima (lee of Point Arena and Cape Mendocino) remain fairly consistent through the night. Thus, a more prominent diurnal signal in the spatial wind evolution on 9-10 June is found at southern latitudes, where the jet was stronger.

Cross-sections perpendicular to the coast along 35°N on 9 June (as in Fig. 38h) at these three times are shown in Fig. 43. At 0500 PDT (Fig. 43a), before the heating cycle begins, the jet is already well established with a maximum of 23 m s^{-1} at about 360 m elevation about 75 km offshore. By 1100 PDT (Fig. 43b), the vertical extent of 18 m s^{-1} winds has decreased, but the jet core remains at about 350 m. This core has strengthened to 27 m s^{-1} and has moved closer to shore by some 20 km. At 2000 PDT (Fig. 43c), the strongest winds have moved in much closer to shore in a pronounced low-level (below 200 m) extension of the offshore core, which has remained at about the same vertical and horizontal location and increased slightly in magnitude to 28 m s^{-1} . At this time, the offshore extent of the high winds is near its maximum.

The tendency for the jet core to move down and closer to the coast in response to daytime heating was discussed in Burk and Thompson (1996) and was detected by others during CW96. However, upon examination of this and other cross-sections during the diurnal cycle, a fairly consistent offshore core of higher winds, whose distance offshore remains relatively constant, becomes apparent. The diurnal heating cycle results in an extension of that core in a downward and coastward finger of maximum winds, which may exceed the magnitude of the outer core, but often does not. Thus, the majority of the diurnal variability in the near-shore winds takes place in these daily extensions of the offshore core.

The cross-sections in Fig. 38 illustrate a dramatic variability in the structure of the MBL and the location of strongest and weakest winds relative to the six major topographic features in Table 1. While no attempt will be made here to reanalyze each of those cross-sections at different times of the day, the cross-sections from 39°N are presented (Fig. 44) to describe the diurnal cycle at a location close to the inception of a

wind maximum. This latitude is north of where the jet on 9 June has broadened significantly, and as such no dominant offshore maximum is present. The jet core is a near-shore feature only, and it undergoes little diurnal change in position while strengthening during the day from 16 to 20 m s⁻¹. The prominent enhanced winds over the terrain at this latitude are quite evident at 1100 PDT (Fig. 44b) and 2000 PDT (Fig. 44c), but are relatively insignificant at 0500 PDT (Fig. 44a), which is an indicator of the reduced flow over the coastal terrain at that time of day.

Corresponding sections for 14-15 June event are shown in Figs. 45 and 46. At 35°N (Fig. 45), there is little diurnal change in the wind pattern. The broad offshore maximum persists in about the same position vertically and with respect to the coast, and undergoes only moderate intensification from 19 m s⁻¹ at 0500 PDT (Fig. 45a) to 23 m s⁻¹ at 1100 PDT (Fig. 45b) and 2000 PDT (Fig. 45c), with a corresponding lowering of the inversion height. Interestingly, the slope of the isentropes toward the coast is more apparent at 0500 PDT than it is later in the day, and there is a long near-shore (and lower) extension of the offshore core similar to that normally expected in the afternoon and early evening. This area of the coast is characterized by a long stretch of high terrain (the Santa Lucia Mountains) very close to the coast. A possible explanation for this reverse timing of jet core behavior is that as heating takes place on land on this day, which is characterized at this latitude by a deep marine layer and relatively weaker winds, the near-shore pressure gradient is reoriented slightly such that there is an increased component of the flow at low levels onto this steep terrain. This onshore component causes convergence close to shore as the flow impinges on the terrain and is redirected, albeit with frictional loss, down the coast. The result is a localized deepening of the marine layer at the coast or, more accurately, a cancellation of the tendency for the marine layer to shallow at the coast. This deeper marine layer serves to prevent the coastal jet core from moving down and in as it might at other locations. Indeed, an examination of low-level wind directions near the shore (not shown) indicates a subtle turning toward land in the afternoon and evening relative to morning and night, which occurs in other locations, but which is less effectively blocked in most areas.

The stronger flow and shallower marine layer during the 9-10 June event apparently masked this relatively subtle effect in the model, and a more typical diurnal

evolution is seen on that day. This is consistent with the greater diurnal evolution of the spatial distribution of winds on 9 June mentioned previously. Notice also that the diurnal signal in the Buoy 28 winds, in this region, was actually greater on 14 June than on 9 June. As hypothesized in Chapter IV, this is assumed to be caused in the real atmosphere by the diurnally modulated frictional effect, as the flow near the surface interacts with the topography (as discussed above), and outweighs the reduction in the larger-scale tendency toward reduced diurnal change on 14 June.)

At 39°N, the cross-sections during the 14-15 June event (Fig. 46) are quite similar to those during the 9-10 June event (Fig. 44), except that jet magnitudes are higher throughout the day. The strongest winds again occur at 2000 PDT (Fig. 46c), along with the largest lateral extent of higher winds. As on 9 June, little diurnal change in jet core position occurs at this latitude, as the jet is fairly close to the coast and is strongly tied to the presence of the nearby topography, which in this case is Cold spring Mountain near Point Arena.

Finally, along-shore cross-sections at the diurnal minimum (0500 PDT) on 9 and 14 June, which are analogous to the 1900 PDT cross-sections in Fig. 40, are shown in Fig. 47. On 9 June (Fig. 47a), winds in each of the relative maxima along the coast are weaker than at 1900 PDT, and exceed 24 m s^{-1} only near San Francisco. The positions of each of the relative minima are very close to where they are at 1900 PDT, which is to be expected, since they are controlled by topography that is in close proximity to the cross-section. A prominent feature of this section is the 12 m s^{-1} isotach that extends farther aloft, above 700 mb in association with the three major areas of isentrope descent downwind of the terrain near Point Arena, Point Sur, and Point Conception. These higher winds aloft are due to the stronger synoptic flow above the 850 mb level at that time of day than 14 hours later. Another difference between 0500 PDT and 1900 PDT is the distinct minimum above the marine layer south of the sharp isentropic descent in the lee of Point Sur. The winds in the low-level maximum just below this feature are significantly weaker than at 1900 PDT, which may contribute to a less prominent elevation of isentropes farther to the south in response to the Point Conception topography. Given that this diurnal change is much less apparent on 14 June, this is further evidence of the increased diurnal variability at southern latitudes on 9 June.

On 14 June (Fig. 47b), apart from being more energetic late in the day than in the early morning, the cross-sections at 0500 PDT and 1900 PDT (Fig. 40b) are strikingly similar. The primary features (weak wind areas, relative low-level wind maxima, areas of elevated isentropes and steep isentropes slopes) are in the same locations along the coast and have the same backward tilt aloft in the higher wind and isentropes slope areas. The weaker wind areas downwind from the sharp isentropes descents above the marine layer are again more pronounced at 0500 PDT than later in the day. These weak wind areas are evidence of relatively low-momentum air from above being brought down to low levels as the flow descends the isentropic surfaces in the lee of major topographic features, as discussed by Strom et al. (1999).

In summary, significant diurnal variability in the coastal jet winds is predicted by COAMPSTM, especially in the near-shore region. Localized changes in isentropes slopes and shifting of the position and intensity of relative maximum and minimum winds occur as the heating cycle progresses on land. The magnitude of this diurnal change appears to be strongly related to location along the coast, synoptic conditions, depth of the marine layer and speed of the large-scale flow. While not specifically examined in this study, the diurnal change is presumably also related to cloud cover near the coast, intensity of sea breeze circulations, and the nature of the heating cycle inland. While this study was not intended to be a detailed examination of this diurnal cycle, it has revealed, or confirmed, the following diurnal tendencies: (i) coastal jet winds tend to be highest in the late afternoon and early evening, both near-shore and, to a lesser extent, offshore; (ii) MBL depth tends to shallow close to the coast in the late afternoon and early evening, with an associated increase in wind speeds; (iii) high wind areas in the lee of topography are accentuated and elongated late in the day relative to early morning; and (iv) the relatively continuous offshore jet core, when it is present (as it is far enough to the south of major topography), often extends an inshore secondary maximum lower and closer to the coast late in the day.

While these diurnal tendencies are noted, it is perhaps more relevant to this study that the basic characteristics of the MBL and coastal jet persist through the day, regardless of diurnal heating. The nearly continuous offshore coastal jet is set up by the large-scale synoptic conditions discussed earlier. The jet strength varies, but it remains

fairly strong throughout the day. Closer to shore, diurnal changes are more evident. However, the flow interacts with the coastal topography in a persistent way. Specifically, the tendency persists for winds to impact the terrain and cause upward deflections in isentropic surfaces (corresponding to a weakening of the low-level winds). A sharp descent of those surfaces occurs in the lee of the terrain, which appears to be directly linked to the high wind areas in the lee of each of these coastal features. While the magnitudes and shapes of the relative wind maxima and minima along the coast change somewhat during the day, their existence and the positions along the coast of their inception do not.

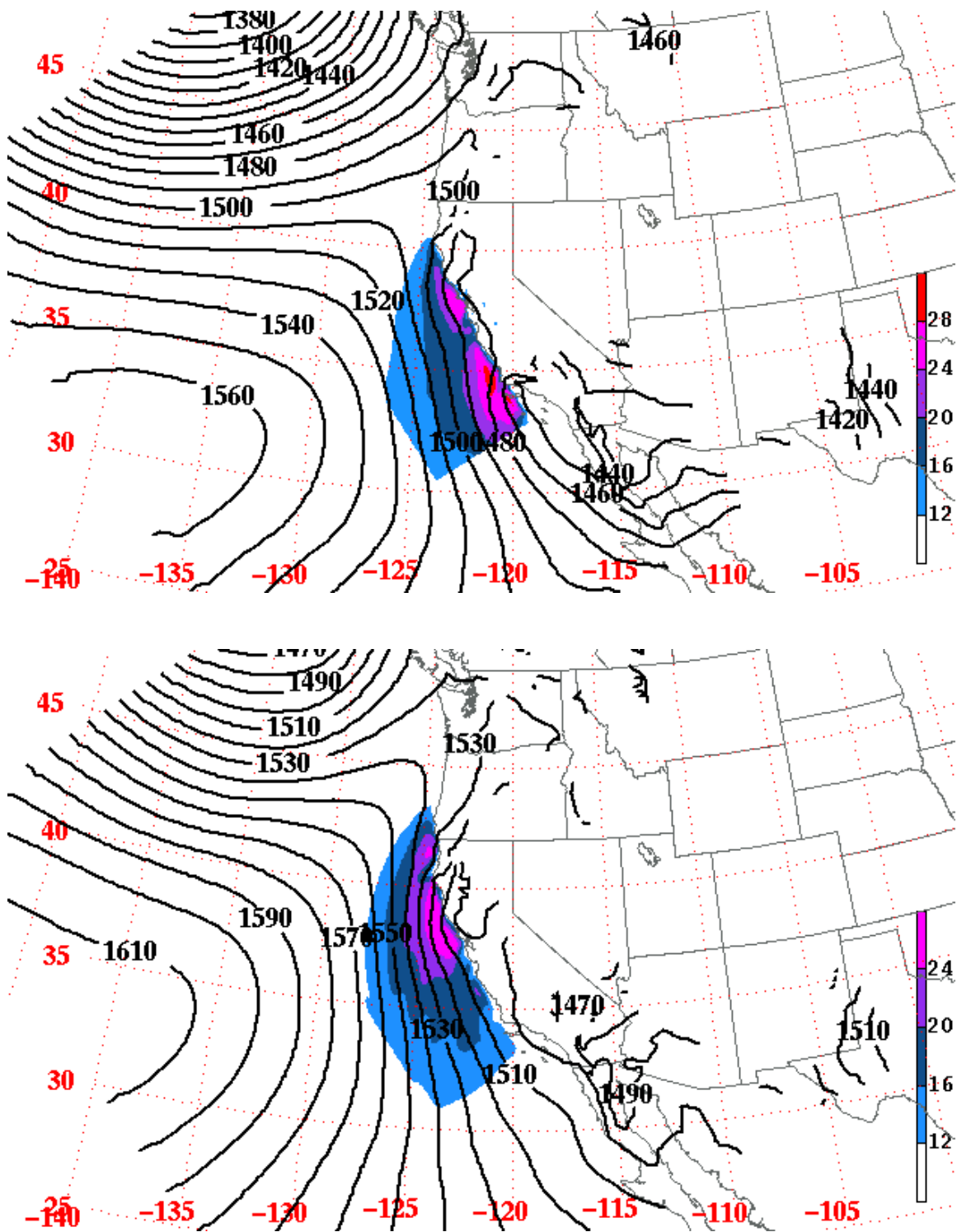


Figure 36. COAMPS 850 mb heights (m, 10-m interval) from the 27-km nest, with isotachs at 980 mb (shaded above 12 m s^{-1}) from the 9-km nest, valid at 1900 PDT on (a) 9, (b) 14, and (c) 17 June 1996. Straight edges of 12 m s^{-1} winds correspond to the limit of the 9-km nest.

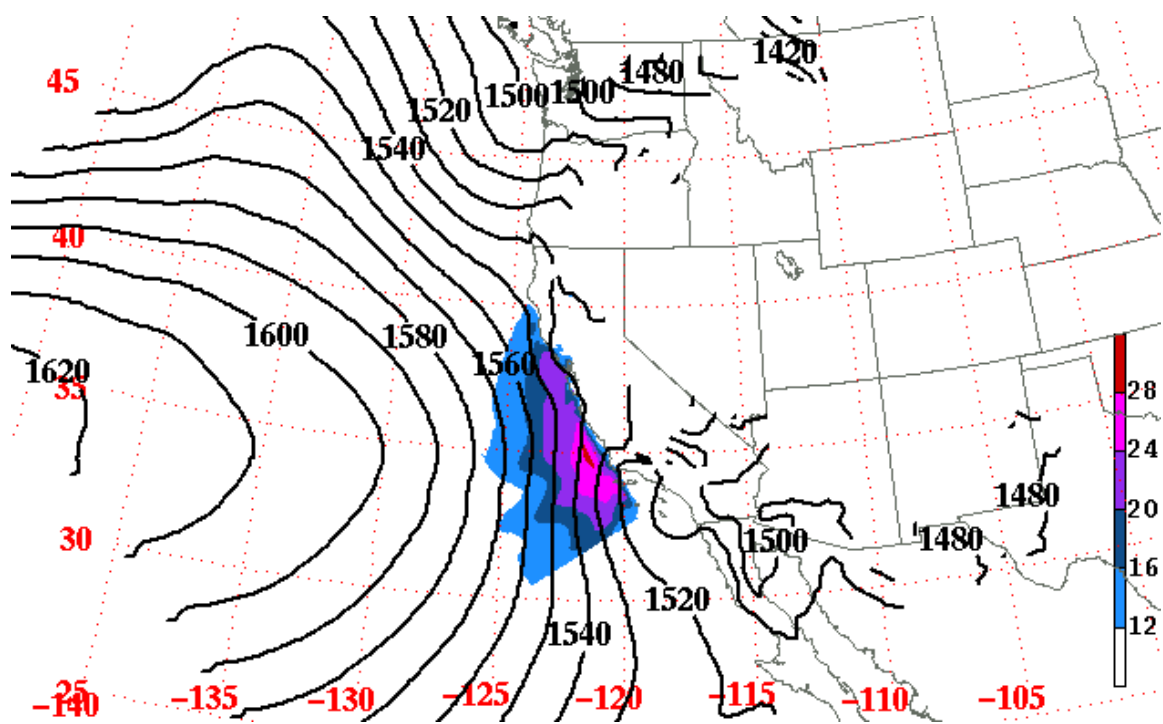


Figure 36. Continued.

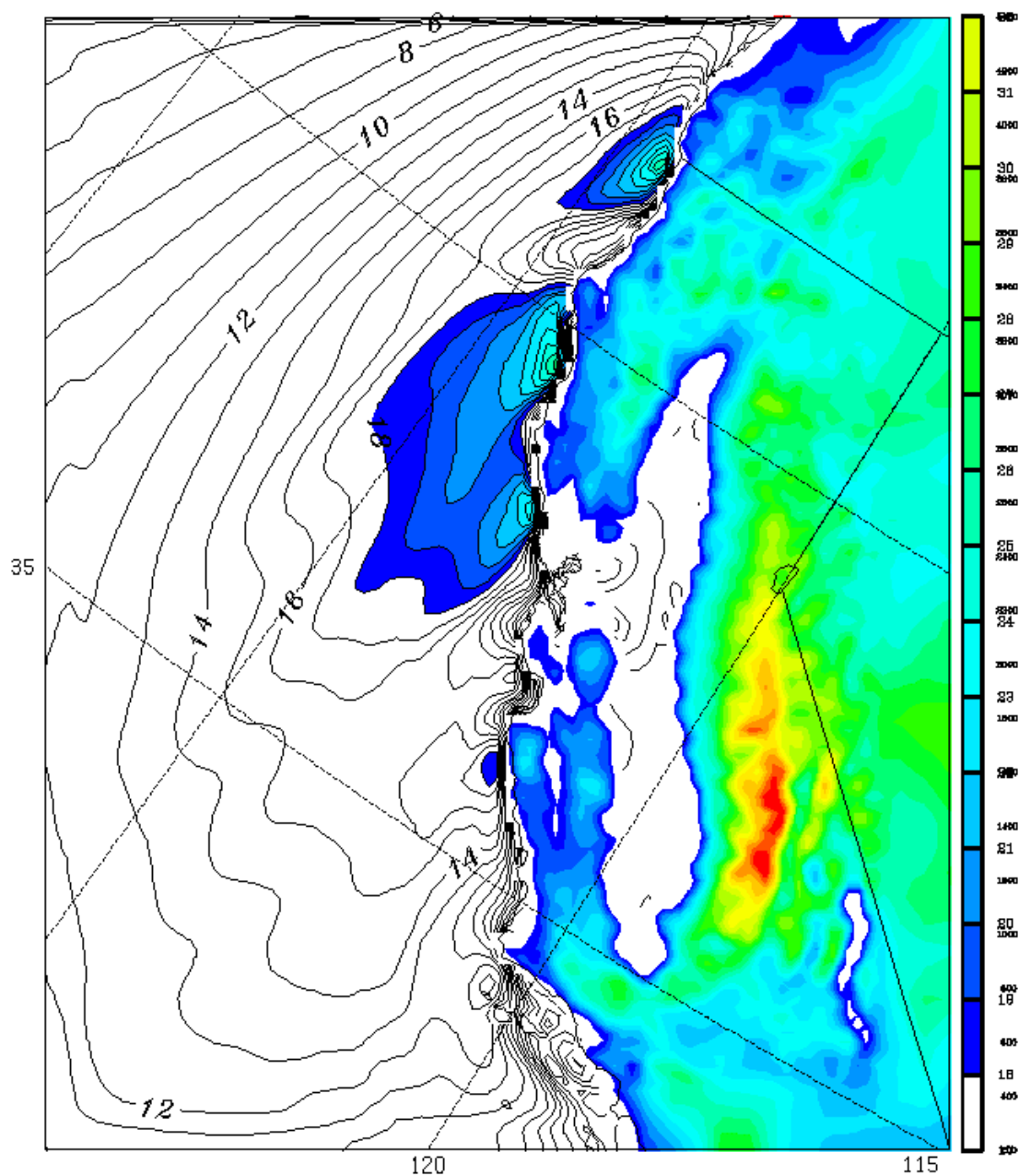


Figure 37. 1000 mb isotachs (m s^{-1}) from COAMPS valid at 1700 PDT 14 June 1996, with color shading above 18 m s^{-1} to highlight areas of highest winds along the coast. Also shown with color shading are the terrain heights above 400 m with a 200-m contour interval.

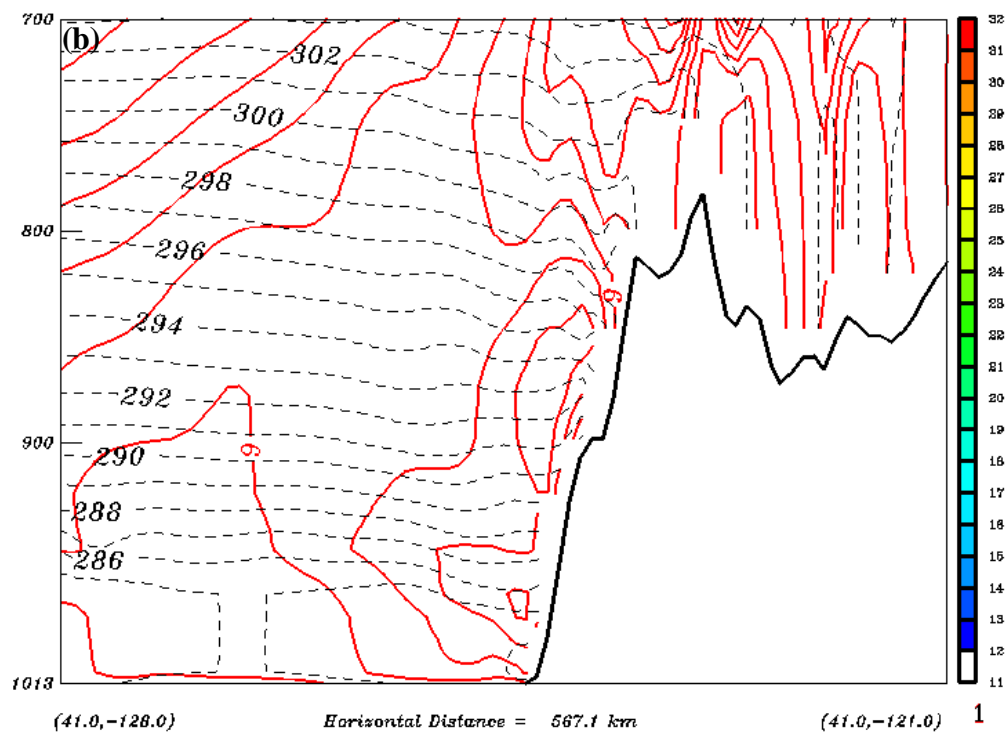
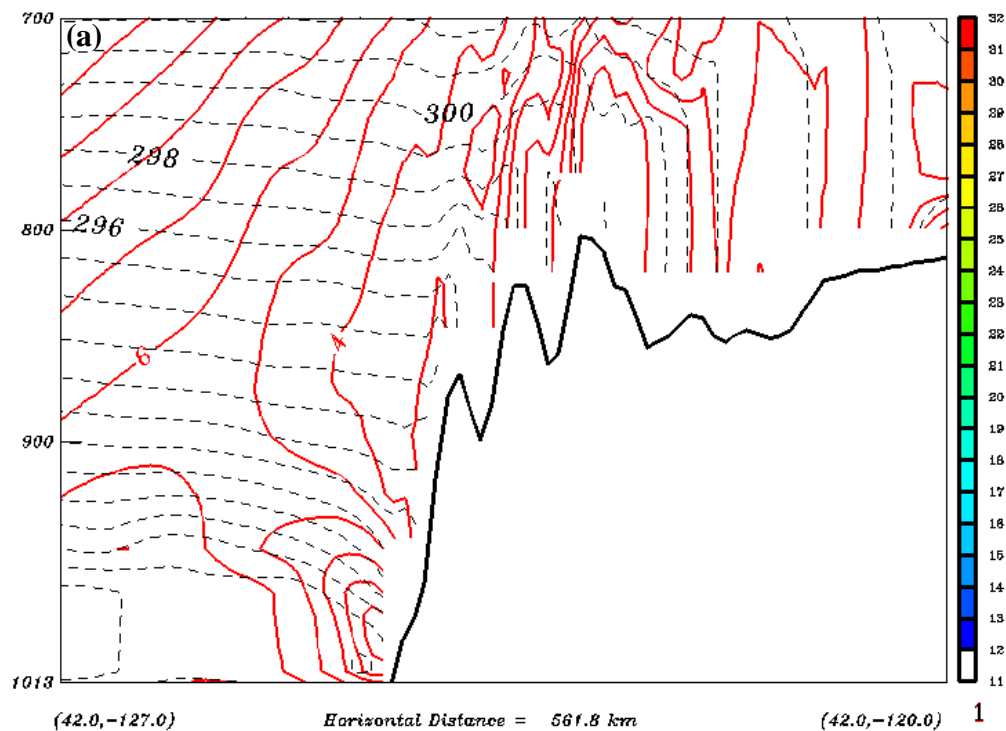


Figure 38. East-west cross-sections from COAMPS valid at 1900 PDT 9 June 1996 of winds (solid lines, 1 m s^{-1} contour interval, color shading above 12 m s^{-1}) and potential temperatures (dashed lines, 1 K contour interval) along (a) 42°N , (b) 41°N , (c) 40°N , (d) 39°N , (e) 38°N , (f) 37°N , (g) 36°N , (h) 35°N , and (i) 34°N .

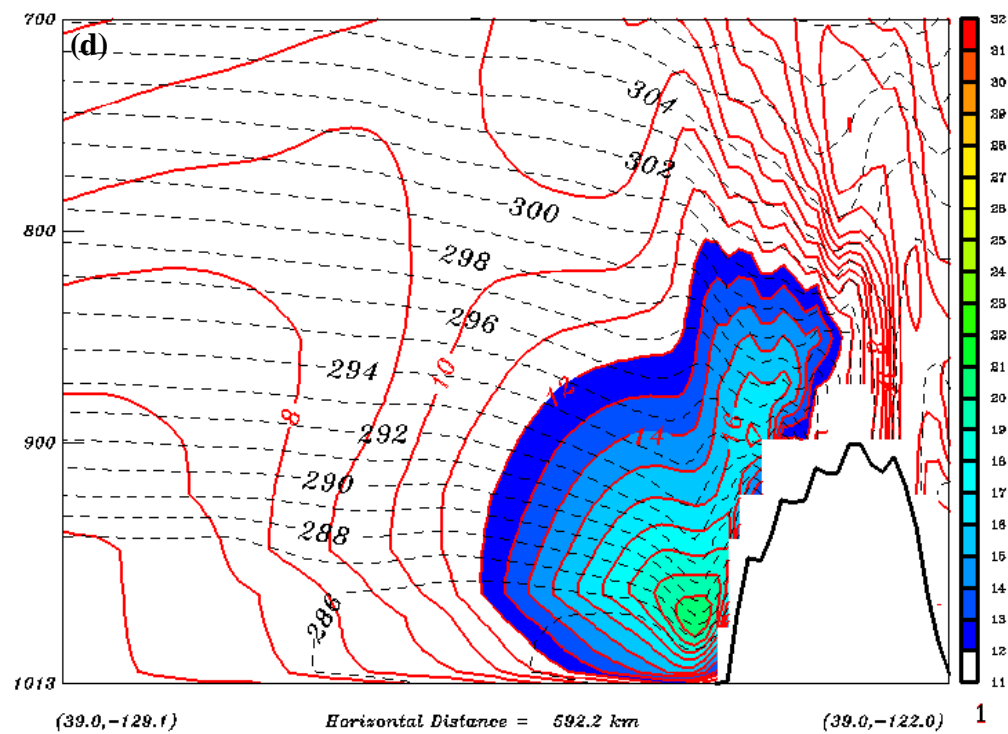
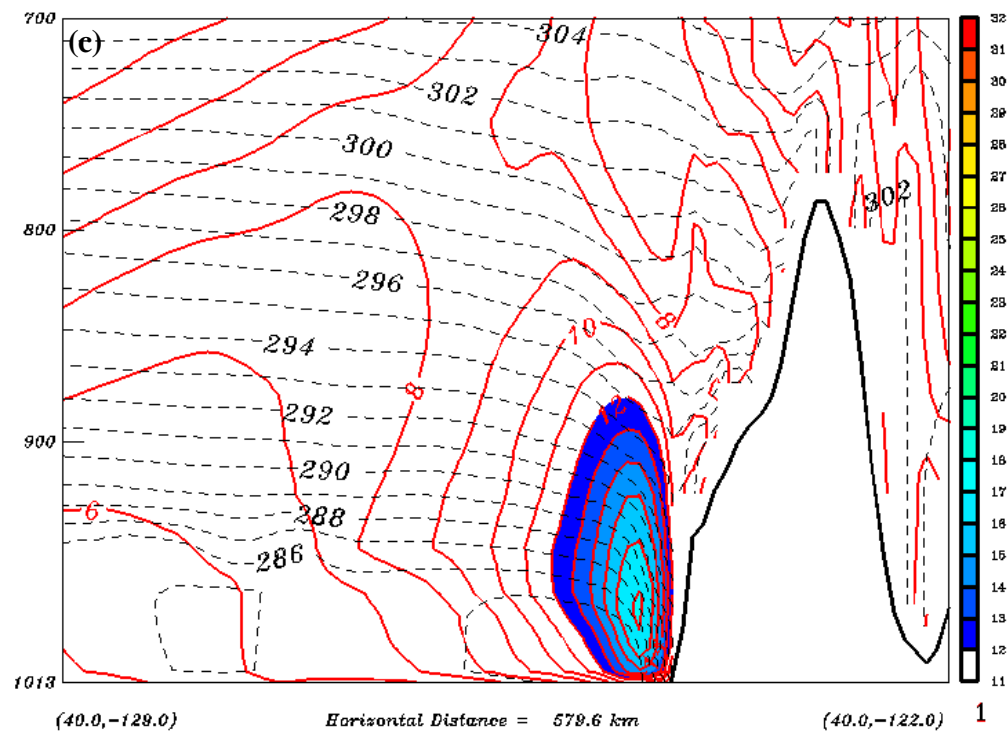


Figure 38. Continued.

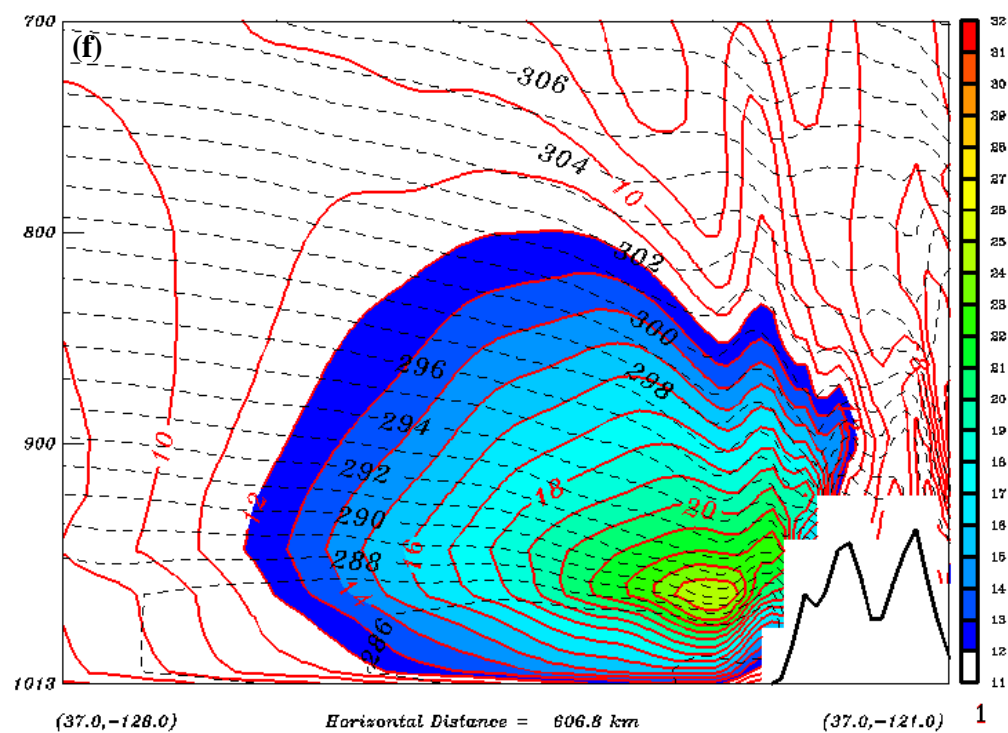
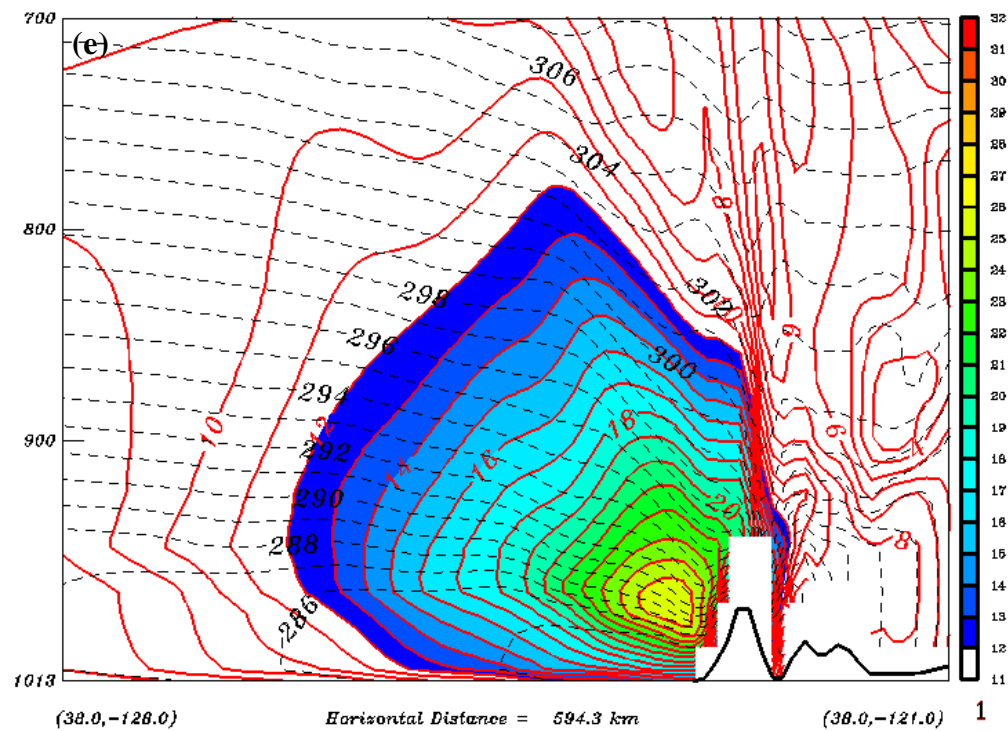


Figure 38. Continued.

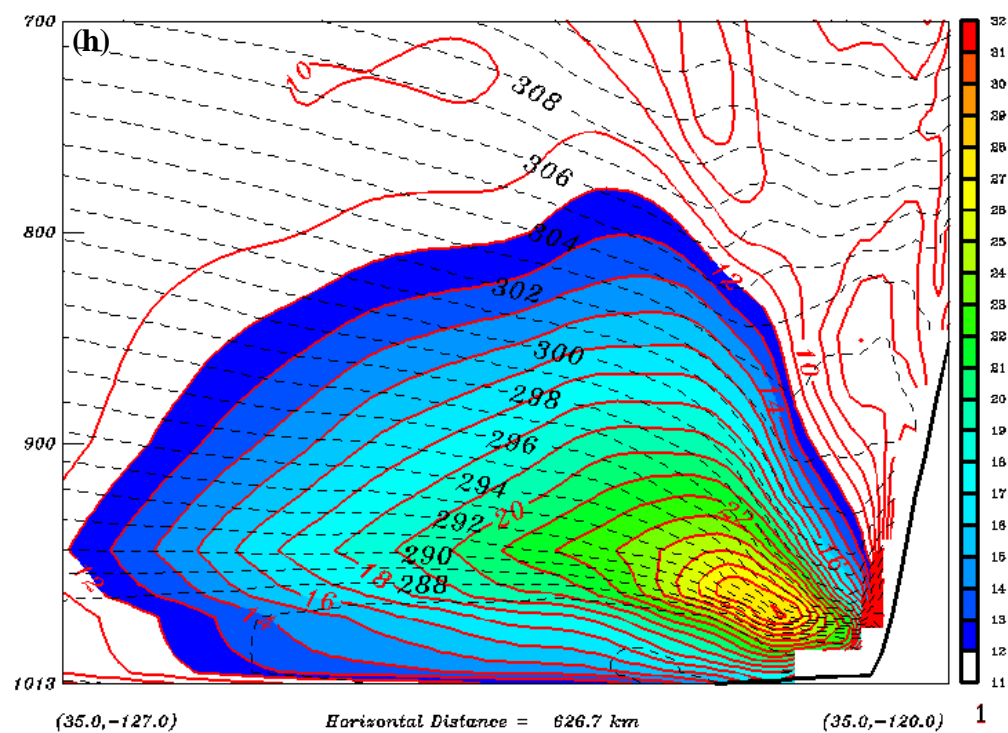
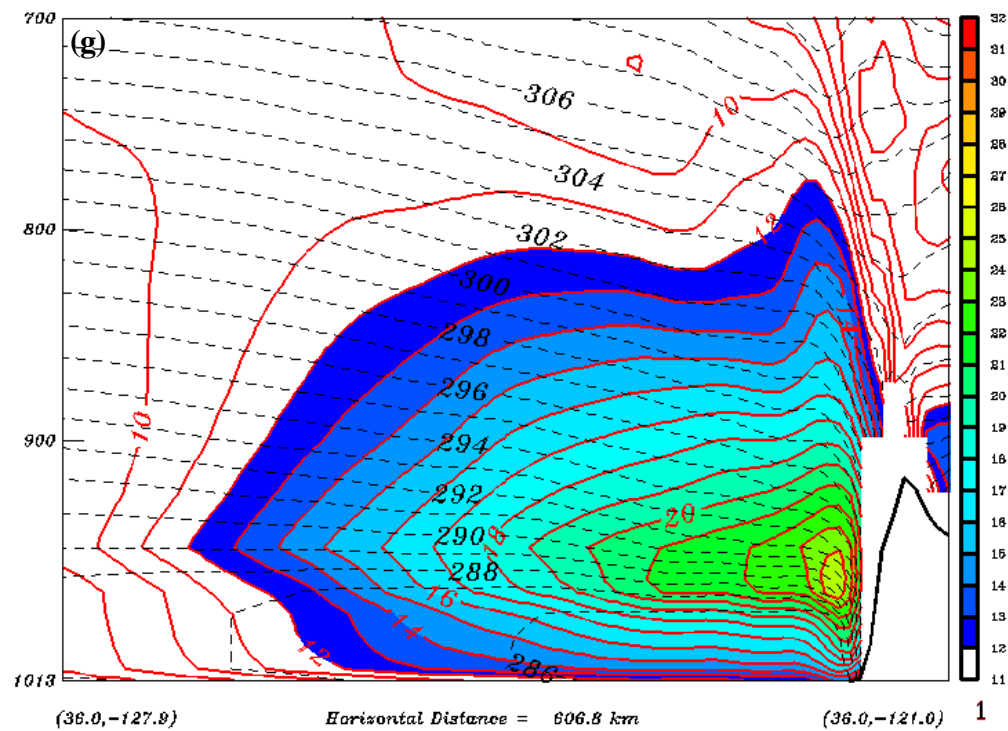


Figure 38. Continued.

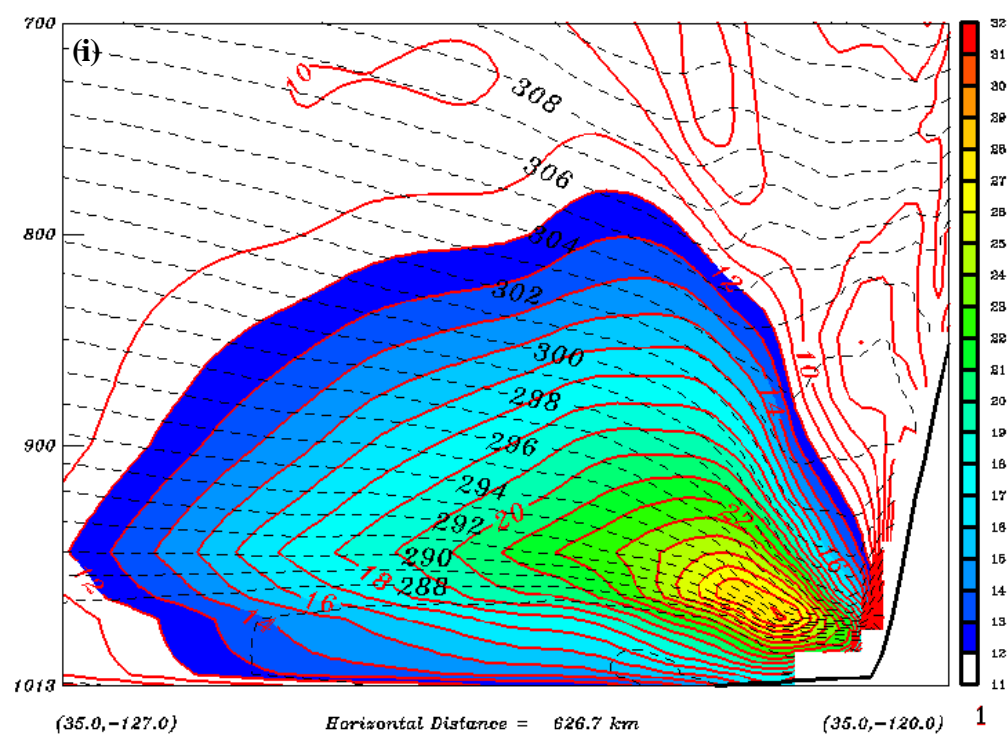


Figure 38. Continued.

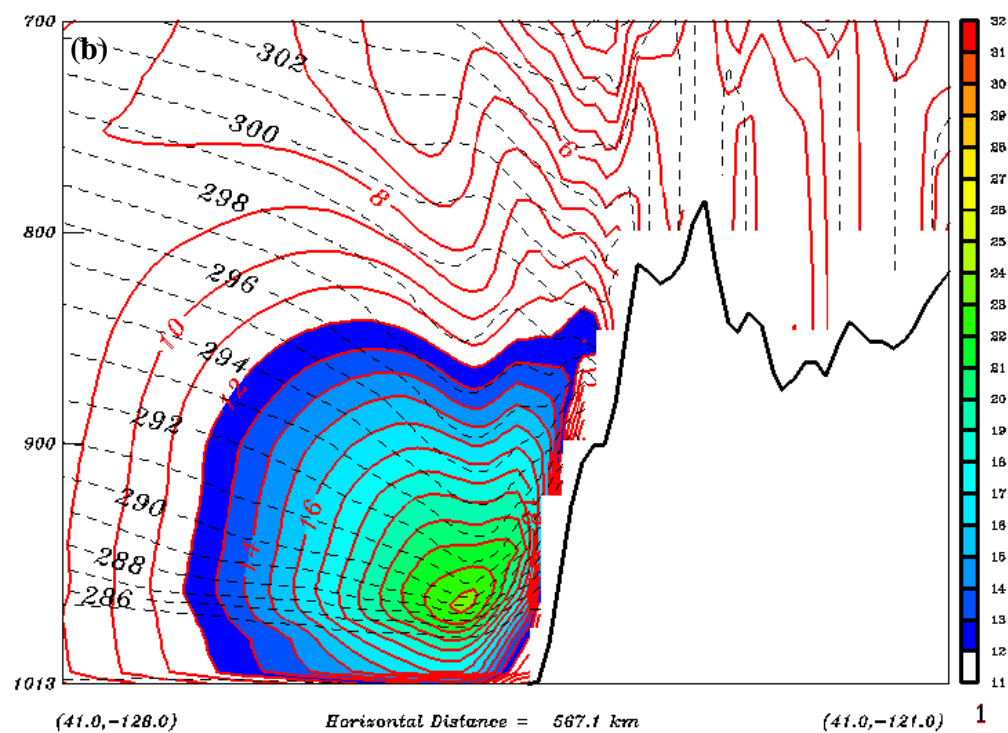
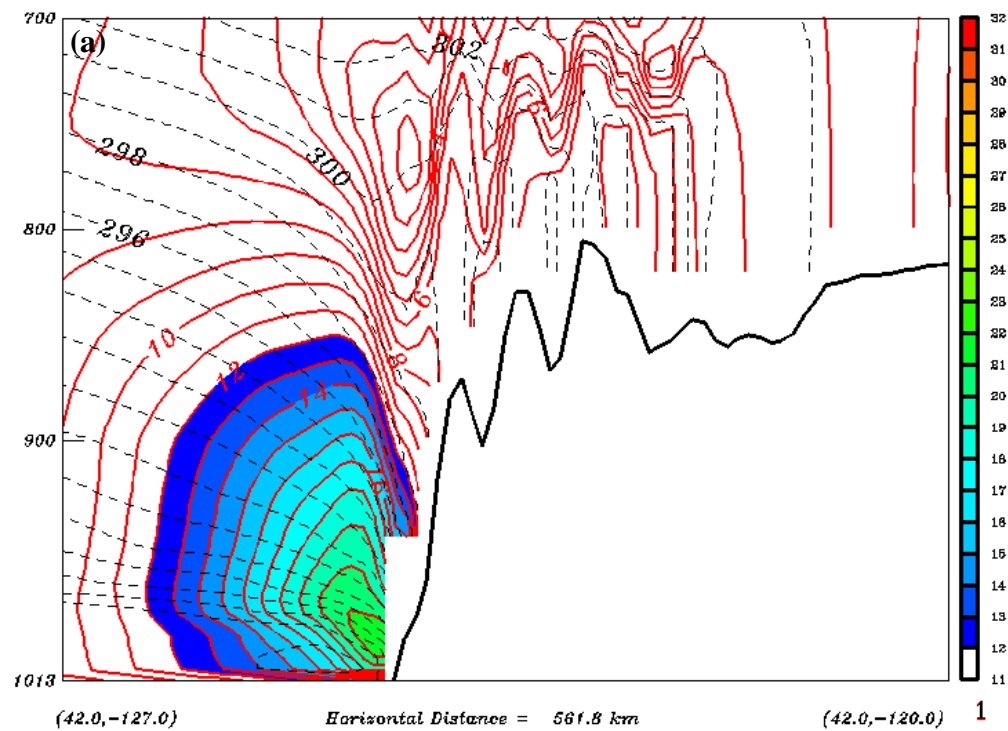


Figure 39. As in Fig. 38, except for 1900 PDT 14 June 1996.

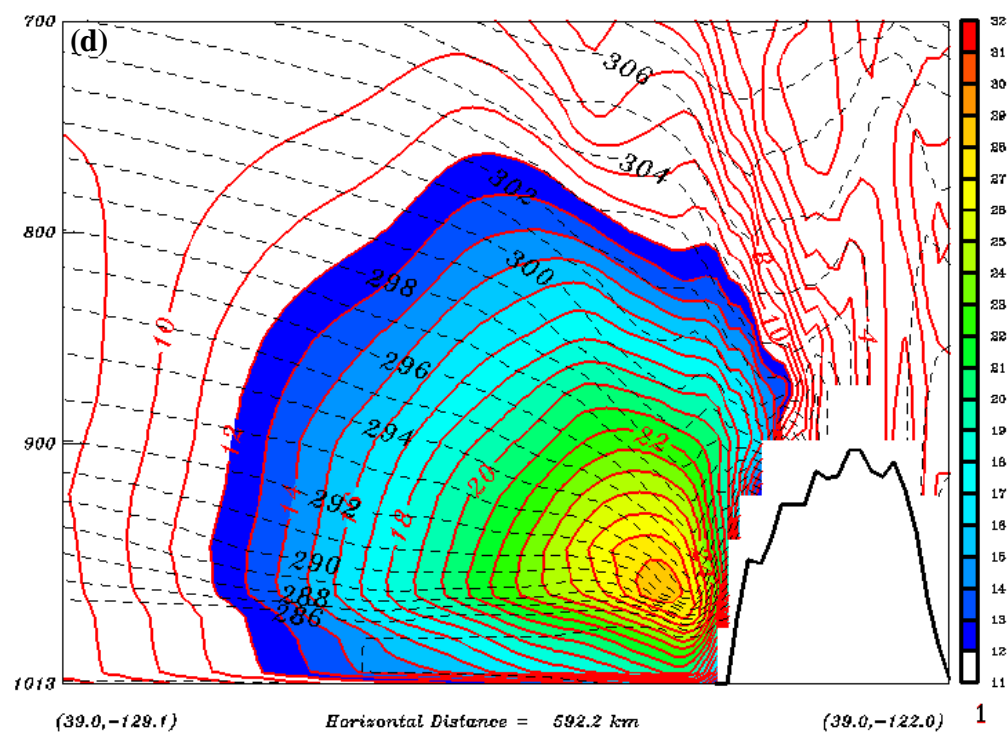
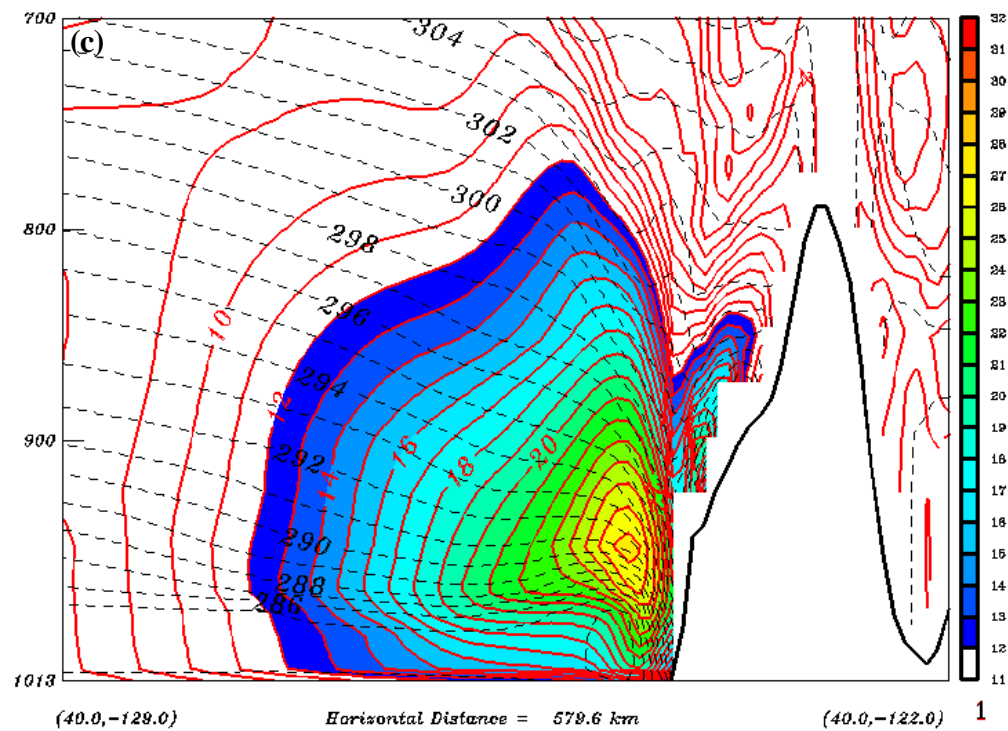


Figure 39. Continued.

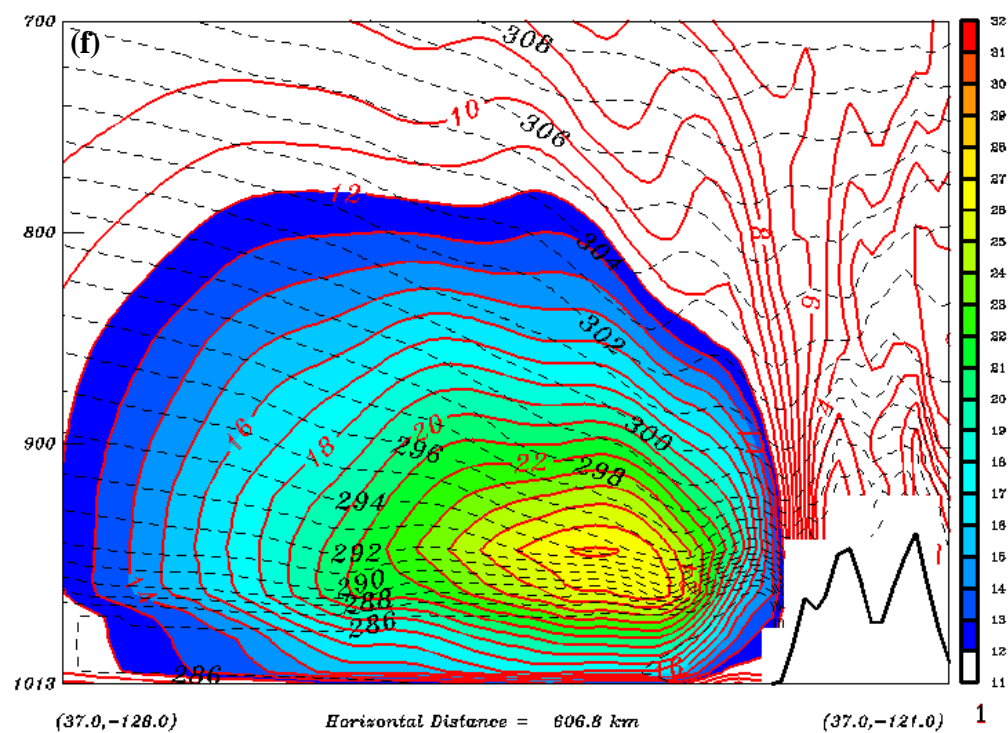
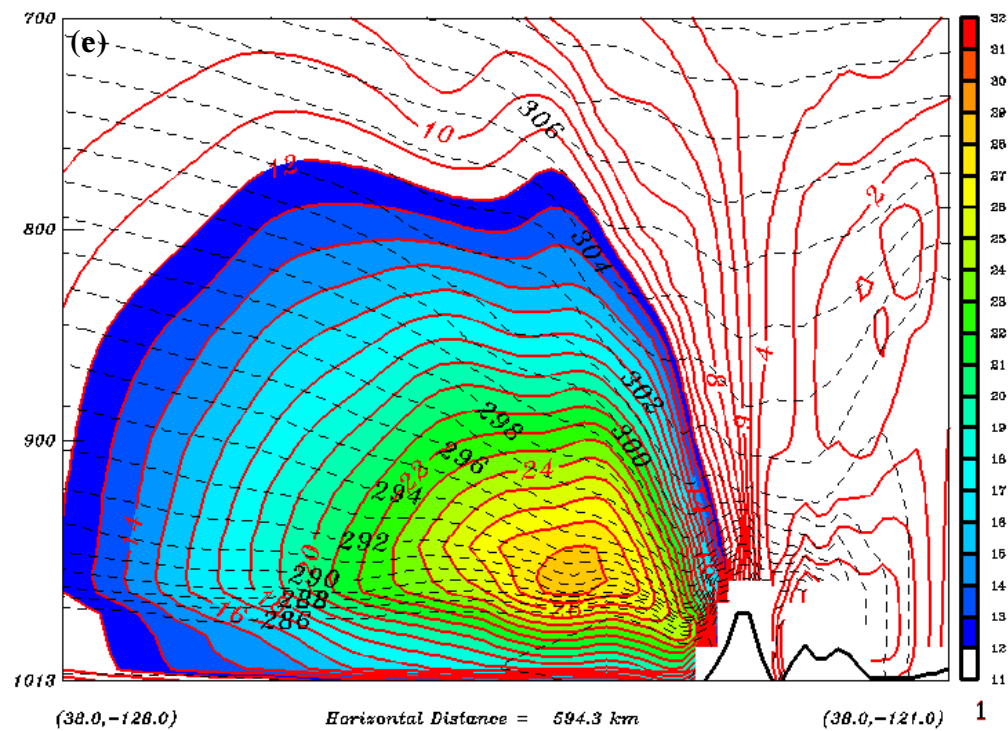


Figure 39. Continued.

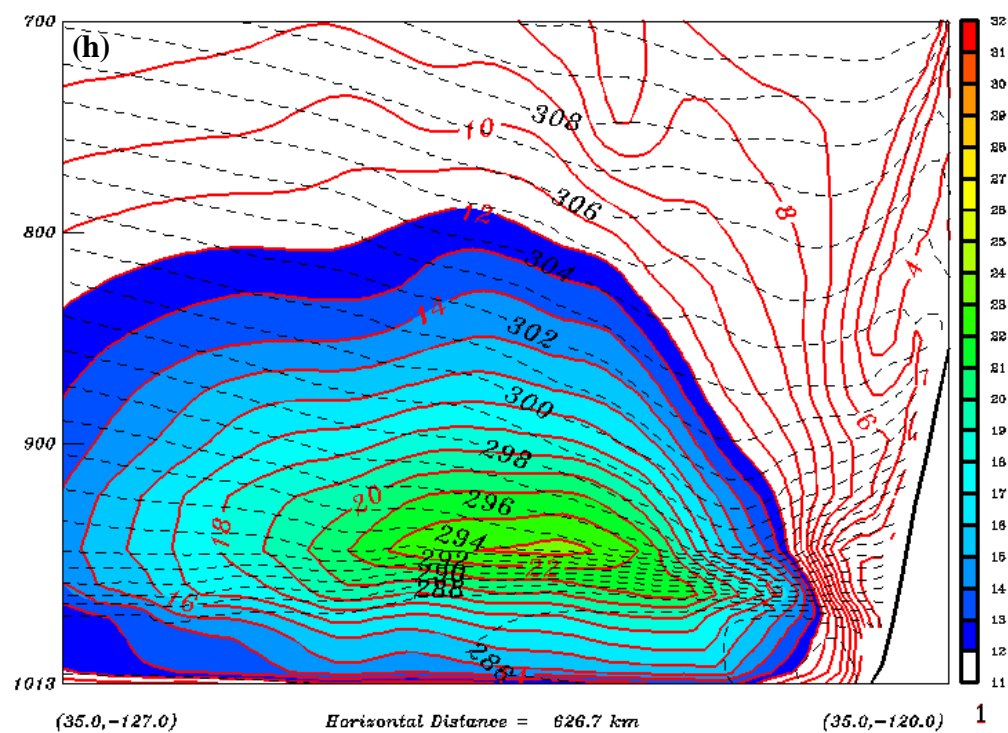
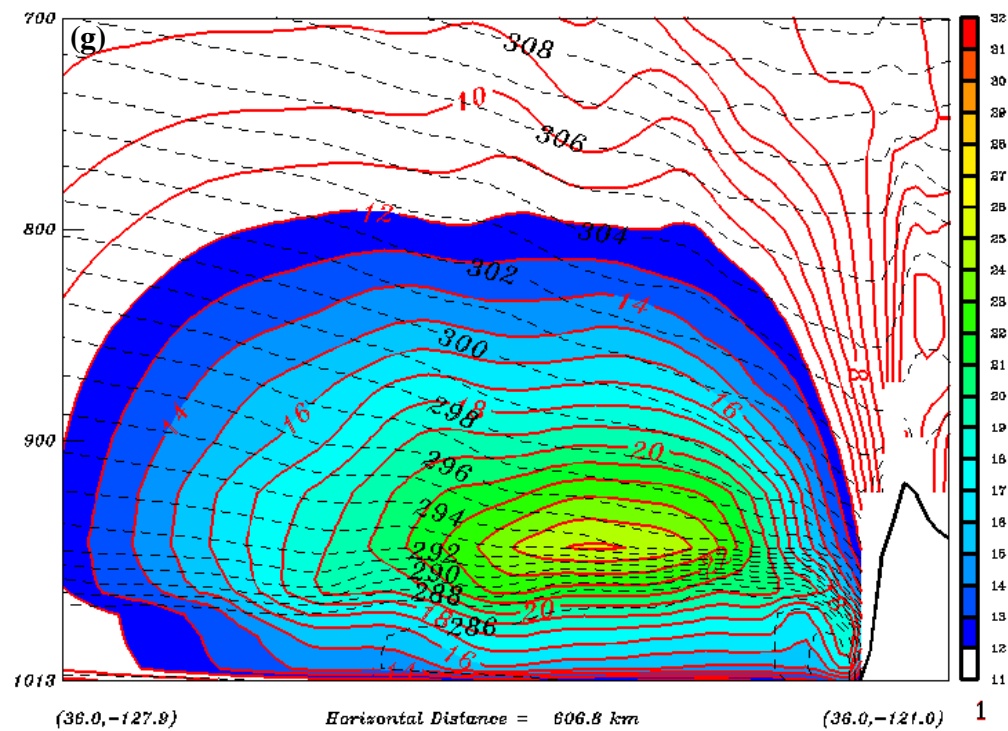


Figure 39. Continued.

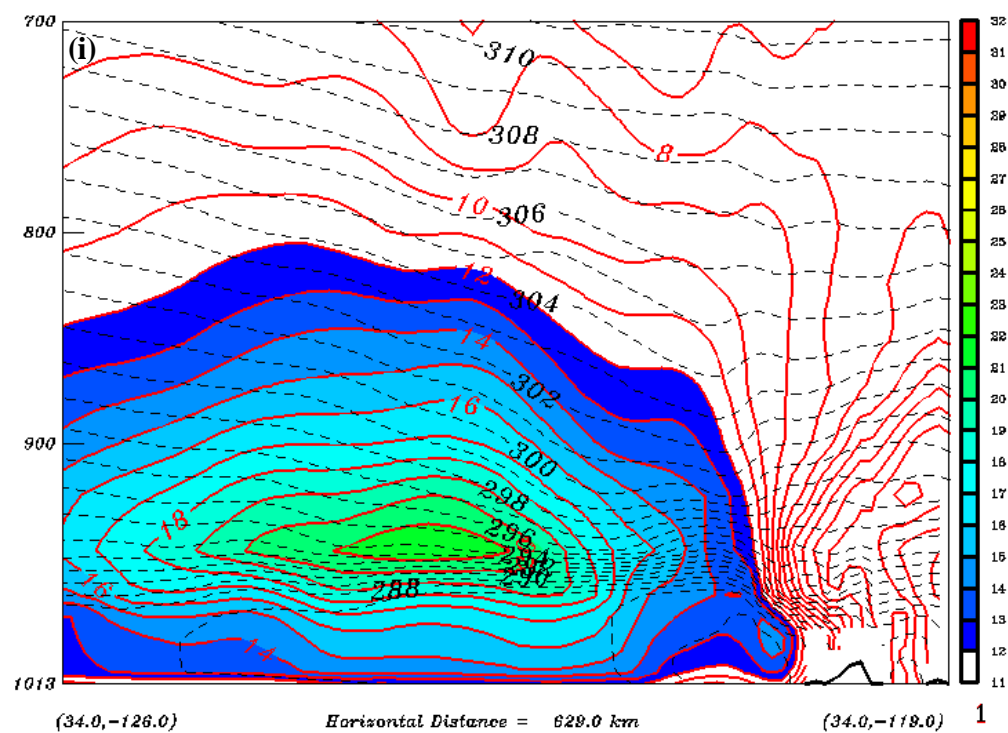


Figure 39. Continued.

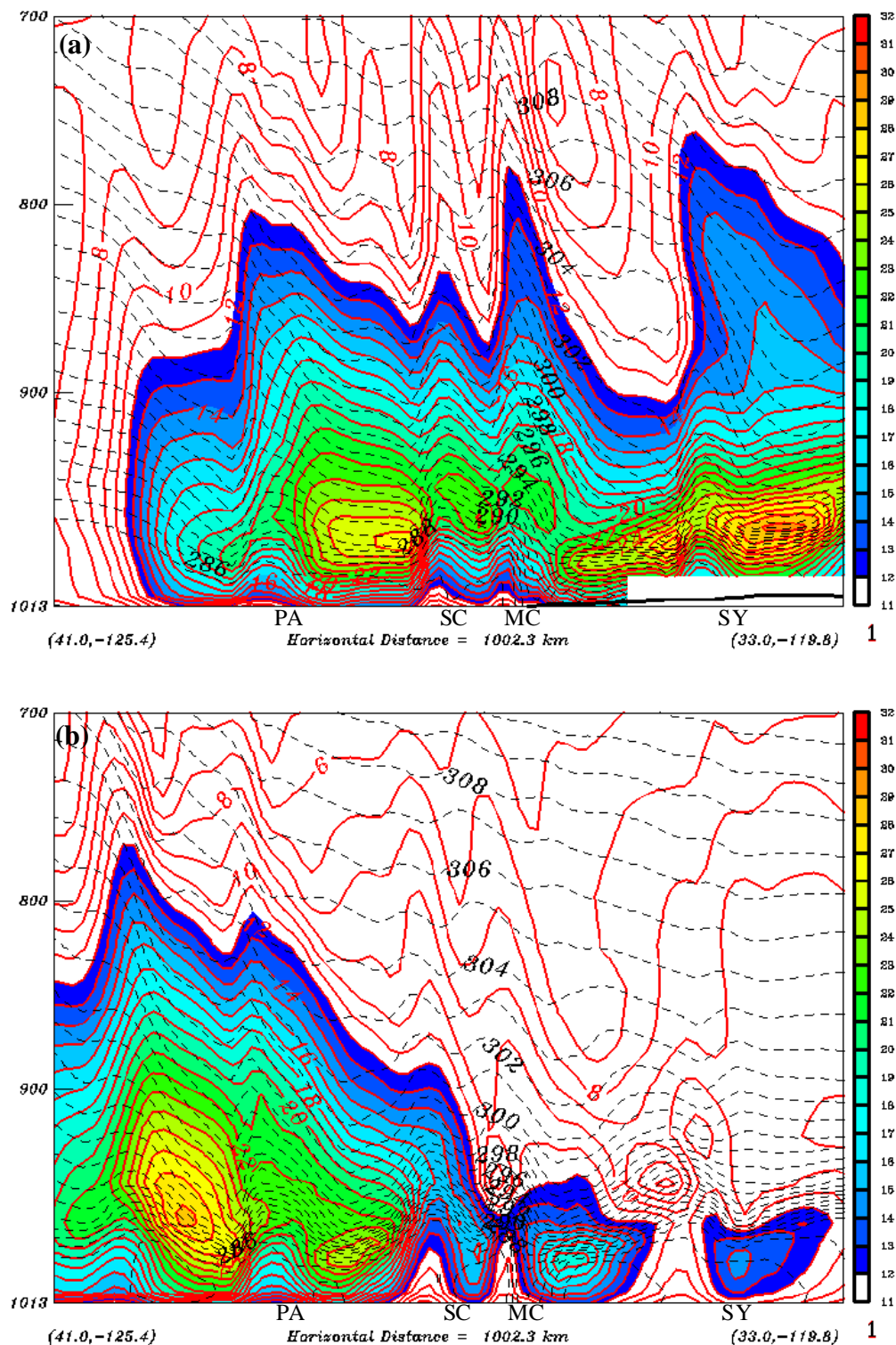


Figure 40. Near-shore along-coast cross-section (shown in Fig. 8) from COAMPS valid at 1900 PDT on (a) 9 June and (b) 14 June 1996. The plot convention is as in Figs. 38-39. Note the approximate along-coast locations of Point Arena (PA), the Santa Cruz Mountains (SC), Mount Carmel (MC), and the Santa Ynez Mountains (SY).

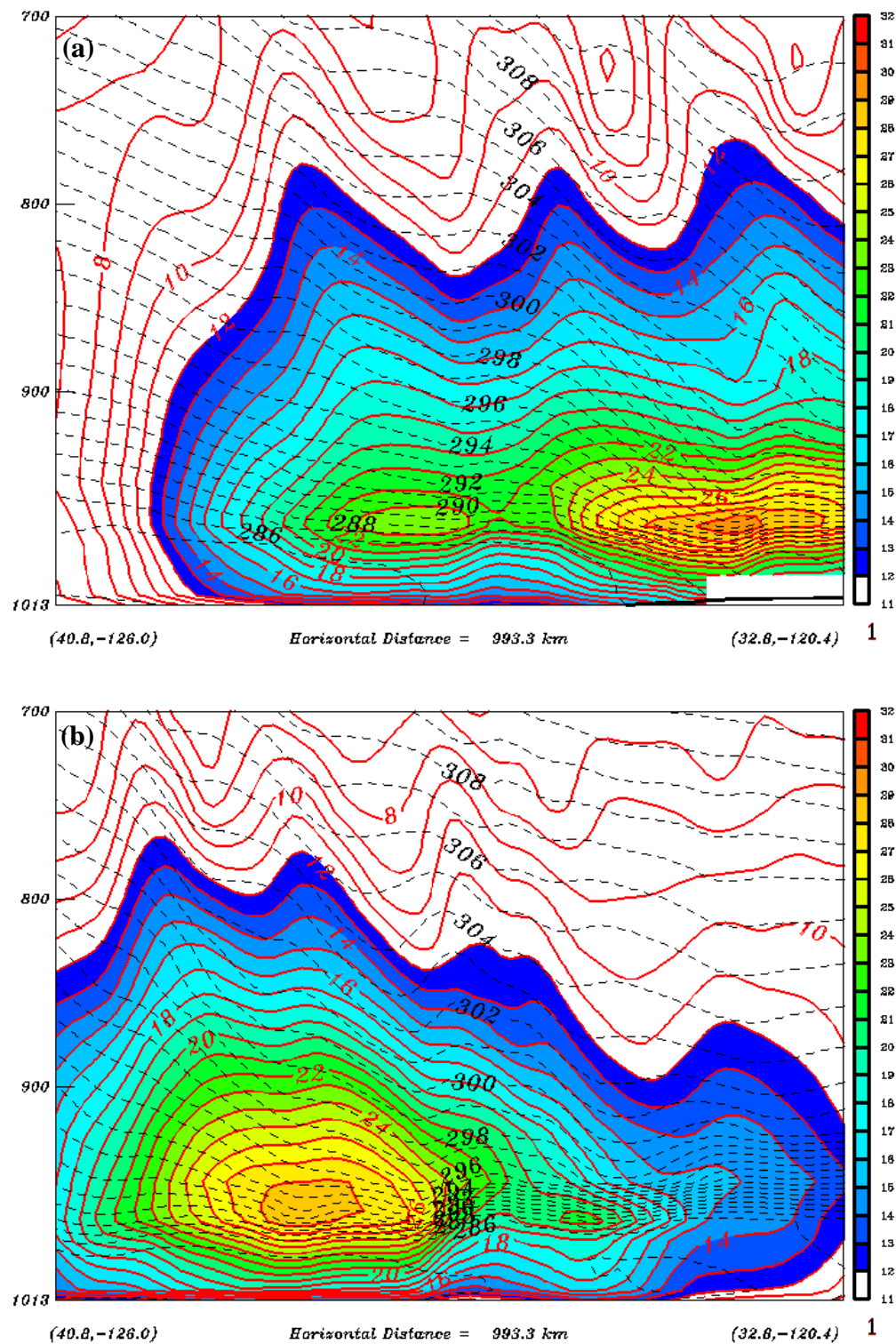


Figure 41. As in Fig. 40, except along an offshore section (parallel, but 50 km farther from shore) that is shown in Fig. 8.

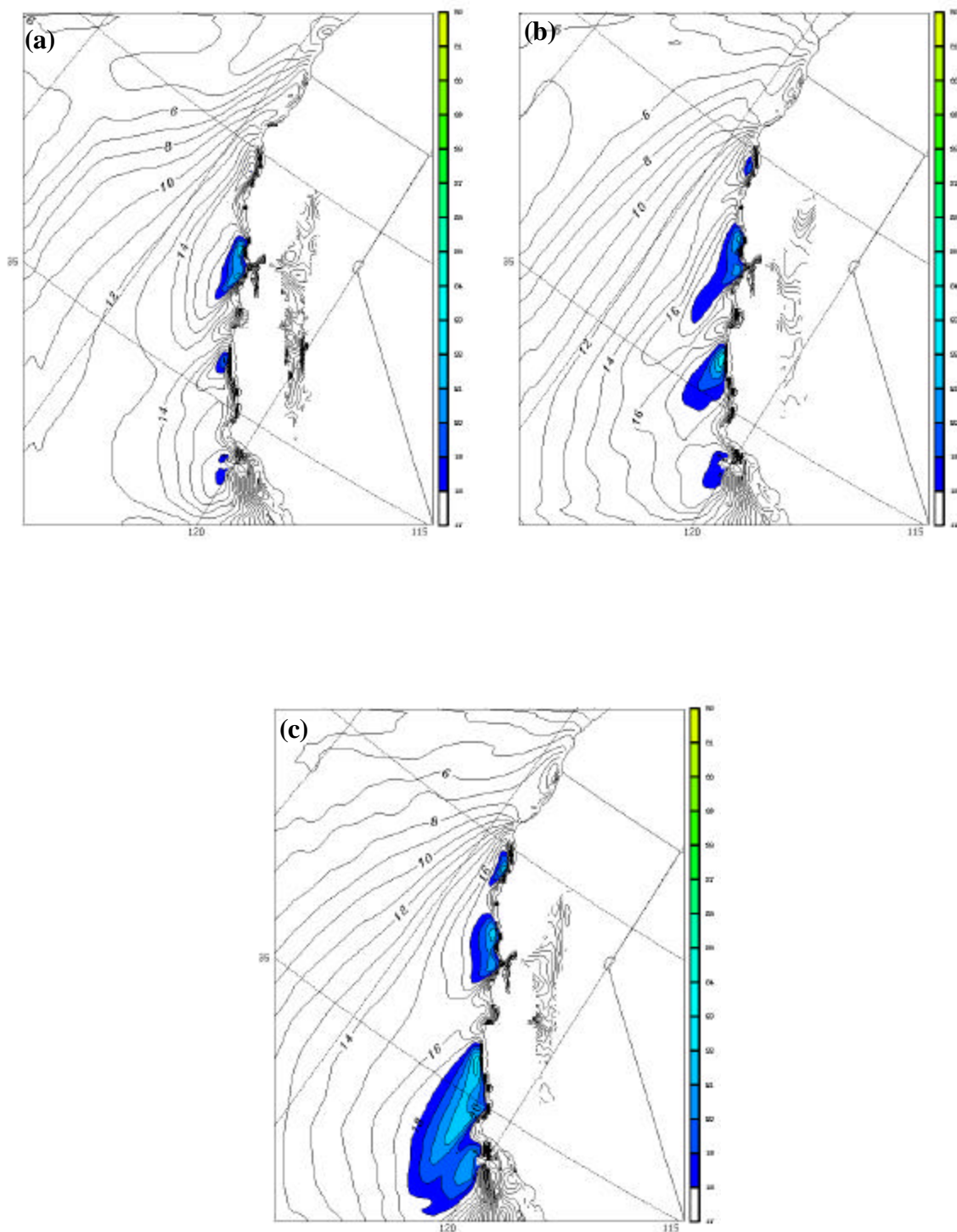


Figure 42. 1000 mb isotachs (m s^{-1} , color shading above 18 m s^{-1}) from COAMPS valid at (a) 0500, (b) 1100, and (c) 2000 PDT 9 June 1996.

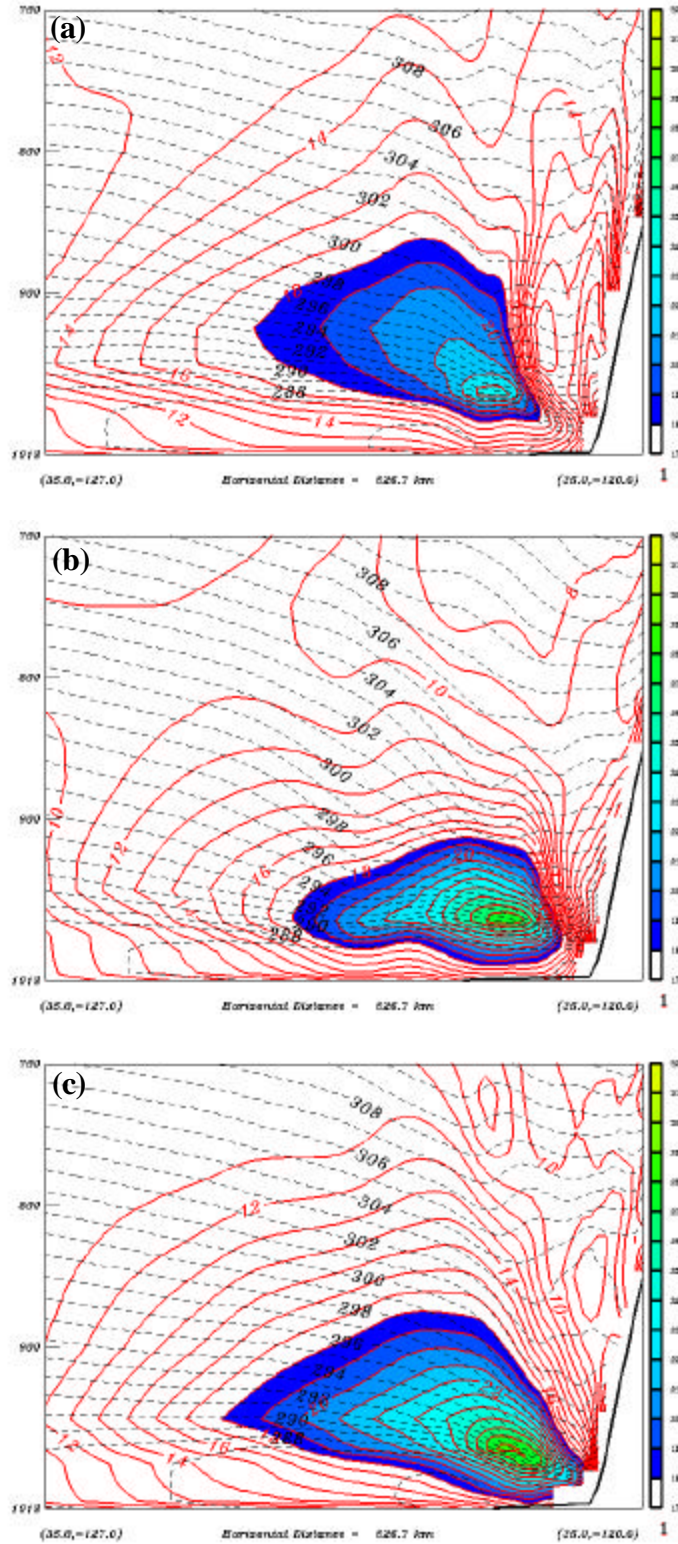


Figure 43. Cross-sections of COAMPS winds (solid, m s^{-1}) and potential temperature (dashed, K) along 35°N (as in Fig. 38h), valid at (a) 0500, (b) 1100, and (c) 2000 PDT 9 June 1996. Winds above 18 m s^{-1} are color shaded.

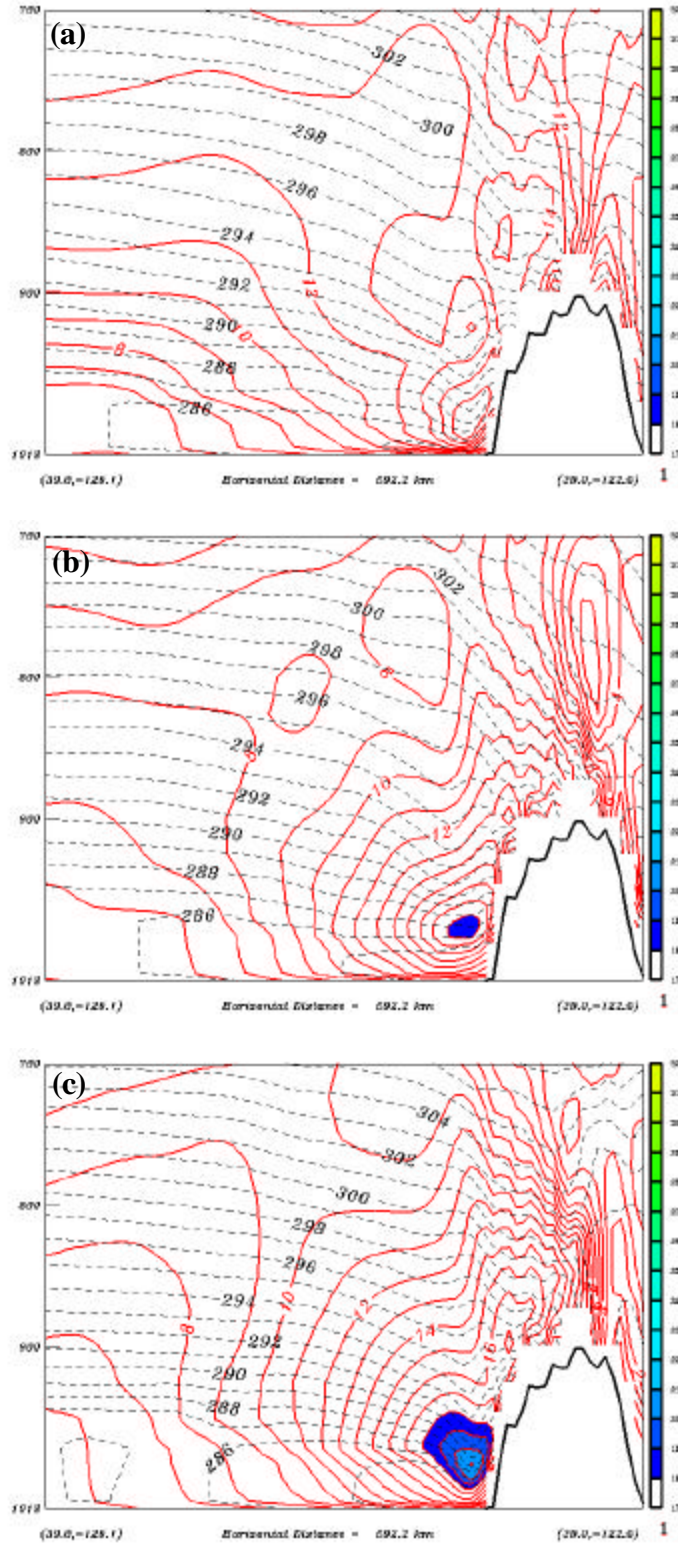


Figure 44. As in Fig. 43, except cross-section is along 39°N.

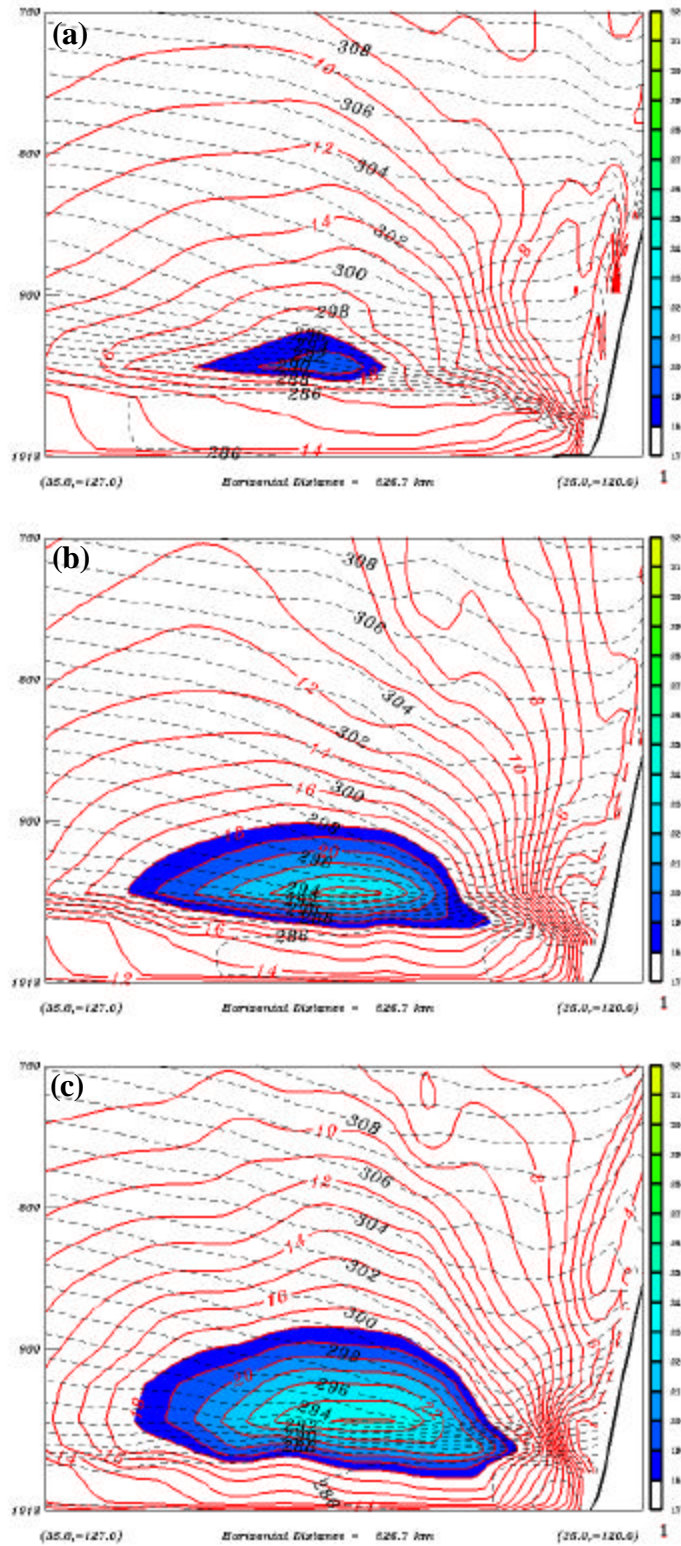


Figure 45. As in Fig. 43, except cross-sections are valid at (a) 0500, (b) 1100, and (c) 2000 PDT 14 June 1996.

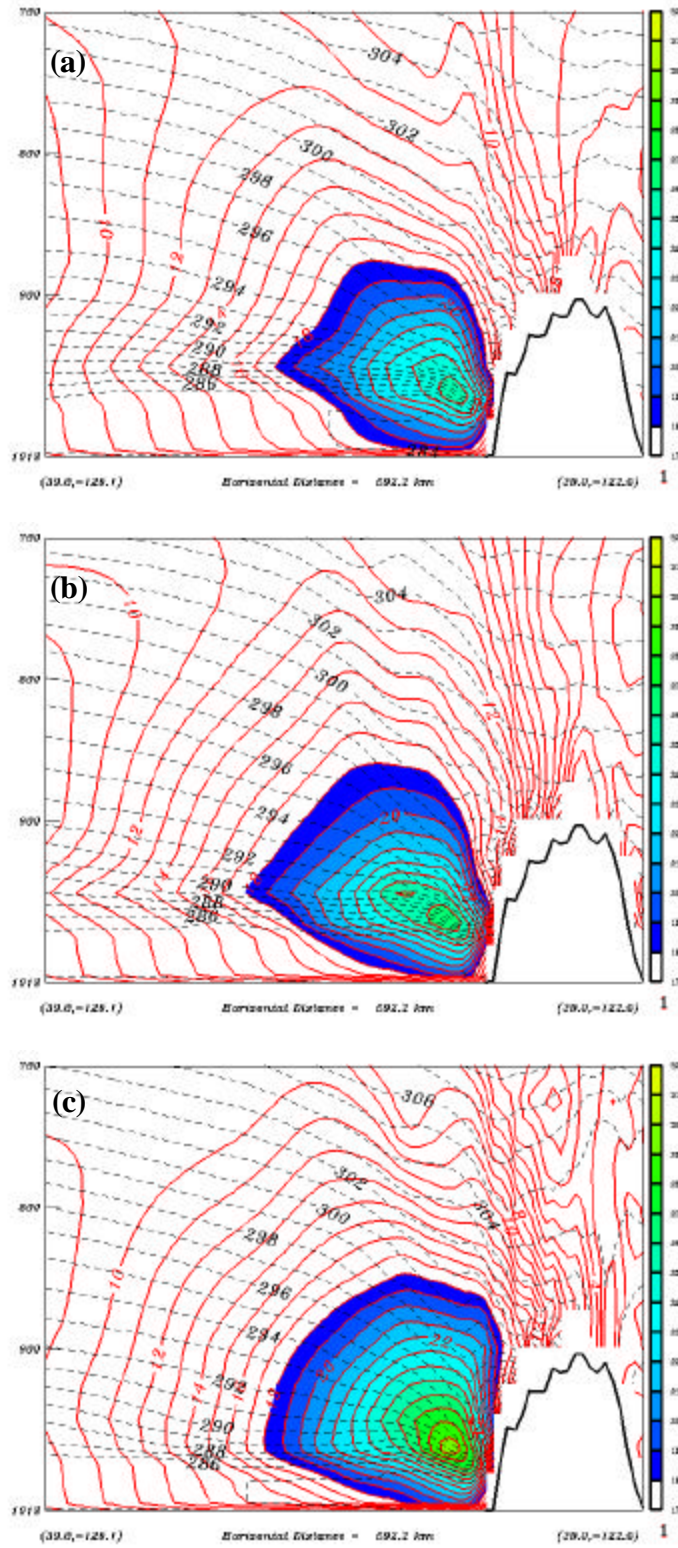


Figure 46. As in Fig. 45, except cross-sections are along 39°N.

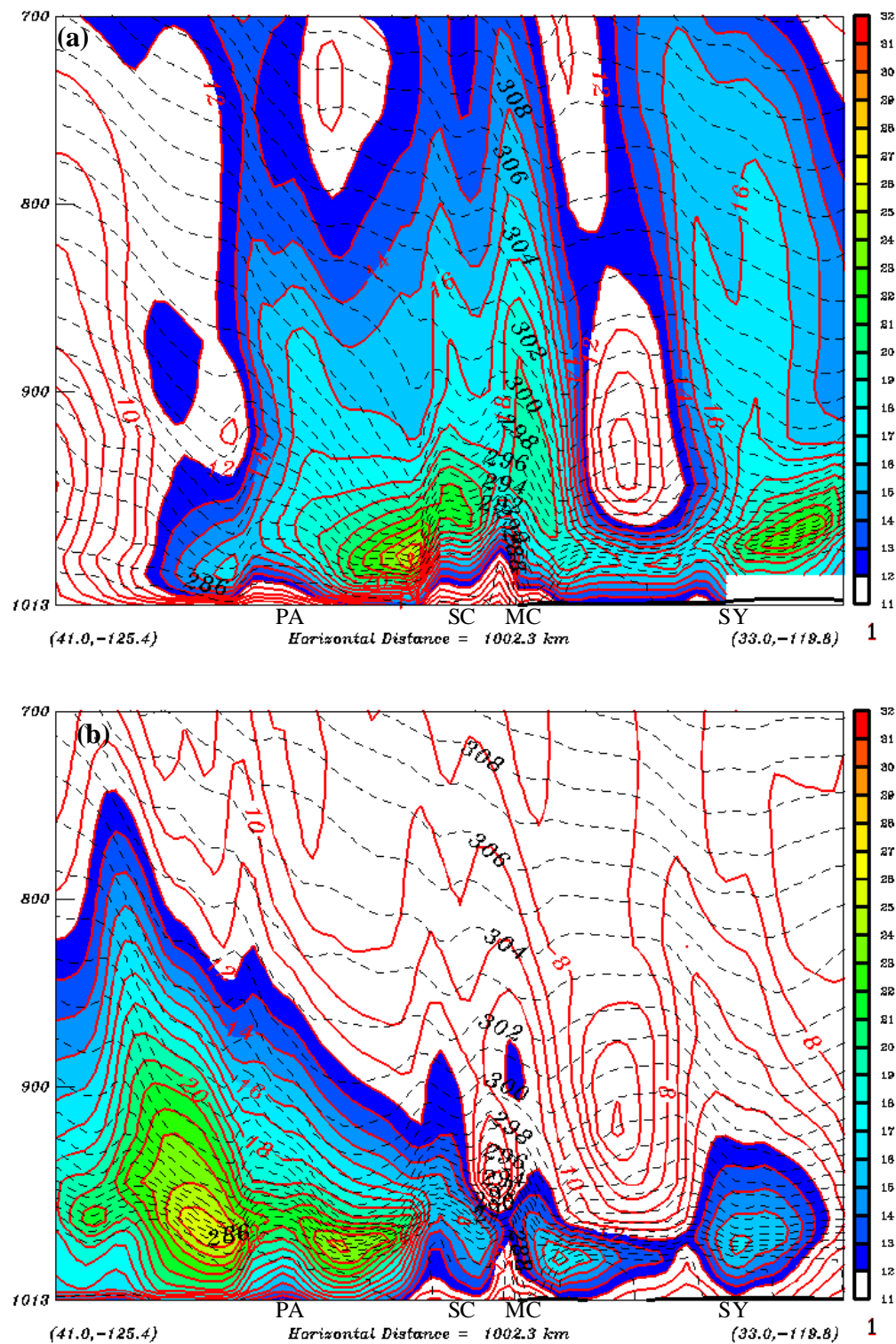


Figure 47. Along-coast cross-sections of winds (solid, m s^{-1} , shaded above 12 m s^{-1}) and potential temperatures (dashed, K) valid at 0500 PDT on (a) 9 June, and (b) 14 June 1996. Cross-sections are in the same position as those in Fig. 40.

VII. DISCUSSION

A. SUMMARY OF FINDINGS

A consistent picture of the nature of the summertime lower atmosphere along the California coast and the distribution of winds meeting the criteria for characterization as a coastal jet has emerged. The coastal jet is an extremely persistent feature of the wind pattern during a large portion of the year, and was present to varying degrees on every day of this study, which included the period from 5 June to 28 June. Its relative position along the coast is very closely tied to the 850 mb pressure pattern in that a northward or southward shift in the 850 mb ridge that extends to the northeast from the eastern North Pacific high will directly result in a corresponding shift of the position of the coastal jet winds. When the 850 mb ridge is displaced to the north, as characterized by the 14-15 June event in this study, the higher coastal winds are also displaced to the north, and vice versa. From a surface pressure perspective, this meridional displacement of the coastal jet is due to a shift in the location of the downcoast component to the pressure gradient, which is favorable for enhanced coastal jet winds. This simple relationship alone provides an excellent dynamic link between the synoptic scale and the expected location along the coast of increased winds, both near the coast and well offshore.

The vertical core of coastal jet winds is consistently within the strong temperature inversion at the top of a well-mixed marine boundary layer. As such, the vertical position varies spatially and temporally as changes occur in the topography of the marine layer. A general trend exists for lower inversion bases from offshore toward the coast, and for localized depressions in the marine layer depth downstream of major coastal topography. Due to continuity requirements, these large-scale and mesoscale depressions of the marine layer force the flow to accelerate as it enters these areas to conform to its altered boundaries, which result in increased jet wind speeds.

The jet is a significantly larger feature than is often discussed in the literature. After its inception south of where the 850 mb ridge axis crosses the coast, the jet widens to the south with an outer edge that extends farther west as the coast turns gradually to the east, which results in jet-magnitude, coast-parallel winds to over 500 km offshore in

many cases. The meridional extent of the jet can be from southern Oregon to the latitude of Baja California. The portion of the jet far from shore has little temporal or spatial variability. Close to the coast, important spatial variability occurs regularly, and in consistent locations relative to coastal topographic features. Based on the synoptic 850 mb and surface pressure patterns, the large-scale position of higher winds can be used to make a reliable mesoscale forecast when coupled with this knowledge of along-coast variability.

Six areas from southern Oregon to Point Conception have relatively high mountains very close to the coast: Sugarloaf Mountain and Chetco Peak in southern Oregon, Taylor Peak near Cape Mendocino, Cold spring and Big Mountains near Point Arena, the Santa Cruz Mountains, Mount Carmel and the Santa Lucia Range near Point Sur, and the western end of the Santa Ynez Mountains near Point Conception. Each of these mountainous areas forces a characteristic signature in the wind flow response from near the surface, through the inversion, to well above the inversion. Analyses of along-shore cross-sections very close to the coast (but still offshore) indicate that when the upstream flow encounters such a feature, it is at least partially forced up the side of the topography. This upslope flow causes a rise in isentropic surfaces over the terrain, which begins well upstream from the obstruction. Coincident with this rise is an area of weak winds below, since the combined effects of marine layer deepening and adiabatic cooling of any rising air, both within and above the marine layer, produce higher pressures near the surface, which locally weakens, or even reverses, the larger-scale pressure gradient. On the lee side of the topographic feature, the flow descends rapidly, as evidenced by a sharp descent of isentropic surfaces. This descent occurs through a deep layer that extends to heights well above both the marine layer and the topography. Beneath this descent of isentropes in the lee of the terrain is a low-level area of rapid wind acceleration, which leads to a low-level wind maximum directly beneath the area of depressed isentropic surfaces downstream of the descent. This acceleration is caused, at least in large part, by a reduction in surface pressure associated with the descent of warmer air and the associated depression of the marine layer.

As this signature is analyzed in a cross-section over water (Fig. 40) some 25 km offshore from the mountains mentioned above, there is clearly an offshore expression of

this flow response. However, this response is not limited to the near-shore region, as it can be found more subtly in along-shore cross-sections much farther offshore. This offshore extension is corroborated in a series of cross-coast sections that sample the downstream effects of these responses out to 200 km or more from the coast.

The localized reorientations of the surface pressure gradient associated with the accelerations of the wind in the lee of capes and points has been characterized in the literature as an expansion fan response to hydraulically supercritical flow encountering a bend in the coastline. This supercritical flow theory depends on marine layer and inversion characteristics and does not consider changes above the inversion. Given that there is clearly a flow response to heights much greater than the marine layer depth, it is hypothesized here that such responses at low levels are not driven purely by these expansion fan dynamics, but are indeed largely due to mountain wave effects as air above the marine layer flows over the six coastal high points mentioned.

B. IMPACT OF FLOW ABOVE THE MARINE LAYER

To examine this mountain-effect hypothesis, first consider the cross-section in Fig. 48 that is oriented roughly along the flow direction. This cross-section begins over the southern Oregon terrain, crosses over water between there and Cape Mendocino, crosses the cape close to the summit of Taylor Peak, and ends over open water farther downstream. The model representation of the terrain is visible along the bottom of these sections. In keeping with the earlier discussions, analysis in this section will focus on 9 and 14 June. Similar sections from 17 June reveal similar results to those discussed here. Shown in this and following cross-sections are potential temperatures and scalar tangent winds in the plane of the cross-sections. Since the sections are aligned with the low-level flow parallel to the coast, the scalar tangent winds very closely match the absolute winds below about 700 mb.

In Fig. 48a from the 9-10 June event, the weak jet maximum south of Cape Blanco is visible as an 8 m s^{-1} contour, but no apparent downward slope in isentropes exists on the south face of the terrain. It thus appears that in this single case, the relatively subtle jet feature may be due to adjustment to the coastal bend, although it should be noted that the Froude number of the incident flow indicates that it is subcritical. This behavior is consistent with observations by Strom et al. (1999) and Dorman et al.

(1999), which demonstrated that an expansion fan response can occur even when the flow is slightly subcritical. At Cape Mendocino, there is a slight upward slope of isentropes in the lower levels, as the relatively weak flow approaches the terrain, and a sharp descent in the isentropes on the downslope and in the lee of the mountain. Note the upstream tilt of the isentropic bend pattern with height. The isentropes reach a minimum height and then rebound slightly and level off farther downstream at a lower height relative to upstream. The region of lower potential temperature surfaces and inversion height is also the location of the low-level wind maximum.

On 14 June (Fig. 48b), the flow at this latitude is much stronger than during the 9-10 June event, which results in a pronounced drop in isentropic surfaces over both the southern Oregon terrain and Cape Mendocino. The resulting low-level maximum wind in the north is thus much stronger than on 9 June, and the upward slope of isentropes as the flow approaches Cape Mendocino is more pronounced. Following a given pressure surface (850 mb, for example) along the cross-section, it is clear that winds immediately above the terrain are higher than those upstream or downstream. This relative wind maximum exhibits an upstream tilt with height analogous to that in the potential temperature isolines. While the magnitude of the wave in the flow over Taylor Peak is clearly larger than on 9 June, the angle of the tilt on both days is essentially equivalent. Winds on the downstream slope of the terrain are again much higher than those on the upwind side at any level, which agrees with the findings of Burk and Thompson (1996) at Cape Mendocino. Finally, an area of weak low-level winds is clearly evident on the upstream side of the cape, which also has a deeper marine layer and higher surface pressures.

Similar plots over the high terrain near Point Arena are shown in Fig. 49. This section begins over land in the coastal mountains north of Point Arena, crosses close to Cold Spring Mountain, and then crosses the coast south of Point Arena. Despite the northern end of the section being fairly far from shore (about 22 km), the flow remains almost exactly in the plane of the section, which is parallel to the general coastal orientation. The southern end is offshore from San Francisco Bay. While the effects are less distinct in this cross-section, the same basic observations recur. On 9 June (Fig. 49a), the isentropes in the low levels undergo a drop in elevation as the flow approaches

the coast, and end up at a lower level downstream. Although it is more subtle than at Cape Mendocino, the descent of the isentropes on the downslope side of the terrain tilts backward with height and extends to at least 700 mb. Low-level high winds in the lee are associated with a compressed marine layer that results from this descent off the terrain. Notice the extension back over the face of the terrain of higher winds from the low-level maximum over the water. The same pattern is evident on 14 June (Fig. 49b). The magnitude of the more subtle isentropic wave is higher on 9 June than on 14 June, when the incident flow speed above the terrain was slightly weaker (14 m s^{-1} versus 16 m s^{-1}). The upstream tilt of the mountain-induced wave is less obvious on both days, but the tilt angle appears similar on the two days.

To examine the complex topographic interactions between San Francisco and Point Sur, a cross-section is drawn from just west of the Golden Gate southeastward across the Santa Cruz Mountains, through Monterey Bay and across Mount Carmel (Fig. 50). The potential temperature pattern on 9 June (Fig. 50a) is more complex than that near the isolated terrain of Cape Mendocino, with a wavelike pattern developing in response to the nearby terrain features. However, the upward isentrope displacement over the Santa Cruz terrain is followed by a downward deflection over Monterey Bay. These isentropes do not have an opportunity to descend to their upstream levels before beginning the rise toward Mount Carmel. As such, the marine layer compression and wind maximum in Monterey Bay are not as developed as they would be in the absence of the terrain farther south. Clearly visible upwind of both topographic features is the upward slope of isentropes in the low levels characteristic of impingement upon the steep terrain. The relative wind maxima above the terrain exhibit an upstream tilt, as does the wave in the isentropic surfaces. The upstream tilt in this case is greater than over the narrow terrain drop at Cape Mendocino (Fig. 48), and the wave shape in the isentropes appears to conform to the more gently varying terrain in this region. The 14 June section (Fig. 50b) has weaker inshore winds at this latitude, but still exhibits the upward low-level isentropic slope upstream of each feature and a weak response in the lee of the Santa Cruz Mountains. The wave pattern above the terrain on this day clearly has a reduced magnitude, which is associated with the lower incident flow speed.

A cross-section to illustrate the flow over the Santa Lucia Mountains to the downwind effect is difficult to draw, since the coastline does not make as significant a bend away from the direction of flow. Thus, the cross-section in Fig. 51 begins in Monterey Bay, crosses directly over the northern Santa Lucia range, and emerges over the coast farther south at an oblique angle. The upward deflection in isentropes on the upwind side of the terrain is again apparent on 9 June (Fig. 51a), as are the increased winds over the terrain relative to winds at the same level upstream and downstream. A downward slope in the isentropes is evident over the terrain, and a given isentropic surface is much lower downstream than it was upstream. The marine layer is depressed on the south end of the section, where the highest winds of the section are found. The 14 June section (Fig. 51b) does not have any significant difference in the boundary layer structure between the upwind and downwind sides of the terrain, which is consistent with the deep marine layer and weak winds that were present on that day. While there is a relatively weak jet maximum at low levels in the lee of Point Sur on the 14th, it is not depicted by this cross-section. Rather, the section emerges over the ocean inside and farther south than the wind maximum occurs.

The area sampled in the southern portion of the section lies within the band of inshore weak winds that was discussed previously. Further, the low-level wind maximum on 14 June south of Point Sur is quite localized and appears (similar to the 9 June maximum near the Oregon border) to be primarily associated with an expansion fan effect in the absence of significant flow over the terrain. If the cross-section from 9 June (Fig. 51a) were skewed such that it crossed the coast in this area at a sharper angle (not shown), it would reflect a slightly more depressed marine layer and higher winds offshore. At this time of day on the 9 June, a significant offshore component to the winds at 850 mb existed over the coast well south of Point Sur. Thus, the scalar tangent winds at that level are less representative of the actual winds. A cross-section parallel to the flow in that region (not shown) reveals a somewhat more pronounced isentropic response than that in Fig. 51a, although it does not extend as far vertically as in the cross-sections farther north.

As a final example of the flow response over the major terrain features near the coast, the cross-section in Fig. 52 begins over land, crosses the high terrain north of Santa

Barbara, and crosses the coast near the western Channel Islands. The characteristic sharp downward deflection of isentropes beginning on the lee side of the terrain at low levels and extending vertically with a backward tilt is clearly visible to a height of 700 mb in the 9 June case (Fig. 52a). Increased winds above the terrain and a pronounced relative minimum in wind speeds over the coastline (above the inversion), as lower momentum air is brought down, is particularly well developed in this case. These characteristics are also evident in the 14 June cross-section (Fig. 52b), despite the weaker incident winds and relatively subtle wave response over the terrain on that day.

The clearest wave examples in this study are in the flow over Cape Mendocino on 14 June (Fig. 48b) and Point Conception on 9 June (Fig. 52a). However, it is apparent that at all locations along the coast where significant coast-parallel winds are directed onto major terrain that is in close proximity to shore, an upstream upward isentrope deflection at low levels and increased wind speeds above the terrain occur. Above the inversion, the isentropes tend to remain fairly level approaching the terrain, and then are sharply deflected downward on the lee side, which excites a vertically propagating wave that is present in both the isentrope and wind speed patterns up to 700 mb or more. The shape of this wave appears to be closely tied to the shape of the mountain that generates it. The wave exhibits an upstream tilt with height, with an angle that varies with the shape of the terrain, but does not change as the incident flow speed is increased. A direct relationship is predicted between flow speed and the magnitude of the wave. When the incident flow approaches the terrain from over the ocean, the marine layer deepens on the upwind side, which contributes to the tendency for higher pressures and weaker winds upstream. A strong downslope flow is predicted on the lee flank of the mountain, with associated adiabatic warming and downstream shallowing of the marine layer (and thus a column with warmer air aloft). Both the deeper warm column and shallower cool marine layer contribute to lower surface pressures, which creates a low-level acceleration into the maximum wind area in the lee of the topography. This effect is evident to varying degrees in all six areas discussed in this study, which seems to confirm that expansion fan effects are not required for the creation of wind maxima downwind from coastal bends. Stated another way, no coastal bend is required for the creation of focused areas of high winds along the coast.

The offshore flow above the marine layer previously mentioned for the 9-10 June event begins about midway down the Big Sur coastline and extends beyond Point Conception. This offshore flow creates an elongated area of downslope flow, compressed marine layer, and reduced surface pressures along this part of the coast, which appears to be the cause of the very large low-level maximum on that day near the peak of the wind cycle. During the nighttime hours, this flow was weaker and more coast-parallel, and the scale of the low-level wind maximum was greatly reduced. Thus, it appears that while offshore flow is not required for the creation of a wave in isentropes and streamlines, it can alter the spatial extent of the maxima that occur in the lee of topography.

It was noted in Chapter VI that a strong tie exists between the location of the major coastal mountains and the location of the wind maxima offshore, with a consistent direction from one to the other. While the cross-sections above are aligned roughly in this same direction, and thus illustrate the flow response over and in the lee of the topography, to fully examine the relationship between flow direction above the marine layer and the spatial extent of the wind response in the lee, wind directions at 850 mb are plotted with terrain height and 1000 mb isotachs. The coast is divided into three segments for these plots, which are shown for each of the three events in Fig. 53 (north), Fig. 54 (central) and Fig. 55 (south).

The northern plots reveal an 850 mb flow on 9 June (Fig. 53a) that is weak, but roughly aligned with the coastline along the southern Oregon coast, although there is an onshore component. A weak wind maximum is present at 1000 mb, as discussed previously. This low-level maximum is adjacent to the coast immediately southwest of Chetco Peak, which is the high terrain close to the coast in southernmost Oregon. Flow over that peak is quite weak with a significant onshore component. As described in Chapter VI, this wind maximum appears to be due entirely to flow expansion related to the coastal turn to the east in that area. Farther south, the flow over Cape Mendocino is stronger and has an onshore component on the north side. However, the flow is directed across Taylor Peak with sufficient magnitude to generate the wave depicted in the Fig. 42a cross-section. The direction of the flow over the terrain is aligned with the maximum

winds in the lee, although a northern extension of that maximum again reaches to the coast immediately southwest of Taylor Peak.

A significantly different 850 mb flow pattern exists on 14 June (Fig. 53b), which is associated with the more northerly position of the ridge on that day. The flow is quite strong across Chetco Peak and has an offshore component, which leads to a downstream wind maximum whose center is again aligned along the 850 mb flow from the peak and whose spatial extent is greatly increased relative to that on 9 June. The relatively weak 1000 mb winds on the upwind side of Taylor Peak are quite evident as parcel trajectories ascend the upward sloping isentropes seen in cross-section (Fig. 48b). The flow at 850 mb is turned slightly more onshore on the north side of Cape Mendocino as it accelerates over the peak, and then turns more to the right (offshore) as it is directed over the downstream low-level wind maximum. This low-level high wind area again reaches to the north to the coastline southwest of the peak.

Finally, the flow on 18 June (Fig. 53c) over the southern Oregon terrain is directly onshore and no coastal jet structure exists in that region on that day. The flow over Cape Mendocino is weaker and more onshore (similar to the 9-10 June event), and a weaker downstream wind maximum is predicted, although its position is consistent with that on 9 June and 14 June.

The northern extensions of each downstream maximum, which reach to the coast in each simulation just to the southwest of the significant terrain (particularly evident on the south side of Cape Mendocino), are very consistent features. While the offshore and downstream extent of the low-level wind maxima vary considerably from day to day and within the diurnal cycle, these inception points do not, despite changes in the flow above the marine layer. Therefore, it could be concluded that these inception locations are tied more directly to the expansion of the low-level flow brought about by the coastal turn than to the wave in the flow above. Another interpretation is that these northern inception locations at the coast exist at the location where the flow down the lee slope of the mountain encounters the coastline at the trough of the wave, which occurs in the same location. This relationship again emphasizes the assumption that both the expansion fan effect and the mountain wave phenomenon are active in determining the spatial extent of

accelerated downstream winds, except in the case of very weak flow over the topography, when only expansion effects are important.

The flow in Fig. 54 from Cape Mendocino, over Point Arena, and into the lee maximum near Point Reyes is remarkably similar on each of the three days. The absolute low-level wind maximum in the lee of Cape Mendocino is in the same location during each event, although on the strongest day (14 June-Fig. 54b) the flow off Taylor Peak is particularly strong and oriented with more of an offshore component than on 9 June (Fig. 54a) or 17 June (Fig. 54c). The nearly coast-parallel winds south of the peak on 17 June are associated with the weakest wind maximum of the three days. While not shown in the Cape Mendocino cross-sections of Fig. 48, it is important to note that despite this lack of flow from mountaintop out over open water, a similar wave in the flow over Cape Mendocino occurred on 17 June as on the other days, although with reduced magnitude. The low-level trough of that wave is associated with the lee maximum in the same location as 9 June (Fig. 54a) and 14 June (Fig. 54c), again augmented by expansion fan effects to the north.

The 850 mb flow over Point Arena exhibits a similar direction and magnitude during all three events, with its direction oriented toward a wind maximum at low-levels on the north side of Point Reyes. The flow into that maximum is slightly more offshore on 14 June (Fig. 54b) than during the other two events. On 9 June (Fig. 54a) and 17 June (Fig. 54c), this maximum extends to the south in a second lobe of high winds near the entrance to San Francisco Bay. This maximum is a response to the low-level divergence present on those days in association with a strong sea-breeze flow through the Golden Gate. The cooler conditions and deeper marine layer on 14 June resulted in a much reduced sea breeze flow on that day (as evidenced in COAMPSTM by decreased low-level divergence near the mouth of the Bay), which kept the offshore wind maximum limited to its northern location, associated only with flow response to the terrain near Point Arena. At the southern end of Figs. 54a-c, the relative low-level minimum on the upwind side of the Santa Cruz Mountains is most pronounced on 14 June (Fig. 54b). This is apparently because the isentropes can rise and the marine layer deepen on that day more effectively (and more similarly to other locations) due to the reduced subsidence in the presence of the decreased sea-breeze circulation. The nature of the wind maximum south

of Point Arena, and downstream minimum, is strongly influenced by the character of the San Francisco Bay sea breeze. Finally, the stronger flow over Cape Mendocino on 14 June (Fig. 53b) also produces a jet maximum that reaches farther offshore and downstream than on the other two days, in response to a more pronounced wave over the terrain, such that the low-level maximum is evident in Fig. 54b. While this is true in the 1000 mb isotachs, it becomes more apparent slightly higher, where the offshore extensions of these lee maxima typically have their core.

The southern set of plots (Fig. 55) is particularly illustrative of the nature of the lee wind maxima at low levels relative to the flow at 850 mb. The flow above the marine layer approaches the Monterey Peninsula and the high terrain near Point Sur from a consistent northwesterly direction during each of the three events, although it is weakest on 14 June (Fig. 55b). The weaker incident flow on that day produces a weaker low-level wind maximum that is quite localized to the south of Point Sur. Given the very weak wave response over the terrain on that day, this maximum again appears to be primarily an expansion fan effect. Its offshore and downstream extent are quite limited by the weak flow over the terrain near Mount Carmel in the north and along the length of the coast to Point Conception. In contrast, the flow over the terrain is much stronger on 9 June (Fig. 55a) and 17 June (Fig. 55c), and makes a pronounced offshore turn south of the highest terrain in the northern Santa Lucia Range. The resulting low-level wind maxima have considerable offshore and southern extent. In particular, they have an elongated coast-parallel inner edge induced by the offshore flow over the entire southern Santa Lucias, which causes an elongated compression of the marine layer along that portion of the coast. The stronger flow over the Santa Ynez Mountains on 9 June and 17 June produces an additional lee maximum that merges with the Santa Lucia maximum south of the plot.

C. COMPARISON WITH MOUNTAIN WAVE THEORY

The isentropic pattern over each of these topographic interactions is quite consistent with basic mountain wave theory, as outlined in Durran (1986). An important quantity in determining the behavior of these waves is the Scorer parameter L^2 , given by

$$L^2 = N^2/N^2 - (1/N)d^2V/dz^2,$$

where N is the Brunt-Vaisala frequency and V is the speed of the mean flow. Durran and others have shown that as the flow moves over the terrain, either evanescent waves, which damp with height and are stacked vertically above the terrain (Fig. 56a), or vertically propagating waves, which tilt with height and do not damp (Fig. 56b), will result, depending on the product of the mountain half width a and the square root of the Scorer parameter. If this product aL is much less than 1, evanescent waves result. If it is much greater than 1, we expect vertically propagating waves. Burk and Thompson (1996) show aL to be much greater than unity in the case of flow over Cape Mendocino, which suggests the vertically propagating wave is the correct solution in this case. Given the relatively small half width of Taylor Peak, as compared to the other topographic features mentioned in this study, we would expect this solution to also be valid over each of the coastal mountains discussed. There are two mathematically possible solutions for these vertically propagating waves. The first of these calls for downstream wave tilt with height. This seems counterintuitive, given that the mountain exerts a force on the atmosphere in the opposite direction from the flow. The conclusion is that the only physical solution for the vertically propagating wave is the one that describes an upstream tilt with height.

Comparing the flow over the mountains in this study (Figs. 48-52) with the idealized flow over a sinusoidal series of mountains shown in Fig. 56b, the similarities are obvious. The waves tilt back with height, which results in compression of the flow down the lee side (as best seen at Cape Mendocino). Further, Durran (1986) computes a Fourier series representation of an isolated mountain ridge, which is somewhat closer to the type of topographic interaction discussed in this study. The idealized flow over such a ridge is shown in Fig. 56c, again for the case of a mathematically wide ridge, which applies in each of the cases discussed here. This idealized profile has an evolution of the waveform with height that results in the shape of the mountain being reflected in the shape of the wave aloft at intervals of $2\pi/L$, where L is again the square root of the Scorer parameter. This idealized flow pattern is also similar to that observed in that low-level strong flow is predicted on the lee side and weak flow on the upwind side of the terrain and the character of the wave evolves with increasing height. In addition, only one

waveform is produced by the mountain instead of a series of mountain waves downstream. Whereas the theoretical solutions are in terms of streamlines in the flow above the mountain, the cross-sections in this study show the flow in terms of potential temperature isolines. Given the adiabatic nature of the flow, an examination of streamlines from COAMPSTM in this study reveals that the flow very closely follows the isentropes.

Both theoretical examples show waves that do not decay with height, whereas the waves in this study do exhibit such a decay, which begins at approximately the 700 mb level. This difference is considered to be a result of the assumption of constant stability and vertical wind shear with height in the idealized solutions. Since the nature of the wave response is dependent on the product of the square root of the Scorer parameter and the mountain scale, this decay with height above 700 mb is examined relative to vertical changes in N and V . Cross-sections of Brunt-Vaisala frequency (not shown) reveal that stability is quite high in the inversion, decreases sharply above, and then remains relatively constant with height to the tropopause. No significant changes with height are evident above about 900 mb. Thus, the vertical variations in static stability do not seem to be related to the wave decay. On the other hand, the winds are closely aligned with the coastal orientation (and with each cross-section above) to a level of about 700 mb, and then directional shear begins with the winds backing with height. The 700 mb level is also consistently the level at which a relative vertical wind minimum occurs in all cases. Thus, at about the level at which the vertically propagating waves in the model decay, the winds begin to increase with height and have a direction different from the lower flow that excited the wave. These changes in wind speed, and in directional and speed shear, alter the Scorer parameter, which in turn changes the expected character of the wave response. The altered flow regime aloft effectively damps the mountain wave generated over the topography from reaching heights above about 700 mb. Despite this deviation from the two-dimensional idealized mountain wave, it is clear that vertically propagating, upstream tilting waves induced by flow over topography are present along the California coast during this study. Note that the wave magnitudes are directly proportional to the incident flow speeds. These waves contribute to weaker winds upstream and serve to

accentuate the flow down the lee side of the topography with stronger winds downstream due to alterations of the low-level pressure gradient below the wave.

This description of mountain waves has thus far been two-dimensional. To extend that to the three-dimensional atmosphere, it is necessary to consider the flow response away from the mountain. While there is undoubtedly a perturbation to the east over land, this is considered to be a complex interaction with varied topography and was not the focus of this study. The offshore extension of the response is expected to be a similar wave that in addition to its vertical decay, also decays with distance offshore from the topography. This is evident in COAMPSTM in that the elevated isentropes indicative of each wave, which are seen in both the along-coast and cross-coast cross-sections presented previously, have relatively large amplitudes near the topographic generation point and decay offshore as they extend southward at an angle to the coast. Similarly, the regions of depressed isentropes between these ridges, which are associated with higher coastal jet winds, extend offshore at the same angle. The effect of the disturbance in the flow should be felt by atmospheric parcels to a distance of one Rossby radius of deformation, which is $O(100 \text{ km})$ in this area. Since the incident flow is supercritical, the adjustment occurs only downstream, at a characteristic angle away from the mountain. In another departure from the idealized mountain wave theory, the atmosphere in the boundary layer on the downstream side of the wave is experiencing increased divergence due to both the expansion and wave effects. This divergence effectively removes the restoring force that would otherwise cause the inversion to quickly rebound to its upstream height. Subsidence on the flank of the eastern North Pacific high holds the inversion down at the new level on the downstream side of the mountain. This lack of a rapid return of a given streamline to its upstream height accounts for the large down-coast extensions of the low-level wind maxima. Downstream extent of these maxima appears to be controlled by only a gradual upward slope in isentropic surfaces or by the flow encountering the next coastal mountain.

It is important to note that offshore flow above the marine layer, which occasionally does occur, is not required to excite these mountain waves that will have an impact on the low-level pressure pattern offshore as described. While flow of sufficient magnitude over the topography is required, the direction of that flow need only be

roughly aligned with the coast to produce waves in the flow that extend over the coastal MBL and alter the low-level winds. Since the flow direction is nearly always along-coast during this time of year, these favorable conditions for mountain wave-induced localized wind maxima and minima are generally present. Subtle changes in the wind direction above the marine layer serve only to alter the angle and offshore extension of the weak and strong wind areas.

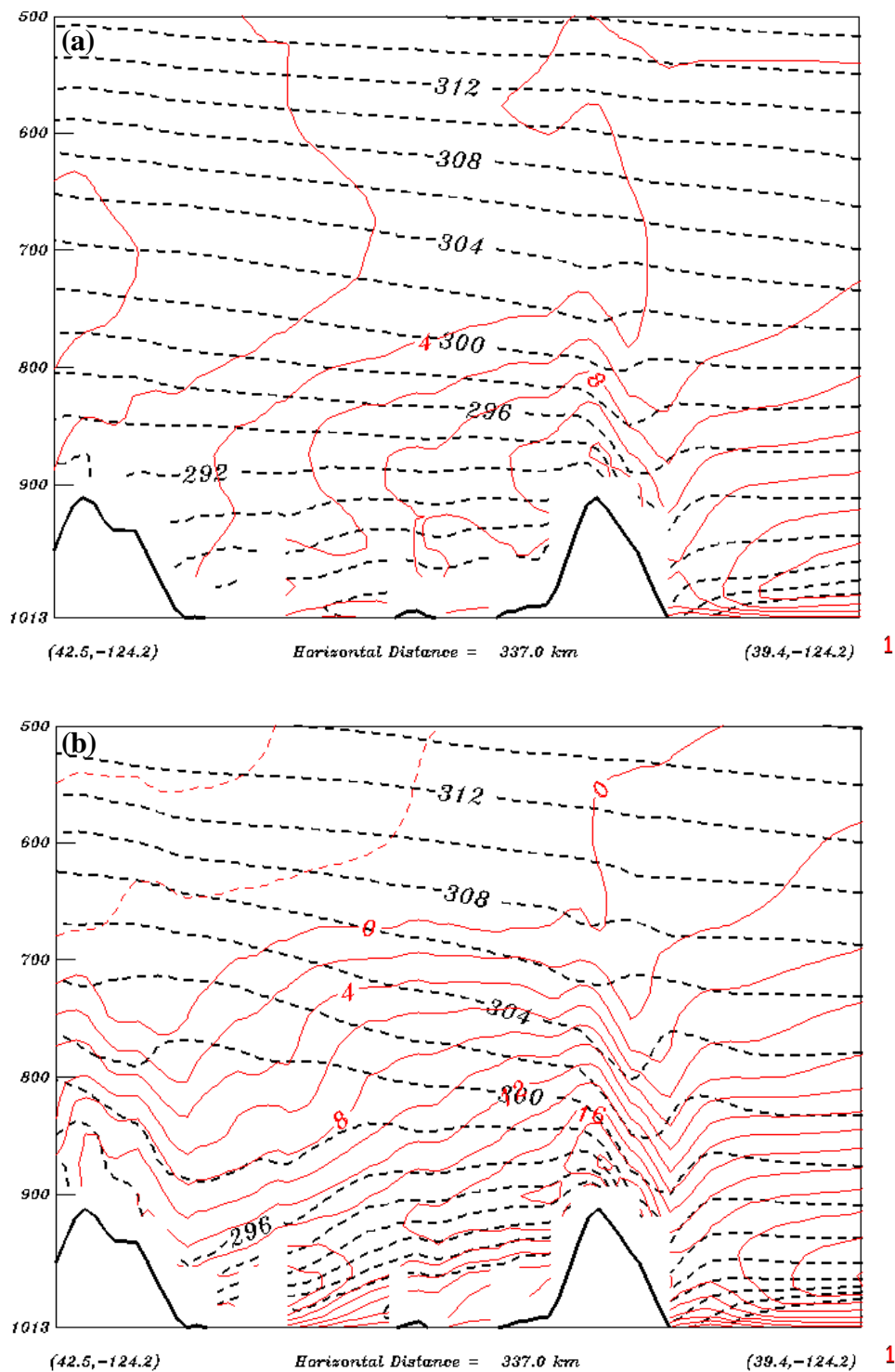


Figure 48. Along-coast cross-sections of scalar tangent winds (solid, m s^{-1} , 2 m s^{-1} contour interval) and potential temperatures (dashed, K, 2K contour interval) from COAMPS beginning over land in southern Oregon, crossing over water off northern California, and crossing Cape Mendocino near Taylor Peak. Sections are valid at 1900 PDT on (a) 9 and (b) 14 June 1996.

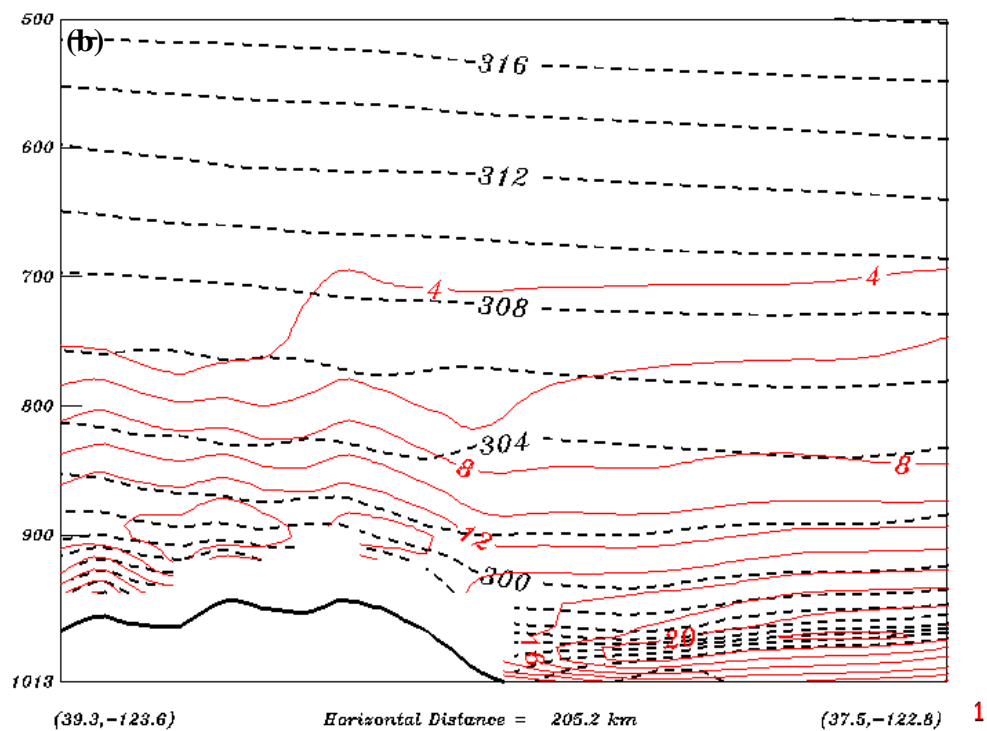
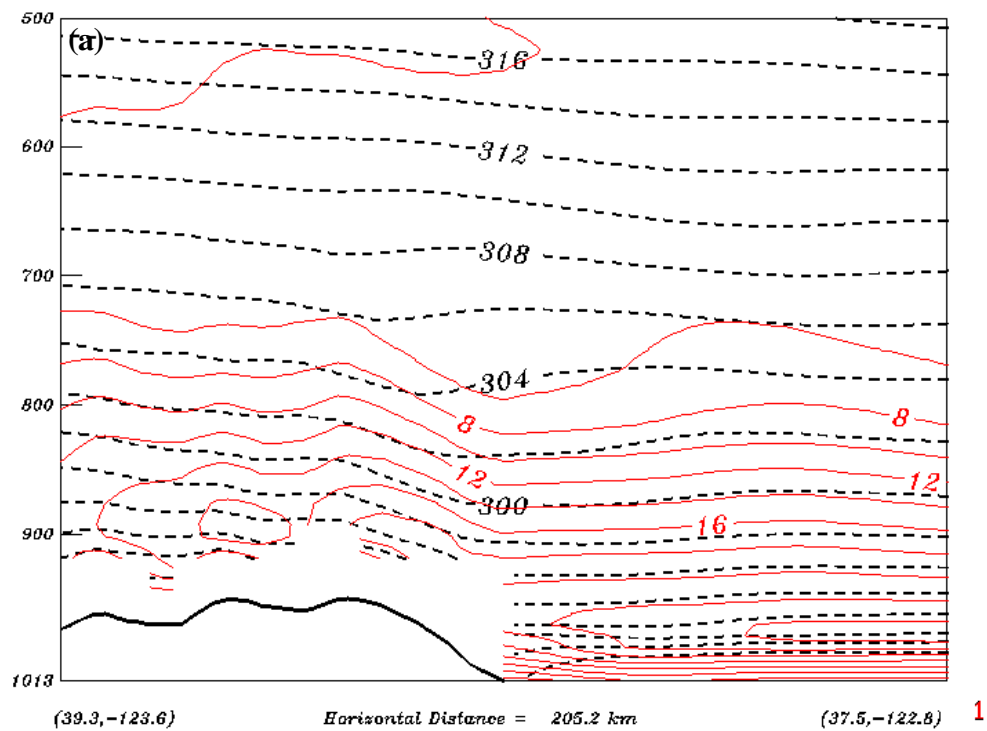


Figure 49. As in Fig. 48, except cross-section begins over land near Point Arena, crosses near Cold Spring Mountain, and ends over water to the south of the point.

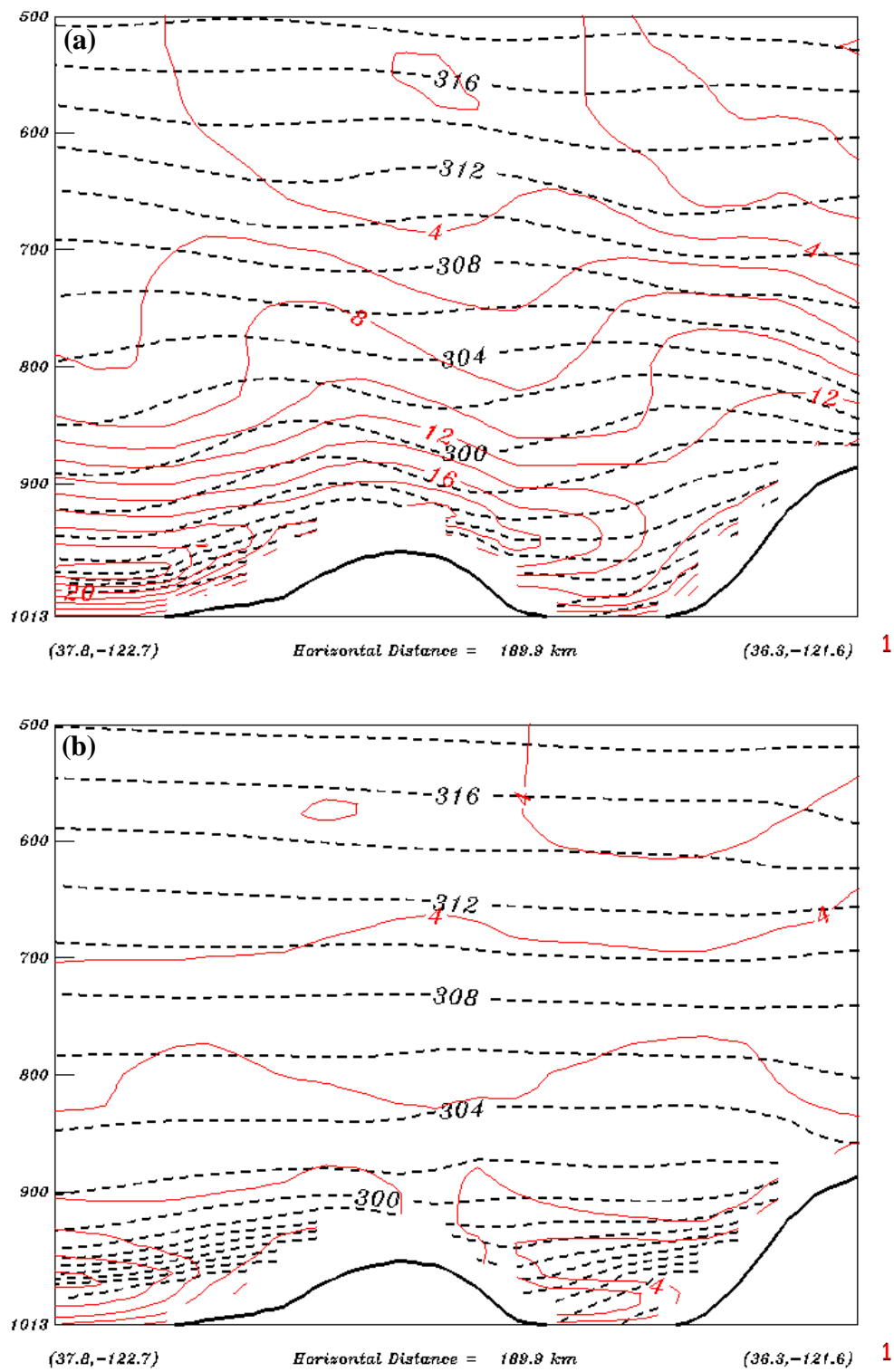


Figure 50. As in Fig. 48, except cross-section crosses over the Santa Cruz Range, Monterey Bay, and Mount Carmel in the northern Santa Lucia Mountains.

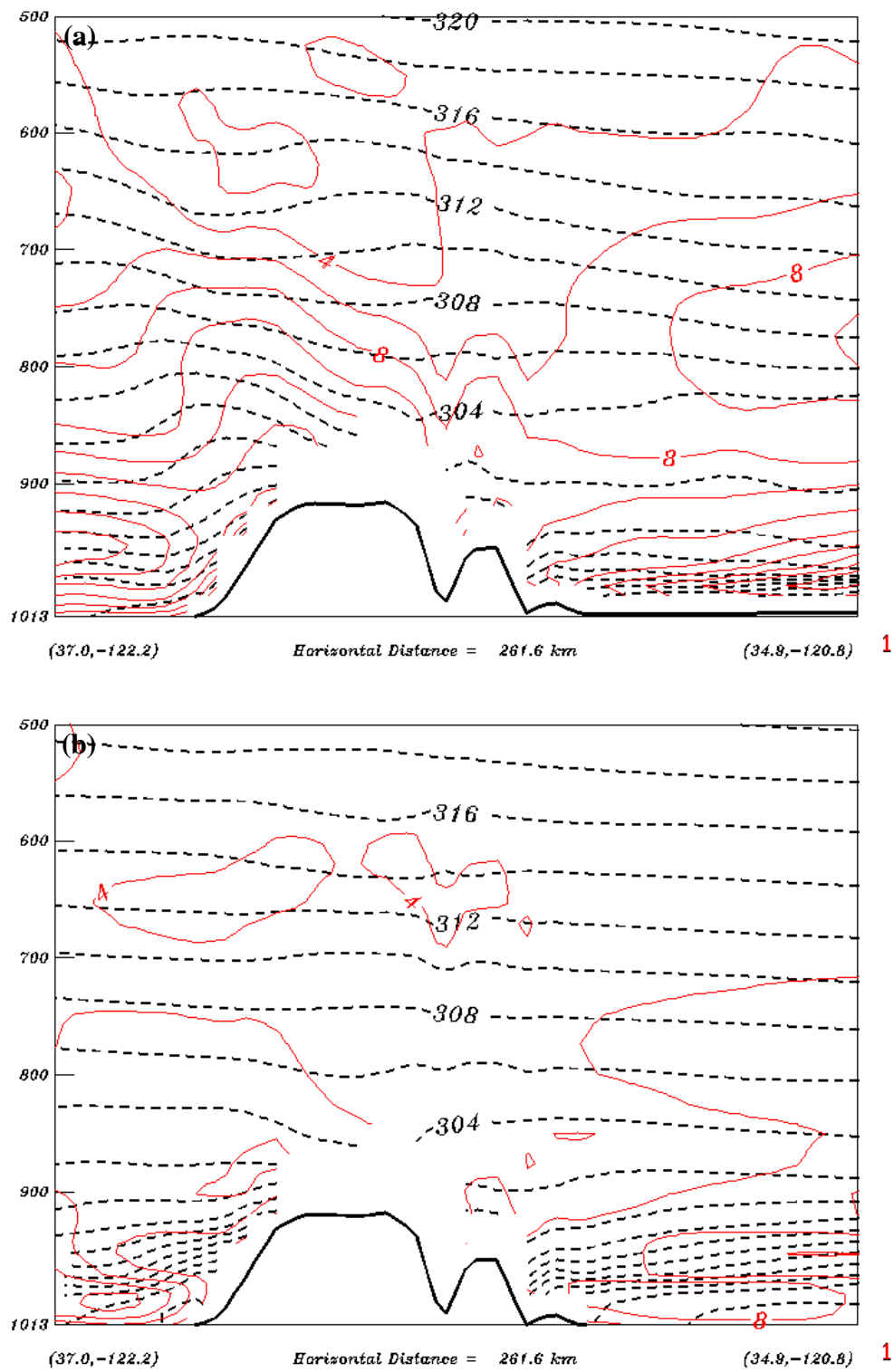


Figure 51. As in Fig. 48, except cross-section begins over Monterey Bay, crosses the northern Santa Lucia Range, and crosses the coast at an oblique angle along the Big Sur coast.

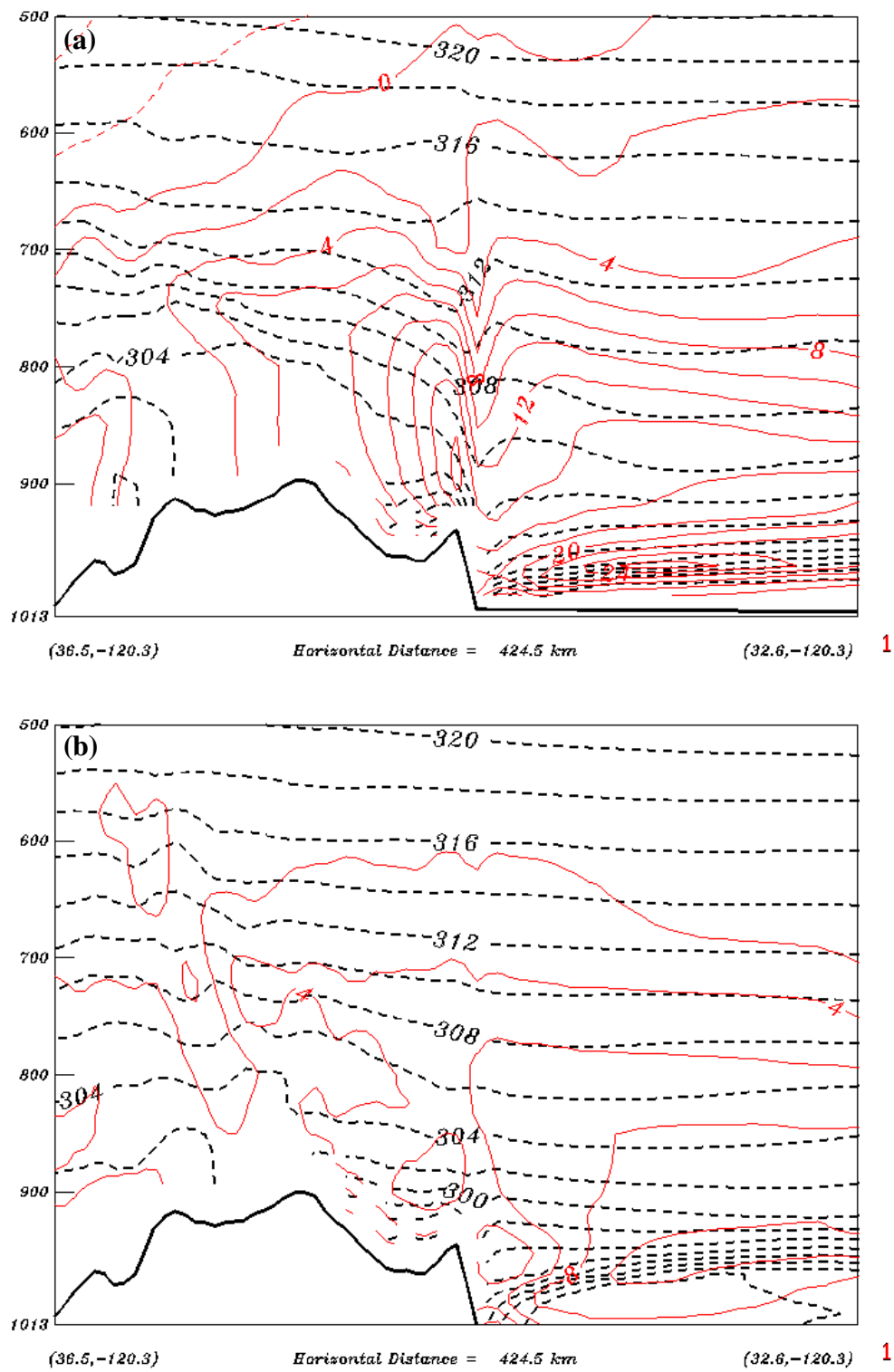


Figure 52. As in Fig. 48, except cross-section begins over the mountains northeast of Point Conception and emerges over water east of the point.

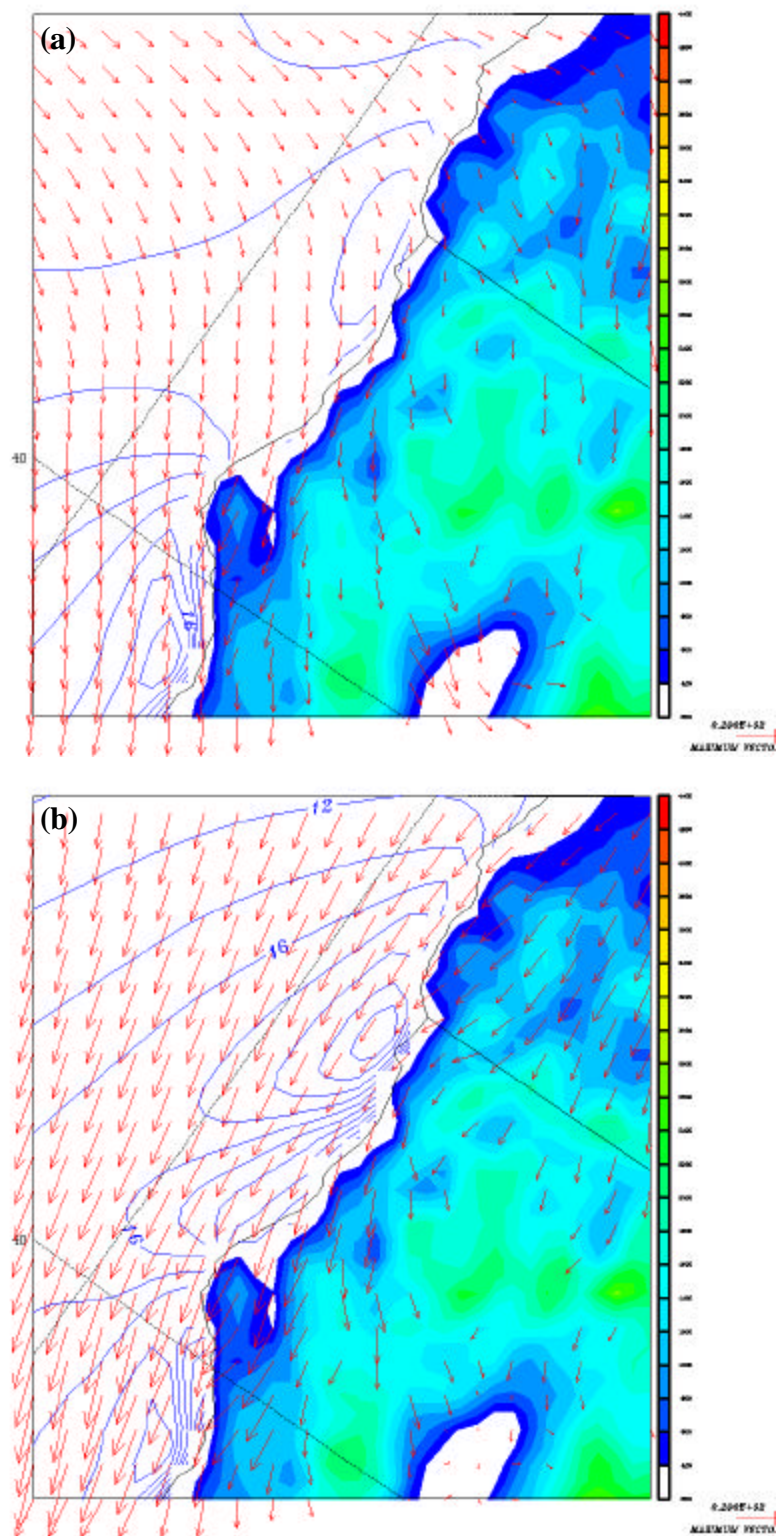


Figure 53. 850 mb wind (arrows, length proportional to speed) and 1000 mb isotachs (2 m s^{-1} contour interval) from COAMPS for the northern portion of the coast from southern Oregon to northern California, valid at 1900 PDT on (a) 9, (b) 14, and (c) 17 June 1996. Note 10 m s^{-1} scale arrow. Terrain is shaded at a 200-m contour interval above 400 m.

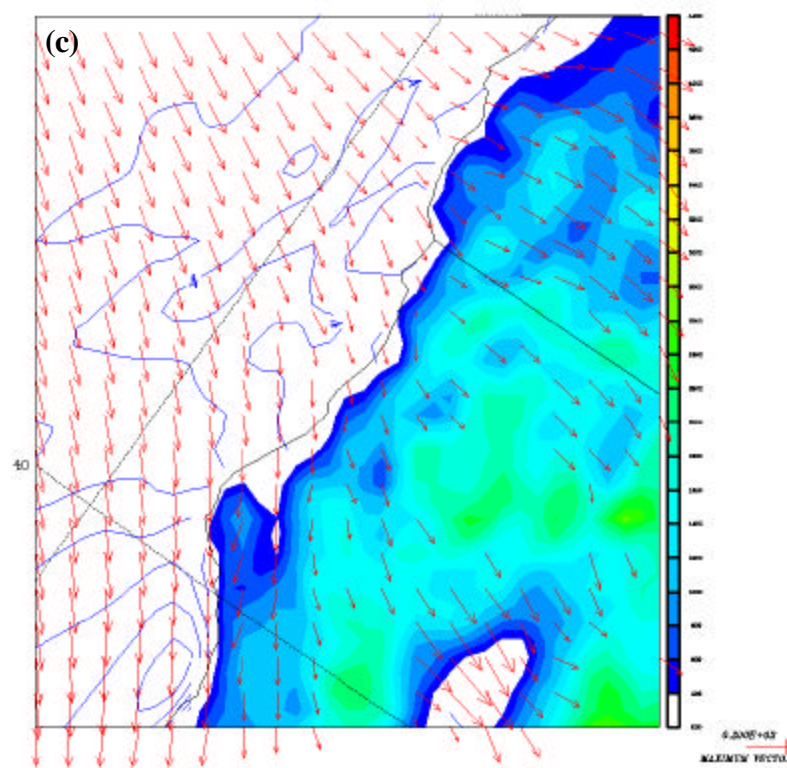


Figure 53. Continued.

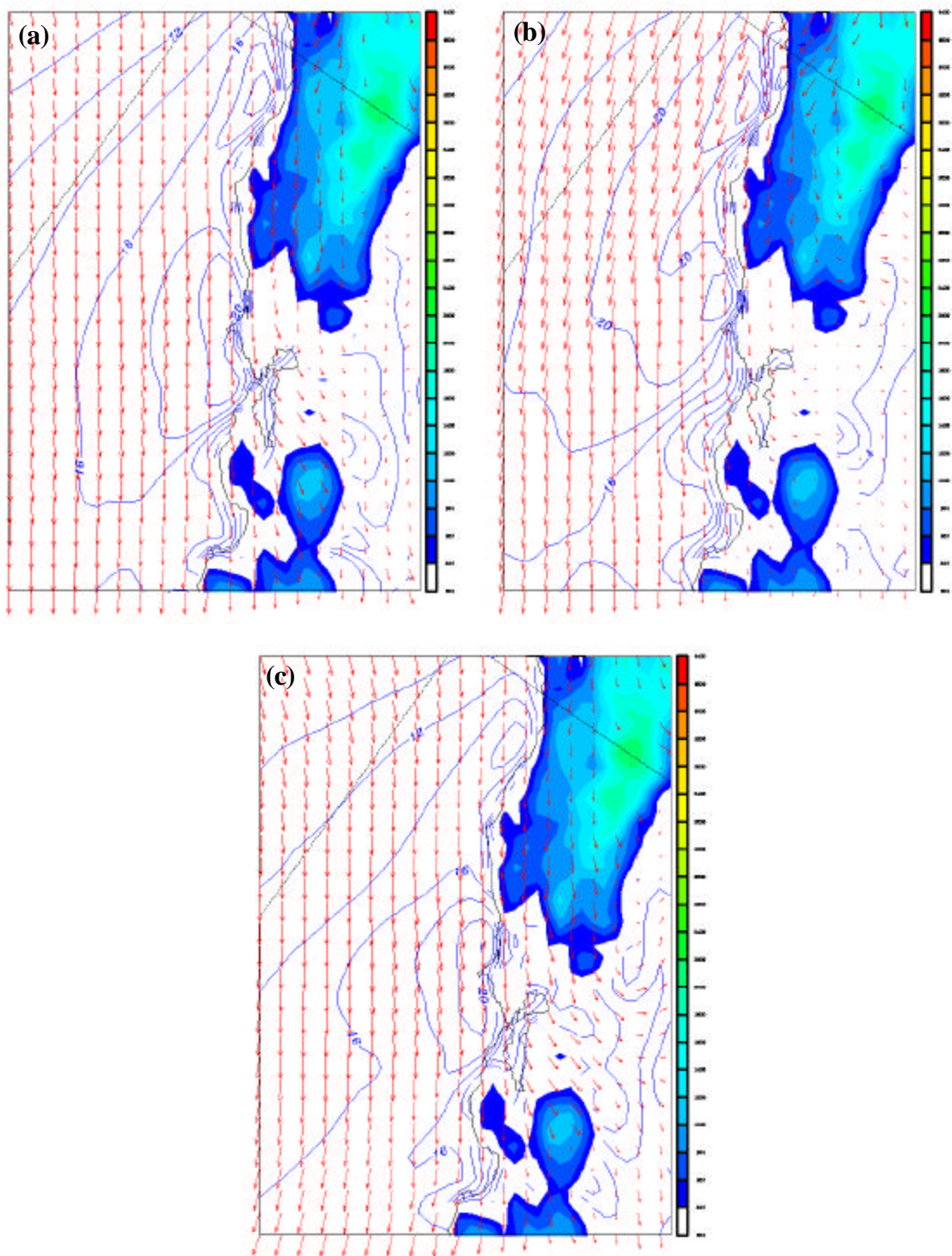


Figure 54. As in Fig. 53, except for the central portion of the coast.

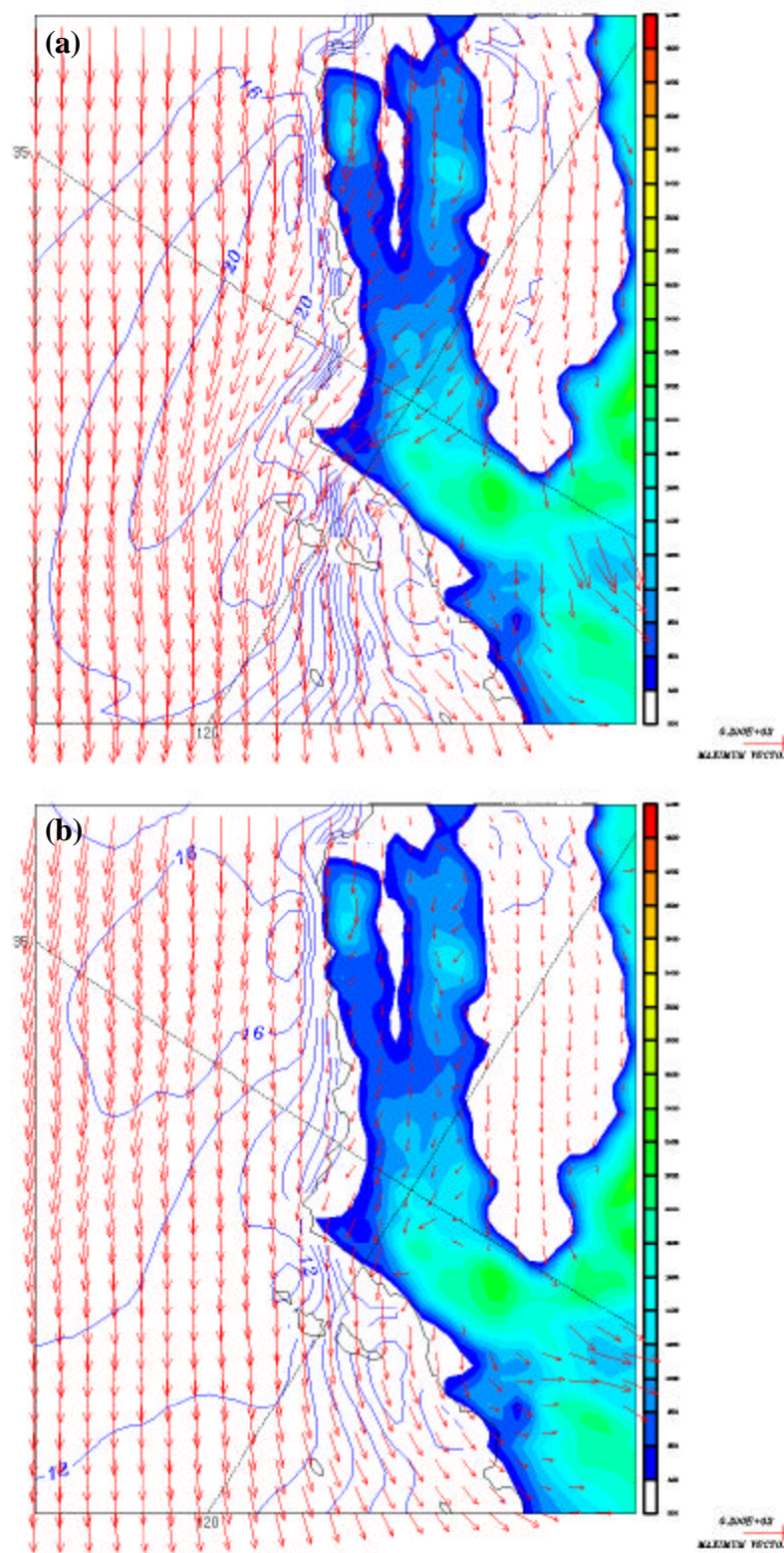


Figure 55. As in Fig. 53, except for the southern portion of the coast.

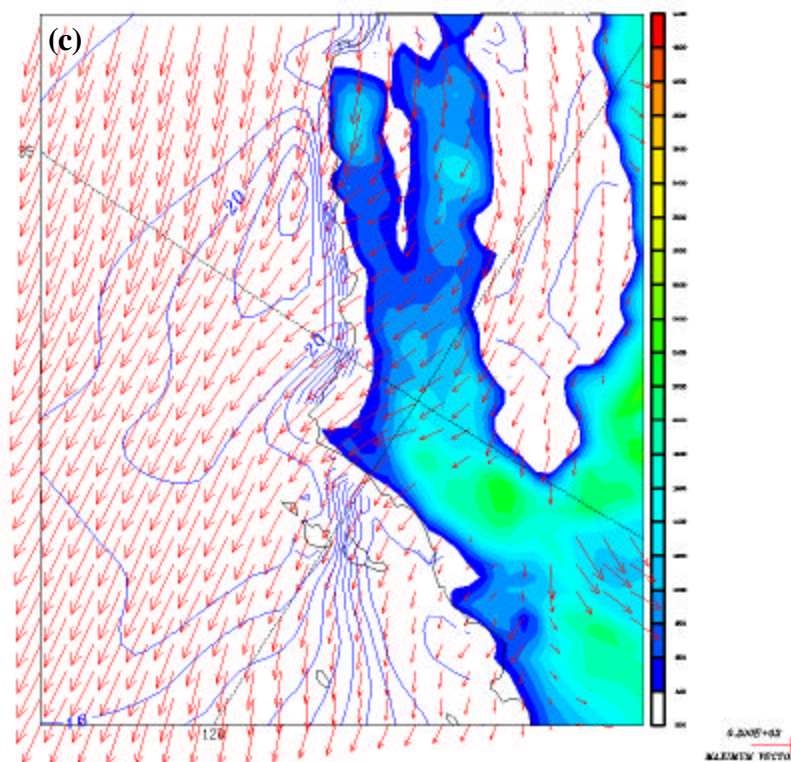


Figure 55. Continued.

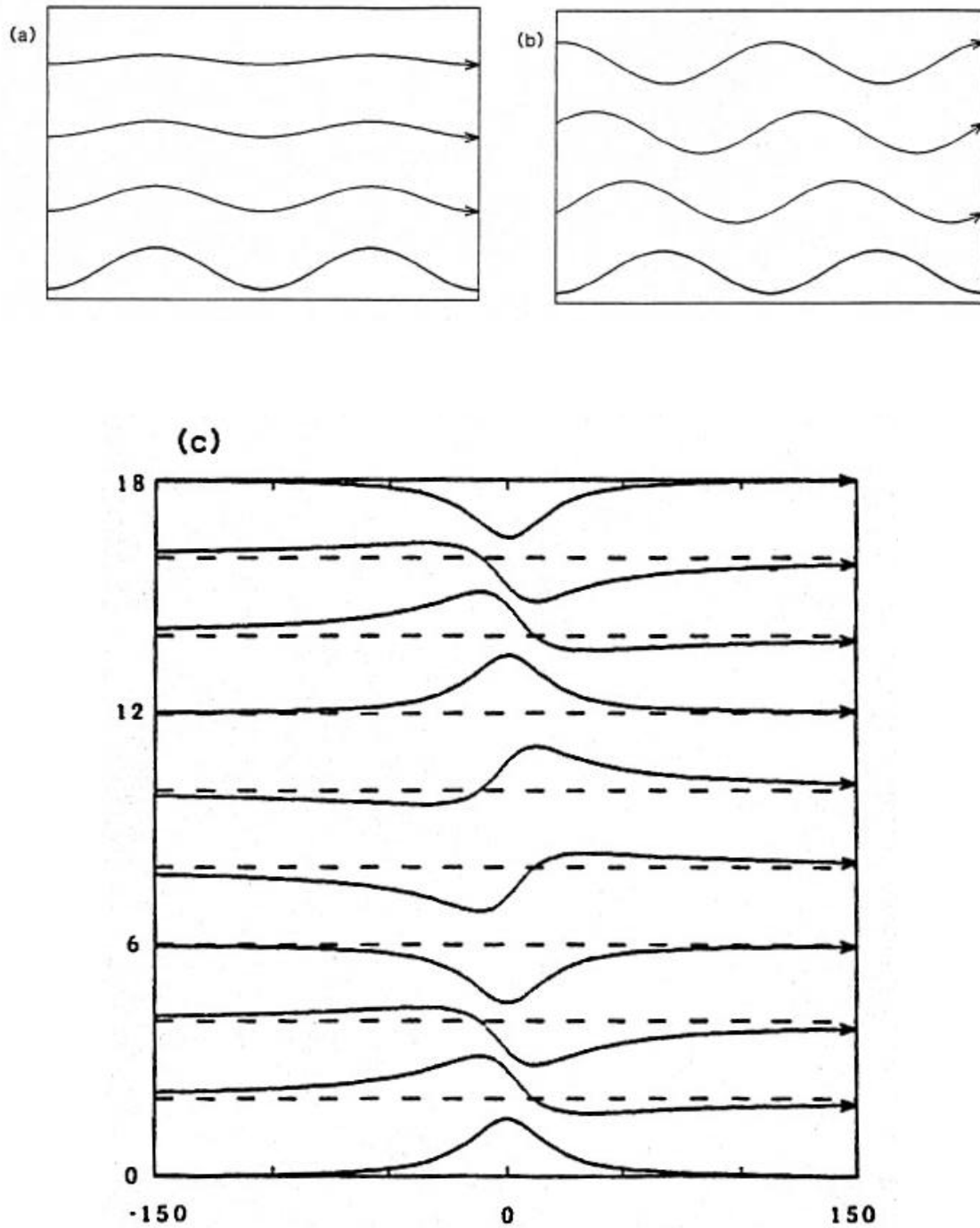


Figure 56. Theoretical mountain wave solutions for the case of (a) a sinusoidal series of infinite mountain ridges with $aL \ll 1$, (b) a sinusoidal series of mountains with $aL \gg 1$, and (c) a bell-shaped ridge (from Durran 1986).

VIII. CONCLUSIONS AND RECOMMENDATIONS

A. PROJECT SUMMARY

The low-level wind feature known as the California coastal jet is examined in detail, which is expected to contribute to improved forecasts of low-level winds off the United States west coast. Similar characteristics are to be expected in other coastal regions where cold ocean currents lie in proximity to warm land areas, such as during the southwest monsoon along the Somali coast. To achieve this better understanding of the coastal jet, an extensive data set, including land stations, offshore buoys, wind profiler data, and satellite imagery was examined. Analysis of the data suggested a direct relationship between along-shore pressure gradient and the magnitude of coastal jet winds, and (surprisingly) an inverse relationship between winds and the cross-coast pressure gradients. To explore this structure, provide a large-scale description of coastal jet tendencies, and shed light on the body of literature concerning flow interaction with coastal topography, a mesoscale model was run with a 9 km horizontal resolution in its inner nest and fairly fine vertical resolution (45 levels), particularly in the lower 1500 m of the atmosphere. The COAMPSTM model was initialized with a three-dimensional, multiquadric analysis technique that allows improved representation of key coastal atmospheric structures over traditional analysis methods. The model output was compared with available in situ data and with respect to the observations from previous studies, and was found to produce mesoscale structure that is generally consistent with both types of validation sets. With confidence in the model results thus established, a range of inferences have been made relative to the evolution of the coastal marine boundary layer and associated coastal jet winds based on the three COAMPSTM integrations.

B. CONCLUSIONS

The coastal jet, which is defined as the region of increased coast-parallel, low-level winds adjacent to the continent with the maximum winds in the thermal inversion at the top of a well-mixed boundary layer, has very large spatial extent. In the past, it has been described primarily in terms of its near-shore response near capes and points.

However, the COAMPSTM model predictions indicate the coastal jet is a broad feature whose existence depends only on the frequently occurring juxtaposition of offshore high pressure and a thermal low over the adjacent land. In these predictions, the jet can extend 500 km or more offshore and generally has a length roughly equal to the length of the California coastline.

The position along the coast of this broad region of increased winds is governed by the synoptic-scale circulation, and specifically the extension of the 850 mb ridge to the northeast of the eastern North Pacific high, which is another persistent feature of the summertime synoptic pattern. The location of the axis of this ridge with respect to the coast governs the establishment of the downcoast low-level pressure gradient necessary for the inception of coastal jet winds. When the 850 mb ridge axis is shifted to the north, the region of higher winds is initiated farther north well up the Oregon coast. Such a ridge position results in surface isobars farther south attaining a more coast-parallel orientation, such that the downgradient flow is directed into the topography, which results in weaker winds. As mentioned in Chapter VII, there may also be a tendency for the weaker winds to occur more abruptly in relation to an offshore extension of marine layer deepening associated with flow impingement on topography. An 850 mb ridge axis located farther south results in the higher wind region beginning farther south and the jet reaches maximum speeds farther south.

Increased winds due to the presence of a warm continent are not limited to the boundary layer and inversion. Coast-parallel winds that are elevated above regional means are consistently seen well above the marine layer, both near the shore over topography and well offshore. This acceleration of winds aloft is particularly evident late in the diurnal heating cycle, as the large-scale thermal contrast between land and sea is extended to greater heights (thermal low reaches higher), but is evident at other times of day as well.

Jet winds increase from offshore toward the coast in association with decreased marine layer depth. This marine layer depth change is quite gradual well offshore, but can be much sharper near the coast, especially in the late afternoon and early evening, and more so downstream of a significant coastal topographic feature.

The coast of southern Oregon and California is characterized by significant topography along most of its length. However, six locations are identified with particularly high terrain (i.e., well above the normal height of the marine boundary layer and inversion) within 20 km of the shoreline. Each of these locations is shown to induce a characteristic response in the marine boundary layer structure and thus an alteration of the near-shore wind pattern. On the north side of such a topographic feature, the flow within the marine layer is slowed in response to a localized decrease or reversal in the downcoast pressure gradient caused by the combined effects of marine layer deepening, adiabatic cooling of air at higher levels rising up the terrain, and the higher pressure associated with flow impingement on the upwind side of a mountain. Near the top of the terrain, the flow remains relatively unperturbed until it reaches the mountain top, and then it is accelerated down the lee slope, which causes adiabatic warming and a downstream compression of the cool marine layer. These effects combine to lower the near-surface pressure, which causes an acceleration of wind in the boundary layer and inversion.

The low-level flow over the coastal topography has an offshore extension represented by an area of elevated isentropes and upward deflections in the streamlines. Although this flow response decays with distance from the terrain, it can extend well offshore. Even 100 km or more from the shoreline, the flow that is forced up and over these features can result in similar downstream accelerations far from the coastal mountain that generated them. This offshore and downstream extension accounts for the large size of these lee acceleration regions, especially on days when the incident flow is strong. In fact, the upward and downward slopes in the isentropes, the acceleration of the flow downstream, and the size of the downstream wind maximum (and upstream minimum) all appear directly proportional to the magnitude of the incident flow.

A response to the coastal flow over topography extends to considerable heights above the marine layer. A vertically propagating wave with upstream tilt is predicted in each case where sufficiently strong flow passes over one of the six coastal topographic features discussed. This response is shown to be consistent with mountain wave theory. Extending this two-dimensional wave theory to the three-dimensional atmosphere as simulated in the model, it can be seen that each mountain-induced wave has a

considerable offshore and downstream extent. This offshore extension of the wave corresponds to the elevated isentropes and then sharp isentrope descents mentioned above. Evidence of the disturbance in the flow caused by interaction with the mountain is seen in the model to a distance of approximately one Rossby radius of deformation, at a characteristic angle downstream, due to the supercritical nature of the flow. Due to divergence in the marine layer on the downstream side of the wave, isentropes are slow to rebound to near their upstream heights, which accounts for the large spatial extent of the low-level wind maxima.

Close to shore, the area of lower pressures and shallow marine layer depth downstream of a coastal topographic feature may or may not be accentuated by the expansion of supercritical flow around an associated coastal bend. In the case of flow in the lee of the southern Oregon mountains on 9 June, a jet structure is predicted in the winds even though there is very little flow over the topography. This case suggests the predominance of expansion fan dynamics on that day at that location. It is therefore concluded that at locations along the coast where there is a coastal bend in close proximity to the six topographic features mentioned, a combination of supercritical expansion and mountain wave dynamics may be occurring. Both cause a lee-side lowering of pressures, shallowing of the marine layer, and increased winds near the coast. However, it is the mountain wave that accounts for the large extension of these features offshore and downstream, as clearly seen in the presence of these waves in the offshore isentropic surfaces.

The results of this study can be of immediate use for improved forecasts in coastal regions, particularly those analogous to the California coast. With an understanding of where to expect increased coastal winds with respect to the synoptic 850 mb pattern, combined with an understanding of the nature of the flow interaction with each of the six coastal topographic features mentioned herein, a forecaster has the ability to produce a wind forecast of considerable fidelity and skill. That is, given the consistent existence of a coastal jet in summer and that mesoscale structure is driven largely by geographically fixed objects, improved forecasts are possible.

C. RECOMMENDATIONS FOR FURTHER STUDY

Several avenues are suggested for more extensive study of these coastal wind phenomena, and their relationship to other coastal processes. First, and perhaps most importantly, a more complete data collection is needed, particularly well offshore and in the vicinity of each of the six coastal topographic features, to refine the interplay between supercritical flow response, flow blocking, and mountain wave dynamics. Remote sensing of coastal MBL structure with offshore wind profilers, further lidar collection from aircraft (or other technologies that allow three-dimensional representation) of marine layer inversion height distributions, and close examination of cloud structure in high-resolution satellite imagery promise to shed light on the exact nature of the flow interaction with the coastal mountains. Also, measurements of the flow over those mountains, particularly with mountaintop and lee-side measurements, would be most beneficial in terms of better quantifying the relationship between the incident flow and the downstream response. Aircraft mapping of the offshore extension of one or more of these mountain waves would provide valuable model validation, and allow a better quantification of these offshore effects.

Further modeling studies with finer horizontal resolution are recommended to more accurately capture the small-scale details of the response to coastal terrain. Specifically, the nature of the sharp decreases in wind speeds on the upstream side of the topography, and the character of near-shore, weak wind areas downstream are not adequately represented with 9 km resolution.

A variety of model sensitivity studies is recommended to test some key hypotheses related to jet behavior near coastal topography. Specifically, removal of the diurnal heating cycle would clarify the nature of the diurnal cycle of winds near the coast. It is expected that in the presence of a warm continent at a constant temperature, the jet features found in this study would continue very consistently, as they are directly tied to fixed topographic features.

As mentioned in Chapter VI, the lee acceleration and low-level wind maximum south of the Santa Cruz Mountains appear in the model to be unable to fully establish themselves before the flow encounters the high terrain south of the Monterey Peninsula, which forces it to ascend and slow aloft, increases the surface pressures and similarly

slows the winds near the surface in the southern Monterey Bay. This suggests a sensitivity study in which the terrain is removed south of Monterey Bay. The expected result is winds at and above the surface near the city of Monterey that would be much higher than modeled in this study or routinely observed.

A third sensitivity study is suggested in which the model coastline is replaced by an idealized straight coastline, or perhaps a series of three straight coastlines – from Oregon to Cape Mendocino, from Cape Mendocino to Point Conception, and from Point Conception southward. Topography would be retained in the same positions, but lesser coastal bends, such as those at Point Arena, Point Sur, and near Monterey Bay would be eliminated. Given the finding here that a coastal bend is not required for the creation of distinct low-level wind maxima, it is expected that while the magnitude and spatial extent of the low-level wind features would be somewhat altered by the removal of supercritical expansion effects, their existence and approximate position relative to the coastal mountains would not.

A more complete understanding of the coastal jet requires consideration of other coastal processes, and particularly the land-sea breeze circulations that occur along much of the coast. These circulations clearly exist on several scales, from a localized mountain-valley breeze along the Big Sur or Mendocino coasts to the effect of heating over the coastal mountains, the Salinas Valley (affecting the winds near Monterey Bay), the Central Valley (with its major effect along the entire coast, but especially near the mouth of San Francisco Bay), to the large-scale heating of the Sierras and the entire desert interior. These circulations on varying scales make it difficult to predict the diurnal signal in pressure patterns and wind response. Characterization of the effects of each of these scales of heating at a given location promises to lend much to our understanding of the winds offshore, both at a given beach and in the large-scale coastal jet.

No attempt was made here to relate these wind patterns to the cloud distribution. The effects of the winds discussed here on the boundary layer cloud pattern, and the feedback effects of that pattern on the winds, are another area recommended for extensive study. Of note, the satellite image in Fig. 22b (top) from the afternoon of 14 June reveals a pattern of clear skies in the north and extensive stratus cover farther south that is

associated with a deeper marine layer and weaker winds, as discussed. The northern edge of these clouds coincides with the increase in marine layer depth, which appears to be tied, at least in part, to strong flow to the north encountering the Santa Cruz Mountains on that day. This is just one example of the potential for expanding the improved understanding of topographic flow interaction to improved forecasts of the cloud and moisture distribution.

Finally, forcing an ocean model with high-resolution winds that are consistent with a mountain wave response promises to yield improved understanding of near-shore ocean processes. In particular, the prediction of coastal upwelling events should be significantly improved by forcing with winds that are accentuated in the correct locations with respect to the major coastal mountains.

THIS PAGE INTENTIONALLY LEFT BLANK

LIST OF REFERENCES

- Beardsley, R.C., C.E. Dorman, C.A. Friehe, L.K. Rosenfeld, and C.D. Winant, 1987: Local atmospheric forcing during the Coastal Ocean Dynamics Experiment: A description of the marine boundary layer atmospheric conditions over a Northern California upwelling region. *Journal of Geophysical Research*, **92**(C2), 1467-1488.
- Bunker, A.F., 1965: A low-level jet produced by air, sea, and land interactions. *Report 1*, Sea-Air Interaction Lab, Washington, D.C., 225-238.
- Burk, S.D., and W.T. Thompson, 1996: The summertime low-level jet and marine boundary layer structure along the California coast. *Monthly Weather Review*, **124**, 668-686.
- Chao, S.Y., 1985: Coastal jets in the lower atmosphere. *Journal of Physical Oceanography*, **15**, 361-371.
- Dorman, C.E., 1985: Hydraulic control of the northern California marine layer (abstract). *EOS Transactions*, **66**, American Geophysical Union, 914.
- Dorman, C.E., and C.D. Winant, 1995: Buoy observations of the atmosphere along the west coast of the United States, 1981-1990. *Journal of Geophysical Research*, **100**, 16029-16044.
- Dorman, C.E., D.P. Rogers, W.A. Nuss, and W.T. Thompson, 1999: Adjustment of the summer marine boundary layer around Point Sur, California. *Monthly Weather Review*, **127**, 2143-2159.
- Durran, D.R., 1986: Mountain waves. *Mesoscale Meteorology and Forecasting*, P.S. Ray, Editor, American Meteorological Society, 472-492.
- Elliott, D.L., and J.J. O'Brien, 1977: Observational studies of the marine boundary layer over an upwelling region. *Monthly Weather Review*, **105**, 86-98.
- Enfield, D.B., 1981: Thermally driven wind variability in the planetary boundary layer above Lima, Peru. *Journal of Geophysical Research*, **86**, 2005-2016.
- Gerber, H., S. Chang, and T. Holt, 1989: Evolution of a marine boundary layer jet. *Journal of Atmospheric Science*, **46**, 1312-1326.
- Grossman, R.L., and C.A. Friehe, 1985: Vertical structure of the southwest monsoon low-level jet over the Arabian Sea. *Journal of Atmospheric Science*, **42**, 1312-1326.

- Hardy, R.L., 1971: Multiquadric equations of topography and other irregular surfaces. *Journal of Geophysical Research*, **76**, 1905-1915.
- Hodur, R.M., 1997: The Naval Research Laboratory's coupled ocean/atmosphere mesoscale prediction system (COAMPS). *Monthly Weather Review*, **125**, 1414-1430.
- Hogan, T.F., and T.E Rosmond, 1991: The description of the U.S. Navy Operational Global Atmospheric Prediction System's spectral forecast model. *Monthly Weather Review*, **119**, 1786-1815.
- Johnson, A., and J.J. O'Brien, 1973: A study of an Oregon sea breeze event. *Journal of Physical Oceanography*, **5**, 761-772.
- Klemp, J., and R. Wilhelmson, 1978: The simulation of three-dimensional convective storm dynamics. *Journal of Atmospheric Science*, **35**, 1070-1096.
- Large, W.G., and S. Pond, 1981: Open ocean momentum flux measurements in moderate to strong winds. *Journal of Physical Oceanography*, **11**, 324-481.
- Lester, P.F., 1985: Studies of the marine inversion over the San Francisco Bay area: A summary of the work of Albert Miller, 1961-1978. *Bulletin of the American Meteorological Society*, **66**(11), 1396-1402.
- Liu, W.T., K.B. Katsoros, and J. Businger, 1979: Bulk parameterization of air-sea exchange of heat and water vapor including the molecular constraints at the interface. *Journal of Atmospheric Science*, **36**, 1722-1735.
- Louis, J.F., 1979: A parametric model of vertical eddy fluxes in the atmosphere. *Boundary Layer Meteorology*, **17**, 187-202.
- Mellor, G.L., and T. Yamada, 1972: Development of a turbulence closure for geophysical fluid problems. *Reviews of Geophysical Space Physics*, **20**, 851-875.
- Nuss, W.A., and D.W. Titley, 1994: Use of multiquadric interpolation for meteorological objective analysis. *Monthly Weather Review*, **122**, 1611-1631.
- Parish, T.R., 2000: Forcing of the summertime low-level jet along the California coast. *Journal of Applied Meteorology*, **39**, 2421-2433.
- Reynolds, D.W., 1998: Regional scale model simulations of the California coastal jet: Comparisons with a near shore and offshore boundary layer wind profiler. Second Conference on Coastal Atmospheric and Oceanic Prediction and Processes, Phoenix, AZ, American Meteorological Society Preprints, J26-J29.

- Rogers, D.P., C.E. Dorman, K.A. Edwards, I.M. Brooks, W.K. Melville, S.D. Burk, W.T. Thompson, T. Holt, L.M. Strom, M. Tjernstrom, B. Grisogono, J.M. Bane, W.A. Nuss, B.M. Morley, and A.J. Schanot, 1998: Highlights of Coastal Waves 1996. *Bulletin of the American Meteorological Society*, **79**, 1307-1326.
- Samelson, R.M., 1992: Supercritical marine-layer flow along a smoothly varying coastline. *Journal of Atmospheric Science*, **49**, 1571-1584.
- Strom, L., M. Tjernstrom, and D.P. Rogers, 1999: Observed dynamics of topographically forced flow at Cape Mendocino during Coastal Waves 1996. *Journal of Atmospheric Science*, submitted.
- Winant, C.D., C.E. Dorman, C.A. Friehe, and R.C. Beardsley, 1988: The marine layer off northern California: An example of supercritical channel flow. *Journal of Atmospheric Science*, **45**, 3588-3605.
- Zemba, J., and C.A. Friehe, 1987: The marine atmospheric boundary layer jet in the Coastal Ocean Dynamics Experiment. *Journal of Geophysical Research*, **92**, 1489-1496.

THIS PAGE INTENTIONALLY LEFT BLANK

INITIAL DISTRIBUTION LIST

1. Defense Technical Information Center
Ft. Belvoir, Virginia
2. Dudley Knox Library
Naval Postgraduate School
Monterey, California
3. Dr. Wendell A. Nuss
Department of Meteorology
Naval Postgraduate School
Monterey, California
4. Dr. Carlyle H. Wash
Department of Meteorology
Naval Postgraduate School
Monterey, California
5. Dr. Russell L. Elsberry
Department of Meteorology
Naval Postgraduate School
Monterey, California
6. Dr. Qing Wang
Department of Meteorology
Naval Postgraduate School
Monterey, California
7. Dr. Leslie K. Rosenfeld
Department of Oceanography
Naval Postgraduate School
Monterey, California
8. Dr. Douglas Miller
Department of Meteorology
Naval Postgraduate School
Monterey, California
9. Dr. Kenneth L. Davidson
Department of Meteorology
Naval Postgraduate School
Monterey, California

10. Dr. Robert L. Haney
Department of Meteorology
Naval Postgraduate School
Monterey, California
11. Dr. Roger T. Williams
Department of Meteorology
Naval Postgraduate School
Monterey, California
12. Dr. Roland Garwood
Department of Oceanography
Naval Postgraduate School
Monterey, California
13. Mr. Robert Creasey
Department of Meteorology
Naval Postgraduate School
Monterey, California
14. Ms. Mary Jordan
Department of Meteorology
Naval Postgraduate School
Monterey, California
15. Commander
Naval Meteorology and Oceanography Command
Stennis Space Center, Mississippi
16. Commanding Officer
Naval Oceanographic Office
Stennis Space Center, Mississippi
17. Oceanographer of the Navy
Naval Observatory
Washington, D.C.
18. LCDR Patrick S. Cross
Aiea, Hawaii
19. Commander
Submarine Forces, U.S. Pacific Fleet
Pearl Harbor, Hawaii
20. Commanding Officer
Naval Pacific Meteorology and Oceanography Center

San Diego, California

21. National Weather Service Forecast Office
Monterey, California

22. Mr. Forrest Williams
Carmel Valley, California